

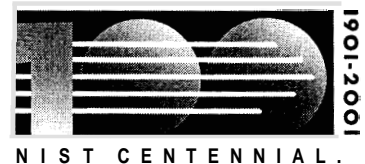
NIST GCR 01-827

Measurements of Temperature in a Hot Gas Laden with Water Droplets

P. Rufino

M. di Marzo

*Department of Mechanical Engineering
Department of Fire Protection Engineering
University of Maryland
College Park, MD 20742*



NIST

National Institute of Standards and Technology
Technology Administration, U.S. Department of Commerce

NIST GCR 01-827

Measurements of Temperature in a Hot Gas Laden with Water Droplets

Prepared for
U.S. Department of Commerce
Building and Fire Research Laboratory
National Institute of Standards and Technology
Gaithersburg, MD 20899

By
P. Rufino
M. di Marzo
Department of Mechanical Engineering
Department of Fire Protection Engineering
University of Maryland
College Park, MD 20742

August 2001
Issued September 2001

U.S. Department of Commerce
Donald L. Evans, Secretary

National Institute of Standards and Technology
*Karen H. **Brown**, Acting Director*

Notice

This report was prepared for the Building and Fire Research Laboratory of the National Institute of Standards and Technology under Grant number 60NANB8D0012. The statement and conclusions contained in this report are those of the authors and do not necessarily reflect the views of the National Institute of Standards and Technology or the Building and Fire Research Laboratory.

MEASUREMENTS OF TEMPERATURE IN A HOT GAS LADEN WITH WATER DROPLETS

P. Rufino, M. di Marzo

Department of Mechanical Engineering
Department of Fire Protection Engineering
University of Maryland
College Park, MD 20742

Prepared for the
Building and Fire Research Laboratory
National Institute of Standards and Technology
as the final report of Grant #60NANB8D0012
for the period May 2, 1999 to August 31, 2001

August 2001

ABSTRACT

Arrays of fire sprinklers are installed in buildings to protect property and occupants against the damages of fire. When a fire occurs, the sprinkler closest to the fire location typically activates first and releases water droplets into the rising plume of hot gases. Part of these droplets is entrained by the plume and may impact on adjacent sprinklers providing evaporative cooling and thus delaying their activation. The current model that simulates the thermal response of fire sprinklers does not include this evaporative cooling effect. Therefore, a new model is proposed to extend the applicability of the previous formulation. The new model includes one parameter, determined experimentally, that is associated to the evaporative cooling effect. Commercially available sprinklers are tested to assess the accuracy of the proposed model for a range of boundary conditions. The sprinkler activation times predicted by the model are found to be in good agreement with the measurements, within the experimental uncertainties. A new methodology to measure the gas temperature and the water volumetric fraction of a gas-water flow is also implemented and the results are compared with those gathered by optical techniques.

FOREWORD

This report describes the research performed during the period May 2, 1999 – August 31, 2001 at the University of Maryland. The research was conducted by Paolo Ruffino with the assistance of Greg Anderson, Kevin Kefauver, Brian Ringwelski and Michael Shaffer under the supervision of Dr. Marino di Marzo. The authors are indebted to Dr. Filippo Gavelli, for his contribution to the design, construction and operation of the ECSAT facility and to Drs. Jungho Kim and Greg Walsh for their guidance in the development of the control system, power supply and data acquisition of the ALTEC sensor. The support and encouragement of Drs. David Evans and Kevin McGrattan of BFRL-NIST during this project were greatly appreciated. This report also constitutes the doctoral dissertation of Paolo Ruffino, which has been successfully defended in July 2001. The ALTEC sensors as well as the wetted sensor are the subjects of a provisional patent application.

TABLE OF CONTENTS

ACKNOWLEDGEMENTS	III
TABLE OF CONTENTS	IV
LIST OF TABLES	VIII
LIST OF FIGURES	IX
NOMENCLATURE	XV
INTRODUCTION	1
FIRE SPRINKLERS	2
Operating elements	4
Sprinkler activation.....	6
Deflector design	7
Rating of Automatic Sprinklers	7
Activation time delay and Response Time Index	8
Overview on the design of a sprinkler array	10
MOTIVATION AND OBJECTIVE OF THE WORK	11
OUTLINE OF THE WORK	13
LITERATURE REVIEW	15
FIRE SPRINKLER TECHNOLOGY.....	16

FIRE PLUME	22
EVAPORATIVE COOLING.....	26
EVAPORATION PROCESS	32
LEIDENFROST TRANSITION PHENOMENA	47
MATHEMATICAL MODEL	56
RTI MODEL.....	56
EVAPORATIVE COOLING MODEL	62
Droplet collection efficiency	66
Modified sprinkler response time	73
Additional remarks	75
EXPERIMENTAL FACILITY	77
FACILITY SET-UP	77
UNIFORMITY OF THE TEST SECTION	83
BLOWER	86
GAS BURNER	87
WATER SPRAY NOZZLES	90
TEST SECTION AND SIMULATED SPRINKLER LINK.....	92
MEASUREMENT TECHNIQUES	94
REFORMULATION OF THE PROBLEM.....	95
DETERMINATION OF EXPERIMENTAL QUANTITIES.....	98
TEMPERATURE MEASUREMENTS	99
OPTICAL MEASUREMENTS	102
GAS VELOCITY MEASUREMENTS.....	105
GAS TEMPERATURE MEASUREMENTS.....	106
DETERMINATION OF THE FUNCTION $F(X)$	114
WATER VOLUMETRIC FRACTION MEASUREMENTS	118
Evaporation process calculation	120

Final expression of the water volumetric fraction.....	128
Analysis in support of the experimental approach.....	129
Theoretical estimate of the volumetric fraction	132
MODEL AND DATA COMPARISON	135
VALIDATION OF THE DROPLET EVAPORATION MODEL	136
Numerical model and results	136
SPRINKLER LINK TEMPERATURE MEASUREMENTS	143
EXPERIMENTAL PROCEDURE	145
Test matrix	146
DATA ANALYSIS	150
Determination of the RTI and the parameter C	151
Dependency of RTI and parameter C on the link size.....	155
Additional considerations.....	159
TESTS ON COMMERCIAL SPRINKLERS	161
Determination of the sprinkler time of activation	162
Concept of equivalent diameter	163
Sprinklers types and experimental conditions	165
Commercial sprinklers - Experimental procedure	169
Results.....	171
SIMULATION OF COMMERCIAL SPRINKLERS.....	176
A NOVEL APPROACH TO TEMPERATURE AND VOLUMETRIC FRACTION	
MEASUREMENTS	185
OBJECTIVES AND PROOF-OF-CONCEPT	186
THE INFLUENCE OF DROPLETS ON SENSORS	187
LEIDENFROST TRANSITION VERSUS GAS VELOCITY	192
DEVELOPMENT OF THE SENSOR.....	194
PROTOTYPE	194

Gas temperature measurement	196
Gas velocity determination.....	202
INFLUENCE OF RADIATION ON THE MEASUREMENT.....	203
INTERMEDIATE DESIGN OF THE SENSOR.....	207
Control system	209
Measurement theory	213
Design feasibility	222
ALTEC sensor experiments	223
WATER VOLUMETRIC FRACTION MEASUREMENT	226
Collection Efficiency	229
Sensor Time Constant	230
Determination of the optimal vet sensor size.....	232
Experiments and results	233
FINAL DESIGN OF THE ALTEC SENSOR	235
Design of the board	237
CONCLUDING REMARKS	240
CONCLUSIONS.....	242
APPENDIX 1 _DROPLET EVAPORATION THEORY	246
APPENDIX 2 _CONFIRMATION OF THE OPTICAL MEASUREMENTS	257
APPENDIX 3 _EES CODE	258
BIBLIOGRAPHY	260

LIST OF TABLES

Table 1. Classification of automatic sprinklers	8
Table 2. <i>RTI</i> for commercially available fire sprinklers	9
Table 3. Performance characteristics of PJ8 and PJ10 nozzles (@ 482 kPa)	91
Table 4. Determination of the initial droplet mean volume. cold condition	123
Table 5. Test conditions	149
Table 6. Physical properties of several sprinkler link materials	164
Table 7. <i>RTI</i> [$\text{m}^{1/2} \text{s}^{1/2}$] of the sprinklers used in the study	166
Table 8. Test matrix	168
Table 9. Sprinkler time of activation [s]: model predictions and experiments	174
Table 10. Test conditions and results	179
Table 11. Radiation measurements (¹ calculated values)	206

LIST OF FIGURES

Figure 1 . Solder-type sprinklers.....	5
Figure 2. Bulb-type sprinklers	5
Figure 3. Schematic of a lever automatic sprinkler	6
Figure 4. Facility used in the experiments at FRMC. Test section is 0.3 m wide by 0.15 m high	18
Figure 5. Two-layer fire scenario investigated by Cooper (1995).....	20
Figure 6. Fire scenario studied by Alpert in 1972	23
Figure 7. Temperature and velocity distribution in a fire plume near the ceiling	25
Figure 8. Typical surface temperature distribution on aluminum and macor for a) t/t _{evap} =0.3 and b) t/ t _{evap} =0.9	29
Figure 9. Experimental setup (diMarzo & Tinker, 1995)	30
Figure 10. Average surface temperature transient (0 experimental points, ♦ numerical points). Initial surface temperature 131 °C (top), 151 °C (bottom); water mass flux 0.50 g m ⁻² s ⁻¹ (top), 0.96 g m ⁻² s ⁻¹ (bottom)	31
Figure 11. Schematic of experimental set-up for deposition tests	34
Figure 12. Physical model investigated by Fu and Yang (1989).....	37
Figure 13. Temperature distributions for various droplet diameters (Fossa, 1995) .	41

Figure 14. Bi-directional probe and response of the probe versus Reynolds number	
.....	45
Figure 15. Experimental arrangement for free jet tests	46
Figure 16. Variation of the Leidenfrost transition with pressure	48
Figure 17. Configuration of the problem studied by Yao et <i>al.</i> (1988)	50
Figure 18. Boiling regimes and Leidenfrost transition definition (Bernardin et <i>al.</i> , 1997).....	52
Figure 19. Experimental apparatus used by Bernardin (1997)	53
Figure 20. Critical heat flux and Leidenfrost transition in the plane Temperature- Weber number (Velocity) for various droplet impacting frequencies	54
Figure 21. Heat transfer between hot gas and fire sprinkler.....	57
Figure 22. Calculated gas streamlines and trajectories of 1 mm dia. droplets injected by a spray nozzle on the axis of a fire plume (Alpert. 1984).....	63
Figure 23. Diagram for the evaporative cooling model	64
Figure 24. Potential flow solution for the gas flow around the sprinkler link.....	67
Figure 25. Trajectory of water droplets for different values of Z	70
Figure 26. Collection efficiency as a function of the droplet inertia	72
Figure 27. Layout of the ECSAT facility	79
Figure 28. Flow field across the circular orifice	80
Figure 29. Position of the measurement rake and temperature distribution in the test section (dry conditions top, wet conditions bottom)	84
Figure 30. Water uniformity check	85
Figure 31. Pictures of the test section for various angles of the mirror M	85

Figure 32. Gas exhaust blower	86
Figure 33. Natural gas burner	88
Figure 34. Gas burner control diagram	89
Figure 35. Water spray setup	91
Figure 36. PJ8 spray nozzle	92
Figure 37. Diagram of the test section	93
Figure 38. Location of the thermocouples in proximity of the test section (dimensions in meters)	101
Figure 39. Optical set-up for velocity and water volumetric fraction measurements	102
Figure 40. Snapshot of the water droplets in the gas stream (negative)	104
Figure 41. Temperature distributions along the duct and gas temperature estimate (3 PJ8 nozzles, top and 1 PJ10 nozzle, bottom. $U=3.8$ m/s in both cases)	108
Figure 42. Determination of x_E	111
Figure 43. Fit of the experimental points ($\lambda=1.6$)	112
Figure 44. $f(x)$ versus the coordinate x along the duct ($\lambda=1.5$)	117
Figure 45. Droplet size distribution (courtesy of Bete Fog Nozzle, Inc.)	119
Figure 46. Droplet mean volume during the evaporation process	127
Figure 47. Water volumetric fraction versus the gas velocity	131
Figure 48. Typical temperature distributions in <i>dry</i> and wet conditions	133
Figure 49. Gas temperature profile in dry and wet conditions ($U=7.1$ m/s)	140
Figure 50. Temperature difference between dry and wet conditions ($U=5.6$ m/s) .	142
Figure 51. Temperature difference between dry and wet conditions ($U=6.7$ m/s) .	142

Figure 52. Temperature difference between dry and wet conditions ($U=7.1$ m/s) .	143
Figure 53. Measure of RTI from dry condition tests	152
Figure 54. RTI values for different tests ($d = 6.4$ mm)	152
Figure 55. Determination of the evaporative cooling parameter	154
Figure 56. Values of parameter C for various gas conditions	154
Figure 57. RTI for different brass cylinders, same operative condition	158
Figure 58. Parameter C for different brass cylinders, same operative condition ...	158
Figure 59. Fit to determine the evaporative cooling constant C	160
Figure 60. Commercial sprinklers (clockwise from top-left SE, SR, QR, QE)	167
Figure 61. Sprinkler QE: different orientations	167
Figure 62. Sprinkler frame	171
Figure 63. Measured times of activation (SE sprinkler. Condition B. ♦dry, 0 wet)	172
Figure 64. Sprinkler time of activation: comparison between the predictions of model and the experimental data.....	175
Figure 65. Results for Condition G: SE sprinkler (top). SR sprinkler (middle). QR sprinkler (bottom).....	182
Figure 66. Results for Condition H: SE sprinkler (top). SR sprinkler (middle). QR sprinkler (bottom).....	184
Figure 67. Heat exchanges between a droplet, the gas flow and a wire	188
Figure 68. Leidenfrost transition versus Weber number and the droplet frequency (in droplets per minute) according to Bernardin et al. (1997)	193
Figure 69. Preliminary sensor configuration	195

Figure 70. Control system of each heater in the preliminary sensor	196
Figure 71. Dry condition results: evaluation of the constants in Equation (7.15) ..	200
Figure 72. Comparison between two different methodologies	201
Figure 73. Comparison between the results obtained with the CTA and the PTV technique	203
Figure 74. Intermediate design of the sensor _supporting frame	208
Figure 75. Detail of the connection between the wire and the copper round	209
Figure 76. Control wiring scheme	211
Figure 77. Heaters' temperature versus the hot gas temperature (calculated values)	212
Figure 78. Linearity of $g(w)$	218
Figure 79. Calibration curve: <i>dry</i> and wet results	220
Figure 80. Velocity-temperature correlation for a natural convection plume versus the ECSAT facility operating conditions.....	221
Figure 81. Comparison between the temperature measured by the ALTEC sensor and the values read by a thermocouple in dry conditions	223
Figure 82. Temperature comparison in wet conditions.....	225
Figure 83. Wires temperature versus the gas temperature (experimental results) ..	226
Figure 84. Dependency of the evaporative cooling on the diameter	228
Figure 85. Collection efficiency as a function of the diameter	230
Figure 86. Time response of a cylinder versus its diameter ($T_G=150\text{ }^{\circ}\text{C}$, $U=4\text{ m/s}$)	231
Figure 87. Experimental results for the water volumetric fraction readings	234

Figure 88 . Final version of the control board	236
Figure 89 . Modification of the wire support terminals	239
Figure 90 . Final assembly of the ALTEC sensor	239

NOMENCLATURE

a	thermal diffusivity, $\text{m}^2 \text{s}^{-1}$
A	cross-sectional area orthogonal to the gas flow, m^2
b, b'	exponent in Equations (7.11) and (7.13)
B	mass transfer number, $B = \frac{c_p \cdot (T_G - T_d)}{A}$
Bi	Biot number, $Bi = \frac{h \cdot L}{k_s}$
c, c_p	specific heat, specific heat at constant pressure, $\text{J kg}^{-1} \text{ } ^\circ\text{C}^{-1}$
C	evaporative cooling parameter, $^\circ\text{C s}^{1/2} \text{ m}^{-1/2}$
C_1, C_2, C_3	constants
\hat{C}	evaporative cooling constant, $^\circ\text{C s}^{1/2} \text{ m}^{-1}$
C_D	drag coefficient
d	simulated sprinkler link diameter or cylinder diameter, m
D	characteristic diameter of the water droplet distribution, m
$f(x)$	ratio between water volumetric fraction at location x and initial volumetric fraction
\bar{f}	force acting on the unit volume, N m^{-3}
F, F'	coefficients in Equations (7.11) and (7.13)

$F_{H,C}$	sight factor between hot and cold wire
G	specific mass flow rate, $\text{kg (s m}^2\text{)}^{-1}$
h	convective heat transfer coefficient, $\text{W m}^{-2} \text{ }^\circ\text{C}^{-1}$
H	ceiling height, m
H^*	ratio of the ceiling height by the spacing between the sprinklers
i	current, A
k	thermal conductivity, $\text{W m}^{-1} \text{ }^\circ\text{C}^{-1}$
K_1, K_2, K_3	constants
l	wire length, cm
L	length, m
m	mass, kg
m	mass flow rate, kg s^{-1}
N	number of droplet size bins
Nu	Nusselt number, $Nu = \frac{h \cdot d}{k_G}$
n	number of droplets
n_i	number of droplets in the i-th size bin
Pr	Prandtl number $Pr = \nu / \alpha$
Q	heat power, W
r	radial distance, m
R	resistance, Ohm
Re_d	Reynolds number based on the simulated sprinkler link diameter $Re_d = U \cdot d / \nu_G$
Re_D	Reynolds number based on the droplet diameter $Re_D = U \cdot D / \nu_G$

RTI	Response Time Index, $\text{m}^{1/2} \text{s}^{1/2}$
S	heat transfer surface, m^2
t	time, s
Δt	time interval, s
δt	time interval as defined in Equation (7.5), s
T	temperature, $^{\circ}\text{C}$
ΔT	asymptotic temperature difference between dry and wet distribution, $^{\circ}\text{C}$
δT	temperature correction, $^{\circ}\text{C}$
U	gas velocity, m s^{-1}
U_x, U_y	components of the gas velocity vector \vec{U} , m s^{-1}
v_x, v_y	components of the droplet velocity vector \vec{v} , m s^{-1}
V	volume, m^3
V_j^*	dimensionless residual water volume
ΔV	voltage difference, V
\dot{V}	volumetric flow rate, $\text{m}^3 \text{s}^{-1}$
V_M	droplet mean volume, m^3
V_M^*	averaged droplet mean volume, m^3
V_i	volume corresponding to i-th size droplet, m^3
x	axial coordinate along the duct, m
(x,y)	rectangular coordinate system
x_E	distance of complete evaporation from the nozzles location, m
w	ratio of resistances

We	Weber number $We = \frac{\rho \cdot U^2 D}{\sigma_{\text{sup}}}$
Z	inertia parameter as defined in Equation (3.17)

Greek

a	platinum thermal coefficient, Ohm °C ⁻¹
β	water volumetric fiaction, ppm (1 ppm = 10 ⁻⁶)
γ	platinum reference resistance, Ohm
χ	parameter in Equation (5.16), °C
E	camera shutter speed, s ⁻¹
ϵ_{rad}	emissivity
κ	collection efficiency
λ	exponent of the water volumetric fiaction evolution
μ	dynamic viscosity, Pas
$\phi, \delta, \omega, \xi, \zeta$	constants
τ	time constant, s
τ_1, τ_2	coefficients of the ALTEC calibration curve, °C
η	exponent in Equations (6.11) and (6.12)
Θ	dimensionless temperature
σ	Stefan-Boltzman constant, W m ⁻² °C ⁻⁴
σ_{sup}	superficial tension of water, N m ⁻¹

ρ	density, kg m^{-3}
ν	kinematic viscosity, $\text{m}^2 \text{s}^{-1}$
A	latent heat of vaporization of water, J kg^{-1}

Subscripts and Superscripts

0	initial time
20	measured at 20°C
A	sprinkler activation
B	bridge bottom left resistor
BS	bottom side resistor
c	critical
C	cold heater
Cell	relative to the grid cell in numerical calculations
cond	conductive
conv	convective
eq	equivalent
evap	evaporation or evaporative
d	droplet
D	dry conditions
fb	film boiling
G	gas
H	hot heater

l	laser light
L	liquid
max	largest value
rad	radiative
Ref	reference value
room	property evaluated at room condition
S	sprinkler link
TS	Test Section
U	bridge upper left resistor
V	vapor
x=0	at the location of the water nozzles
w	wire
W	wet conditions
wall	at the solid surface or wall
'	dimensionless value

Acronyms

ALTEC	Above Leidenfrost Temperature Evaporative Cooling (sensor)
CHF	Critical Heat Flux
EC	Evaporative Cooling (model)
ECSAT	Evaporative Cooling Sensor Accuracy Test (facility)
LFP	Leidenfrost point or Leidenfrost transition

QE	Quick response solder-Element sprinkler
QR	3-mm bulb Quick Response sprinkler
SE	Solder-Element sprinkler
SR	5 -mm bulb Standard Response sprinkler

Note: all the quantities will be measured or calculated in S.I. units.

CHAPTER 1

INTRODUCTION

Fire detection systems are installed in residential and commercial buildings to protect property and occupants from fire. One of the ~~most~~ important characteristics of a fire detection system is the capability to detect a fire in the early stages, when it is still small. An early detection and activation by fire suppression devices are important for two main reasons: first, because it allows more time for the evacuation of the occupants; second, because it increases the chances of successfully suppressing the fire before extensive damage is caused. In fact, small, controllable fires generally exist for more than half a minute after ignition when flames are confined by inert barriers or air gaps to a distinct portion of the total available fuel. Subsequently, there is a period of rapid fire spread to the surrounding combustible materials. The resulting fully developed fire may also be of nearly constant intensity, but large enough to endanger the building structure in the absence of a sprinkler system. It is thus desirable to detect a fire ~~as~~ soon as possible.

FIRE SPRINKLERS

Ceiling mounted devices that do not interfere with normal room arrangement are generally preferred for fire protection purposes. There are two main types of fire detection devices. The first type is actuated by radiation, which is a significant portion of the local thermal energy release in a fire. However, the most common devices depend on the movement of the hot products of combustion engulfing the **sensor**. Thermal-actuated and smoke-actuated detectors constitute the second type of detection devices. This dissertation focuses on the temperature-activated fire sprinklers with particular emphasis to the interaction between the sprinkler itself and the hot gases.

The rapid growth of business and industry in the nineteenth century and the resulting increase in fire hazards and property values brought about the need for more adequate protection against fire. Unless a fire was discovered in its early stages, simple fire protection such as water pails, standpipes and hose equipment proved inadequate. Although fire control was made easier by improving the design of building constructions, relatively little progress was made in reducing fire loss involving late detection until the advent of automatic sprinklers. Automatic sprinklers are devices that automatically distribute water on a fire in sufficient quantity either to extinguish it entirely or to prevent its spread in the case that fire is far away **from** the water discharged by sprinklers. The water is fed to the sprinklers through a system of piping, suspended from the ceiling, with the sprinklers placed at regular intervals along the pipes. The orifice of the sprinkler head is normally closed by a disk or cap held in place by a temperature sensitive releasing element.

The automatic sprinkler was designed initially in the late **1880's** to protect the flammable ceiling structures of New England textile mills from the damages of a fire. The old style sprinkler directed about half of the water upward to protect the ceiling structures, while the remaining water and that bouncing off the ceiling was directed toward the fire on the floor. Even if the sprinkler was over-dimensioned, it remained essentially unchanged until **1950**, when Factory Mutual Research Company (FMRC) developed the Spray sprinkler, recognizing the importance of the water distribution in the protection of storage facilities from fires. This type of sprinkler was designed to direct all the water toward the fire on the floor and it was later accepted by the National Fire Protection Agency (NFPA) as the Standard sprinkler in **1953**. Since World War II, there have been continuous changes in manufacturing and storage practices, especially the introduction of lift trucks to stock more materials in higher warehouses. This has dramatically increased the risk of fire in storage facilities and the challenge to sprinkler protection systems. FMRC initiated a long-range sprinkler technology research program in **1970** to study the principles of sprinkler fire protection and to provide a sound technical basis for solving the above mentioned problems. The results of the study have been used to develop new and more effective fire control and fire suppression sprinkler systems: the Large-Drop sprinkler system (**1971-1980**) to control high-challenge storage fires, the Residential sprinkler system (**1976-1979**) to maintain a survivable environment in residential areas and the Early Suppression Fast Response (ESFR) sprinkler system (**1984-1986**) to suppress rather than control high challenge fires (Yao, 1999).

Operating elements

Under normal conditions, the discharge of water from an automatic sprinkler is retrained by a cap or valve held tightly against the orifice by a system of levers and links pressing down on the cap and anchored firmly by struts on the sprinkler. In particular, we will refer to the temperature sensitive element of this system of components simply as *sprinkler link*.

A common fusible-type automatic sprinkler operates upon the fusing of a metal alloy of predetermined melting point. Various combinations of levers, struts and links are used to reduce the force acting on the solder joint so that the sprinkler will remain closed using the smallest possible amount of metal and solder in its parts. This minimizes the time of operation by reducing the mass of fusible metal to be heated. A fusible sprinkler is shown in Figure 1, where the sprinkler link is clearly visible in between the orifice cap and the deflector. The solder material used with automatic sprinklers is alloy of optimum fusibility composed principally of tin, lead, cadmium and bismuth.

A second type of operating element utilizes a frangible bulb (Figure 2). The small bulb of glass contains a liquid that does not completely fill the bulb, leaving a small gas bubble entrapped in it. As the liquid is heated up, the bubble is compressed and

absorbed by the liquid. As soon as the bubble disappears, the pressure rises rapidly and the bulb shatters, releasing the valve cap. The operating temperature depends on the amount of liquid into the **glass** bulb.

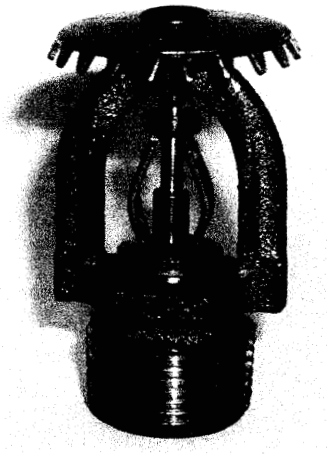


Figure 1. Solder-type sprinklers

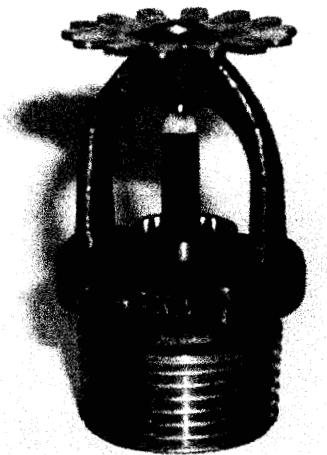


Figure 2. Bulb-type sprinklers

Sprinkler Link Ratio

Figure 3 shows how the closing force acts in the lever-type automatic sprinkler. The mechanical pressure normally exerted on the top of the cap or valve is much larger than the pressure by the water below, so that the eventuality of a water leakage is very remote. When the temperature of the sprinkler link raises to the activation temperature, the necessary force for the sprinkler to activate is produced initially by the levers, then by the mechanism of the link parts and finally by the stress in the solder between the link components. The third force is relatively modest because of the solder weakness at the operative temperature. Also, the sprinkler frame and the other parts have a sufficient degree of elasticity to produce a sharp release of the operating components.

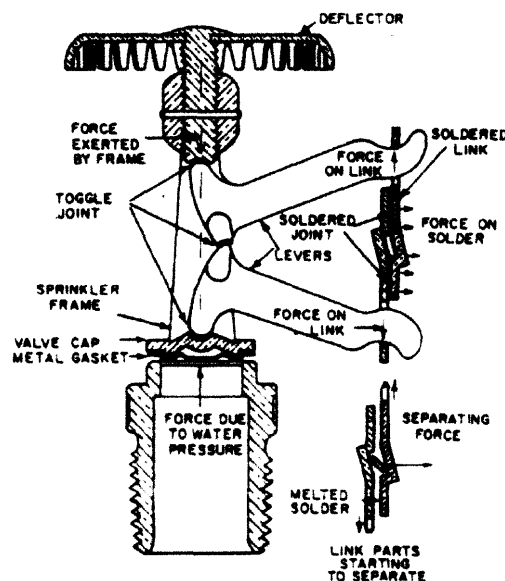


Figure 3. Schematic of a lever automatic sprinkler

Sprinklers like the Solder Element sprinkler (SE) and the Quick response solder Element sprinkler (QE) used in the present study feature different types of operating mechanism and lever configuration. Other sprinklers employ solder material under compression, tension or tension and shear stress.

Deflector design

Attached to the **frame** of the sprinkler is a deflector against which the stream of water is directed and breaks up into a spray. The amount of water released on the fire depends on the flowing water pressure and the size of the sprinkler orifice. A flowing pressure of 7 psi is considered a minimum for appropriate action. Hydraulically calculated systems are designed considering the available water supply pressure.

Rating of Automatic Sprinklers

Automatic sprinklers have several temperature ratings that are based on standardized tests in which a sprinkler is immersed in a liquid and the temperature of the liquid raised very slowly until the sprinkler activates. The temperature rating of all solder-type automatic sprinklers is stamped upon the link. For the other types, the temperature is stamped upon some of the releasing parts. The maximum room temperature is generally closer to the activation temperature for frangible bulb than for

solder element sprinklers because the solder type starts to lose strength a little bit before its melting point. Table 1 reports the standard classification of fire automatic sprinklers based on their temperature ratings.

Max. Ceiling temperature (°C)	Temperature rating (°C)	Classification	Color code
38	57 to 77	Ordinary	Uncolored
66	79 to 107	Intermediate	White
107	121 to 149	High	Blue
149	163 to 191	Extra High	Red
191	204 to 246	Very Extra High	Green
246	260 to 302	Ultra High	Orange

Table 1. Classification of automatic sprinklers

Activation time delay and Response Time Index

The time delay between the onset of the fire and the activation of the sprinkler depends upon several parameters, such as the placement of the sprinkler with respect to the fire, the dimensions of the enclosed space, the energy generated by the combustion and the “sensitivity” of the sprinkler. Buoyancy pushes the hot products generated by a fire toward the ceiling while mixing with room air to form a hot-gas plume. Impingement of the fire plume on a ceiling results in a gas flow near the

ceiling even at a considerable distance from the fire axis. This type of flow is responsible for transferring hot gases to the thermally actuated detection devices. The rate of heat released by the burning fuel and the room dimensions are the main parameters of considerable importance in any discussion of fire-induced convection near the room ceiling. Basic research on fire-induced convection has improved the theoretical analysis for predicting gas velocity, temperature and dimensions of the gas flow induced by fires. Experiments performed on large-scale facilities involve the use of several different types of combustible materials to gather more detailed information on the interaction between gases and the room walls.

Sprinkler Type	RTI [(ms)^{1/2}]
Sprinkler “SE”	100
Sprinkler “SR”	90
Sprinkler “QR’	40
Sprinkler “QE”	30

Table 2. *RTI* for commercially available fire sprinklers

Also, the size and the composition of the metal link influence the sensitivity of the sprinkler. Other conditions being equal, the sensitivity of a sprinkler is inversely proportional to the time required for the link to melt. Therefore, sprinklers are also

rated according to their Response Time Index (*RTI*), which characterizes the rapidity of the sprinkler's response to a fire. Table 2 shows the *RTI* values for some commercially available sprinklers.

The concept of the *RTI* for characterizing the thermal response of automatic sprinklers has become quite well known in the 70s, although the term was not used until 1980. The *RTI* is the product of the thermal time constant of the sprinkler link and the square root of the gas flow velocity. This parameter is reasonably constant for any given sprinkler and is considered sufficient for predicting the sprinkler response for known gas temperatures and velocities near the device itself.

Overview on the design of a sprinkler array

The practical location of the piping and the nozzles relatively to the zone where the fire is most likely to occur is determined by the physical arrangement of the building. The size of the nozzles to be used, the configuration of the water discharge and the water pressure in the pipes need to be determined.

The first quantity to be calculated is the water amount necessary to contain and eventually suppress successfully a fire. This can be obtained by considering the heat of combustion released by the materials present in a room. The choice of the right nozzle

is determined by considering the devices that are capable to deliver the necessary water amount onto the fire. The nozzle type must also be capable to cover the area protected by the sprinklers.

Once the nozzle type and the spacing between the sprinklers have been determined, hydraulic calculations are made to size the piping and the water supply. Water is usually supplied from any of the following:

- Water pipeline of adequate pressure and capacity
- Elevated water tank
- Automatic fire pumps with reliable power supply.

Water demand **has** to be adequate to supply a sufficient number of spray nozzles at an adequate operative pressure. The water demand is calculated in terms of density of uniformly distributed water spray per unit of area protected. The discharge rate per unit of area depends on several considerations, such as the characteristics of the materials possibly involved in the fire and the principal purpose of the protection system: extinguishment, control or prevention of fire.

MOTIVATION AND OBJECTIVE OF THE WORK

Recent full-scale tests on warehouse fires documented a behavior of the sprinklers not corresponding to the predictions of the RTI model. The RTI model considers the

sprinkler link as a cylinder in cross-flow. It is assumed that the only heat transfer between the hot gases flowing under the ceiling and the sprinkler is convective, thus neglecting the presence of water droplets into the airflow. The first sprinkler to activate in case of fire is referred to as *primary* and the surrounding sprinklers are identified as secondary. The tests showed that the primary sprinkler does indeed activate as predicted, but the secondary ones respond after a much longer delay than suggested by the model. In some cases, the sprinklers immediately surrounding the primary do not activate at all, whereas those farther away do. These observations can be justified by considering the presence of water droplets in the gas plume following the activation of the primary sprinkler. In fact, some of the spray droplets do not reach the ground but are entrained and carried away by the ascending plume. Most of these droplets evaporate inside the plume, while a small fraction of the remaining travels far enough to reach the secondary sprinklers and impact on their surface. The subsequent evaporation of the droplets from the link surface produces a cooling effect, which delays the heating of the metal link.

On this basis, the objective of the present study is to provide a revised model for the sprinkler thermal response, which includes the evaporative cooling effect generated by water droplets. Experimental results gathered from simulated sprinkler links will be used to assess the model, while the data obtained from tests on commercially available fire sprinklers will validate the capability of the model to predict the time of activation of fire sprinklers under various conditions. The model also offers the opportunity to develop an innovative way to measure the temperature of air-water flows and the

water volumetric fraction. The resulting sensor will be introduced and described in the second part of the dissertation.

OUTLINE OF THE WORK

The work presented in this dissertation can be subdivided into three parts:

- Formulation of the theoretical model and experimental assessment
- Experiments on commercial fire sprinklers and comparison of the results with the predictions of the model
- Conception, design and testing of the 'Above Leidenfrost Temperature and Evaporative Cooling' (ALTEC) sensor for measurements of temperature in a hot **gas** laden with water droplets

In particular, Chapter 2 reviews previous research projects concerning fire protection systems, fire plumes, impingement of water droplets over solid surfaces and evaporative cooling phenomena. Chapter 3 presents the RTI model and the newly formulated Evaporative Cooling (EC) model, while Chapter 4 describes the 'Evaporative Cooling Sensor Accuracy Test' (ECSAT) facility with its components and instrumentation. The experimental procedures and the measurement techniques are described more in detail in Chapter 5. In particular, several sections are dedicated

to the measurement of the gas velocity, the water volumetric fraction in the hot gas and the wet gas temperature.

The chapter 6 includes the validation of the EC model to predict the activation time of commercially available fire sprinkler.

A detailed insight into the innovative ALTEC sensor and the measurement methodology to obtain the wet gas temperature and the water volumetric fraction are provided in Chapter 7. The evolution of the design from the sensor prototype to its final configuration is shown to the reader, as well. Finally, a **summary** of the major findings of the research project is provided in the Conclusions.

CHAPTER 2

LITERATURE REVIEW

In the following sections, a detailed analysis of the most significant papers available in literature will be given. Special consideration will be paid to investigations that have addressed the following topics:

- The fire sprinkler technology.
- The generation of hot gas plume in case of a fire.
- The evaporative cooling effect produced by liquid droplets impacting over a solid surface.
- The evaporation process of water droplets in a hot gas flow.

Also, an overview on the Leidenfrost phenomenon will be presented in the last section of this chapter as a theoretical background to the second part of the dissertation.

FIRE SPRINKLER TECHNOLOGY

The time delay for the activation of a given sprinkler can be predicted by modeling the link as a lumped heat capacity and calculating its transient thermal response to hot gases flowing over it (Heskestad and Bill, 1988). This approach is commonly followed to determine the placement of fire sprinkler arrays in buildings and it is known as RTI model. According to the predictions of the model, the first sprinkler to activate (primary) will be the one closest to the location of the fire. If the water released by the primary sprinkler is not sufficient to extinguish the fire, this will grow and the hot gases will reach the surrounding secondary sprinklers. Still according to the RTI model, the secondary sprinklers will also activate, after a certain time delay, and release more water on the fire. Therefore, the model is used to optimize the spacing between the sprinklers, in order to maximize the chance of containing the fire while retaining a sufficient pressure in the water supply. The effect of conductive heat transfer through the sprinkler support can be properly quantified as described by Heskestad and Bill (1988). In this paper, they review the original thermal response model leading to the *RTI* concept and outline the plunge test devised for measuring the *RTI*. An attempt is then made to incorporate the conductive heat losses in the model and to develop a method for characterizing these heat losses by conduction. An extensive test program is conducted in the FMRC plunge-test tunnel depicted in Figure 4: four sprinkler types are tested at different combinations of gas temperatures and velocities. The main conclusions are the following:

- The experimental results suggest that the activation heat (e.g. the heat necessary for the solder element to melt, once it ~~has~~ reached the activation temperature) is not an important factor for industrial type sprinklers. This results in a significant simplification when modeling the thermal transient of a sprinkler link, since it can be assumed that the sprinkler activates immediately after it reaches the temperature of activation.
- Given a sprinkler type, the RTZ values measured for gas velocities ranging from 1.5 to 3.5 m/s and several gas temperatures are reasonably constant. However, the RTZ presents a tendency to slightly increase for the lowest gas velocities investigated.
- Modifications are proposed for the original response theory to consider the conductive heat losses in certain fire situations. The conductive heat loss is assumed proportional to the difference of temperature between the sensible element and the sprinkler plug. In the modified model, the thermal response of the sprinkler depends on the RTI and a conduction parameter.
- Conductive heat losses are primarily important at low gas temperatures and low gas velocities. As the fire intensity grows, the influence of the conductive loss becomes less significant.

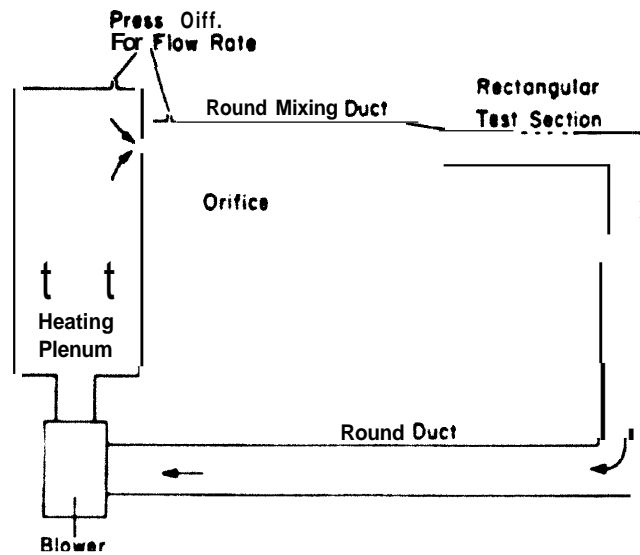


Figure 4. Facility used in the experiments at FRMC. Test section is 0.3 m wide by 0.15 m high

A model for estimating the evaporative heat loss due to the water spray introduced by a sprinkler in a smoke layer is reported by Chow (1989). The author points out that the water droplets evaporate while travelling through the smoke layer. This results in higher cooling and smaller air-drag effects. However, the water droplets may not be able to reach the burning objects. The model investigates the evaporation of the sprinkler water spray in the hot smoke layer, providing a scheme to evaluate the penetration of the water. The author states that:

- The droplets initially are heated up by convection; then, when the temperature reaches the boiling point, the drops evaporate at a rate proportional to the heat transfer surface. The ratio between the evaporative heat rate and the convective heat rate while the droplet is moving **from** the sprinkler into the hot gases is considerably small with respect to previous theoretical investigations.
- The total heat absorbed by a water droplet is found to be a function of its initial diameter, elevated to the -0.73 exponent.
- Only the smaller drops evaporate completely into the air, before reaching the fire. No complete evaporation takes place if the droplets have a diameter greater than 0.5 mm.

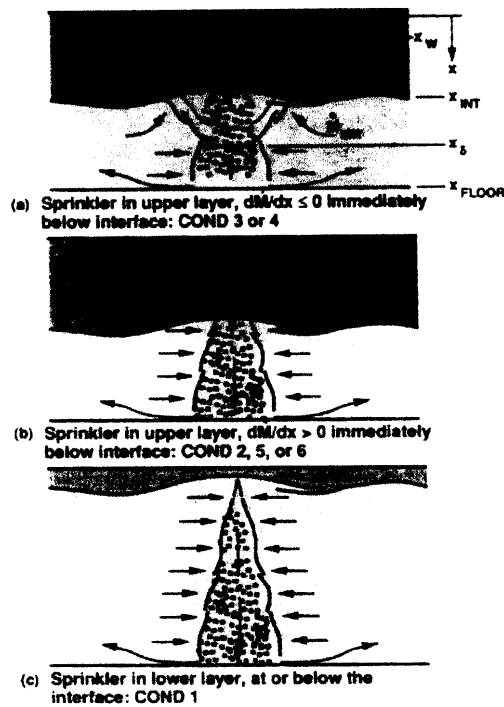


Figure 5. Two-layer fire scenario investigated by Cooper (1995)

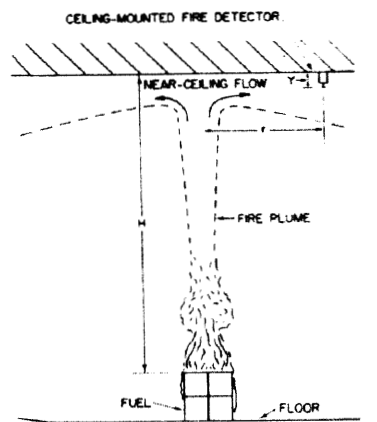
The suppressing performance of a water spray is determined by both the spray characteristics and external factors, such as fuel type and space geometry. Spray dynamics and characteristics have been studied by experiments and numerical simulations. Upon activation of the sprinkler, the buoyant hot smoke layer induced by the fire becomes unstable because of the cooling and dragging effects produced by water droplets. As a result, smoke cannot stay in the upper layer and falls down to the lower portion of the compartment. The consequent smoke accumulation may threaten the safe escape of occupants and hinder the fire fighting (Chow and Cheung, 1999).

Studies on the interaction between a water spray generated by a sprinkler and smoke are important to improve the understanding of these complex processes and to provide effective design parameters for fire protection (Chow and Yao, 2001). A model to simulate the interaction between a sprinkler water spray and a two-layer fire environment under arbitrary combinations of sprinkler elevation, upper and lower layer thickness and gas temperature is documented by Cooper (1995). The model simulates the effect of the sprinkler spray as it entrains and drives downward the gases in the upper and lower layers (see Figure 5). Also, a particular objective of the study is to predict the exchange of mass and energy between the two layers associated with the operation of the water spray. The study indicates that an abrupt and significant change in the nature of the sprinkler-layer interaction occurs when the upper layer increases in thickness beyond a critical value (for a given upper-layer temperature) or increases in temperature beyond a critical value (for a given thickness). When these values are not exceeded, the sprinkler operation results in a small mixing between the two layers. Conversely, above the critical values, a large flow of gases is transferred from the lower layer to the upper layer. This is caused by entrainment of the lower-layer gases into the upward buoyant flow, initially originated from the warmer gases driven out of the upper layer by the direct action of the spray. Thus, the upper layer would grow in thickness and cause a smoke accumulation in the fire compartment. The control of the temperature and thickness of the upper layer to subcritical values could be useful to guarantee fire sprinkler operation without smoke accumulation in the fire compartment.

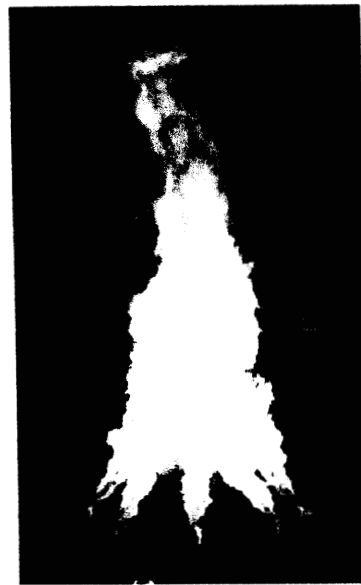
FIRE PLUME

Practically all fires go through an important initial stage in which a buoyant gas stream rises above a localized area, where combustion takes place, into a surrounding space of essentially uncontaminated air. This stage begins at ignition, continues through a possible smoldering interval and into a flaming interval followed by a sudden spread of the flame (*flashover*). The buoyant **gas** flow is generally turbulent, except when the fire source is really small. This buoyant gas stream is known as *fire* plume.

The properties of fire plumes are important in dealing with problems related to fire detection, fire heating of materials and smoke accumulation. They are also important to fire protection systems. Figure 6 shows a schematic representation of a fire plume originating from a flaming source. Combustion products, driven off from the burning objects by the buoyancy force, **mix** with the surrounding air and form a hot gas plume. The flow field profile could be the time-averaged temperature rise above the ambient temperature or the concentration of carbon dioxide generated by the fire or the axial velocity in the fire plume. The temperature is nearly constant in the bottom part of the flame and begins to decrease in the upper part of the flame, where cooler air mixes with the combustion products. The velocity is highest somewhere before the tip of the flame and **begins** to decrease afterwards. The heat released by the fire is convective and radiative. The convective heat flux is carried away by the hot plume above the fire, while the remaining portion of the heat released by the burning materials is radiated in all directions.



(Above). Schematic diagram of the gas flow induced by a fire.



(Right). Photograph of the heptane spray fire. Ceiling height above spray nozzles is 26 ft, and heptane flow rate is 12 gpm.

Figure 6. Fire scenario studied by Alpert in 1972

An understanding of the behavior of the fire plume and fire induced flow near the ceiling of a room is necessary to optimize the response time and the placement of the detectors. An experimental and theoretical project is developed by Alpert (1972) to study natural convection associated with large fires where the flames are comparable in height to the ceiling. Extensive measurements of gas temperature are made during the test fires to determine how the gas temperature varies with the distance from the ceiling and the radial distance from the fire axis. The analysis of the data shows that, far away from the impinging point of the fire plume on the ceiling, the maximum gas temperature occurs a few inches below the ceiling and that the temperature decreases to the room temperature value a few feet below the ceiling itself. Further, inside the

hot plume, the gas temperature increases with the vertical distance below the ceiling and decreases with the radial distance from the fire axis as expected. An expression for the gas temperature is written as follows:

$$T_{\max} = T_{\text{room}} + \frac{0.80}{H} \cdot \left(\frac{Q}{r} \right)^{2/3} \quad \text{for } r > 0.18 \cdot H$$

$$T = T_{\text{room}} + 2.52 \cdot \frac{Q^{2/3}}{H^{5/3}} \quad \text{for } r \leq 0.18 \cdot H$$
(2.1)

Q is the intensity of the fire (W), r the radial distance from the fire (m), H the ceiling height (m) and $T_{\max}, T_{\text{room}}$ the maximum gas temperature and the room temperature (°C), respectively.

Velocity measurements are also made during the tests, finding this expression for the maximum gas velocity:

$$U_{\max} = \frac{0.075 \cdot Q^{1/3} H^{1/2}}{r^{5/6}} \quad r > 0.15 \cdot H$$

$$U_{\max} = 0.36 \cdot \left(\frac{Q}{H} \right)^{1/3} \quad r \leq 0.15 \cdot H$$
(2.2)

The velocity is expressed in (m/s). Figure 7 reports the distribution of velocity and temperature as functions of the radial distance from the plume impingement point on the ceiling.

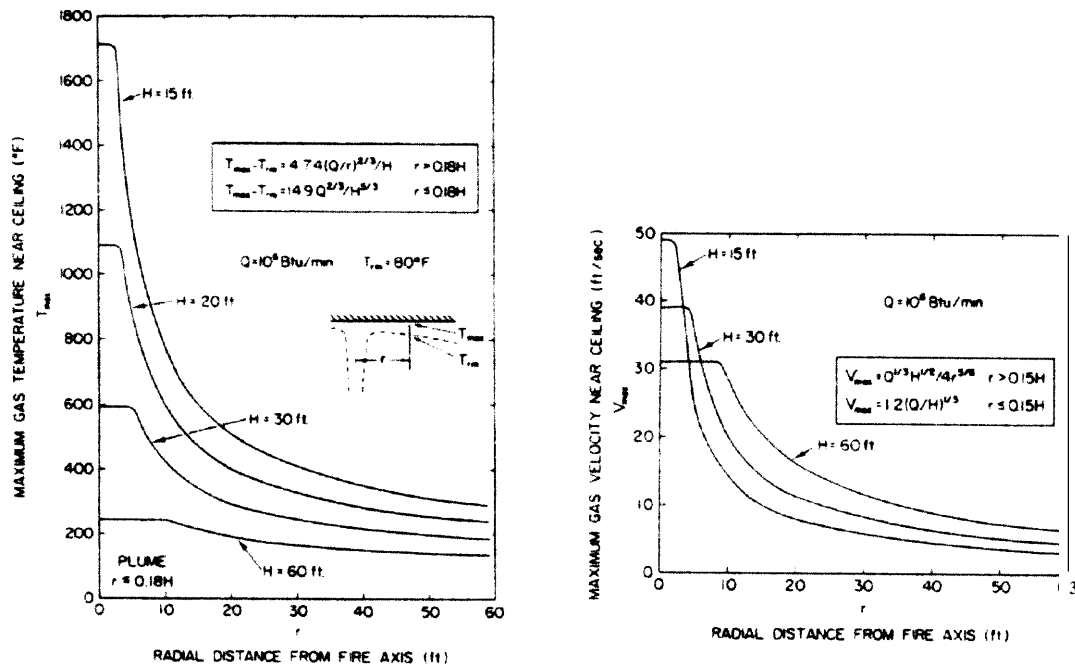


Figure 7. Temperature and velocity distribution in a fire plume near the ceiling

The study shows that fire detectors should be located vertically no more than 6 percent of the ceiling height below the ceiling itself. Besides, fire sprinklers should be placed at intervals of one fourth of the ceiling height to optimize their response time. In fact, smaller spaces do not improve significantly the activation time of the sprinkler.

EVAPORATIVE COOLING

Several authors attempted to show the effect determined by water droplets impinging over a solid surface. Experimental studies to determine the minimum wall temperature and the total vaporization time of water, octane and carbon tetrachloride mixtures are reported by Betta et al. (1979). The results suggest that the total vaporization time decreases if the wall temperature increases and the droplet initial volume decreases. They also introduce a correlation between the dimensionless vaporization time and the dimensionless volume of the droplets, which is in good agreement with theoretical closures previously available in the literature (Gottfried et al., 1966; Baumeister and Schoessow, 1973).

Grissom and Wierum (1981) suggest that the lowest surface temperature for the existence of spray evaporative cooling can be determined experimentally as a linear function of the impinging spray mass flow rate. For pressures smaller than the atmospheric one, droplet evaporation rate decreases significantly and an optimum working pressure exists for any desired surface heat flux. Over the range of heat fluxes investigated in the study, the mechanism driving the evaporative cooling appears to be the conduction heat transfer in the droplet bulk, while evaporation takes place only at the droplet-gas interface. Further, spray film cooling at atmospheric pressure behaves like ordinary pool boiling. However, at vacuum pressures, the prevalent mechanism is conductive throughout the liquid film without nucleate boiling.

Transient cooling of solid surfaces by water droplet evaporation are investigated through controlled experiments using large heated aluminum cylinders (diMarzo and Evans, 1987). For the case of water droplets impinging the flat surface of a cylinder at near water saturation temperature, the shape of the droplet can be regarded as a spherical segment. The wetted region of the semi-infinite solid surface remains constant in size throughout most of the evaporation process. Also, a constant uniform temperature under the droplet is a reasonable assumption confirmed by previous experimental results. Quantitative predictions of the droplet evaporation time and in-depth transient temperature distribution in the solid have been computed. In the cases studied, a single droplet is deposited on a horizontal nonporous surface with initial temperatures in the range of 75 °C to 100 °C. The liquid-vapor interfacial temperature and the water vapor molar fraction in the air at the exposed surface of the water droplet are deduced from the coupled heat and mass transfer energy balance at the interface. The heat transfer resistance is found fairly close to the mass transfer resistance in the air-vapor region. Also, the energy equation, written in cylindrical coordinate for the semi-infinite metal body, provides information on the spatial and temporal distribution of temperature in the body. The boundary conditions for the energy equation are formulated by using the liquid-solid contact temperature,

expressed as $\frac{T_{wall} \cdot \gamma_{wall} + T_L \cdot \gamma_L}{\gamma_{wall} + \gamma_L}$, $\gamma = \sqrt{\rho \cdot c \cdot k}$. A more compact information is

given in terms of volume of influence. The volume of influence is defined as the volume of the solid region where the temperature variation with respect to the steady-state conduction temperature distribution exceeds a given value of the maximum

possible temperature difference in the solid itself. The volume of influence is correlated linearly with the evaporation time and it is independent from the droplet volume and the initial solid surface temperature. A consequence of this finding is that a simple, closed form expression for the volume of influence can be obtained. The paper is the first step towards the analysis of multi-droplet cooling effect, thus leading to the modeling of spray cooling process.

The evaporation process of a water droplet gently deposited on a solid surface is reported by diMarzo *et al.* (1993). Visual inspection of a tracer suggests that little convective motion is present in the water droplet. Also, the dominant heat transfer mechanism is conductive through the liquid bulk. At the liquid - vapor interface, a small portion of the heat transfer conducted from below through the liquid is transferred to the ambient by convection and by radiation. Most of the heat evaporates the liquid. Based on these observations, a computer code has been developed to solve the governing equations. It predicts the transient temperature profiles on the solid surface as well as into the liquid, the heat fluxes at all points of the liquid domain and the solid domain, the total evaporation time and the transient liquid inventory. The code predictions are compared to the experimental data obtained from tests on a solid surface of aluminum and macor. Figure 8 shows the results for a water droplet of volume equal to 30 μl deposited over aluminum and macor, at different times during the evaporation transient (the evaporation is completed at time t_{evap}).

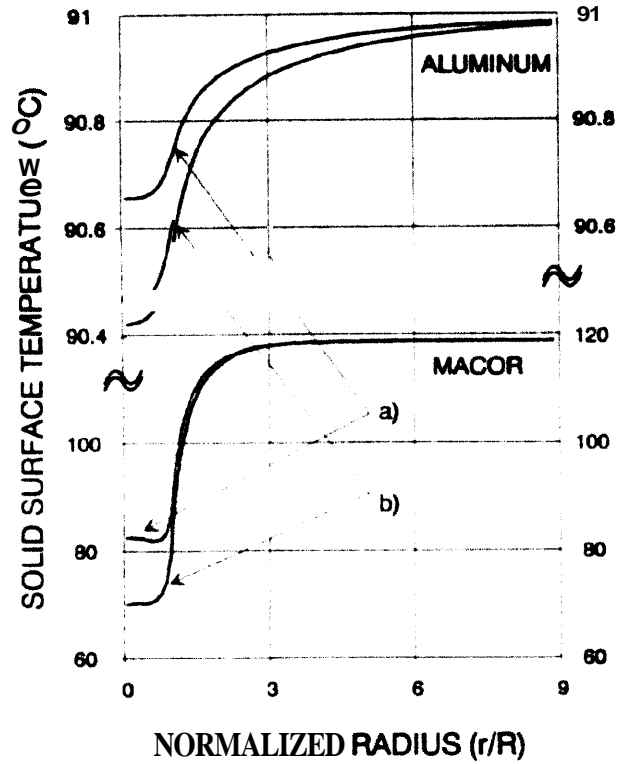


**Figure 8. Typical surface temperature distribution on aluminum and macor for
a) $t/t_{\text{evap}}=0.3$ and b) $t/t_{\text{evap}} 4 . 9$**

In general, the overall performance of the coupled code is reasonable. It slightly over-predicts the experimental data while capturing well the temperature at the droplet edge. The radius of influence is under-estimated. It is worth considering that the heat transfer is mostly one-dimensional in the liquid bulk. In fact, the radial component of

the heat flux accounts for less than 5 percent of the total heat flux, except at the edge of the water droplet.

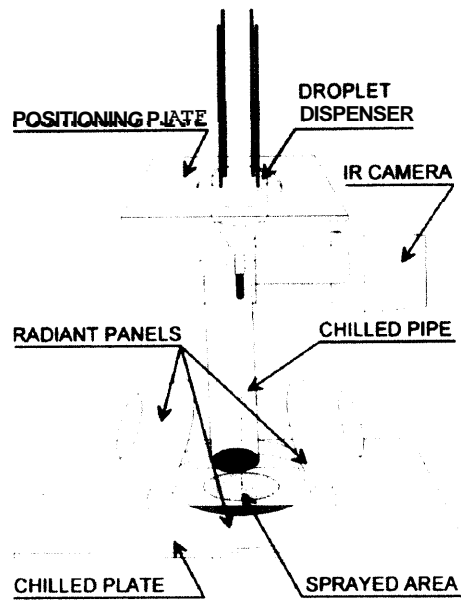


Figure 9. Experimental setup (diMarzo & Tinker, 1995)

di Marzo and Tinker (1996) study the cooling effect of a sparse spray impinging on a semi-infinite solid. Experiments are performed by monitoring the temperature of a solid surface, heated by direct radiation and cooled by sprays of uniform size droplets. Figure 9 shows the experimental arrangement used in the tests.

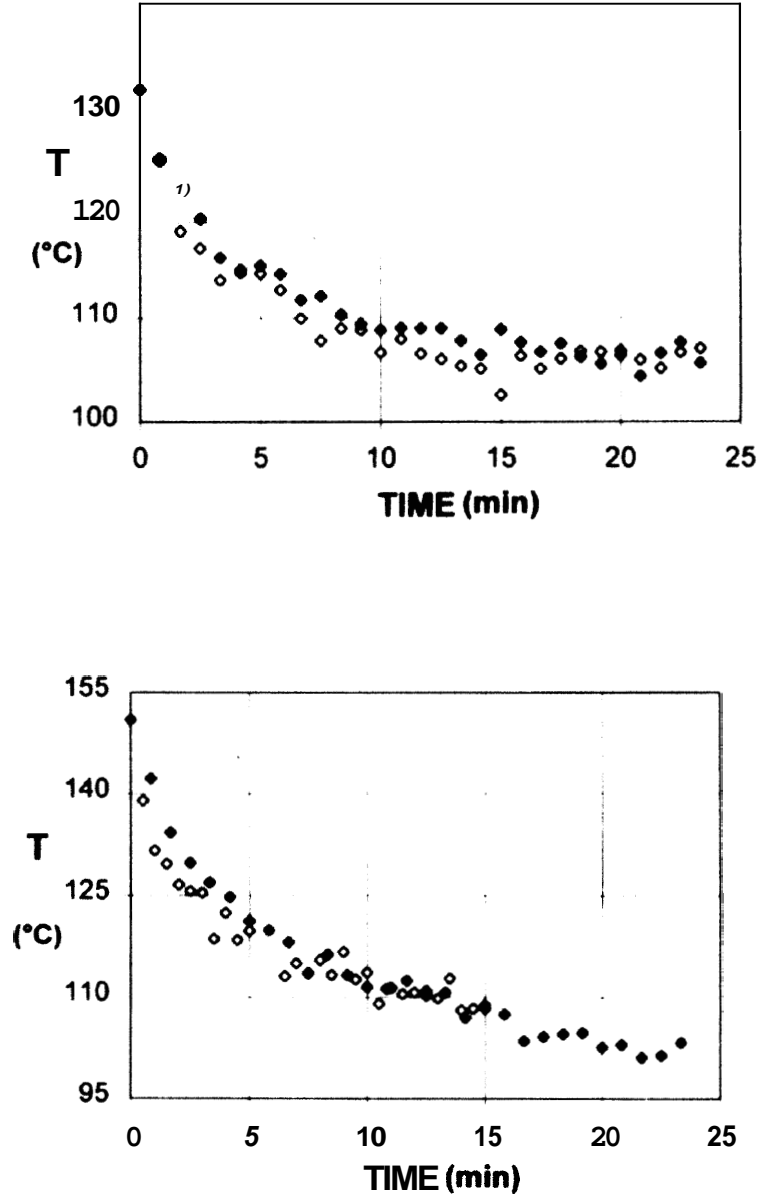


Figure 10. Average surface temperature transient (○ experimental points, ● numerical points). Initial surface temperature 131 °C (top), 151 °C (bottom); water mass flux $0.50 \text{ g m}^{-2} \text{ s}^{-1}$ (top), $0.96 \text{ g m}^{-2} \text{ s}^{-1}$ (bottom)

The surface temperature field in the vicinity of a droplet is calculated by a closed-form solution based on the hypothesis of constant and uniform heat transfer at the solid-fluid interface. The closed-form solution is integrated with the results of a coupled model previously developed, which solves the liquid and solid temperature fields for the evaporative transient. The theoretical solutions are compared with the experimental data. The results suggest that the closed-form solution is slightly different from the experimental data, although the overall transient behavior is consistently predicted over a broad range of conditions. The effect of nucleate boiling under the droplet deposited over the solid surface and the fact that the evaporative process time constant is not a function of the water flux suggest that the substrate properties may play a significant role on the cooling transient.

EVAPORATION PROCESS

Recently, numerous techniques to augment the heat transfer have been developed in designing compact heat exchangers for the effective utilization of thermal energy. Introducing small amounts of liquid droplets in cooling gas medium has been considered as one of these techniques that can realize a remarkable enhancement of heat transfer rates from a solid surface by utilizing the latent heat of the liquid. An experimental study concerning the characteristics of heat transfer from a dry isothermal plate to a two-component mist flow is performed by Hishida *et al.* (1980). Water-air mass flow ratios as low as 2 percent have been investigated. The heat

transfer coefficients in **mist** flow increase with respect to the single phase coefficients with increasing mass flow rate ratio and free stream velocity and with decreasing wall temperature. The measurement of the droplet velocity by Laser Doppler Anemometry indicates the similarity of the velocity distributions into the boundary layer with the single phase ones. The droplet velocity profiles near the wall in the boundary layer are slightly higher than Blasius' profile. This is probably caused by the inertia of the droplets carried from the free stream into the **boundary** layer. At constant Reynolds numbers and wall temperatures, the enhanced heat transfer rates are correlated to the mass flow rate of water for unit cross-sectional area. Also, the wall temperature becomes a very significant factor in the heat transfer process of the system. The augmentation of heat transfer is attributed to the latent heat due to the evaporation of droplets that penetrate the boundary layer and deposit on the heating surface. The effect of the water droplets carried by the hot gas over the heat transfer will be considered in the last part of this dissertation.

Mastanaiah and Ganic (1982) investigate the evaporation process experimentally, finding that, in dispersed turbulent flow, heat transfer takes place by a variety of mechanisms: namely, the heat transfer from the wall to the gas is by single phase convection, the heat transfer from the wall to the deposited droplets by conduction and boiling. In addition, the heat transfer from the wall to the droplets and vapor occurs by radiation if the wall temperature is high. The purpose of the paper is to report new deposition data for air-water droplet flows in a vertical unheated steel tube. A

comparison with data for acrylic tubes under similar conditions is done to evaluate the effect of tube materials on the droplet deposition rate.

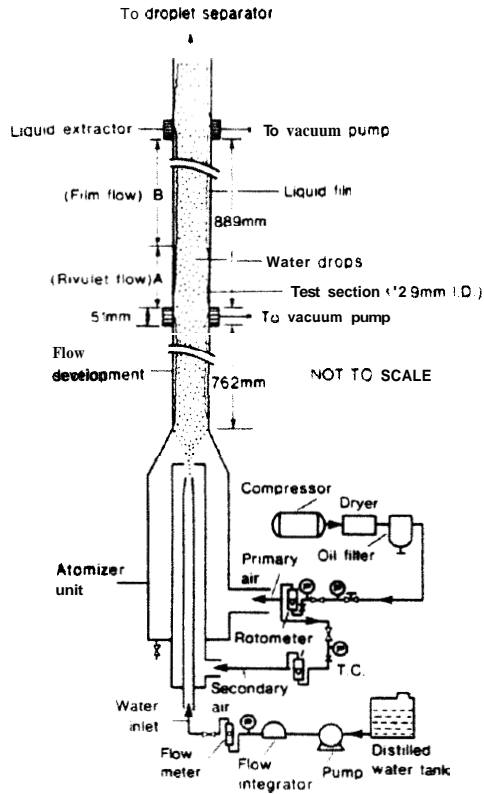


Figure 11. Schematic of experimental set-up for deposition tests

Early experiments by the authors using acrylic tube have indicated that, in the test section, two distinct flow regimes of the liquid **film** formation on the wall are visually observed. In region A, downstream of the inlet (**see** Figure 11), the deposited droplet flow rate is not sufficient enough to form a continuous liquid film around the periphery

of the test section, resulting in a rivulet-type flow (rivulets are several small narrow streams). The configuration of this flow regime is dependent upon the tube surface through the liquid-wall contact angle. The length of region A depends on the Reynolds number, the droplet flow rate and the diameter of the droplets. Region B is characterized by a thin continuous liquid film covering the tube surface due to the increased film flow rate. The surface roughness may also influence the deposition rate. The authors conclude that the data obtained for acrylic tubes may be used directly in the heat transfer analysis of dispersed two-phase flows in metallic tubes provided that there is no significant droplet entrainment.

Renksizbulut and Yuen (1983) propose a study on the heat transfer around simulated and freely suspended liquid droplets in an atmospheric hot air tunnel. The experiments are limited to water, methanol and heptane droplets in a Reynolds number range between 25 and 2000 and a range of mass transfer number B between 0.07 and 2.79. Three methods are used to simulate the droplet suspended in the gas flow. The ~~first~~ method is to use a porous bronze sphere of 6.35 mm diameter with a thin liquid layer coating the surface of the sphere ($200 < Re < 2000$). The second method is to use a perforated brass sphere of 1.58 mm diameter ($50 < Re < 500$). The third method is to create a freely suspended liquid droplet at the end of a capillary tube of 250 μm diameter ($Re < 200$). The data show that, at higher temperatures, evaporation reduces directly the heat transfer rates by a factor depending on the mass transfer number B,

defined as $B = \frac{\rho \cdot c_p \Delta T}{A}$, where ΔT is the temperature difference between the free

stream and the droplet. Indirectly, evaporation affects heat transfer rates through the changes in both the composition and temperature of the surrounding gaseous medium.

Buglayev (1986) investigates various aspects of cooling of gas flow by injection of water droplets. The distance, measured from the water injection point to the point where the evaporation is complete, is determined through a correlation depending on several factors, such as the mass transfer number, the ratio between the mass flow rate of water and gases, the droplet diameter and the initial temperature difference between water and gases. As expected, the analysis shows that the complete-evaporation length increases with the water flow rate, the gas velocity and the droplet diameter, while decreases with the temperature difference between gas and water droplets.

The work by Hwang and Moallemi (1988) deals with the heat transfer by direct contact between a water droplet and its own vapor. The droplet shape is considered approximately constant and sensible heat is the only source of energy for evaporation. The report presents the analysis of a numerical model on evaporation of superheated liquid droplets. The assumptions are the following: non-existence of droplet-to-droplet interactions, the effect of convection in the droplet bulk is neglected, the evaporation process is controlled by the heat transport within the liquid. The theoretical analysis shows that the strong contribution of the droplet internal circulation to the evaporation mass rate can not be neglected and that the interfacial thermal resistance is not significant.

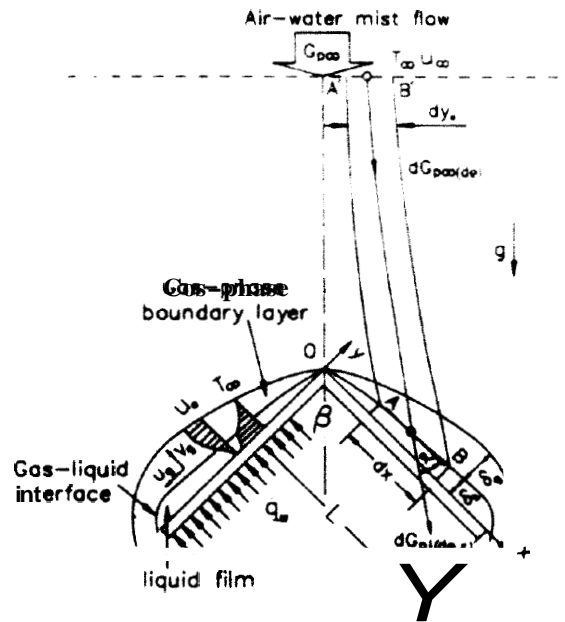


Figure 12. Physical model investigated by Fu and Yang (1989)

Adding water droplets into single-phase flows can enhance the performance of the heat transfer **from** a heated body (Figure 12). The study by Wu-Shung Fu and Cheng Yang (1989) investigates the heat transfer mechanism of a heated wedge with uniform wall heat flux in an air-water mist flow. Two **main** factors are considered: the trajectories and the size distribution of polydisperse droplets. A numerical method is proposed to distinguish whether the surface is in wet region or in a **dry-out** region and to solve the governing equations of the gas phase and the water film simultaneously. In the gas-phase layer, a backward finite difference and central finite difference schemes are used respectively in the two perpendicular directions (see Figure 12 for a definition of the coordinate system). Non-linear coefficients are approximately

substituted by the values of the preceding iteration. In the water film layer, integration is used in one coordinate direction initially and differentiation is employed in the other direction. Results for the wall temperature, the liquid film thickness, the interface velocity and temperature, and the heat transfer coefficient are obtained. The effect of three kinds of heat transfer (gas phase convection, water film sensible heat transfer and evaporation) on the heat transfer coefficient are examined in detail. The conclusions are the following:

- A wet region and a dry-out region may coexist on the wall surface. A discontinuity phenomenon occurs at the water film disappearance point, where the Nusselt number decreases drastically.
- Heat transfer enhancement is significant at large mass flow ratios of water to air.
- The numerical model is effective for solving film-cooling phenomena.

An interactive Eulerian-Lagrangian model of the turbulent transport for evaporating droplets is implemented by Edson *et al.* (1994). A k - ϵ turbulence closure model is used to accurately simulate the stable, near-neutral and unstable boundary layers within the large air-sea interaction tunnel at the Institut de Meccanique Statistique de la Turbulence (IMST) in France. The results are then used within the Lagrangian model. The coupled model gives excellent agreement with droplet dispersion measurements made during their 1988 experimental campaign. Additionally, the coupled model can be used to investigate the interaction between the evaporating droplets and the turbulent fields of temperature and humidity. The Lagrangian model

simulations have been further improved by simply refining the turbulent fields through which the droplets are dispersed. In the field, a k- ϵ model can be used to provide the required Lagrangian model parameters using measurements from the surface and at some reference height to initialize the Eulerian model. The droplet model can then be applied to examine the influence **of** the droplet evaporation and sensible heat release on the surface energy inventory using a variety of source functions. An increase in turbulence intensity due to high winds does not significantly increase the effect that evaporating jet droplets have on the temperature and humidity fields.

Hiromitsu and Kawaguchi (1995) analyze the evaporation process of a suspended droplet for several kinds of paraffin hydrocarbons, distilled water and ethanol in a hot turbulent air flow. The experimental study has been conducted to investigate the influence of the turbulence intensity and scale on the evaporation rate of water droplets and to obtain useful quantitative data using a single suspended liquid droplet. The results show that the droplet evaporation rate increases when the turbulence intensity increases. It is considered that the vapor **mass** transfer is promoted due to the destruction of the vapor layer around the droplet by the turbulent eddies that reduce in size **as** the turbulence intensity increases. When the vapor layer around a droplet is locally broken by turbulent eddies, evaporation will be promoted, since the concentration gradient of vapor at the droplet surface becomes steep **as** the vapor layer becomes thinner. Since measurements of distributions of vapor concentration near a droplet in a turbulent **flow** are impossible, the vapor boundary layer thickness is

calculated as a standard vapor layer using the droplet evaporation model. The main conclusions are the following:

- As the turbulence intensity increases, the droplet evaporation rate increases. The reason is that the droplet evaporation rate is enhanced by an intense turbulent flow due to the increase of vapor mass transfer rate caused by the disturbance of small scale turbulence and the steep gradient of vapor concentration.
- The influence of turbulence on evaporation rate is greater for a slower evaporation case. When the evaporation increases, this influence becomes small.
- The boundary layer thickness of the vapor around a droplet is a useful quantity to evaluate the influence of turbulence on the droplet evaporation in a high temperature flow. The thinner the boundary layer, the higher the influence of the turbulence on the evaporation rate.

A three-components (water liquid, steam and air), one-dimensional model is proposed by Fossa (1995) for the evaluation of the heat transfer and the flow characteristics of a two-phase flow. The study takes into account the deposition and entrainment processes as well as the evaporation and the heat transfer between air and water droplets. The model shows good agreement with the experimental data gathered from upward and downward isothermal mixture tests performed by the same author. The main results concern the temperature distribution of the three components along the duct. The characteristic entry length from the point of the water droplets injection to

the point of equilibrium between the phases has been obtained as a function of the liquid and gas velocity and the inlet temperature (Fossa *et al.*, 1998).

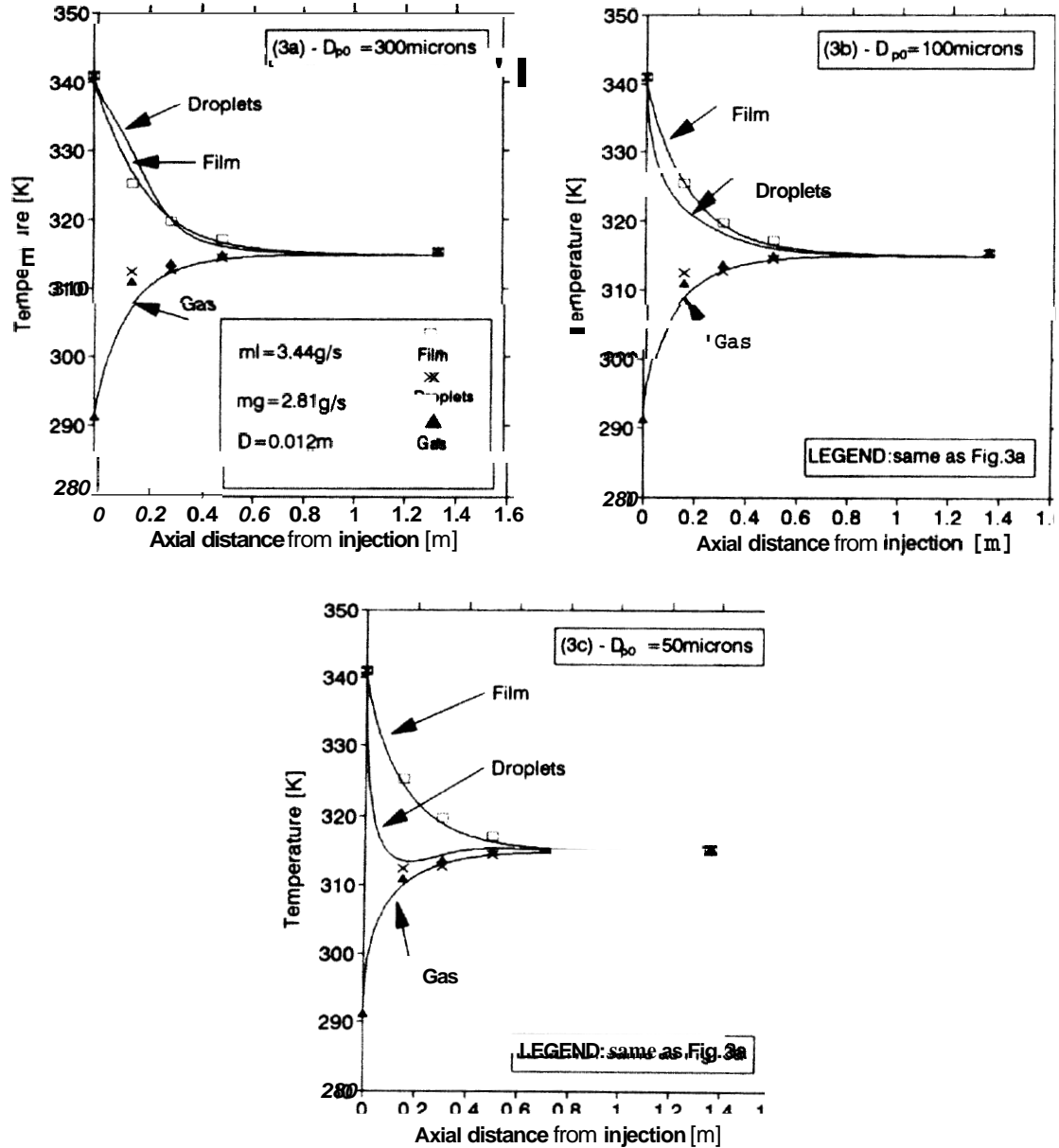


Figure 13. Temperature distributions for various droplet diameters (Fossa, 1995)

Heat transfer of air-water flow in a vertical heating pipe is studied by Kitagawa *et al.* (1998). The axial and circumferential wall temperature distributions are measured for various air-mist mass flow ratios and wall heat fluxes. The measured wall temperature increases sharply at a particular axial location, with a notable variation in the circumferential profile. This sharp increase is conceivably caused by a breakdown of the water **film** rather than its dry-out. A separate unheated experiment is carried out to estimate the droplet deposition velocity and the water film flow rate. A numerical analysis, taking into account heat and mass transfer from the water **film** to the bulk flow, is performed in order to evaluate the mean wall temperature. Good agreement is obtained with the experimental results in the area where the entire inner surface of the pipe is covered with the water film. In this region, the rate of heat transfer is larger than that of a single-phase airflow. This enhancement is caused mainly by the evaporation of the water film. The mechanism of the heat transfer enhancement is discussed in detail using the numerical analysis results. The **main** conclusions are the following:

- Under a high heat flux condition, a sharp increase of the wall temperature caused by the breakdown of the liquid film is observed. Also observed in the downstream region are the wall temperature fluctuations with a large amplitude and a long period, which are caused probably by the unsteady rivulet-like liquid film.
- The droplet deposition rate under the experimental conditions investigated agrees favorably with the results conducted under similar circumstances by previous authors, but is much larger than theoretical predictions based on the assumption

that the droplet concentration distribution in the radial direction is fully developed at the test section.

- The azimuthal distribution of the wall temperature given by the numerical analysis agrees well with the experimental results in the region upstream the liquid **film** breakdown. The analysis has been developed assuming the existence of a uniform liquid **film** around the circumference of the pipe.
- Heat transfer is enhanced by the air-water-dispersed flow. The enhancement is most effective in the uniform liquid **film** region, but much slighter in the rivulet-like liquid film region.

Several attempts have been made previously to develop innovative sensors that allow for measurements of gas temperature or water droplets size distribution in a hot gas flow. During the investigation on atomization and evaporation of water in steam spray coolers, Van Paassen (1974) introduces a thermal device developed for droplet size measurements. The device consists of a thermocouple on which the droplet evaporates by heat removal **from** the thermocouple material near the hot junction. It is called the droplet detecting thermocouple (d.d.t.). The principle is based on the utilization of the correlation between the droplet diameter and the temperature signal of the d.d.t., caused by the droplet. According to the author, the d.d.t. proves to be a dependable device for continuous measurement of water droplets both in air and steam flows, even at high pressures and temperatures. A theoretical analysis of the d.d.t. behavior is provided together with experimental data of d.d.t.s for water droplets with diameters

between 6 μm and 2.4 mm. A good agreement between experimental data and theoretical predictions is reached.

McCaffrey and Heskestad (1976) introduce a new sensor to measure low velocities for fire applications. The device possesses two features particularly interesting in the fire protection research: angular insensitivity and bi-directionality. The latter quality is particularly useful because allows the probe to be positioned without knowing the flow direction. Additionally, larger size inlet of the probe circumvents problems associated with water droplets **and debris** formation present in small Pitot-tubes. Figure 14 shows the configuration of the probe. The device consists of short steel tube, with a diaphragm in the mid-plane and two taps drilled near the diaphragm. The upstream tap feels the stagnation pressure, the downstream tap senses a pressure slightly smaller than the static. Experimental comparisons with hot wire anemometry and Pitot-tube validate this technique and its insensitivity on the inclination angle with respect to the flow direction.

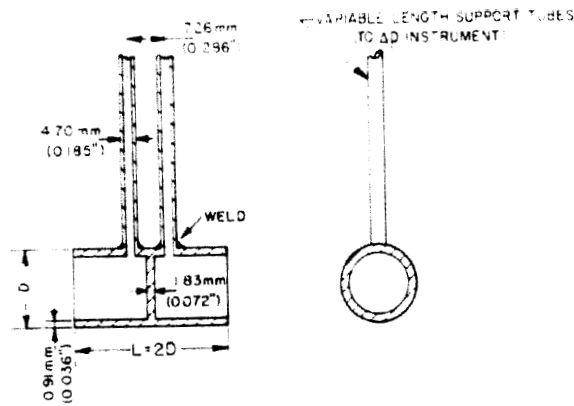


Fig. 1. Bidirectional probe.

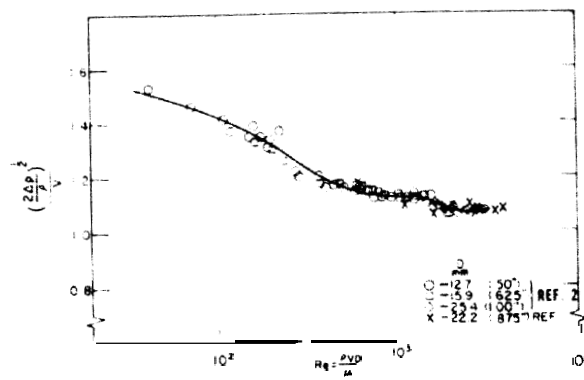


Figure 14. Bi-directional probe and response of the probe versus Reynolds number

A fast-response flow temperature probe based on thin-film heat flux gage technology is developed by Buttsworth *et al.* (1998). The probe utilizes two thin **film** gages located close to the stagnation point of a hemispherical cylinder to measure the temperature of a hot gas flow. The development of the probe is motivated by the need for a fast-response device with a high spatial resolution. As a demonstration of the probe's capacity for fluctuation measurements in a high-speed turbulent flow, the

probe is operated in the free jet arrangement shown in Figure 15, with different operative conditions, showing that accurate temperature and convective heat transfer coefficient measurements can be obtained using the device. In the companion paper, experiments are performed using the probe downstream a high-pressure turbine stage. Both high and low-frequency components of the flow temperature can be accurately resolved. The probe measures a time-averaged flow temperature that is in good agreement with thermocouple measurements made after the rotor.

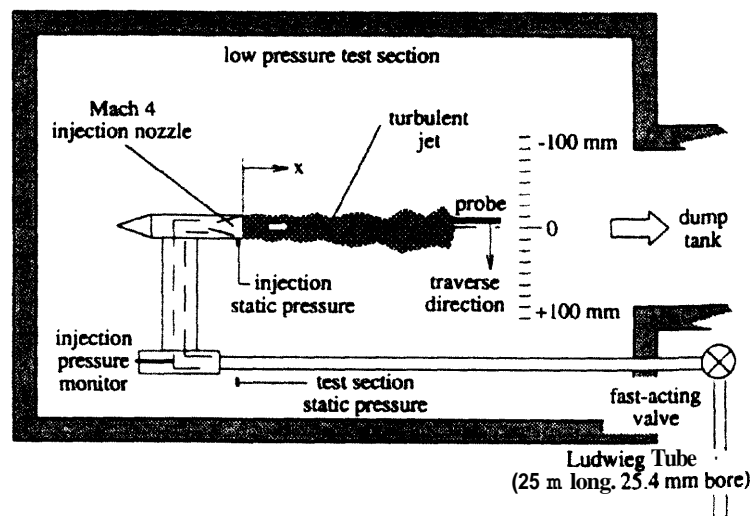


Figure 15. Experimental arrangement for free jet tests

LEIDENFROST TRANSITION PHENOMENA

For many liquids, there is a temperature well above its boiling point called the *Leidenfrost point* or *Leidenfrost transition*. Water has a Leidenfrost point of over 250°C. Consider a simple experiment where a droplet of water is placed on a surface kept at a temperature above the boiling point of water. If the temperature of the surface is below the Leidenfrost point, then the droplet ~~starts~~ to spread out and vaporizes rather quickly. At or above the Leidenfrost point, however, the bottom layer of the droplet vaporizes almost immediately on contact, creating a cushion of vapor that repels the rest of the droplet from the surface. The droplet does not make contact with the surface, and thus no heat can be transferred directly from the surface. At such high temperatures, one might expect that the vapor layer would quickly transfer enough heat to the rest of the droplet to vaporize it. Water vapor, however, is a very poor conductor of heat at these temperatures. Hence, the vapor layer actually acts as an insulator.

In his study, Emerson (1975) compares the maximum evaporation time and the Leidenfrost transition for discrete droplets of water deposited on smooth surfaces of stainless steel, brass and Monel, for various pressures. The study shows that the Leidenfrost transition of water varies with pressure in a way peculiar to the surface material, depending on the "wettability" of the heating surface. It is independent of the thermal diffusivity of the heating surface. In Figure 16, the evaporation time is reported as a function of the temperature of the solid surface, with the pressure as a parameter. The Leidenfrost transition is obtained from the measurement of the

evaporation time as the temperature for which the time is the largest. As one can see, at atmospheric pressure, the Leidenfrost transition is **543 °F** (284 °C), which is a very important result for successfully completing the research project discussed in this dissertation.

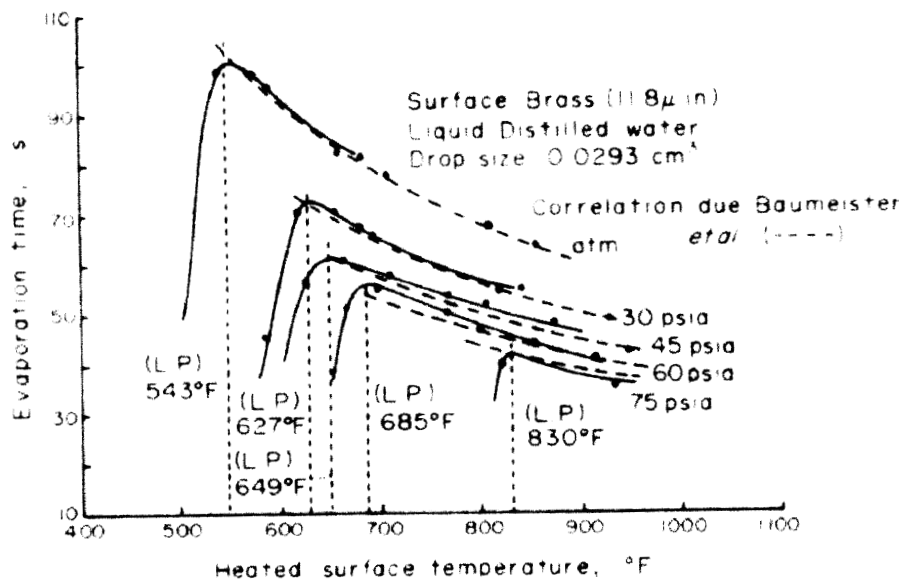


Figure 16. Variation of the Leidenfrost transition with pressure

In 1988, Avedisian and Fatehi have reported an experimental study of the Leidenfrost evaporation characteristics. Experimental observations of the evaporation of water-in-fuel emulsion droplets in **film** boiling on a hot horizontal Surface are conducted. Measurements of the variation of the droplet diameter with respect to time have been performed for various surface temperatures and different initial water volumetric

concentrations. It is found that such emulsions exhibit preferential vaporization so that either the water or the hydrocarbon evaporates ~~first~~. This may be caused by an apparent discontinuity in the evolution of the droplet diameter. Results also suggest that the water evaporation rate decreases if the water content increases. The initially opaque colored droplets appear to clear up during vaporization for several of the emulsions tested. Coalescence of internal water micro-droplets is also observed for water/octane and water/dodecane emulsions.

Experiments with water droplets impacting thin steel strips kept at a temperature above the Leidenfrost transition are reported by Yao *et al.* (1988). High-speed techniques show that the impacting droplets are generally bimodal in size distribution. The volume ratio of these two groups and the mean droplet diameter are a function of the offset of the incoming droplet respect to the center plane of the strip and of the ratio between the diameter of the incoming droplet **and** the strip transversal dimension. The smaller droplets contribute mostly to the liquid-vapor interfacial area for heat and mass transfer.

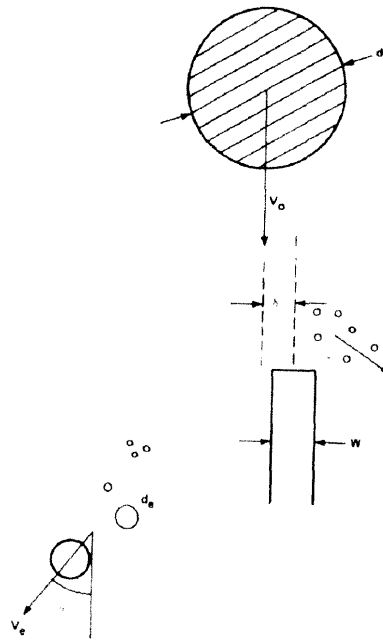


Figure 17. Configuration of the problem studied by Yao *et al.* (1988)

One of the most interesting studies on collision dynamics of water droplets over a rigid surface is accomplished by Hatta *et al.* (1995). In this paper, particular emphasis is given to the above Leidenfrost transition region, for water particles (300-600 μm) impinging on porous surfaces. The main purpose of the paper is to consolidate previous empirical results obtained using larger droplets (2-3 mm) over the range of diameters investigated in this work. Another issue is to clarify the correlation between the droplet Weber number and the coefficient of restitution (the ratio between the droplet velocities after and before impact) when the droplet rebounds **from** the hot surface without disintegrating into a number of particles. Additionally, the resident time of the droplet is examined and discussed by comparing the results with prior

experimental correlations proposed by other authors. The most interesting results are the following:

- The critical Weber number, corresponding to the threshold between the droplet break-up on the surface and the rebounding, is nearly 50 in Hatta's experiments and fairly smaller in comparison with previous authors results (values ranging from 70 to 90).
- The variation of the resident time of the droplets on the surface is in good agreement with the first order vibration period of freely oscillating droplet.
- The coefficient of restitution is larger than 0.5 for Weber numbers smaller than 18 and it decreases with increasing We .

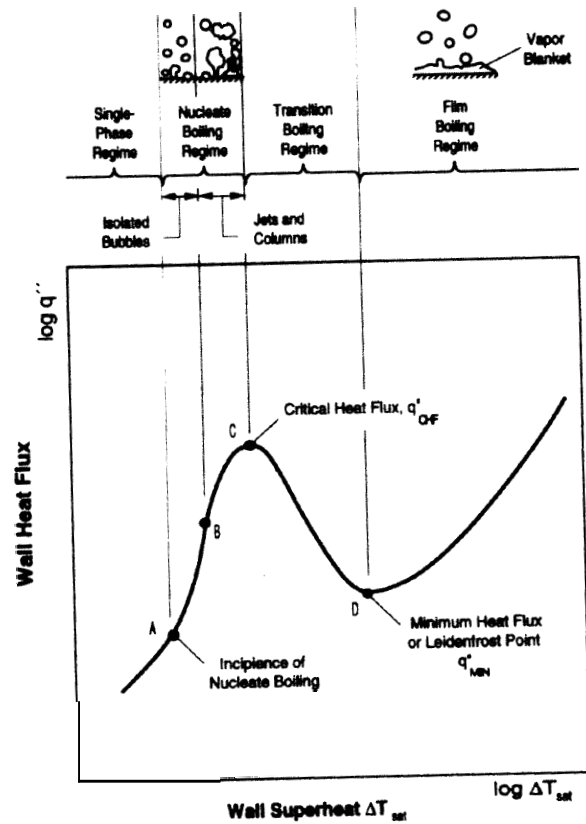


Figure 18. Boiling regimes and Leidenfrost transition definition (Bernardin *et al.*, 1997)

High-speed photographic techniques to record the impact behavior of water droplets over a hot aluminum surface are used by Bernardin *et al.* (1997a). The main parameters influencing the heat transfer and the impact phenomenon are the injection velocity and the surface temperature. The authors vary the surface temperature and the droplet Weber number in order to explore various heat transfer regimes, from film boiling to film evaporation. They notice that, for temperatures corresponding to the critical heat flux and the Leidenfrost transition, the data show little sensitivity to the

drop velocity and the frequency of the impingement. Other important conclusions are that the droplet Weber number **has** a major influence on the spreading characteristics and integrity of the water particles and that increasing the Weber number in all boiling regimes decreases the spreading time and increases the instability of the liquid breakup.

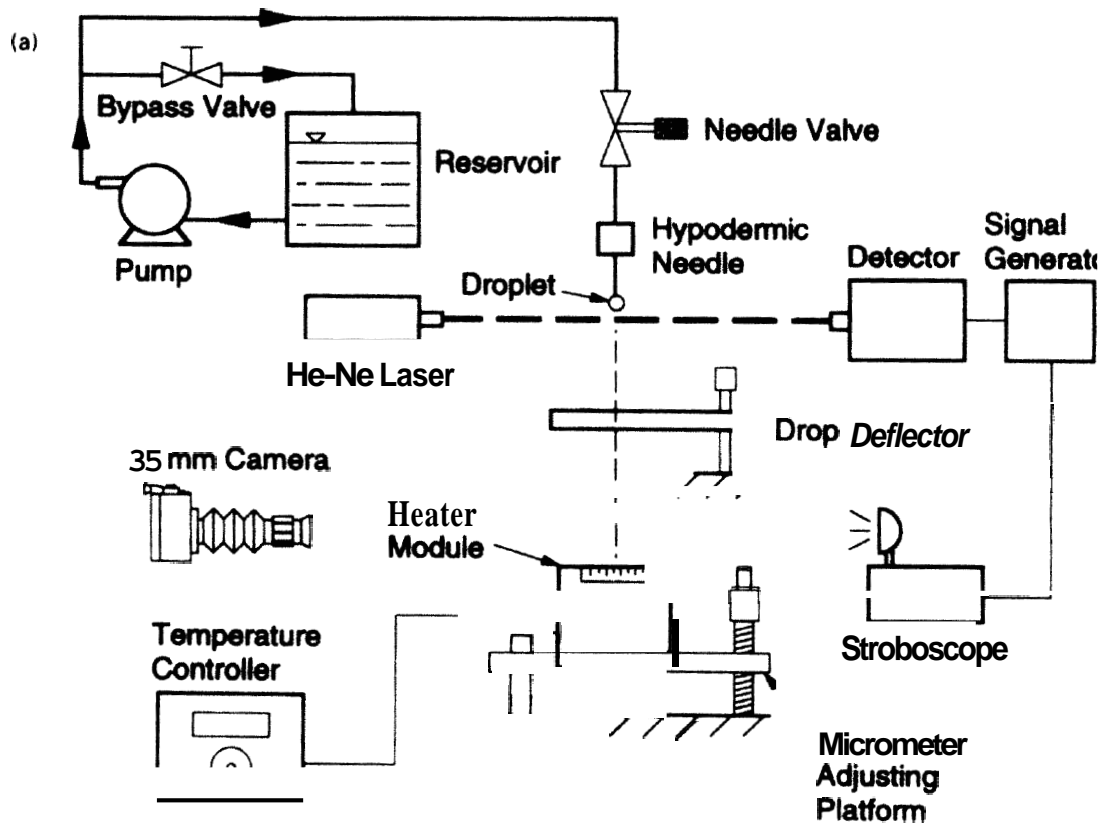


Figure 19. Experimental apparatus used by Bernardin (1997)

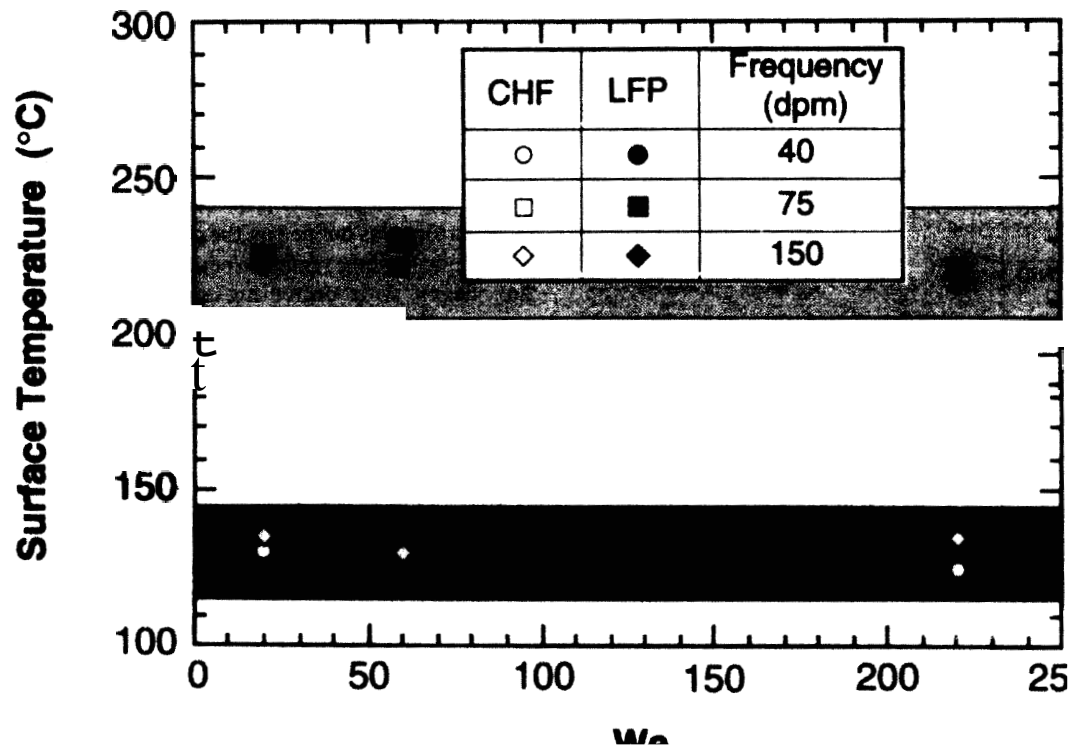


Figure 20. Critical heat flux and Leidenfrost transition in the plane
Temperature- Weber number (Velocity) for various droplet impacting
frequencies

The companion paper by Bernardin *et al.* (1997b) shows the influence of the surface roughness on heat transfer regimes induced by water droplets impacting over metallic surfaces. The ~~most~~ interesting results are ~~as~~ follows:

- The surface temperature is inversely proportional to the droplet lifetime.

- The droplet spreading time decreases with the Weber number.
- The surface roughness influences the boiling regimes. In fact, the surface features induce violent liquid film breakup at high temperature (film boiling) and increase the density of nucleation sites at lower temperature (nucleate boiling and transition boiling regimes).

In Figure 20, the critical heat flux (CHF) and Leidenfrost point (LFP) are reported in the plane Temperature-Weber number for various droplet impacting frequencies. This may suggest that the Leidenfrost temperature is not significantly affected by the velocity of the gas flow (We is proportional to velocity) and it also confirms the value of the Leidenfrost transition already highlighted by Emerson at the beginning of the section.

CHAPTER 3

MATHEMATICAL MODEL

The following sections provide a detailed description of the RTI (Response Time Index) model and the newly formulated EC (Evaporative cooling) model. The purpose of the models is to provide **an** estimate of the activation time for a temperature-activated sprinkler. The presence of water droplets in the hot gas flow is neglected in the RTI model, while it is considered in the new approach, leading to a significant improvement in predicting the activation times of secondary sprinklers.

RTI MODEL

The metal link of a ceiling-mounted fire sprinkler can be schematized **as** a cylinder placed vertically at some distance below the ceiling surface, **as** shown in Figure 21. The small dimensions of these components (about 6-10mm in diameter and 20 mm long) and their relatively high thermal conductivity warrant the applicability of the lumped heat capacity method. Therefore, the energy balance for the link can be written as:

$$\rho_S V_S c_S \frac{dT_S}{dt} = Q_{\text{conv}} + Q_{\text{cond}} + Q_{\text{rad}} \quad (3.1)$$

The subscript 'S' refers to the sprinkler link and Q_{conv} , Q_{cond} , Q_{rad} are respectively the convective, conductive and radiative heat transfer components indicated in Figure 21.

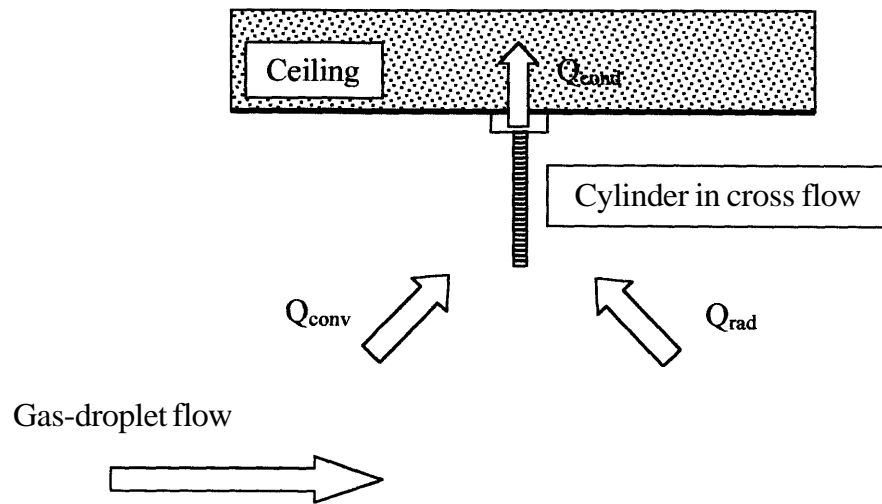


Figure 21. Heat transfer between hot gas and fire sprinkler

During the initial stages, the size of the fire is typically small, so the radiative heat transfer can be neglected. The effect of conductive term can be properly quantified as described by Heskestad and Bill (1988). However the conductive term is typically

negligible with respect to the convective part, since most commercial sprinklers are insulated from the pipe plug (SFPE Handbook, 1995). Therefore, Equation (3.1) reduces to:

$$\rho_S V_S c_S \frac{dT_S}{dt} = Q_{\text{conv}} = h S (T_G - T_S) \quad (3.2)$$

The subscript 'G' refers to the hot gas. ρ_S is the density, V_S is the volume and c_S is the specific heat of the simulated sprinkler link. h represents the convective heat transfer coefficient. Considering the link to be a cylinder of diameter d and introducing the Nusselt number ($Nu = h d / k_G$, k_G being the thermal conductivity of the gas) into Equation (3.2), the following differential equation is obtained:

$$\frac{dT_S}{dt} = 4 \frac{k_G}{\rho_S \cdot c_S} \frac{Nu}{d^2} (T_G - T_S) \quad (3.3)$$

The fluid mechanic interaction of the gas flow with the sprinkler link can be modeled as the cylinder in cross-flow problem. For this configuration and for Reynolds numbers Re_d in between 40 and 1000, the correlation for the convective heat transfer presents a dependence of the Nusselt number on the Reynolds and Prandtl numbers as follows (Zakauskas, 1985):

$$Nu = C_1 Re_d^{0.5} Pr^{0.37} \quad (3.4)$$

The Reynolds and Prandtl numbers are defined, respectively, as:

$$\text{Re}_d = \frac{U d}{\nu_G} \quad (3.5)$$

where U is the free-stream gas velocity and ν_G is the kinetic viscosity of the gas, and:

$$\text{Pr} = \frac{\nu_G}{a_G} \quad (3.6)$$

where a_G is the thermal diffusivity of the gas.

The constant C_l in Equation (3.4) is equal to 0.52 for a cylinder in cross-flow.

Because of the different boundary conditions between the actual problem and the cylinder in cross-flow (in particular, the far-field velocity profile), it is chosen to leave the numerical value of this constant unspecified. Experimental data will be used to determine the value of the parameters that will appear in the final model equation.

Substituting Equations (3.4, 5, 6) into (3.3) gives the following:

$$\frac{dT_S}{dt} = \left[C_2 \frac{k_G}{k_S} \frac{a_S}{a_G} \nu_G^{0.5} \text{Pr}^{-0.63} d^{-3/2} \right] \sqrt{U} (T_G - T_S) \quad (3.7)$$

where $C_2 = 4 \cdot C_1$. The term in square brackets is a function of the link geometry and of the thermo-physical properties of link and fluid. For a given sprinkler, this term can be considered a constant over a wide range of temperatures. Its inverse is known as the *RTI* of the sprinkler link:

$$RTI = C_3 \frac{k_S a_G Pr^{0.63}}{a_S k_G v_G^{0.5}} d^{1.5} \quad (3.8)$$

As pointed out by Heskestad & Bill (1988), the *RTI* is a value practically constant within the range of temperatures usually exploited in fire protection applications. A simple calculation shows that the ratio $a_G \cdot Pr^{0.63} / (k_G \cdot v_G^{0.5})$ changes only by 3 percent for a temperature variation of 250 °C. Since the other quantities in Equation (3.8) do not depend on the gas temperature, the *RTI* can be considered only a function of the cylinder diameter. An experimental validation of the parameter *RTI* will be provided in the model assessment phase of our research project.

Introducing the above expression for *RTI*, the transient energy balance for the thermal link becomes:

$$\frac{dT_S}{dt} = \frac{\sqrt{U} (T_G - T_S)}{RTI} \quad (3.9)$$

Equation (3.9) can be integrated with the initial condition $T_S(t=0) = T_0$ to yield:

$$T^D(t) = T_G - (T_G - T_0) \exp\left(-\frac{\sqrt{U}}{RTI} t\right) \quad (3.10)$$

The superscript ‘D’ indicates that no water droplets are present in the gas stream.

The *RTI* has units of $[(m s)^{1/2}]$ and it is indicative of the thermal inertia of the metal link. A higher *RTI* means that the sprinkler responds more slowly to the presence of hot gases, therefore causing a longer time delay between the onset of the fire and the activation of the sprinkler. On the other hand, a very small *RTI* may cause the sprinkler to be activated by heat sources other than a fire. This is also undesirable, because of the damages that the water spray would cause to the property in case of a faulty activation.

The time required for the activation of a ceiling-mounted fire sprinkler is calculated on the basis of Equation (3.10), coupled with the ceiling-jet model which describes the spreading of the hot gases under the ceiling (Alpert 1972). The same model can be extended to the case of an array of sprinklers, in which case it provides the means to determine the optimum spacing between the sprinklers (SFPE Handbook, 1998).

However, as said in the introduction, recent experiments on fires in a warehouse revealed discrepancies between the predictions of the *RTI* model and the actual behavior of the different sprinklers. The model proved accurate in the simulation of

the primary sprinkler, but it could not accurately predict the response of the secondary sprinklers. These sprinklers, in fact, were observed to activate only after a much longer time than expected and, in some cases, they did not activate at all. The explanation for the deficiency of the RTI model is discussed in the next section, together with the derivation of a new theory that improves its predictive capabilities.

EVAPORATIVE COOLING MODEL

The RTI model described in the previous section does not consider the water that is sprayed into the fire plume when the primary sprinkler is activated. Previous studies (Alpert, 1984) showed that part of the water spray does not reach the ground, but the droplets are entrained and carried away by the ascending plume. Such an eventuality is shown in Figure 22, for the case of a 4 m/s - 1000 K buoyant plume generated by a fire. Therefore, the gas stream contains water droplets and their presence must be taken into account. Indeed, even though the droplets progressively evaporate as they travel within the hot **gas** flow, part of them “survives” long enough to reach the surrounding secondary fire sprinklers. When this happens, it is possible that several droplets impact and deposit on the surface of the metal link; subsequently, the droplets evaporate by removing heat from the metal. This generates a cooling effect on the link, which counteracts the heating process due to the hot gas flow. The net result is that the link takes a longer time to reach the activation temperature. If the evaporative

effect is strong, it is even possible for the sprinkler to fail, that is, the link never melts so the spray does not actuate.

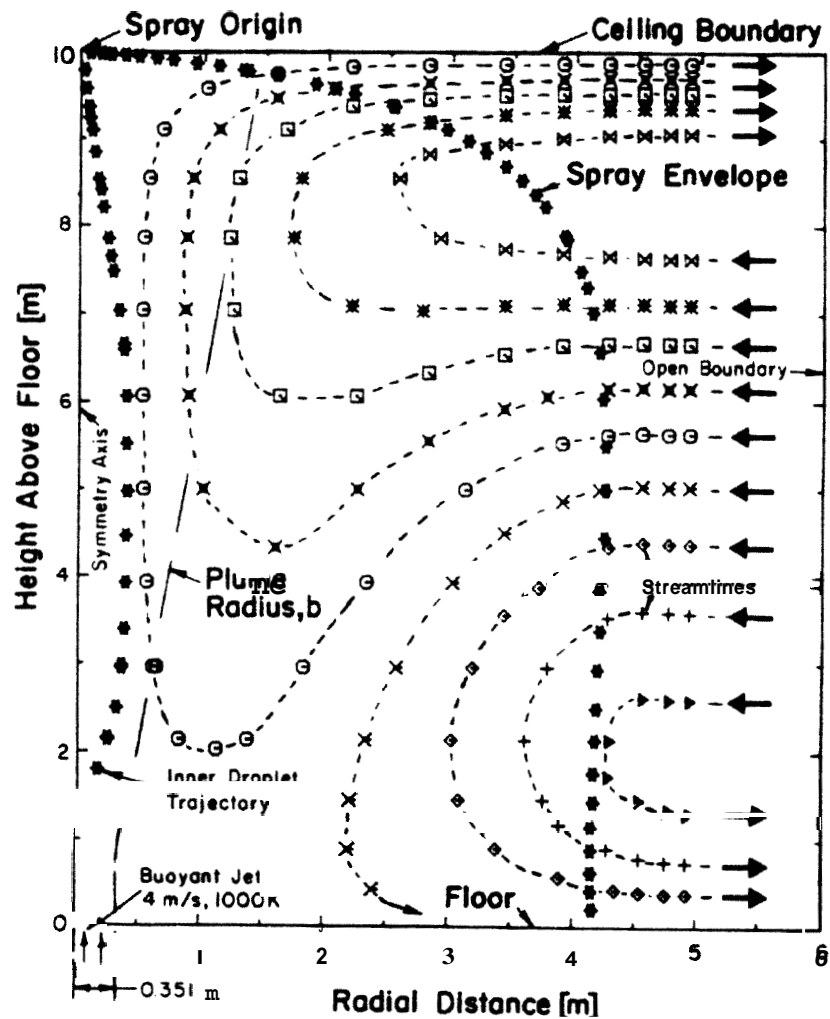


Figure 22. Calculated gas streamlines and trajectories of 1 mm dia. droplets injected by a spray nozzle on the axis of a fire plume (Alpert, 1984)

If this scenario is considered, the previously described phenomenology of the warehouse fire experiments can be explained: before the actuation of the primary sprinkler, there is no water in the gas flow, therefore the RTI model is applicable. After water is sprayed on the fire, water droplets are carried by the gas stream and impact on the surrounding sprinklers, delaying their activation.

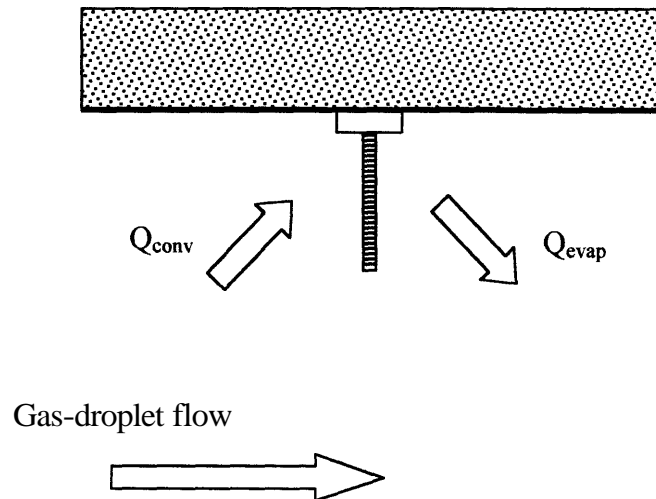


Figure 23. Diagram for the evaporative cooling model

A revised model for the thermal response of a fire sprinkler link is proposed here to overcome the deficiencies of the previous approach. As schematized in Figure 23, the new model includes an additional term (Q_{evap}) in the energy balance for the thermal link (Equation 3.2), to account for the evaporative cooling effect:

$$\rho_S V_S c_S \frac{dT_S}{dt} = Q_{\text{conv}} - Q_{\text{evap}} \quad (3.11)$$

The convective heat transfer term in Equation (3.11) is treated like in the RTI model.

The evaporative cooling term is proportional to the mass flow rate of water droplets that deposit on the link surface. The following assumptions are made:

- The droplets in the gas stream are at saturated liquid conditions. In fact, the thermal response time of water droplets is at most of 217 ms. This indicates that they reach the saturation temperature in less than 261 ms. Since a droplet takes at least 800 ms to travel from the water spray nozzle location to the test section, the droplet is likely to reach the saturation point some time before it impacts the cylinder surface. Therefore, the evaporative cooling per unit mass of water is equal to the latent heat of vaporization, A .
- The droplet specific mass flow rate, G , is constant and uniform throughout the **gas** stream.
- Only a portion of the droplets impacts the surface of the link, while some have sufficiently small inertia to move around the obstacle.
- The water droplets are sparse in the hot gas flow, **so** that no droplet-droplet interactions are considered.

With these assumptions, the evaporative cooling term can be expressed as:

$$Q_{\text{evap}} = \kappa G A_s \Delta \quad (3.12)$$

where κ is the droplet collection efficiency of the sprinkler surface (Fuchs, 1964). The droplet collection efficiency takes into account the effect of the **gas** flow velocity on the droplets as they approach the sprinkler. The following section discusses the derivation of an expression for the droplet collection efficiency κ .

Droplet collection efficiency

The cylinder in cross-flow problem is used to model the fluid mechanic interaction of the link with the hot gas. The flow away from the cylinder has uniform velocity U , which is aligned with the **x-axis** as shown in Figure 24. The potential flow theory (Panton, 1984) is applied to obtain an approximate solution for the gas velocity field around the cylinder, since the Reynolds number based on the cylinder diameter is sufficiently high in our applications ($Re_d > 300$ for a **6.4 mm** diameter cylinder):

$$\frac{u(x,y)}{U} = 1 - \frac{d^2}{4} \frac{(x^2 - y^2)}{(x^2 + y^2)^2} \quad (3.13)$$

$$\frac{v(x,y)}{U} = -\frac{d^2}{2} \frac{xy}{(x^2 + y^2)^2} \quad (3.14)$$

An example of the streamlines for the potential flow (3.13, 3.14) is shown in Figure 24.

The behavior of the water droplets in the gas plume can be determined from the theory of dispersed flows (Crowe *et al.*, 1998). For the typical water volumetric fraction produced by fire sprinklers (about 10^{-6}), the average droplet spacing in the gas plume is very large (more than 80 times the droplets diameter). Therefore, the droplet-droplet interactions are negligible and individual droplets can be treated as isolated.

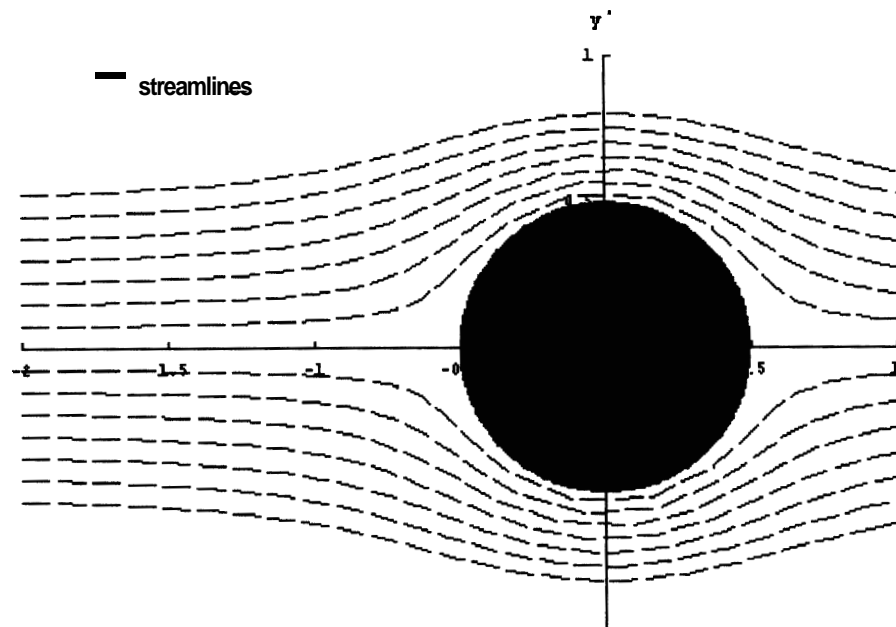


Figure 24. Potential flow solution for the gas flow around the sprinkler link

Changes in the gas streamlines, such as those occurring near the sprinkler link, also affect the entrained droplets. However, the droplets present a certain inertia to these changes, which plays a fundamental role in determining their trajectory and, in particular, whether they impact the solid surface or not. In general, larger droplets respond rather slowly, which makes them more likely to deposit on the link surface, while smaller droplets respond faster and, consequently, are more likely to escape the impact.

The collection efficiency provides a measure of the fraction of droplets that cannot avoid the cylindrical obstacle and deposit on its surface. To determine κ we need to solve the equation of motion for a particle in a gas flow. Under the Stokes flow approximation, this becomes (Panton, 1984):

$$m_d \frac{d\vec{v}_d}{dt} = 3\pi\mu_G D (\vec{U} - \vec{v}_d) \quad (3.15)$$

where the subscript ‘d’ indicates the droplet. Calculations show that a $100\mu\text{m}$ diameter droplet reaches a terminal velocity of less than **0.24 m/s** in our applications. Thus, the Reynolds number based on the droplet diameter and the relative velocity to the gas is equal at most to 0.8, which is smaller than the unity and the Stokes’ approximation in (3.15) is justified. Equation (3.15) can be non-dimensionalized by introducing the following quantities:

$$\vec{v}_d' = \frac{v_d}{U} \quad (3.16a)$$

$$(x', y') = \frac{(x, y)}{d} \quad (3.16b)$$

$$t' = t \frac{U}{d} \quad (3.16c)$$

where d is the diameter of the sprinkler link and U is the free-stream velocity of the ceiling-jet. Therefore:

$$\frac{d \vec{v}_d'}{dt} = \left[\frac{18}{\text{Re}_D \frac{D}{d} \frac{\rho_L}{\rho_G}} \right] (\vec{U}' - \vec{v}_d') \quad (3.17)$$

Let Z be the quantity between square brackets. This quantity represents the inertia of the droplet to changes in the flow field. A closer look at Equation (3.17) shows that the acceleration of the water droplet (**and** therefore the rapidity of the water particle to change trajectory from the straight line) is inversely proportional to the ratio between the droplet size and the cylinder diameter. Also, the ratio between the density of the gas and the density of the liquid plays a relevant role in the phenomenon as well as the velocity of the **gas** in the **free** stream region. Equation (3.17) **can** be solved numerically by using the potential flow solution for the gas velocity. This allows to determine the trajectory of a droplet **as** a function of its initial position, y_o' , in the **free**-stream region. Examples of the droplet trajectories are given in Figure 25, for several values of the inertia parameter Z .

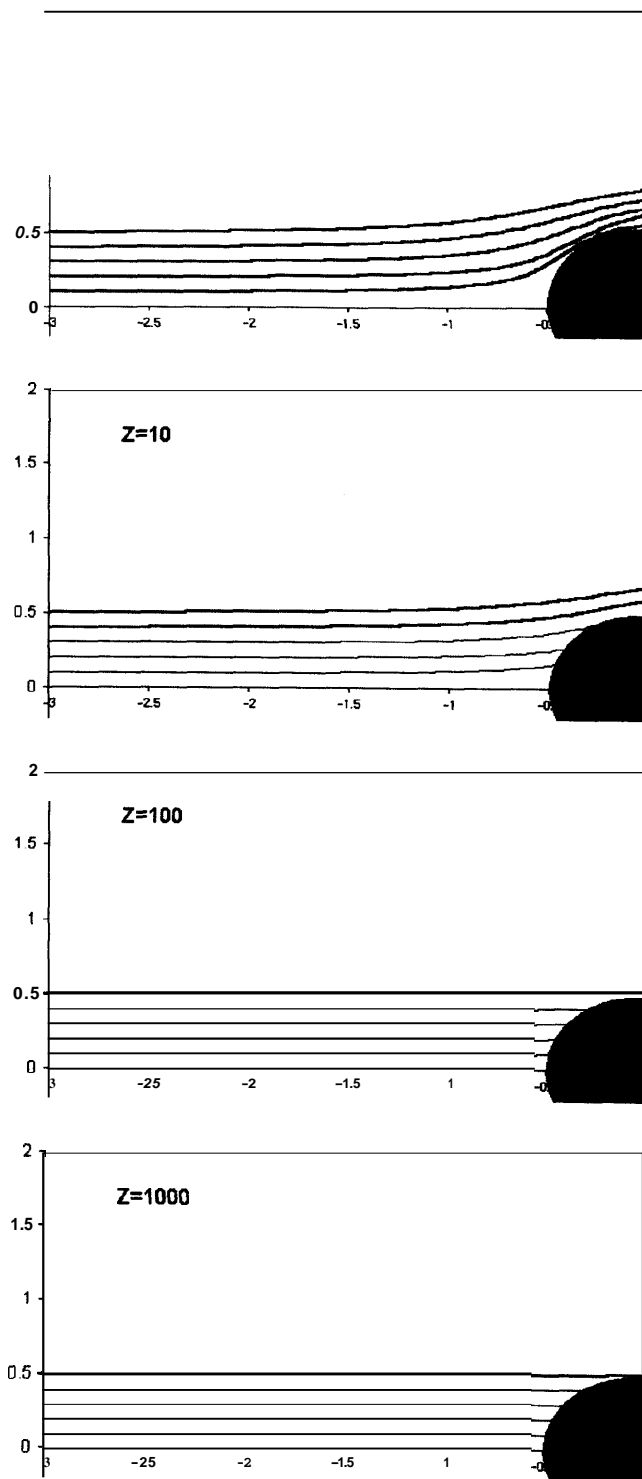


Figure 25. Trajectory of water droplets for different values of Z

From the solution of Equation (3.17) and for any given value of the inertia parameter Z , it is possible to identify a critical initial position, y_0' , such that the droplets with $y_0' \leq y_c'$ impact the link surface, whereas those with $y_0' > y_c'$ flow around the obstacle. In the extreme case of droplets with infinite inertia, the changes in the gas flow field would have no effect on their trajectories. Therefore, they would continue traveling parallel to the x-axis, which means that all and only the droplets in the region $-1/2 < y' < 1/2$ would deposit on the surface of the cylinder. Therefore, the collection efficiency, κ , can be expressed as:

$$\kappa = 2 y_c' \quad (3.18)$$

The collection efficiency is calculated over a wide range of values of the inertia parameter. The following expression is found to best fit the results:

$$\kappa(Z) = \frac{Z^{1.08}}{Z^{1.08} + 8.80} - 0.04 \quad (3.19)$$

Figure 26 shows the fitted curve for the collection efficiency. The collection efficiency is an increasing function of the inertia parameter Z . Also, it reaches an asymptotic value of 0.97 for Z 's larger than 1000. For typical fire sprinkler applications ($U = 5 \text{ m/s}$, $T_G = 230^\circ\text{C}$) and for typical water spray droplet distributions (droplet characteristic mean diameter $D = 65 \mu\text{m}$), the value of Z is about 126. From

the curve shown in Figure 26, the collection efficiency κ is calculated to be in the order of 95 percent. Hence, the collection efficiency curve is near its asymptote in that region, which allows to approximate κ as a constant. This assumption will be verified from the analysis of the experimental data.

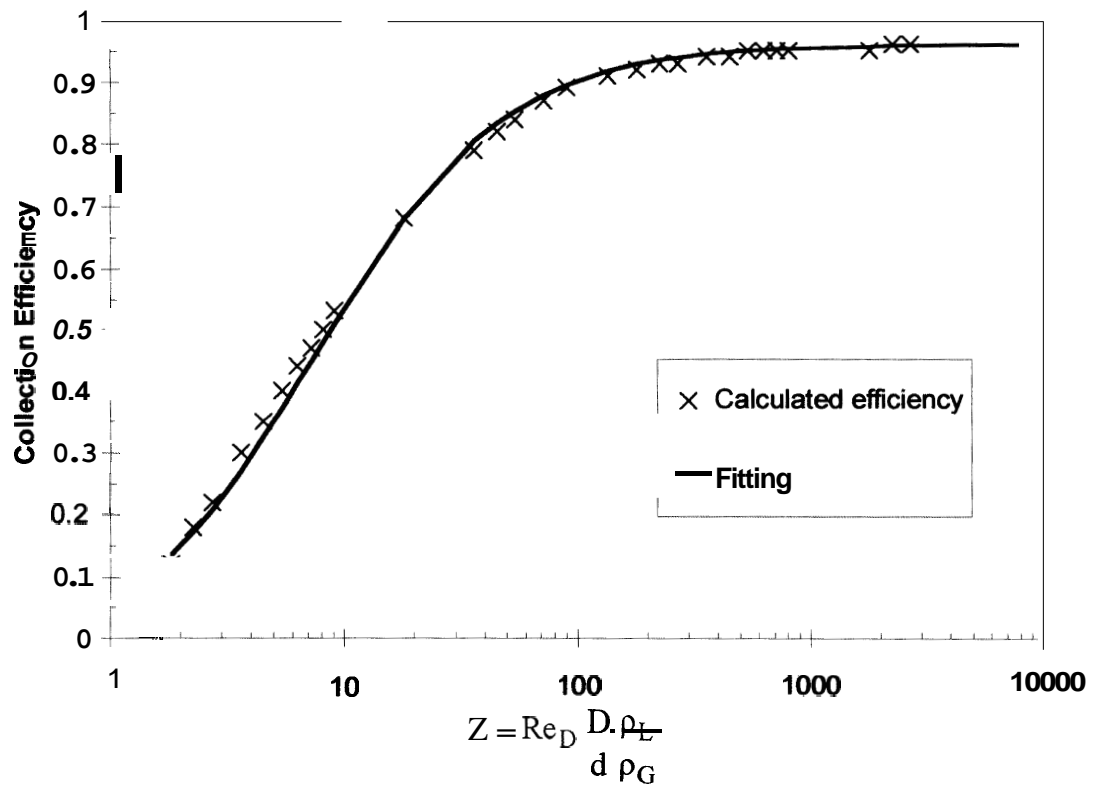


Figure 26. Collection efficiency as a function of the droplet inertia

Modified sprinkler response time

If the convective and evaporative heat transfer terms are introduced in (3.11), the energy balance equation is obtained as:

$$\rho_S V_S c_S \frac{dT_S}{dt} = h S (T_G - T_S) - \kappa G A_S A \quad (3.20)$$

The water specific mass flow rate, G , can be expressed in terms of the droplet velocity, U (supposed equal to the gas velocity since the small droplet size), and volumetric fraction, β , as follows:

$$G = \rho_L U \beta \quad (3.21)$$

The water volumetric fraction can be calculated as the ratio of the volumetric flow rates of water and hot gases through a given cross-section. However, because of the evaporation of the droplets in the gas stream, the value of β is largely dependent on the location under consideration, as well as on the gas temperature and water droplet size distribution. Therefore, a local measurement of β is necessary. Substituting Equation (3.21) into (3.20) gives:

$$\frac{dT_S}{dt} = \frac{\sqrt{U} (T_G - T_S)}{RTI} - \frac{c \cdot U \cdot \rho}{RTI} \quad (3.22)$$

where RTI has already been defined in (3.8) and C is given by:

$$C = \frac{\rho_L A_S \kappa \Lambda}{S} \frac{\sqrt{U}}{h} \quad (3.23)$$

or equivalently:

$$C = C_4 \frac{\rho_L \kappa \Lambda}{P_S c_S d} \text{RTI} \quad (3.24)$$

where C_4 is a constant to be determined experimentally. Equation (3.22) can be integrated with the initial condition $T_S(t=0) = T_0$ to give:

$$T^W(t) = T_G^W - C\beta\sqrt{U} - (T_G^W - T_0 - C\beta\sqrt{U}) \exp\left(-\frac{\sqrt{U}}{\text{RTI}} t\right) \quad (3.25)$$

The superscript ‘W’ indicates that water droplets are now present in the gas stream.

Equation (3.25) represents the proposed solution for the thermal response of a sprinkler link in presence of a flow of hot gases and water droplets. The experimental validation of the model, as well as the quantification of the evaporative cooling parameter C that appears in Equation (3.25) are presented in Chapter 6. Note that if no water is carried by the airflow ($\beta=0$), the solution reduces to that provided by the RTI model.

Additional remarks

For Reynolds number in the range between **40** and 1000, the heat transfer correlation for a cylinder in cross-flow can be expressed as (Zukauskas, 1985):

$$h = C_1 \cdot \frac{k_G}{d} \text{Re}_d^{0.5} \text{Pr}^{0.37} \quad (3.26)$$

Therefore, the parameter C can be evaluated **as**:

$$C = \frac{\kappa \cdot \rho_L \cdot v_G^{0.5} \cdot \Lambda \cdot \sqrt{d}}{C_1 \cdot \pi \cdot k_G \cdot \text{Pr}^{0.37}} \quad (3.27)$$

The ratio $\frac{k_G \cdot \text{Pr}^{0.37}}{v_G^{0.5}}$ is nearly constant over the range of temperatures of concern

(Heskestad and Bill, 1988). Given the dependence of the heat transfer coefficient on the square root of the gas velocity, C is independent of the gas velocity and hence can be considered only a function of the cylinder diameter (see Equation 3.27). **As** in the case of the RTI, the parameter C must be determined by experimental investigation both because of the different conditions between the actual problem and the cylinder in cross-flow case and because the existence of several additional phenomena in presence of water droplets: for example, the incomplete evaporation of the droplets impacting over the surface of the cylinder and/or the dynamic effects due to the fact

that the particles are moving, like the rebounding of a water particle over the surface of the cylinder and the disintegration of a drop into smaller particles. Therefore, the real value of C is expected to be smaller than the value suggested by (3.27).

By introducing Equation (3.10) into Equation (3.25), one obtains:

$$\left(T_G^W - T^W \right) \left(T_G^D - T_0 \right) - \left(T_G^W - T_0 \right) \left(T_G^D - T^D \right) = C \beta \sqrt{U} \quad (3.28)$$

This result suggests that the parameter C may be determined **from** appropriate experiments in both dry and wet conditions that are described in Chapter 6.

For time going to infinity, the asymptotic form of Equation (3.25) provides the following expression for the water volumetric fraction:

$$\beta = \frac{T_G - T^W}{C \sqrt{U}} \quad (3.29)$$

As expected, Equation (3.29) shows that the temperature of a wetted cylinder, T^W , decreases if the water content in the gas flow **and** the velocity of the gas increase.

Once the parameter C is determined, this equation provides an indirect measurement of the water volumetric fraction if the gas temperature **and** velocity are known.

CHAPTER 4

EXPERIMENTAL FACILITY

The model presented in the previous chapter needs experimental validation. For this purpose, the ECSAT facility ~~has~~ been built in the Engineering Laboratory Building at the University of Maryland. The facility is designed to allow for the measurement of the thermal response of a simulated sprinkler ~~link~~ immersed in a hot ~~gas~~ flow. The characteristics of this apparatus permit to perform accurate measurements of the link behavior over a ~~broad~~ range of several parameters, such ~~as~~ the gas temperature ~~and~~ velocity, the water droplet volumetric fraction and the droplet size distribution. The following sections describe the set-up of the experimental facility and the available instrumentation.

FACILITY SET-UP

Experimental facilities for the study of the sprinkler link thermal response typically consist of a closed-circuit duct in which a hot gas flow is established (UL 199,1995;

see also Figure 4). Once the desired conditions are obtained, the sprinkler head is rapidly inserted into the gas flow, and the transient response is studied. This procedure is commonly known as a *plunge* test. The capability of creating steady-state gas flow conditions before inserting the link **has** the advantage of greatly simplifying the analysis of the data, which makes this the standard procedure for testing fire sprinkler performance.

For the present study, which involves a two-phase gas-droplet flow, the plunge-test approach is still applicable, although some modifications are necessary. The **two-** phase flow can still be adjusted until the desired conditions are obtained and a steady state is reached, before inserting the probe. However, the closed-circuit configuration cannot be maintained because of the presence of water droplets in the flow. In fact, the droplets sprayed into the hot gas rapidly evaporate, which causes the relative humidity of the gas mixture to increase. If the flow were re-circulated, the continuous addition of water to the **gas** would alter the composition of the gas to the point where the droplet evaporation process would be affected. To maintain a low relative humidity in the gas stream, therefore, a once-through circuit is chosen **as** shown in Figure 27.

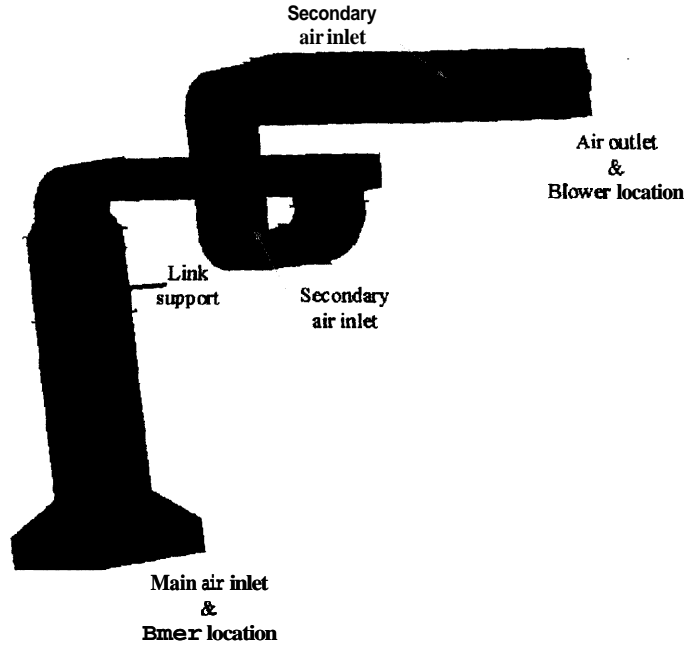


Figure 27. Layout of the ECSAT facility

A blower placed near the outlet of the ductwork generates the gas flow inside the system. The air entering into the duct is heated up by a natural gas burner, and then flows upward through a square duct section (0.61 m x 0.61 m). A honeycomb structure, about 0.2 m thick and made of tightly packed steel wool, is placed in the initial portion of the duct. Its purpose is to force the gas stream to spread over the entire cross-section, as well as to obtain a more uniform temperature distribution. As the hot gas emerges from the honeycomb, it reaches the spray location. A finely atomized water spray is injected into the gas stream, simulating the effect of the activation of the primary sprinkler.

A square-edged circular orifice (0.25 m diameter) is located about 0.49 m downstream of the spray. The orifice represents an abrupt restriction of the cross-sectional area for the two-phase flow. The orifice induces a vena contracta in the flow, which is characterized by the near parallel streamline profile schematized in Figure 28.

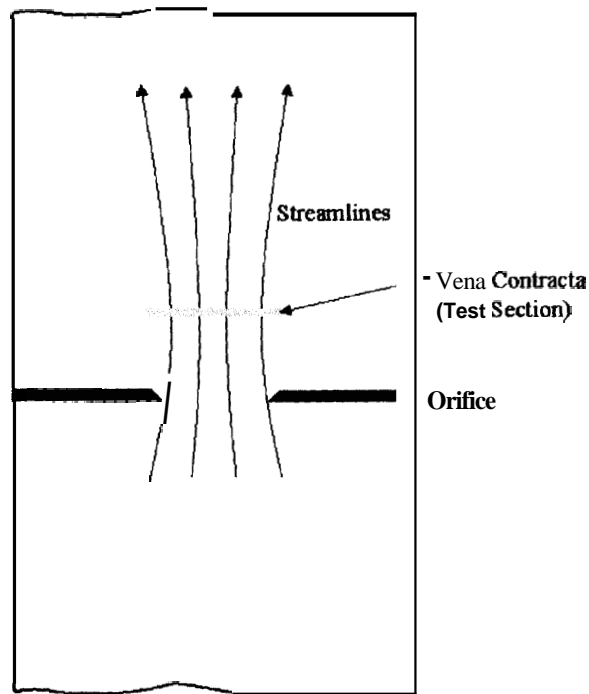


Figure 28. Flow field across the circular orifice

At the location of the vena contracta, which occurs about **0.4** m downstream of the orifice, the mean velocity field is parallel to the axis of the orifice (no radial velocity

component). The range of velocities investigated in this study is in between 3 and 9 m/s. For these values, the Reynolds number associated with the gas flow inside the pipe is larger than 9000, indicating that the flow is yet turbulent before the orifice. Additional turbulent effects at the vena contracta may also be induced by the gas jet produced by the orifice, as it mixes with the slower gases flowing downstream. Clearly, the turbulence level in the test section and the disturbances induced by the gas jet may influence the gas velocity field, in particular its alignment with the axis of the duct. The turbulent friction velocity can be calculated accordingly to the definition (Brodkey, 1995) once the pressure drop between the duct inlet and the vena contracta is estimated by using flow coefficient correlations ("Restriction flow meters for internal flows", Fox & McDonald, 1985). On this basis, the fluctuating radial velocity is estimated by considering the turbulent velocity profile in pipe flows. The results show that the intensity of turbulence, defined as the ratio of the fluctuating radial velocity to the mean gas velocity, is about 5 percent ($U = 5 \text{ m/s}$), which does not seem very significant compared to other inaccuracies present in this study. Furthermore, visual analysis of the pictures taken at the test section shows that the droplet traces do not appear appreciably affected by turbulent phenomena, at least in the low-to-mid range of velocities explored in this project. Also, note that typically 300 particle samples are analyzed to obtain statistically meaningful measurements, thus decreasing the inaccuracies associated with the turbulence level of the gas flow. Double checks on the measured quantities affected by large errors will be performed either experimentally or theoretically, as described in Chapter 5 and 7. On this basis, the vena contracta is chosen as the test section for the plunge-test experiments.

After the vena contracta, the flow spreads and returns to occupy the entire duct cross-section. About **1.5** m after the test section, the vertical duct is reduced to a rectangular cross section (0.30 m x 0.61 m) before turning to proceed horizontally. The horizontal portion of the duct is simply utilized to cool down the hot gases before they reach the blower (which cannot operate above 70 °C). The hot gas is cooled down by transferring heat to the duct walls as well **as** by mixing with the cold air drawn in through the secondary inlets indicated in Figure 27.

The entire duct is made of 1.6 mm-thick galvanized steel. To satisfy the safety regulations, which require the temperature of accessible surfaces to be below 50 °C, the portion of the ductwork located inside the laboratory is insulated with 50 mm thick ceramic fiber insulation and covered with a thin aluminum sheet. Due to space constraints inside the laboratory, the final section of the duct (after the C-shaped turn shown in Figure 27) is located above the laboratory ceiling. This part is not insulated in order to accelerate the cooling of the hot gases and protect the blower **fi-om** high-temperature damage.

The following sections describe the main components of the ECSAT facility, as well as the available instrumentation.

UNIFORMITY OF THE TEST SECTION

Several experiments have been performed to verify that the temperature of the gas flow is uniform and that the water droplets are uniformly distributed over the test section. A measurement rake with four equally spaced thermocouples (type K) is positioned in proximity of the test section, as shown in Figure 29. The analysis of the data shows that the temperature of the **gas** is contained within a 15 percent variation around the average value measured over the test section. This result insures the first objective.

The water uniformity check is provided by changing the orientation of the mirror M to illuminate sequentially all the test section, **as** indicated in Figure 30. The two-phase flow is then recorded by the camera, which displays the distribution of the water droplets that cross the laser light plane, for different values of the angle of incidence of the laser light. The pictures, shown as an example in Figure 31, qualitatively indicate that the water droplets are distributed on the whole test section and that trajectories of the water droplets are aligned with the axis of the duct, compatibly with the assumption of the vena contracta originated by the orifice.

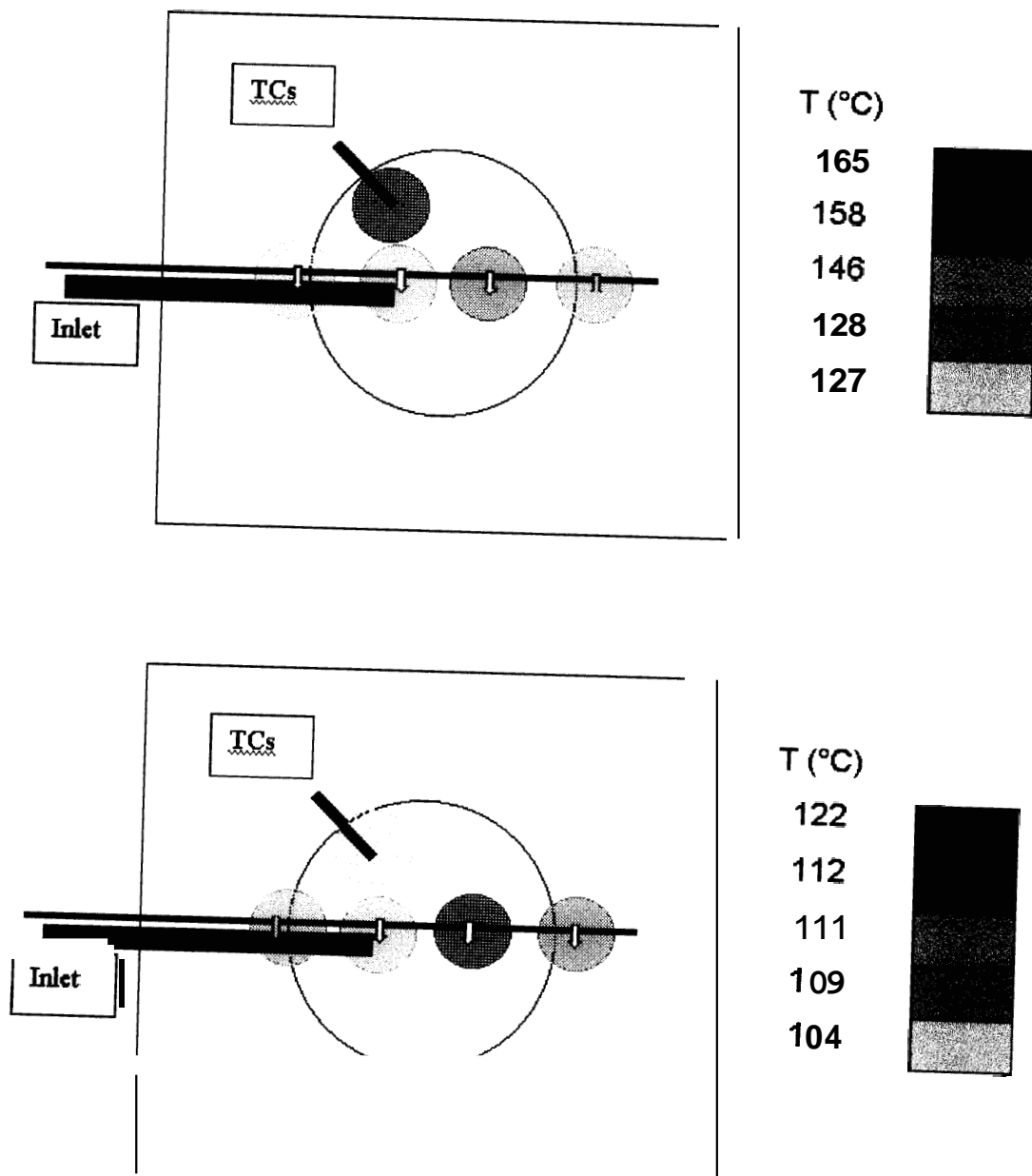


Figure 29. Position of the measurement rake and temperature distribution in the test section (dry conditions top, wet conditions bottom). Each color represents a specific temperature, as indicated in the legend for convenience

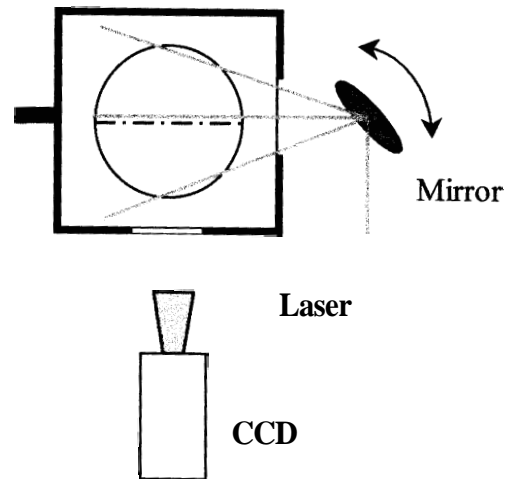


Figure 30. Water uniformity check

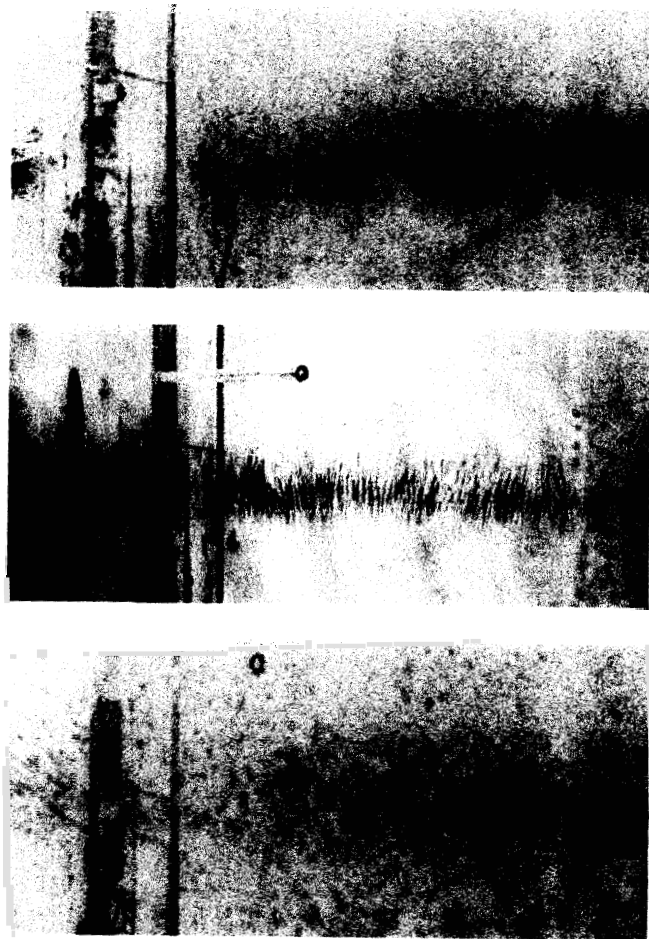


Figure 31. Pictures of the test section for various angles of the mirror M

BLOWER

The gas flow in the duct is induced by a 1.5 horsepower blower (Dayton, model 4C119), shown in Figure 32. In the ECSAT ductwork, the blower can establish a maximum flow rate of approximately $0.473 \text{ m}^3/\text{s}$ (1,000 cfm), which corresponds to a gas velocity of about 9 m/s in the vena contracta, at ambient temperature. Adjustable secondary air intakes are present at different locations along the duct, as shown in Figure 27. Varying the open area of these inlets provides control of the flow rate through the test section; the velocity in the vena contracta can be reduced to a minimum of about 3.0 m/s at ambient temperature.

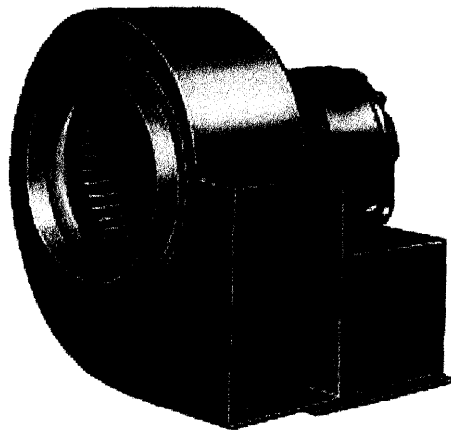


Figure 32. Gas exhaust blower

The blower may be damaged if operating with gas temperatures in excess of 70°C.

Therefore, the gas flow must be cooled down before it reaches the fan. As previously mentioned, the cooling is obtained by mixing the hot gas with the secondary air intakes and by having a long section of non-insulated duct leading to the blower.

A temperature readout is available for the operator to monitor the gas temperature at the blower inlet. If the temperature approaches the safety limit, the operator can activate a set of three sprays that inject water into the final section of the duct, providing additional cooling. In fact, the secondary air intakes cannot be modified during an experiment, because that would also alter the mass flow rate through the test section. A safety temperature switch is also placed immediately upstream of the fan inlet. The switch cuts the power to the burner if the temperature exceeds the safety limit.

GAS BURNER

The air entering the vertical section of the duct is heated up by a natural gas burner (Eclipse Combustion, model 200 JIB-C2), shown in Figure 33. The maximum power output is rated at 73.3 kW (250,000 Btu/hr). However, a set-screw placed along the gas inlet line can be used to reduce this value. Currently, the maximum power output for the burner is limited to about 44.0 kW (150,000 Btu/hr). Fine-tune adjustments of

the burner power output are possible, during the set-up phase of an experiment, by means of a remotely controlled gear motor which is connected to a butterfly valve placed on the gas line.

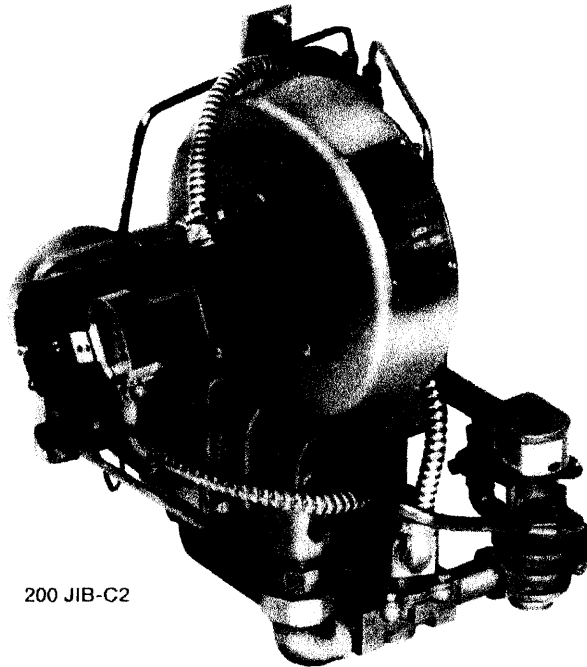


Figure 33. Natural gas burner

The natural gas is premixed with a forced airflow and the resulting air/gas mixture is ignited by a pilot light. Electrically activated solenoid valves control the **gas** flow to both the pilot light and the main combustion chamber. This allows the immediate shutdown of the combustion if the electrical circuit is opened, which can occur by

intervention of the operator or automatically. The operator can control the burner **from** the testing area, along with the rest of the equipment and instrumentation. A switch powers the electrical circuit and another one controls the gear motor. Two temperature-activated safety switches are also connected in series with the main power switch. One is placed immediately upstream of the blower, to protect it **from** overheating. The other one is located in the hooded portion of the duct, to turn the burner off in case the airflow is unexpectedly interrupted. Figure 34 shows a schematic of the wiring of the gas burner controls.

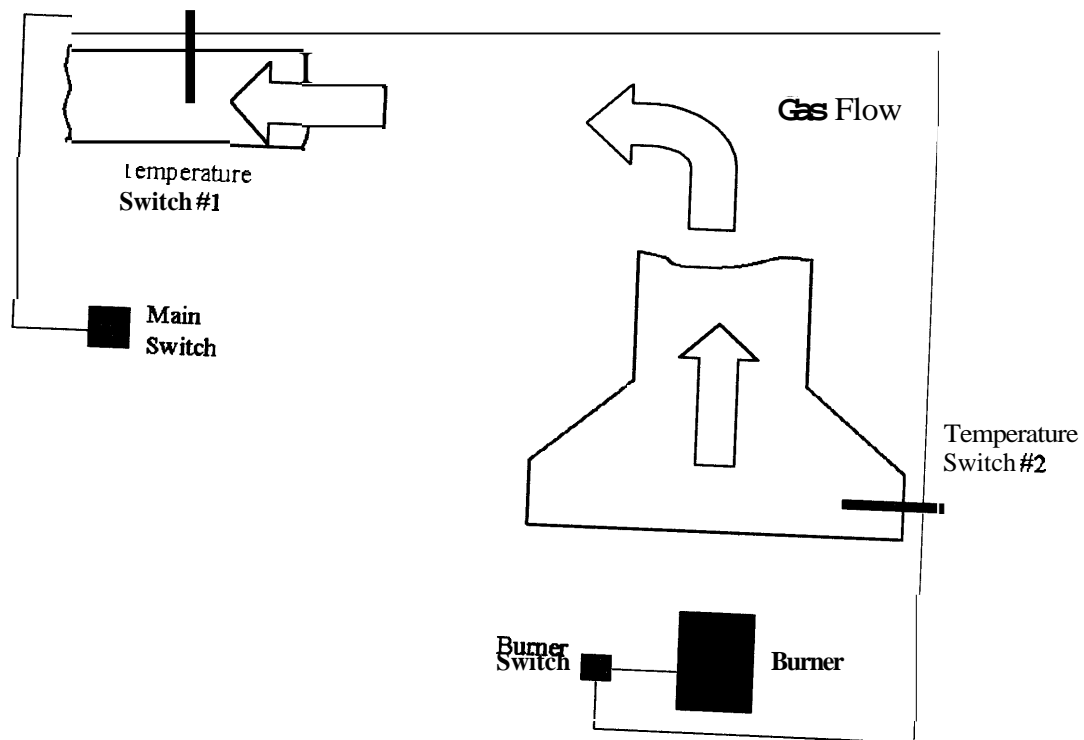


Figure 34. Gas burner control diagram

WATER SPRAY NOZZLES

Five spray nozzles are placed 0.24 m downstream of the steel wool honeycomb.

When the nozzles are active, water droplets are released into the hot gas stream, which carries them towards the orifice **as** shown in Figure 35. The water flow is supplied by a variable-flow gear pump (Cole-Parmer, model GX-74011) which can deliver a maximum flow rate of 0.02 liters/second. The five nozzles are independently controlled by shut-off valves, so that different spray flow rates can be obtained. A flowmeter **has** been inserted in between the water pump and the spray nozzles to measure the total water mass flow rate injected in the gas flow. The FL-110A flowmeter (Omega) **has** a 2% accuracy and a 1% reading repeatability.

Two different spray nozzle sizes are available (BETE Fog Nozzle, models PJ8 and PJ10), which allows to test the sprinkler response under different water flow rates and droplet size distributions. A PJ8 nozzle is shown in Figure 36. Table 3 reports some of the characteristics of the two nozzles at the nominal operating pressure of 482 kPa (70 psig). Currently, only one nozzle type is used at a time.

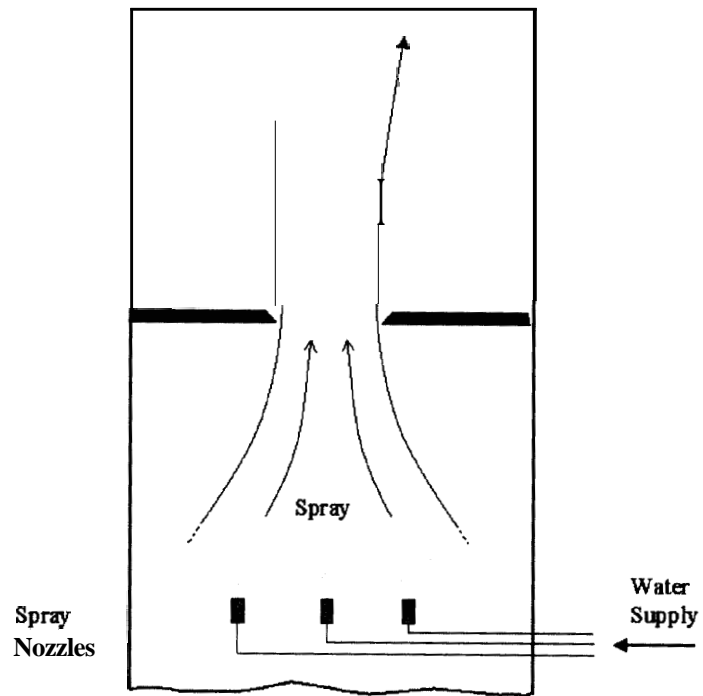


Figure 35. Water spray setup

	Flow Rate (m^3/s)	Characteristic Mean Diameter (μm)	Droplet mean volume (μm^3)
PJ8	$9.45 \cdot 10^{-7}$	65	$1.4 \cdot 10^5$
PJ10	$1.42 \cdot 10^{-6}$	82	$2.9 \cdot 10^5$

Table 3. Performance characteristics of PJ8 and PJ10 nozzles (@ 482 kPa)

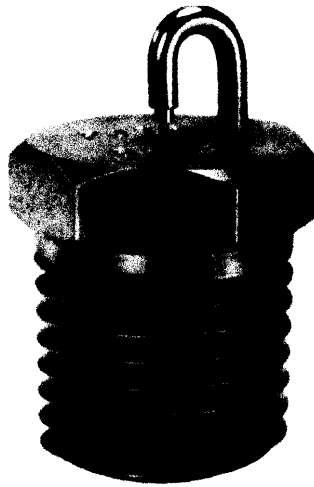


Figure 36. PJ8 spray nozzle

TEST SECTION AND SIMULATED SPRINKLER LINK

The test section is located in the vena contracta of the orifice, where the **gas** velocity is maximum and parallel to the axis of the aperture. This choice provides the cleanest conditions for the study of the sprinkler ~~link~~ response to the gas-droplet flow.

As shown in Figure 37, the simulated sprinkler link penetrates horizontally to the center of the test section. Different simulated sprinkler ~~links~~ have been prepared for testing in the ECSAT facility. They consist of an aluminum cylinder, 3 cm long and with diameter of **6.4 mm**, and an ~~may~~ of brass cylinders with diameters ranging between 2 and 7 **mm**. The links are placed in series with a rigid ceramic insulator (0.15 m long), in order to minimize the conductive heat losses to the support. One

(brass cylinders) or two type-K thermocouples (aluminum cylinder) are placed into the simulated sprinkler link to measure its temperature during the plunge tests. The Biot number of the link is at most in the order of 10^{-4} . Therefore, the link can be modeled as a lumped heat capacity, consistently with the assumptions of the theoretical model presented in Chapter 3.

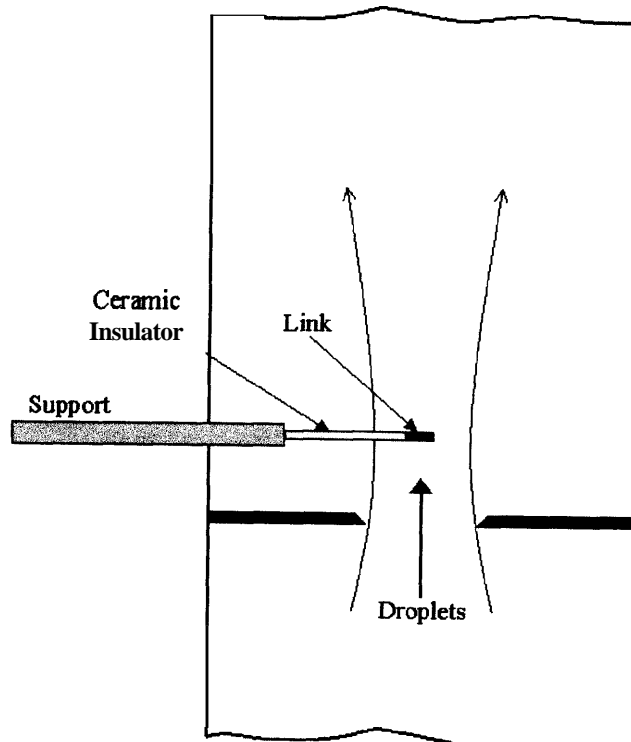


Figure 37. Diagram of the test section

CHAPTER 5

MEASUREMENT TECHNIQUES

The proposed model for the thermal response of a sprinkler link immersed in a two-phase flow of hot **gas** and water droplets is represented by the following equation:

$$\frac{dT_s}{dt} = \frac{\sqrt{U} (T_G - T_s)}{RTI} - \frac{C U \beta}{RTI} \quad (5.1)$$

This equation indicates how the rate of change of the link temperature is determined by the balance of two counteracting effects: the convective heat transferred from the hot **gas** to the link and the cooling effect due to the evaporation of the water droplets from the link surface. The gas and sprinkler temperatures, as well as the gas velocity and the water volumetric fraction, can be directly obtained from experimental measurements, as it will be described in the following. However, this leaves two quantities (RTI and C) to be determined.

The value of C cannot be determined from a single test, but must be derived from the general behavior of the probe subject to a wide range of boundary conditions. In fact,

Equation (3.23) shows that C depends on the thermo-physical and geometric properties of the link as well as on the them-physical properties of the gas-droplet flow. The following procedure has been developed to allow the quantification of C and RTI fi-om the plunge-test simulations conducted at the facility.

REFORMULATION OF THE PROBLEM

The following dimensionless temperature can be defined:

$$\theta = \frac{T_G - T_S}{T_G - T_0} \quad (5.2)$$

where T_0 is the initial temperature of the sprinkler link, before being inserted inside the duct. Therefore, the initial condition for θ is:

$$\theta(t = 0) = 1 \quad (5.3)$$

If a dry gas stream is considered ($\beta = 0$), Equation (5.1) reduces to the original RTI model (3.9), which can be written as:

$$\frac{dT_S}{dt} = \frac{\sqrt{U}}{RTI} (T_G - T_S) \quad (5.4)$$

Introducing the dimensionless temperature θ , this becomes:

$$\frac{d\theta^D}{dt} = -\frac{\sqrt{U}}{RTI} \theta^D \quad (5.5)$$

where the superscript 'D' is added to characterize the dry flow conditions under which the sprinkler temperature is measured. Equation (5.5) can be solved with the initial condition (5.3) to give:

$$\theta^D(t) = \text{Exp}\left[-\frac{\sqrt{U}}{RTI} t\right] \quad (5.6)$$

All quantities in this equation, except RTI , can be directly measured during a single dry-gas plunge test. Therefore, the RTI can be inferred from the experimental data through Equation (5.6).

Introducing the dimensionless temperature into the model equation for a wet **gas** (5.1) and solving with the same initial condition (5.3) gives:

$$\theta^W(t) = \frac{C \sqrt{U} \beta}{T_G - T_0} + \left(1 - \frac{C \sqrt{U} \beta}{T_G - T_0}\right) \cdot \text{Exp}\left[-\frac{\sqrt{U}}{RTI} t\right] \quad (5.7)$$

The superscript 'W identifies wet flow conditions under which the sprinkler temperature is measured. Combining the expressions (5.7) and (5.6), assuming the same gas flow velocity for the two cases (natural convection buoyancy force is negligible in the facility), the following is obtained:

$$\frac{\theta^D - \theta^W}{\theta^D - 1} = \frac{C \sqrt{U} \beta}{T_G^W - T_0} \quad (5.8)$$

Taking a closer look at Equation (5.8), it can be noted that the numerator on the left hand side is the difference between the link dimensionless temperature during a dry and a wet gas plunge test. It indicates the cooling effect due to the presence of the water droplets evaporating on the link surface. The denominator, instead, represents the heating of the link during the dry test.

If the dry test is performed in such a way that $T_G - T_0$ does not change with respect to the wet plunge test, the right hand side of expression (5.8) is a constant for a given sprinkler diameter and given flow conditions. This means that the ratio of the evaporative cooling effect to the heating of the dry link must also be a constant during the experiment. The experimental results will allow to determine whether this assumption is correct. Solving for C from Equation (5.8) gives:

$$C = \frac{\theta^D - \theta^W}{\theta^D - 1} \frac{T_G^W - T_0}{\sqrt{U \beta}} \quad (5.9)$$

All the terms on the right hand side of Equation (5.9) can be determined experimentally. The parameters U , β and $T_G - T_0$ can be controlled in each experiment. According to the assumptions of the proposed model, tests conducted on a given sprinkler link should result in similar values of C over a wide range of variation of the boundary conditions. The initial part of the experimental campaign is meant to verify the validity of such statement, as described in Chapter 6.

DETERMINATION OF EXPERIMENTAL QUANTITIES

From Equation (5.9), one finds that the following quantities must be measured in order to determine the parameter C :

- the link temperature evolution in both dry and wet conditions,
- the gas velocity,
- the gas temperature,
- the water volumetric fraction.

In the following, the procedure to measure each quantity will be described in detail.

TEMPERATURE MEASUREMENTS

A total of 33 type-K thermocouples (TCs) are placed in the ECSAT facility. As previously mentioned, the simulated link cylinder carries one or two TCs, which measure the temperature response after the link **has** been inserted into the **gas** flow. Five more TCs are placed 50 mm above the honeycomb (one at the center of the duct, the other **4** close to the walls), to ensure that the temperature of the hot air emerging from the steel wool is indeed uniform. The remaining TCs are placed along the axis of the duct, downstream of the test section. Several of these TCs are supported by a metal rake and are spaced about 0.14 m apart from each other, **as** shown in Figure 38. The other are placed along the duct 0.15 m from each other. The TCs are placed inside an aluminum tube, held in place by a L-shaped support attached to the external wall of the duct. Extreme care **has** been taken in placing the supports on the duct, filling any possible air leakage with silicon paste and covering completely the thermocouple support with the same insulating material used for the duct. The temperature measurements obtained from these TCs allow for the measurement of the cooling of the gas flow along the duct. **Also**, the presence of the orifice has been considered when determining the spatial distribution of the temperature sensors along the duct. Further, the temperature profile along the duct is used to infer at what distance from the test section all the water droplets evaporate completely.

The current data acquisition board is supplied by Computer Boards, Inc. In conjunction with a 32-channel expansion board, it allows to scan all the readings at a maximum sample rate of 100 Hz. All TCs mount quick-disconnect junctions, which allow a rapid switch of the probes being sampled. Typically, the **5** TCs near the honeycomb are scanned prevalently during the set-up phase of the experiments, when the gas flow conditions are being adjusted to meet the test requirements. Subsequently, when a uniform gas temperature has been obtained, this information becomes redundant; therefore, **some** of these five probes are disconnected and replaced with others to measure, for example, the room temperature during the test of commercially available sprinklers.

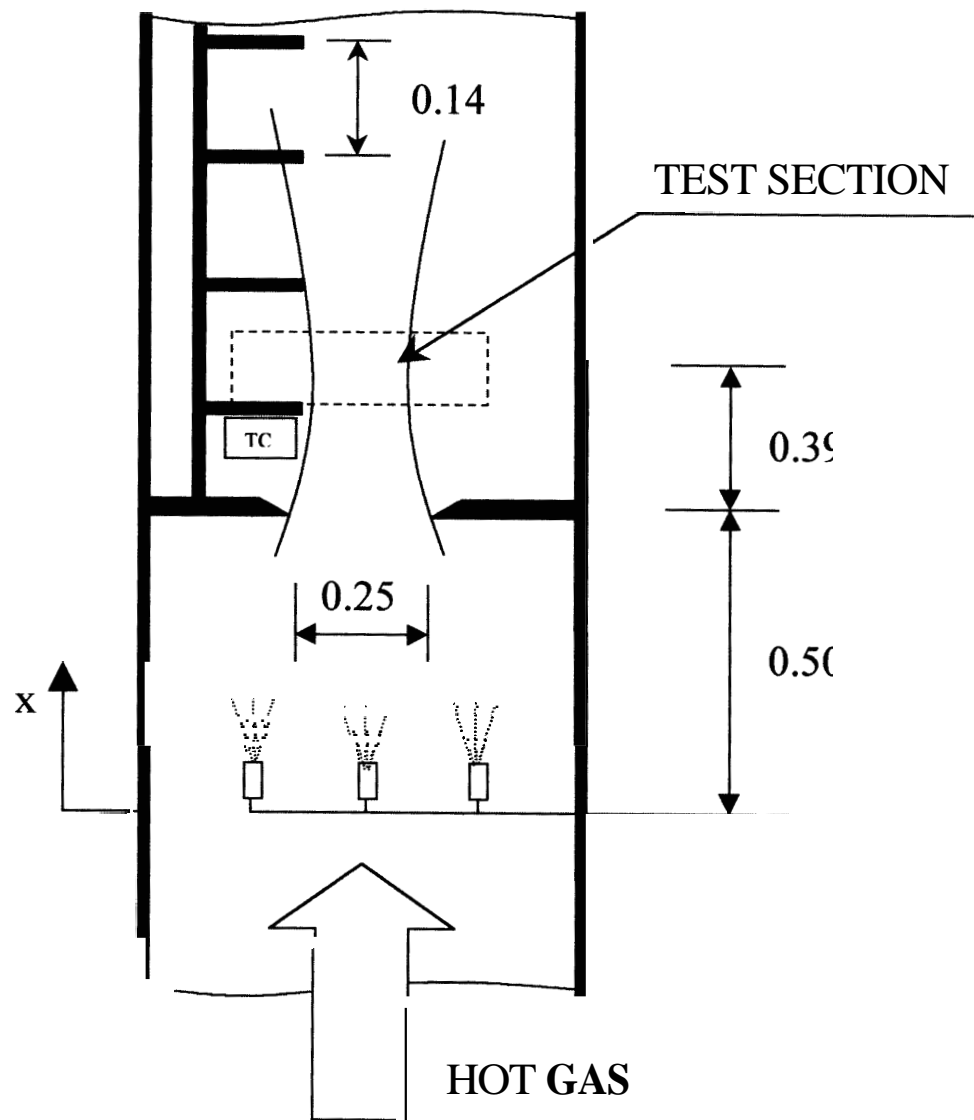


**Figure 38. Location of the thermocouples in proximity of the test section
(dimensions in meters)**

OPTICAL MEASUREMENTS

The velocity of the gas stream and the volumetric fraction of water droplets are measured with an optical technique. A 600 mW Argon-Ion laser (Spectra-Physics model 175-F01) is used to generate a laser beam, which is then spread by a cylindrical lens to form a thin vertical sheet (about 3 mm thick and 40 mm high). The laser sheet enters the duct through a window opening in the duct wall and traverses the test section along the centerline, as shown in Figure 39.

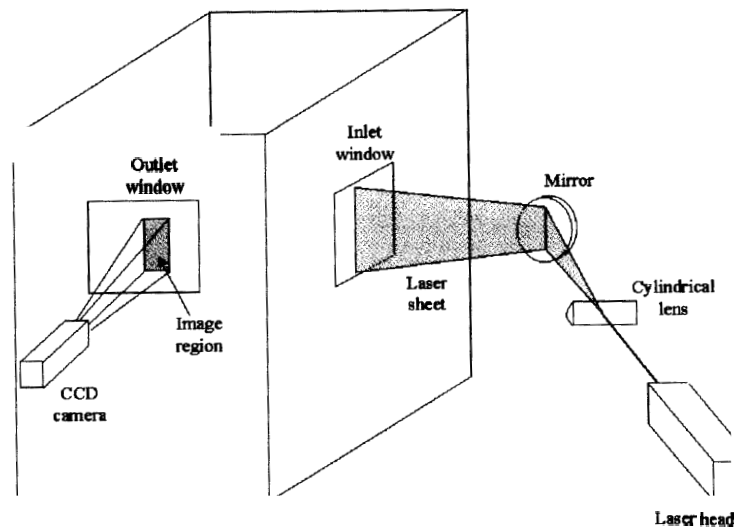


Figure 39. Optical set-up for velocity and water volumetric fraction measurements

The laser sheet is used to illuminate the water droplets in the gas flow. Then, a Couple-Charged Device (CCD) camera focused on the lighted region captures the light scattered by the illuminated droplets. A Cohu camera (series 4910), equipped with a 200-mm manual focus Canon lens, is used for this purpose. The camera collects the light scattered by the droplets that travel through this region while the shutter is open. Because of the characteristics of the flow in the vena contracta, the droplets flow vertically, which means that the droplets entering the laser-sheet volume from the bottom face are likely to leave it through the top face. Therefore, the droplets are continuously illuminated while in the laser sheet, and their path is captured on the CCD snapshot as a trace. The software that controls the operation of the CCD (Image-Pro Plus) saves the snapshots taken by the camera as bitmap images, as shown in Figure 40.

The length and the number of the traces left by the droplets that cross the laser sheet in the exposure time of the camera can be measured by analyzing the images of the test section. The software allows for the measurement of the length of the droplet traces by clicking with the mouse on the endpoints. In order to perform the measurement, the length-measuring tool has to be previously calibrated to give the actual length of each droplet trace. The calibration process has been possible by placing a sheet of graph paper (grid spacing of 1 mm) in the plane of the laser light, perpendicularly to the camera view. The image of the graphic paper has then been used as a reference for the calibration of the software tool. The number of droplets crossing the cross sectional area of the laser beam is counted manually for every image. A set of 20 pictures is

analyzed to get a statistically meaningful value of the average droplet trace length and a set of 30 pictures is used to evaluate the number of droplets. The velocity of the droplet can be calculated by dividing the length of the trace by the exposure time of the image (i.e., the inverse of the camera “shutter speed”). The characteristics and placement of the camera allow to focus on a region which measures 13 mm in the direction of the flow and 10 mm across. The CCD has a resolution of **640** by **480** pixels (the camera is placed on its side, so that the 640 pixels are aligned with the direction of the flow). Therefore, each pixel corresponds to 20 μm . The shutter speed can be varied from 125 to 10000 s^{-1} , making it possible to optimize the trace lengths for different velocities to minimize the measurement error.

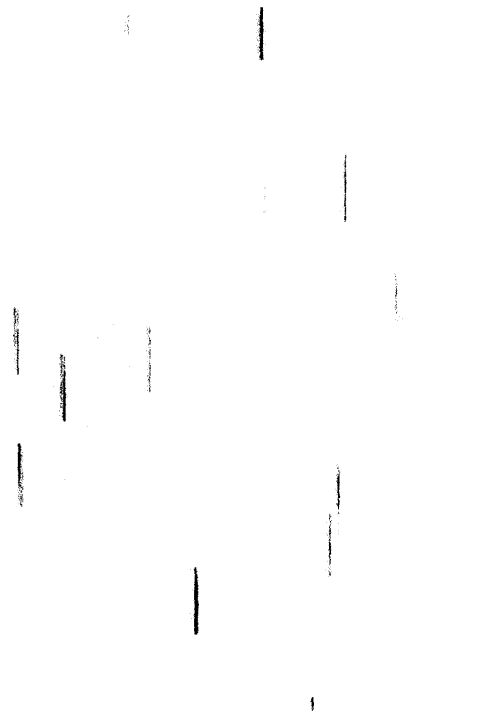


Figure 40. Snapshot of the water droplets in the gas stream (negative)

GAS VELOCITY MEASUREMENTS

Particle Tracking Velocimetry (PTV) provides the gas velocity measurements in the cross-section (Adrian, 1991; Crowe *et al.*, 1998). Thirty measurements are made to obtain a statistically meaningful value of the length of the traces left in a picture by water droplets while travelling across the laser light. The velocity is then calculated dividing the average trace length by the exposure time of the CCD camera, or equivalently:

$$U = L \cdot \epsilon \quad (5.10)$$

Note that the droplets introduced in the gas flow have a maximum volumetric mean diameter of less than 100 μm . This results in a relative terminal velocity of less than 0.24 m/s (which, at 150°C, corresponds to a relative Reynolds number of less than 0.8, see page 68). Since the estimated gas velocity is in excess of 3.5 m/s, the measured droplet velocity lags the actual gas velocity by less than 7 percent. Because almost 300 particle samples are analyzed, it is possible to calculate the standard deviation of the trace length L , which typically is 4 percent of the average value. Therefore, the error on the **gas** velocity measurement is about 10 percent. The turbulence level in the test section and the disturbances induced by the gas jet created by the orifice may influence the measurement of the gas velocity. In fact, their effect would be to disturb the alignment of the gas velocity with the axis of the duct. However, the reasons mentioned at the beginning of Chapter 4 guarantee the validity of the PTV technique

for our applications. Also, the results provided by the PTV technique has been validated by comparing the readings with a CTA (Constant Temperature Anemometry) technique accordingly to what described in Chapter 7, "Gas velocity determination". The average discrepancy between the two methodologies is smaller than 5 percent.

GAS TEMPERATURE MEASUREMENTS

Thirty-three thermocouples (type K, $\pm 2^\circ\text{C}$) are placed inside the duct, both before and after the test section, to measure the gas temperature distribution in the facility and monitor the conditions during the experiment. Figure 41 shows the typical temperature distribution, for both dry and wet conditions. A comparison between the two values of the gas temperature measured at the test section, T^L and T_G , clearly shows the effect of the evaporative cooling in wet conditions. From the same figure, it can be observed that:

- Due to the heat losses to the external environment, the gas temperature drops as the flow proceeds downstream the orifice.
- The gas temperature upstream the spray nozzle location is equal in both dry and wet conditions.
- About 2 m downstream the test section, the slope of the temperature distribution for the wet case becomes equal to the temperature distribution for the *dry* case.

This indicates that the water is completely evaporated and the temperature is affected only by the heat losses to the environment.

Therefore, the thermocouple sensors measure the gas temperature at the location before the sprays and at the location after the complete evaporation of the water. To determine the gas temperature between the sprays and the location of complete evaporation of the water, some information concerning the rate of vaporization of the droplets is needed. Consider the energy balance written for the airflow **as**:

$$\rho_G \dot{V}_G c_G (T^D - T_G) = \rho_L \dot{V}_G (\beta_0 - \beta) \Lambda \quad (5.11)$$

The temperature difference between the two temperature profiles far away from the orifice can be related to the heat required to vaporize the water droplets. Consider the asymptotic temperature difference, ΔT , between the two traces in Figure 41, that is associated with the heat transferred from the air to the water droplets. This temperature difference can be expressed in the following form:

$$\Delta T = \frac{H_L \cdot \beta_0 \cdot \Lambda}{\rho_G \cdot c_G} \quad (5.12)$$

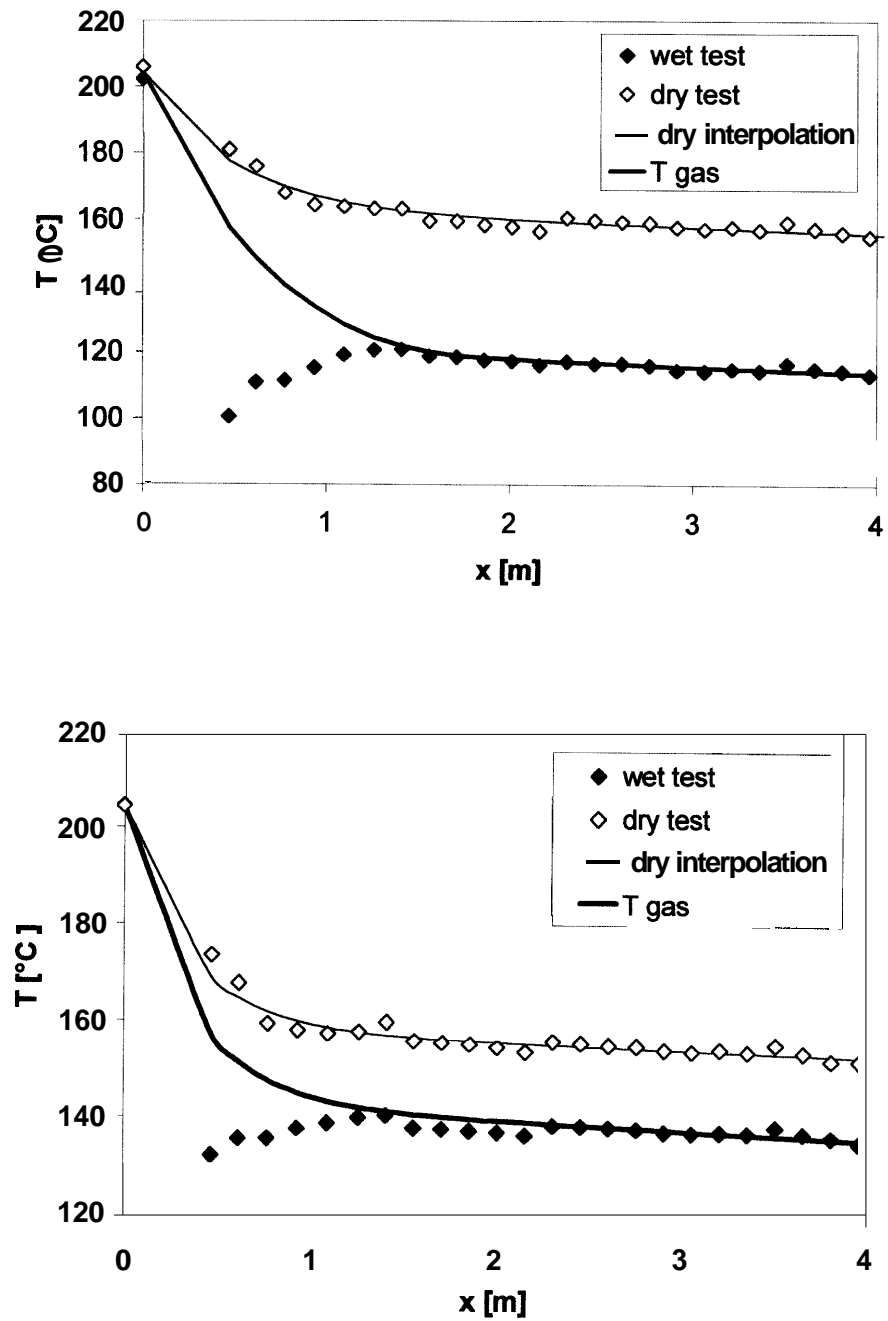


Figure 41. Temperature distributions along the duct and gas temperature estimate (3 PJ8 nozzles, top and 1 PJ10 nozzle, bottom. $U=3.8$ m/s in both cases)

With Equation (5.12), Equation (5.11) can be simplified as:

$$T^D - T_G = \Delta T \cdot [1 - f(x)] \quad (5.13)$$

The function $f(x)$ links the initial volumetric fraction to its evolution along the duct,

$$f(x) = \frac{\beta}{\beta_0}.$$

The energy balance equation written for a sensor wetted by the droplets yields a relation of proportionality between the convective heat input to the sensor and the latent heat associated with the vaporization of the droplets that deposit over its surface:

$$\rho_S c_S V_S \frac{dT_S}{dt} = h \cdot S \cdot (T_G - T_S) - \rho_L U \cdot A_S \cdot \beta \cdot \kappa \cdot \Lambda \quad (5.14)$$

At steady state, Equation (5.14) simplifies as:

$$h \cdot S \cdot (T_G - T^W) = \rho_L U \cdot A_S \cdot \beta \cdot \kappa \cdot \Lambda \quad (5.15)$$

Considering the volumetric fraction evolution during the evaporation process,

Equation (5.15) can be rearranged as:

$$T_G - T^W = \chi \beta_0 f(x) \quad (5.16)$$

By adding Equation (5.13) and Equation (5.16), one may find that the functional $f(x)$ can be expressed in the following form:

$$f(x) = \frac{T^D - T^W - \Delta T}{\chi \beta_0 - \Delta T} \quad (5.17)$$

Note that $f(x)$ is equal to 1 at the spray nozzles location and it is equal to zero for x greater or equal to x_E , where all the water drops are evaporated. The best representation of the data is obtained with a form of the functional given as:

$$f(x) = \begin{cases} \left(1 - \frac{x}{x_E}\right)^\lambda & x < x_E \\ 0 & x \geq x_E \end{cases} \quad (5.18)$$

More details on the reasons that lead to this choice of the function $f(x)$ are provided in the following section. The procedure to obtain the distance of evaporation along the duct x_E and the exponent λ is straightforward. From the plot of the temperature distribution along the duct for the wet conditions, one may notice that all the water is evaporated when the slope of the profile becomes similar to the profile measured in dry conditions. This also is equivalent to say that x_E is the location after which the difference of temperature ΔT between the dry and wet traces is almost constant. Figure 42 shows how the distance of complete evaporation, x_E , is actually determined.

For instance, in Figure 41, it is quite evident that the water droplets are evaporated completely after 1.7 meters **from** the spray nozzle location for the 3-PJ8 case and after 1.4 meters for the 1-PJ10 case, respectively. The larger distance of evaporation in the case of 3-PJ8 is consistent with the fact that more water is injected into the **gas** flow and more space is needed to evaporate completely the water droplets.

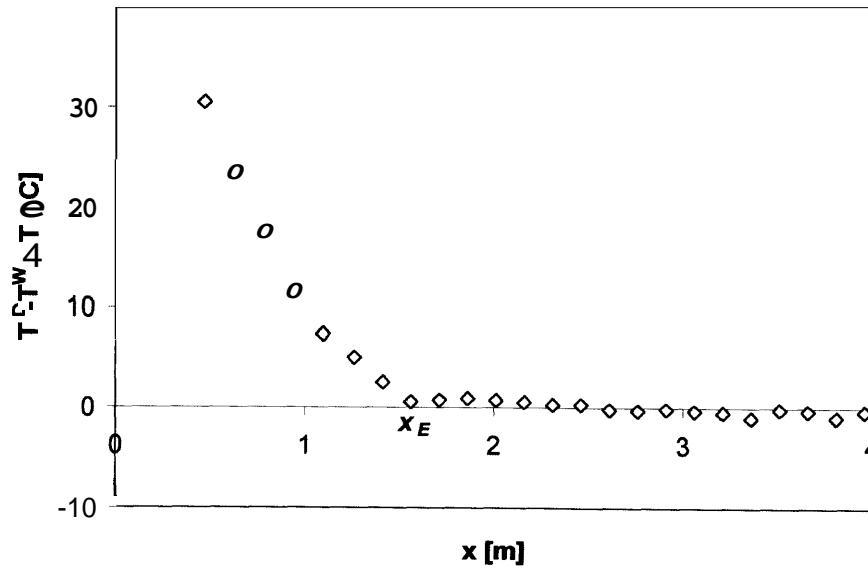


Figure 42. Determination of x_E

The value of λ is found through an interpolation of the experimental data $T^D - T^W - \Delta T$ versus the duct coordinate x , according to Equations (5.17) and (5.18). Figure 43 reports a fit of the experimental data. It is clear that only the points up to the distance

of complete evaporation are considered, while the others are not taken into consideration. This is because the function $f(x)$ is set to zero for x values greater or equal to x_E . Further, this technique provides a double check for the determination of the parameter C and the water volumetric fraction, as it will be clarified in the following sections.

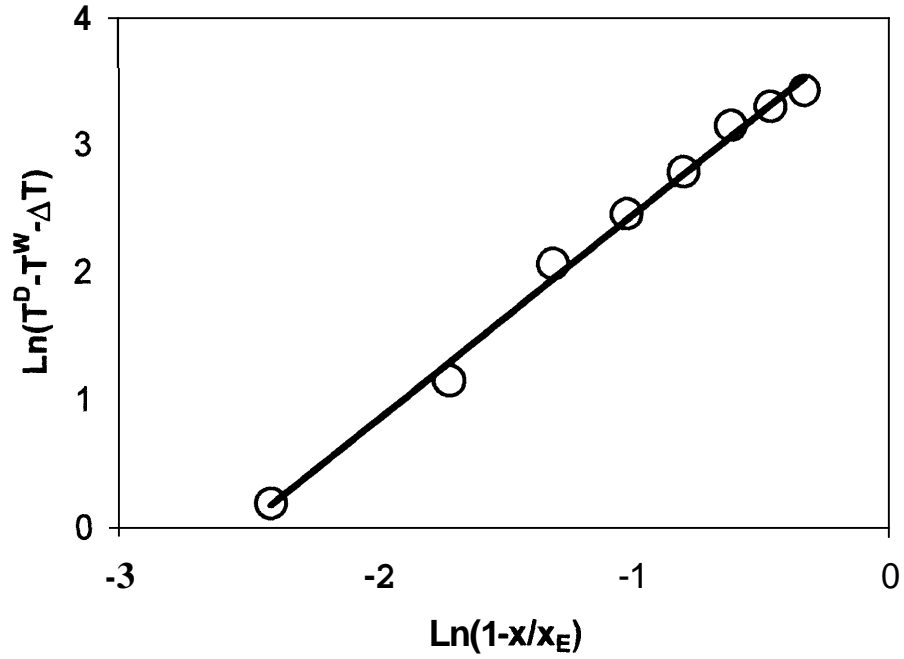


Figure 43. Fit of the experimental points ($\lambda=1.6$)

From these results, it follows that the interpolation describing the gas temperature is obtained by substituting Equation (5.18) into Eq. (5.13) to yield:

$$T_G = \begin{cases} T^D - \Delta T \cdot \left[1 - \left(1 - \frac{x}{x_E} \right)^\lambda \right] & x \leq x_E \\ T^D - \Delta T & x > x_E \end{cases} \quad (5.19)$$

It follows that the intersection of the curve represented by (5.19) with the location of the test section provides the wet **gas** temperature at the test section.

The value of the slope of the wet gas temperature distribution at point $x = x_E$ is obtained by deriving Equation (5.19) with respect to x , thus finding the following expression:

$$\frac{\partial T_G}{\partial x} = \begin{cases} \frac{\partial T^D}{\partial x} - \lambda \frac{\Delta T}{x_E^\lambda} (x_E - x)^{\lambda-1} & x \leq x_E \\ \frac{\partial T^D}{\partial x} & x > x_E \end{cases} \quad (5.20)$$

Since λ is experimentally found to be a number always greater than the unity (very close to 1.6), the slope of the gas temperature at point x_E is equal to the slope of the dry temperature distribution. Further it approaches this value gradually, without discontinuities or abrupt changes that would be unexpected in this process. Therefore, we conclude that the **fitting** curve chosen to represent the **gas** temperature is reasonable and validates the procedure by which we have also determined x_E .

The gas temperature in dry conditions is represented with an exponential fit of the following form:

$$T^D(x) = (T_{x=0} - \delta) e^{-\alpha x} + \phi x + \delta \quad (5.21)$$

The constant ϕ represents the slope of the trace for $x > x_E$ due to the heat losses to the ambient.

DETERMINATION OF THE FUNCTION F(X)

The evaporation of a liquid droplet is a subject of great interest to multiple applications, such as evaporative cooling, combustion, industrial burners and propulsion. In these applications the objective is to determine the diameter of the water droplet as a function of time and the amount of time it takes to completely evaporate.

Consider an airflow where water droplets of diameter D_0 are injected continuously. An expression of the diameter of the droplet as a function of time can be obtained from the theory (see Appendix 1) as:

$$D^2 = D_0^2 - \zeta \cdot t \quad (5.22)$$

where ζ is constant depending on the liquid and air thermal properties. If Equation (5.22) is non-dimensionalized dividing both sides by D_0^2 , we can obtain the following relationship:

$$\left(\frac{D}{D_0}\right)^2 = 1 - \zeta \frac{t}{D_0^2} \quad (5.23)$$

In our analysis we are interested in finding the droplet diameter evolution as a function of the coordinate x along the duct. If the gas is flowing inside a duct at a constant velocity U , we can couple time and space as:

$$x - x_0 = U \cdot (t - t_0) \quad (5.24)$$

By considering that at time $t_0=0$ the position of the gas particle is $x_0 = 0$ and substituting the resulting expression into Equation (5.23), we obtain:

$$\left(\frac{D}{D_0}\right)^2 = 1 - \zeta \frac{x}{U \cdot D_0^2} \quad (5.25)$$

Equation (5.25) may be simplified by considering that, at the location where the water droplet is completely evaporated (x_E), the diameter is equal to zero. Therefore:

$$0 = 1 - \zeta \frac{x_E}{U \cdot D_0^2} \quad \text{or} \quad x_E = \frac{U \cdot D_0^2}{\zeta} \quad (5.26)$$

Substituting Equation (5.26) into Equation (5.25), one may find the following final expression for the diameter of a liquid droplet **as** a function of the duct location:

$$\frac{D}{D_0} = \left(1 - \frac{x}{x_E} \right)^{1/2} \quad (5.27)$$

As explained in the following section, the water volumetric fraction is linearly proportional to the droplet volume (or, equivalently, to the cube of the droplet diameter) and to the number of droplets that cross a given section of the duct. Since we are now considering a monodisperse flow of droplets of equal initial diameter, the evaporation rate is the same for any droplet and the number of droplets crossing a given section is the same at any location of the duct where water is still not completely evaporated. Therefore, the water volumetric fraction can be expressed as:

$$f(x) = \frac{\beta}{\beta_0} = \left(\frac{D}{D_0} \right)^3 = \left(1 - \frac{x}{x_E} \right)^{3/2} \quad (5.28)$$

In our case, the water spray is polydisperse. However the analysis developed to **determine the evolution of the droplet mean volume (later in this chapter) shows that,** for the spray nozzles employed in this project, the number of droplets carried by the

gas flow decreases accordingly to $\left(1 - \frac{x}{x_E}\right)^\lambda$. Therefore, considering an average mean volume of the droplets V_M^* as calculated in the following sessions, the functional $f(x)$ can be expressed in the following form:

$$f(x) = \frac{\beta}{\beta_0} = \left(1 - \frac{x}{x_E}\right)^\lambda \quad (5.29)$$

Figure 44 plots the function $f(x)$ versus the coordinate x along the duct, where the solid line is the theoretical prediction based on Equation (5.29).

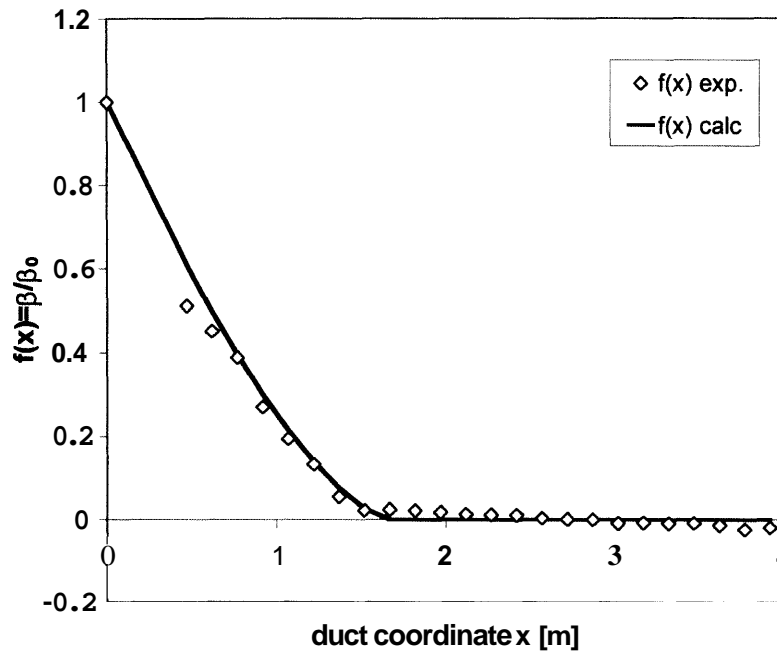


Figure 44. $f(x)$ versus the coordinate x along the duct ($\lambda=1.5$)

WATER VOLUMETRIC FRACTION MEASUREMENTS

The water volumetric fraction is defined as the ratio of the volumetric flow rate of water droplets over the total volumetric flow rate. Since in our situation the water content in the flow is very low (order of 1 ppm), we can express the volumetric fraction as:

$$\beta = \frac{\dot{V}_L}{\dot{V}_G} \quad (5.30)$$

The droplet size distribution, provided by the manufacturer of the spray nozzles used in the experiments (Bete Nozzle Fog, Inc.), is shown in Figure 45. The nozzles are identified as PJ8 and PJ10 respectively. The droplets are grouped by size into N bins, each bin containing n_i droplets of diameter D_i . As said in the previous chapter, in the images taken by the camera, each pixel corresponds to $20 \mu\text{m}$. This is likely to limit our capability to resolve droplets with a diameter of less than $20 \mu\text{m}$. Therefore, we will neglect the presence of water droplets with a diameter of less than $20 \mu\text{m}$.

However, Figure 45 shows that, for both nozzle sizes, the contribution of these droplets to the water volume is negligible. Further, Figure 26 shows that the collection efficiency for these droplets is small, that is, they tend to follow the air stream and do not impact the link. Hence, they do not contribute to the evaporative cooling of the link and can be neglected without significantly affecting the results.

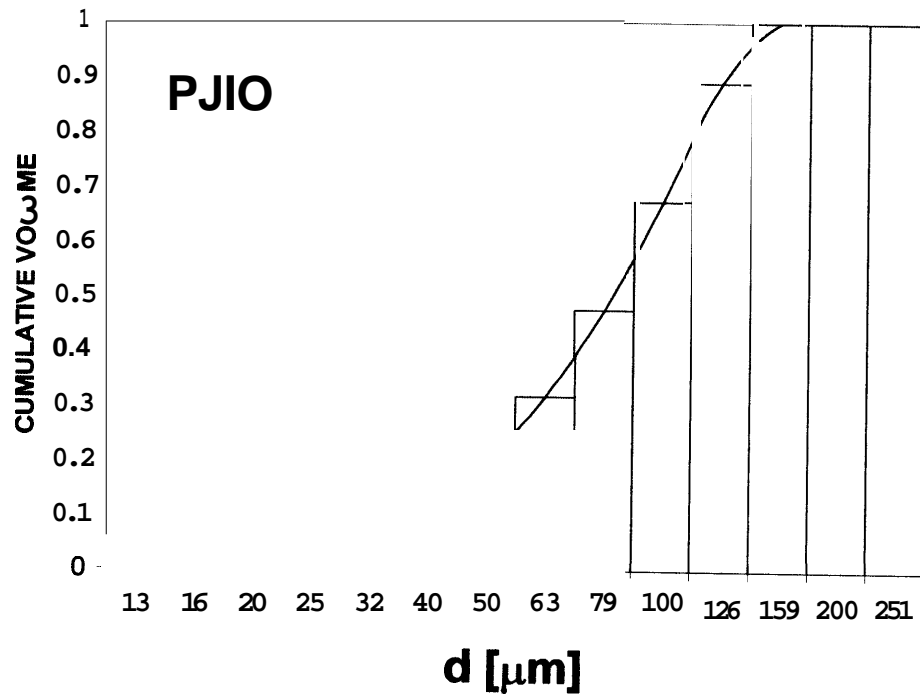
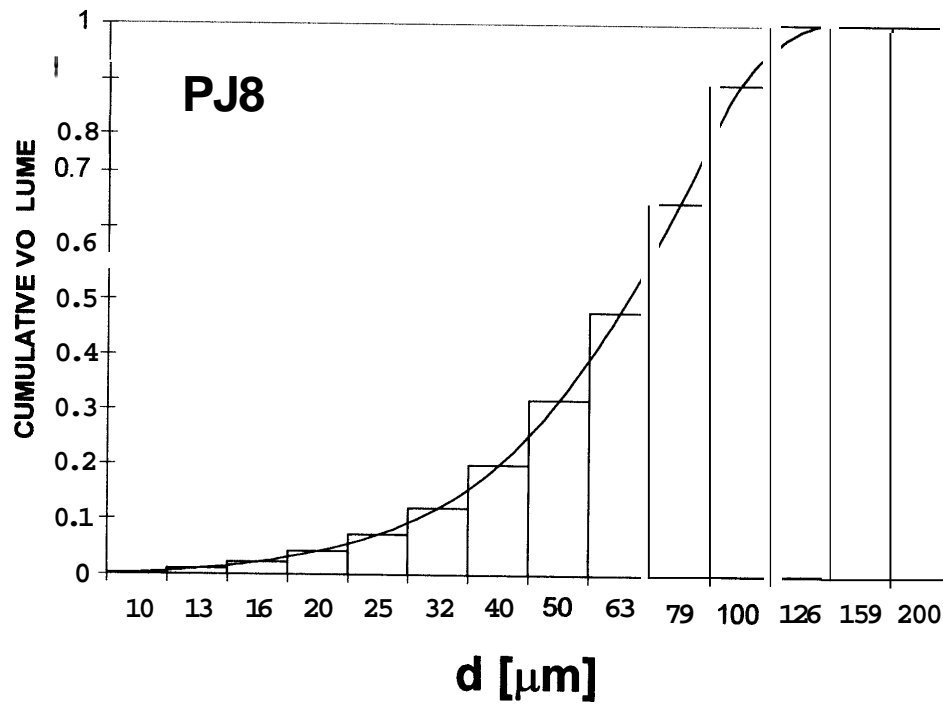


Figure 45. Droplet size distribution (courtesy of Bete Fog Nozzle, Inc.)

It is reasonable to assume that the evaporation rate is proportional to the droplet diameter (see Appendix 1). Further, since the water volumetric fraction is in the order of parts per million, it is also reasonable to assume that no coalescence between droplets occurs. Typically in our applications, the ratio of the distance between two droplets and the diameter of a droplet is in the order of 1000, which is largely in excess of the critical value suggested by Crowe *et al.* (1998) to treat the drops as isolated particles. Under these circumstances, over a given time interval, each droplet would lose by evaporation a shell of equal thickness. Consequently, the residual water volume and droplets number can be calculated at **any** time during the evaporation process, **as** presented in the following section.

Evaporation process calculation

Consider the droplet size distribution as reported in Figure 45. The droplet mean volume is defined as:

$$V_M = \frac{\pi}{6} \frac{\sum_{i=1}^N n_i D_i^3}{\sum_{i=1}^N n_i} \quad (5.31)$$

As noted in the previous section, the calculation has to be made over several instants during the evaporation process, **starting** from time t_0 , when the water is injected into the air-flow, to instant t_{evap} , when the total amount of liquid has evaporated. Therefore, a notation with two subscripts is introduced in this computation, where the ~~first~~ subscript refers to the size bin and the second refers to the instant of calculation. For example $n_{5,3}$ refers to the 5th size bin and to the time step t_3 .

With this notation, we can also define the dimensionless residual water volume as:

$$V_j^* = \frac{\sum_{i=j}^N n_{i,j} D_{i,j}^3}{\sum_{i=0}^N n_{i,0} D_{i,0}^3} \quad (5.32)$$

which is a measure of the liquid water still present into the flow.

The fundamental assumption in this calculation is that the derivative of the droplet diameter with respect to time is inversely proportional to the diameter of the droplet, according to the D^2 law (Appendix 1):

$$\frac{dD}{dt} = -\frac{K}{D} \quad (5.33)$$

The second assumption is that the contribution of the droplets with a diameter smaller than $20\text{ }\mu\text{m}$ to the total water volumetric flow rate is negligible for the reasons explained in the previous section. Therefore, at time t_0 , the droplet mean volume $V_{M,0}$ can be calculated as follows:

$$V_{M,0} = \frac{\pi \sum_{i=1}^N n_{i,0} D_{i,0}^3}{6 \sum_{i=1}^N n_{i,0}} \quad \text{for all } i\text{'s such that } D_{i,0} \geq 20\text{ }\mu\text{m} \quad (5.34)$$

The initial droplet mean volume, calculated upon the data provided by Bete Fog Nozzles Inc., is equal to $1.4 \cdot 10^5\text{ }\mu\text{m}^3$ and to $2.9 \cdot 10^5\text{ }\mu\text{m}^3$, for the **PJ8** and **PJ10** nozzle type respectively. A series of tests is made in "cold" conditions. Since no evaporation takes place (except that by mass transfer, which is very low at these temperatures), the same quantity of water is present in any section of the duct. In this way, since the flowmeter provides the volumetric flow rate of the water injected into the airflow, it is possible to measure the droplet mean volume by a manual counting process applied at the test section. One nozzle (**PJ8** or **PJ10**) at the time is activated and forty images of the test section are taken. The water volumetric flow rate divided by the number of droplets manually counted at the test section and multiplied by the time of exposure of the camera gives an estimate of the droplet mean volume $V_{M,0}$. The results (reported in Table 4) compare favorably with those provided by the manufacturer, leading to an

overestimation of the volume for the PJ8 nozzle (+11%) and an underestimation for the PJ10 nozzle (-17%).

	PJ8	PJ10
Number of drops counted at the test section ($\mathbf{E} = 1/1000 \text{ s}^{-1}$)	4.1	4.2
Water volumetric flow rate (m^3/s)	$0.945 \cdot 10^{-6}$	$1.42 \cdot 10^{-6}$
Droplet mean volume $V_{M,0}$ (μm^3)	$1.7 \cdot 10^{-13}$	$2.4 \cdot 10^{-13}$

Table 4. Determination of the initial droplet mean volume, cold condition

At the subsequent time t_I , we eliminate the size bin b_I , defined as the size bin with the lowest diameter, larger or equal to $20 \mu\text{m}$ and we consider that it is completely evaporated. By integrating Equation (5.33) with the initial condition $D=D_0$ at $t=t_0$, the following formula is obtained:

$$D^2(t) - D_0^2 = -\zeta \cdot (t - t_0) \quad (5.35)$$

As one may notice, in the time interval $(t-t_0)$, the droplet diameter decreases by the same quantity for any given water droplet undergoing the evaporation process since ζ

is a constant. Let us assume that the time t_l is defined as the moment in which the size bins have shifted to the left of Figure 45 by one place. Equivalently, one may define t_l as the instant when the size bin of diameter $20\text{ }\mu\text{m}$ is completely evaporated and the next one has reduced its diameter to $20\text{ }\mu\text{m}$ (the lowest diameter class we can resolve). Therefore, at time t_l , we are able to calculate the diameter $D_{i,l}$ for each size bin, according to the formula:

$$D_{i,l} = \sqrt{D_{i,0}^2 - (D_{2,0}^2 - D_{1,0}^2)} \quad (5.36)$$

Do note that the quantity $(D_{2,0}^2 - D_{1,0}^2)$ is a constant for any size bin, since $D_{2,l} = D_{1,0}$ (bin shift) and from Equation (5.35).

Since the droplets do not interact with each other as assumed in the previous section, the droplet number $n_{i,j}$ does not change while the bin is being "shifted" to the left of Figure 45. Therefore, $n_{i-l,l} = n_{i,0}$ and we can calculate the droplet mean volume at the time step t_l as:

$$V_{M,l} = \frac{\pi}{6} \frac{\sum_{i=1}^{N-1} n_{i,l} D_{i,l}^3}{\sum_{i=1}^{N-1} n_{i,l}} \quad (5.37)$$

In general, for any time t_j the following formulas can be written:

$$D_{i,j} = \sqrt{D_{i,j-1}^2 - (D_{2,j-1}^2 - D_{1,j-1}^2)} \quad (5.38)$$

$$n_{i-1,j} = n_{i,j-1} \quad (5.39)$$

$$V_{M,j} = \frac{\pi}{6} \frac{\sum_{i=1}^{N-j} n_{i,j} D_{i,j}^3}{\sum_{i=1}^{N-j} n_{i,j}} \quad (5.40)$$

If the droplet mean volume and the dimensionless residual water volume are calculated at each time step until complete evaporation, we obtain the result shown in Figure 46. The diamonds in the chart represent the ratio between the droplet mean volume at each time t_j divided by the initial droplet mean volume plotted against the dimensionless residual water volume at the same time t_j .

As the evaporation progresses, Figure 46 basically shows that the droplet mean volume remains nearly constant because the total water volume and the number of droplets not yet completely evaporated decrease. Initially, the number of droplets decreases more rapidly than the total water volume. In this way, the droplet mean volume tends to increase. For dimensionless residual water volumes smaller than 0.4, only the largest drops have yet to evaporate. Therefore, the number of droplets

remains quite unchanged, while the total water volume decreases significantly. As expected, the droplet mean volume **begins** to decrease and eventually collapses when all the remaining water is about to evaporate completely. An average droplet mean volume V_M^* can be calculated for dimensionless residual water volumes greater than 0.1. This average, referenced to the initial droplet mean volume $V_{M,0}$, is represented by the dotted lines in Figure **46**. The assumption of considering the droplet mean volume constant during the evaporation process introduces an error of 15% for the PJ8 nozzle **and** 20% for the **PJ10** nozzle, respectively. Similar results are reported for instance by Cui et al. (2000) for pure water and water containing carbon dioxide.

However, we can increase the accuracy by estimating analytically (see Appendix 1 or Equation (5.29)) the water content still present in the flow and picking a better value of the droplet mean volume from the plots shown in Figure **46**. In fact, in **our** applications, temperature and velocity are related to each other for the reasons explained in the following chapter (see "EXPERIMENTAL PROCEDURE"). This limits the variability of the water volumetric fraction to a small interval so that the dimensionless residual water volume reported in Figure **46** ranges from **0.4** to 0.8. The errors associated with the determination of the droplet mean volume are therefore considerably reduced to less than 10%.

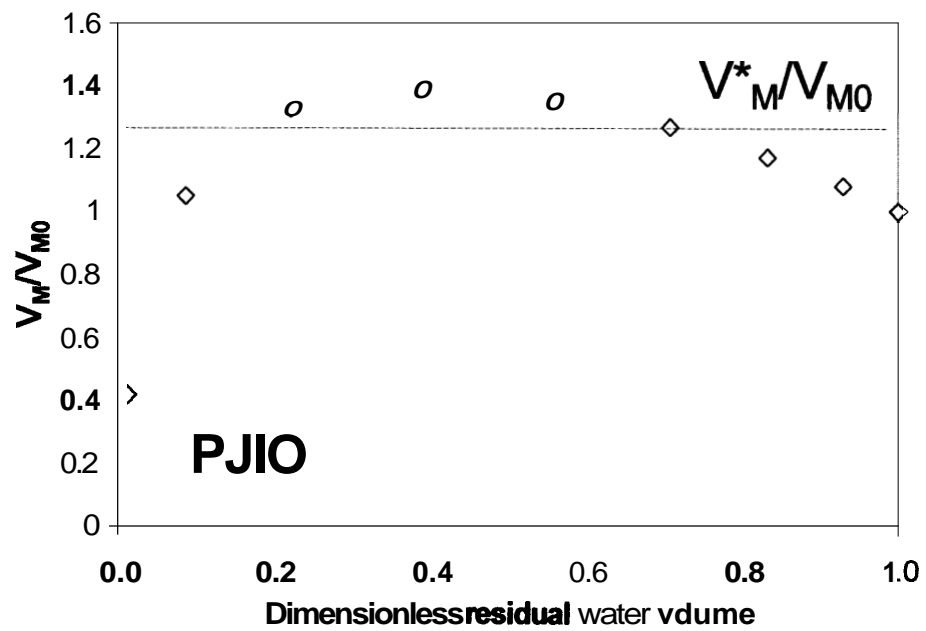
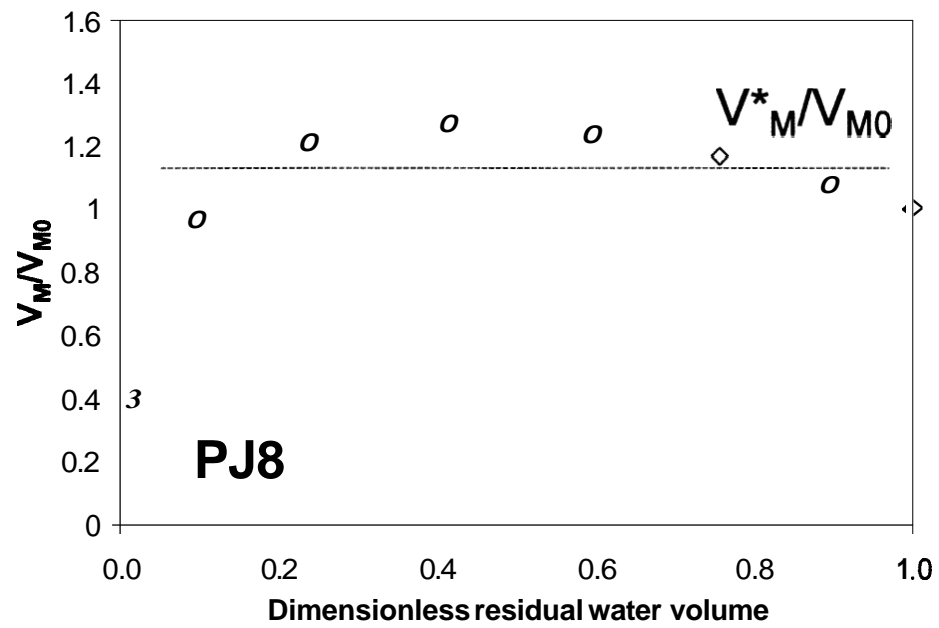


Figure 46. Droplet mean volume during the evaporation process

Final expression of the water volumetric fraction

With the previous information, the water volumetric flow rate is calculated by taking images of the gas-droplets flow and counting the droplets that cross the test section during the time $1/\varepsilon$, where ε is the camera shutter speed. The water volumetric flow rate, measured at the test section, can be expressed as:

$$\dot{V}_L = n V_M^* \varepsilon \quad (5.41)$$

From Equation (5.30) and (5.41), the water volumetric fraction can be calculated as:

$$\beta = \frac{n V_M^* \varepsilon}{U A_I} \quad (5.42)$$

The cross sectional area A_I is given by the product of the laser sheet thickness (2.8 ± 0.5 mm) times the width of the field of view (10 mm). The laser sheet thickness has been determined by placing a sheet of graph paper (grid spacing of 1 mm) perpendicular to the laser beam and measuring the transversal dimension. The measurement was made at the window on the right side of the duct (see Figure 39). Since the width of the laser beam gradually changes with the distance from the source, this may translate into an inaccuracy associated with the determination of the cross sectional area A_I . However, the transversal dimension of the duct is only 30 cm and the distance from the laser source to the window is about 150 cm, resulting in an inaccuracy, which is likely to be negligible when compared to others. All terms on the

right hand side of Equation (5.42) are known or can be readily measured. At steady state, a set of thirty pictures of the flow is taken and the number of traces crossing the area A_l is counted. The error associated with the determination of the water volumetric fraction is the sum of the following errors:

- error on the determination of n at $E = 125$: 20%
- error on V_M^* : 10%
- error on U : 10%
- error on A_l : 17%.

Therefore, Equation (5.42) provides an estimate of the water volumetric fraction with an uncertainty of 57 percent.

Analysis in support of the experimental approach

From Equation (5.42) it is evident that the water volumetric fraction, measured at the test section, depends on the following parameters:

- The gas temperature, which influences the number of droplets n that cross the laser sheet.
- The gas velocity, which affects simultaneously n and the gas volumetric flow rate.
- The nozzle type used to inject water into the hot gas flow, the number of active nozzles and the pressure of injection.

It is quite obvious that, at constant gas velocity, for any given spray nozzle, the effect of increasing gas temperatures is to increase the evaporation rate of the drops and therefore to decrease the number of droplets that reach the test section. Therefore, other parameters being constant, an increase in the gas temperature creates a decrease in the water volumetric fraction calculated at the test section.

Things are a little more complicated when determining the dependency of the water volumetric fraction on the gas velocity. In fact, β is influenced by the gas velocity in two counteracting ways: on one hand, a larger gas velocity means a larger **gas** volumetric flow rate at the denominator of (5.30); on the other hand, other parameters being constant, an increase of the **gas** velocity boosts the number of droplets that reach the test section before evaporating, augmenting therefore the water volumetric flow rate measured at the test section. A series of experiments is performed by changing the gas velocity in the duct and keeping the gas temperature constant to determine which of the two effects **has** the major influence over the volumetric fraction. The same nozzle type (one PJ8) is employed during the all series of tests. Figure 47 reports the experimental findings, indicating that a raise of the gas velocity results in a decrease of the water volumetric fraction read at the test section. The solid line represents instead the water volumetric fraction as a function of the gas velocity calculated analytically by the D^2 law.

At constant gas temperature and velocity, changing a nozzle type, for example, from PJ8 to PJ10, increases the water volumetric flow rate injected into the flow and the droplet mean volume. Thus, the water volumetric fraction can be increased by "scaling up" the nozzle type and/or using more nozzles of the same type at the same time. Also, a larger injection pressure could be used to increase the volumetric fraction of water in air, but it is better to avoid this technique because it modifies the droplet size distribution. In the following, changing the injection pressure will not be an option.

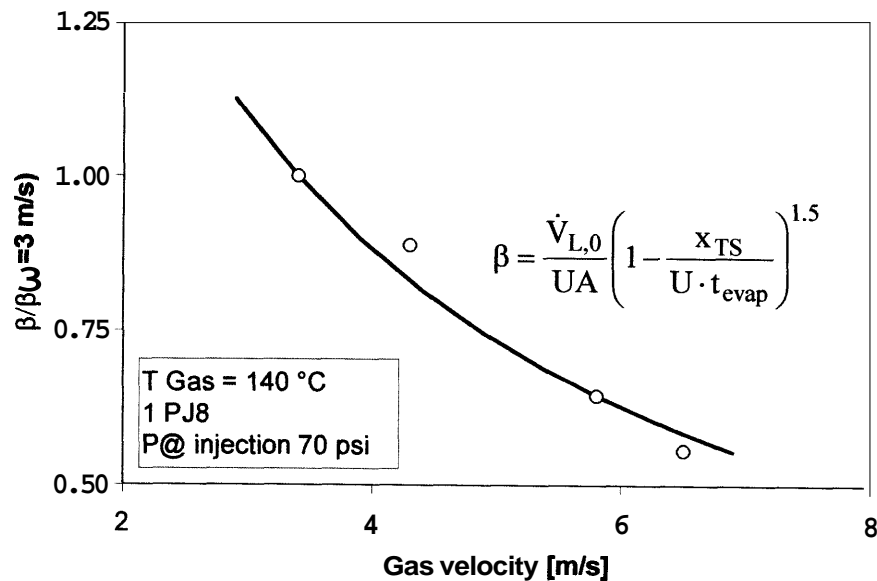


Figure 47. Water volumetric fraction versus the gas velocity

Consequently, the only realistic way to change the water volumetric fraction independently from the gas temperature and the gas velocity is to change either the nozzle type or the number of active sprays (i.e. to change $\dot{V}_{L,0}$).

Theoretical estimate of the volumetric fraction

Consider the gas in dry conditions at velocity U and temperature T^D . If water droplets are added to the gas flow, we know that the gas temperature drops to the value indicated as T_G , while the velocity does not change significantly because natural convection is in our case negligible with respect to the circulation induced by the blower. In this situation, the heat released by the gas stream is equal to the heat necessary for the water droplets to evaporate, as suggested by the following expression:

$$\dot{m}_G \cdot c_{p,G} (T^D - T_G) = (\dot{m}_{L,0} - \dot{m}_L) \cdot \Lambda \quad (5.43)$$

By recalling the definition of water volumetric fraction, one may write the following relation:

$$\beta_0 - \beta = \frac{\rho_G}{\rho_L} \cdot \frac{\dot{m}_{L,0} - \dot{m}_L}{\dot{m}_G} \quad (5.44)$$

where β_0 is the volumetric fraction evaluated at the spray nozzle location. By substituting Equation (5.44) into (5.43), it is possible to express β as follows:

$$\beta = \beta_0 - \frac{\rho_G \cdot c_{p,G} \cdot (T^D - T_G)}{\rho_L \cdot \Lambda} \quad (5.45)$$

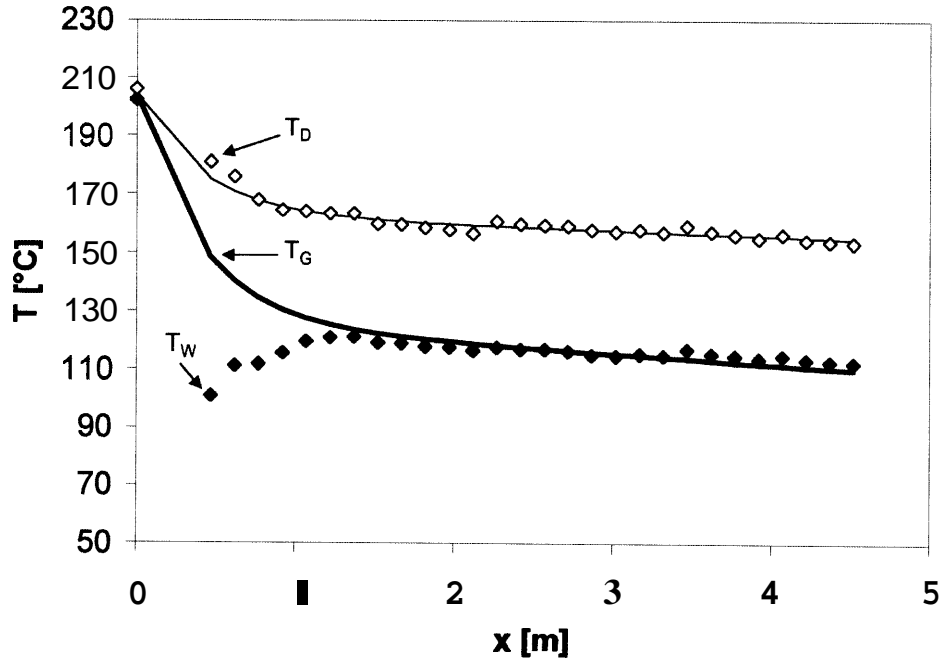


Figure 48. Typical temperature distributions in dry and wet conditions

Figure 48 (representative of a typical experiment) suggests a difference of temperature $T^D - T_G$ equal to 30°C. The thermodynamic properties of air are calculated at temperature T_G , while the density of water is evaluated at 100°C and atmospheric

pressure, since the water is supposed to be at the saturation point. The volumetric fraction at the spray location is given by the ratio between the pump volumetric flow rate (measured by a rotameter) and the gas volumetric flow rate. In this example, β_0 is equal to 6 ppm. This results in ~~an~~ estimated value of β equal to 3 ppm (~~as~~ opposed to the value of 3.7 ppm found experimentally).

Since the measurement of water volumetric fraction is a quite delicate point in the experimental assessment of the EC model, Equation (5.45) is applied to the experimental tests **performed** at the ECSAT facility in order to double-check the values obtained with optical techniques. Data are available in Appendix 2 and do confirm that the optical methodology is viable, at least within the uncertainty highlighted in the previous sections.

CHAPTER 6

MODEL AND DATA COMPARISON

The following sections are dedicated to the validation of the model through experimental testing of simulated sprinkler links exposed to a hot **gas** flow. After an initial part reporting a comparison between the experimental results gathered at the ECSAT facility and the results obtained from numerical simulations performed with the Fire Dynamics Simulator (FDS) of NIST, the procedure to determine the evaporative cooling parameter and its dependency on the simulated sprinkler link size will be presented. Also, the results obtained from a number of tests performed on commercial **fire** sprinklers will be reported making a comparison with the predictions of the model. Finally, the concept of equivalent cylinder will be introduced and discussed.

VALIDATION OF THE DROPLET EVAPORATION MODEL

The ECSAT facility at the University of Maryland is designed to study the evolution of water droplets in a gaseous stream and to characterize the response of sensors that are simultaneously exposed to the hot gases and to the water droplets. The tests performed at the ECSAT facility have been used to validate the FDS droplet evaporation model. The results gathered from the tests are analyzed in terms of water volumetric fraction as a function of the coordinate along the duct. The experimental data are obtained for a broad range of conditions of gas velocity and temperature. The boundary conditions are characterized in order to provide the necessary input to the FDS. The FDS model consists of a large eddy simulation algorithm combined with a Lagrangian water droplet-tracking algorithm. The FDS is used to simulate a variety of fire-induced flows, including those with sprinkler sprays. Validation of sprinkler droplet heat transfer is crucial in predicting the cooling effect of water droplets in real fire scenarios. The FDS calculations are compared with the information gathered from the ECSAT facility to fully assess the performance of the model.

Numerical model and results

Temperature measurements of dry and droplet-laden air within a vertical duct are used to validate the droplet tracking and heat transfer routines in the NIST FDS, a computational fluid dynamics model of fire and fire-related phenomena. The model is used to simulate the flow of hot gases through a vertical duct with a square cross

section of dimensions 0.61 m by 0.61 m. A water injection nozzle at the base of the computational domain is simulated and the duct centerline temperature profile is compared with the corresponding dry temperature profile.

The purpose of the calculations is to validate the relatively simple heat transfer model between the droplets and the hot gas that is employed in the FDS model. A brief description of the droplet trajectory and heat transfer models is included here. The entire FDS code is described in more detail in McGrattan *et al.* (2000). The water injection nozzle is modeled as a point source of monodisperse water droplets of diameter 82 μm . The flow rate from the nozzle is $1.42 \cdot 10^{-3}$ l/s. It is assumed that the droplets exit the nozzle through a cone directed upwards at an angle of 70° from the vertical at a velocity of 1 m/s.

In the FDS model, there is a two-way coupling between the water droplets and the hot gas where both heat and momentum are transferred. The momentum transferred from the droplets to the gas is represented in the momentum equation, obtained by **summing** the force transferred from each droplet in a grid cell and dividing by the cell volume.

$$\vec{f} = \frac{\pi \sum \rho_L C_D D^2 (\vec{v}_d - \vec{U}) \cdot |\vec{v}_d - \vec{U}|}{8 \cdot V_{\text{Cell}}} \quad (6.1)$$

The trajectory of an individual droplet is governed by the following equation:

$$\frac{d}{dt}(m_d \cdot \vec{v}_d) = m_d \cdot \vec{g} - \frac{1}{8} \rho_L C_D \pi D^2 (\vec{v}_d - \vec{U}) \cdot |\vec{v}_d - \vec{U}| \quad (6.2)$$

The **drag** coefficient is a function of the local Reynolds number $\frac{|\vec{v}_d - \vec{U}| \cdot D}{\nu_G}$ as:

$$C_D = \begin{cases} 24 / \text{Re} & \text{Re} < 1 \\ 24 \cdot (1 + 0.15 \cdot \text{Re}^{0.687}) / \text{Re} & 1 < \text{Re} < 1000 \\ 0.44 & \text{Re} > 1000 \end{cases} \quad (6.3)$$

The droplet temperature **and** droplet mass are governed by the following equations:

$$\frac{dT_d}{dt} = \frac{S \cdot h \cdot (T_G - T_d)}{c_L \cdot m_d} \quad T_d < T_{\text{evap}} \quad (6.4)$$

$$\frac{dm_d}{dt} = - \frac{S \cdot h \cdot (T_G - T_d)}{A} \quad T_d = T_{\text{evap}} \quad (6.5)$$

The convective heat transfer coefficient may be expressed as:

$$h = \frac{\text{Nu} \cdot k_G}{D}, \quad \text{Nu} = 2 + 0.6 \cdot \text{Re}^{1/2} \text{Pr}^{1/3} \quad (6.6)$$

In the simulations, a 4 meters section of the duct is used **as** the computational domain. In the actual experiments, the duct **has** a 90° bend, but this is not included in the simulation because the model uses a rectangular geometry nodalization. The incoming flow is prescribed at a duct cross section consistent with the location of the steel wool layer in the actual test rig. The velocity and temperature profiles are uniform, with the values taken **from** the measurements. The circular orifice within the duct is approximated with a roughly circular saw-toothed cut-out. A uniform grid of 30 mm resolution is **used** for the entire 4 m by 0.6 m by 0.6 m section. The walls of the duct are assumed to be at constant temperature. For one particular experiment, calculations are performed with grid resolutions of 40 mm and 15 mm, in addition to 30 mm, with only a 5% difference in centerline temperatures. In all three cases, the basic flow structure is evident. Grids at coarser resolution than **40 mm** could not resolve the recirculation zones just above the circular orifice. The walls of the duct are assumed to be thermally thin, with thermal properties derived for steel. Heat is lost to the surrounding environment by assuming a constant heat transfer coefficient for free convection. Radiation losses **from** the duct to the room are neglected. Typically, the duct walls reach a temperature of about 90°C for inflow temperatures of about 200°C.

Three calculations are run with flow velocities of 5.6, 6.7 and 7.1 m/s through the orifice. The initial temperature in the simulations is 167, 194 and 241 °C respectively. Figure **49** illustrates the temperature profile along the duct, both in wet and *dry* conditions, for the simulation at 241 °C and 7.1 m/s. The experimental results are shown **as** well. The plot clearly indicates that:

- The temperature prediction simulated by the code is qualitatively similar to the experimental temperature profile. However, the water droplets induce a faster cooling of the hot gas when compared with the experimental data.
- The quantitative difference between the experimental data and the numerical simulation is somewhat significant. In particular, in absence of water droplets, the initial cooling of the gas is less in the simulation than in the experiment, whereas the slope of the temperature profile indicates that the heat losses to the environment are larger in the simulation than in the experimental case.

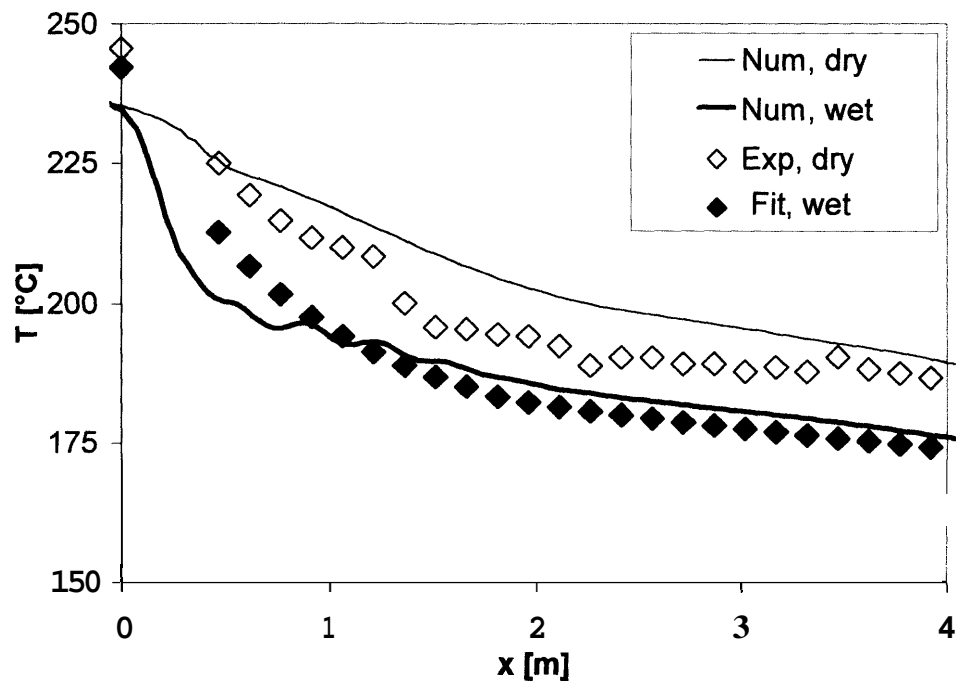


Figure 49. Gas temperature profile in dry and wet conditions ($U=7.1$ m/s)

In Figures 50-52, the difference between the dry and wet profile is reported against the duct coordinate, for the simulations and the experimental data as well. It can be observed that:

- The numerical values present an initial overshoot followed by a rapid decrease to their asymptotic value. Several oscillations can be noticed in the simulation, as well. The amplitude of both the initial overshoot and the oscillations increases with increasing velocity of the gas.
- The differences between the experimental dry and wet temperatures at the thermocouple farthest from the nozzle are similar to the calculated values.

Therefore, one may conclude that the code is capable to simulate reasonably well the overall evaporative process. The discrepancies between the simulations and the experiments are probably caused by the difficulty in accounting for the boundary conditions and the heat exchange between the water droplets and the hot gas. On one hand, the heat transfer between the droplets and the gas appears to be higher than expected experimentally. On the other hand, the heat exchanges at the walls appear to be underestimated in the ~~first~~ section of the duct and overestimated thereafter. Nonetheless, the agreement reached in predicting the temperature difference between a dry and a droplet-laden flow is satisfactory.

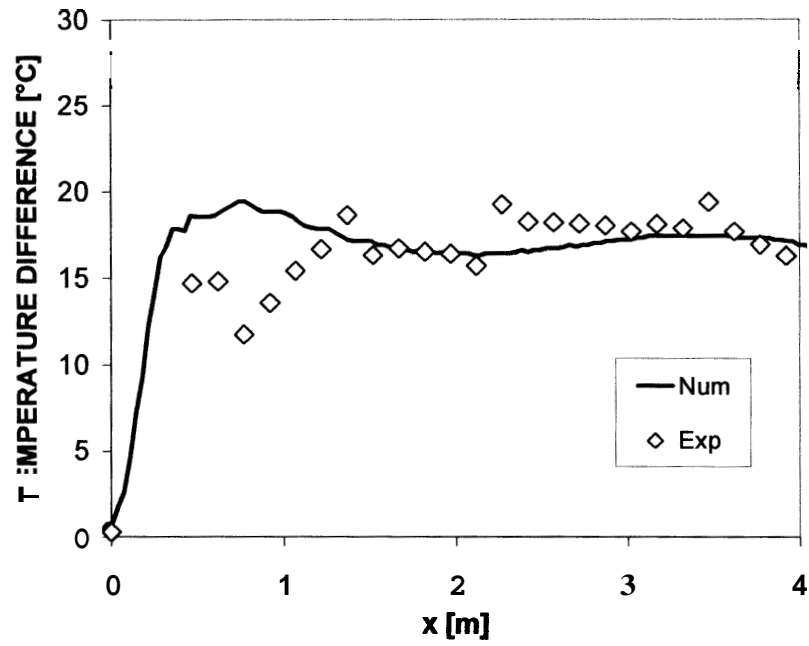


Figure 50. Temperature difference between dry and wet conditions ($U=5.6$ m/s)

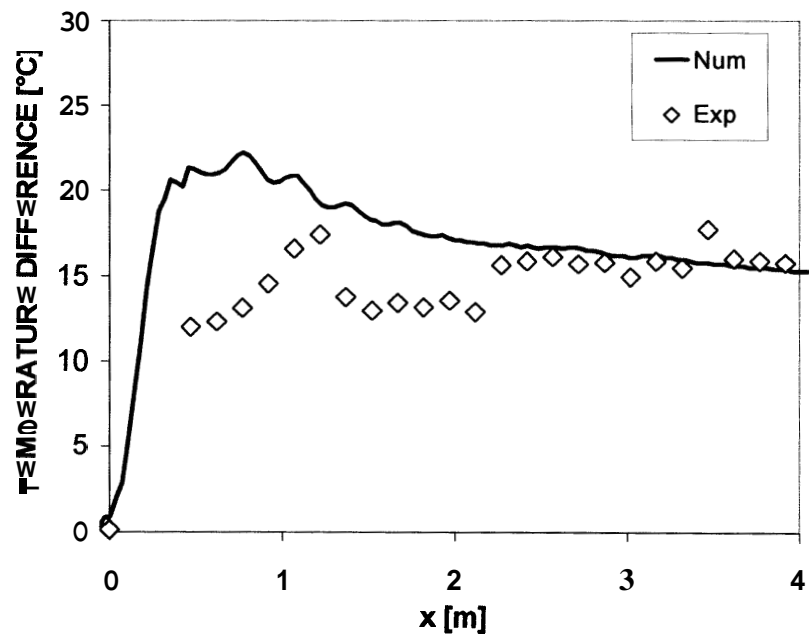


Figure 51. Temperature difference between dry and wet conditions ($U=6.7$ m/s)

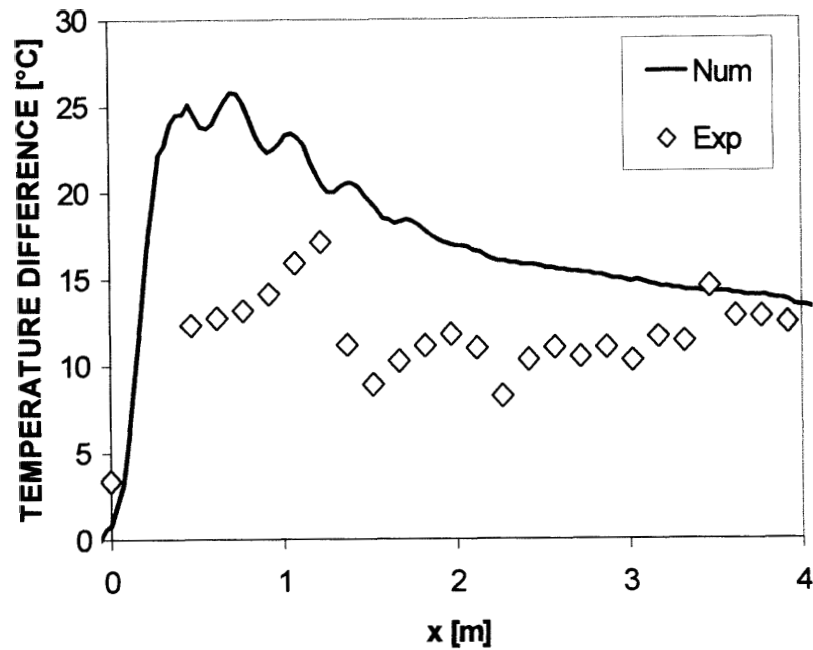


Figure 52. Temperature difference between dry and wet conditions ($U=7.1$ m/s)

SPRINKLER LINK TEMPERATURE MEASUREMENTS

In the tests for the determination of RTI and evaporative cooling parameter C , a small aluminum cylinder and a series of brass cylinders is used to simulate the time response of a sprinkler link subjected to a hot gas flow. The cylinders have a diameter of up to 7 mm. One or two thermocouples are inserted along the cylinder axis and the thermocouple beads are located at the cylinder center point. This set-up is used to measure the initial link temperature, as well as the transient simulated sprinkler link temperature profile under wet and dry conditions. It is necessary to determine whether

the temperature is uniform throughout the whole cylinder. Consider the Biot number defined as:

$$Bi = \frac{h * L}{k_s} \quad (6.7)$$

h is the convective heat transfer coefficient, L is the characteristic length defined as the ratio between the volume and the surface area of the cylinder and k_s is the conductivity of the simulated sprinkler link material. From the theory, one should remember that the temperature is uniform throughout the cylinder bulk (*lumped heat capacity* problem) if the Biot number is smaller than 0.1.

The range of temperatures and velocities explored in our experiments is 100 - 250 °C and 3 - 9 m/s respectively. Under these circumstances, the heat transfer coefficient is at most equal to 100 W/(m² °C), resulting in a Biot number of less than 10⁻³, well below the lumped heat capacity condition.

EXPERIMENTAL PROCEDURE

The procedure followed during the tests can be subdivided into three parts:

SYSTEM SET-UP. The apparatus is started and adjustments are made to the gas burner power and to the air intake louvers, until the specified gas temperature and velocity are obtained. The system is then allowed to reach steady state.

WET CONDITION TEST. The water sprays are activated, creating a two-phase flow of hot gas and water droplets in the duct. The water flow rate and droplet size distribution can be adjusted by varying the type of spray and the number of active sprays. While the two-phase flow reaches the steady-state, the sprinkler link is maintained at the initial temperature T_0 . Once the system conditions are stabilized, the gas velocity and the water volumetric fraction are measured with the optical techniques described in the previous chapter. Subsequently, the recording of the thermocouple measurements is initiated and the sprinkler link is inserted into the test section. The plunge test ends when the link temperature reaches a plateau. At this point, the link is extracted and returned to its initial temperature, T_0 . The plunge-test procedure is repeated three times, with the same boundary conditions, in order to establish the repeatability of the results.

DRY CONDITION TEST. After the completion of the three wet tests, the water sprays are turned off and the system is allowed to reach a new steady state under single-phase gas flow conditions. In order to have test conditions (in particular, the

gas temperature) comparable with the wet case, the initial link temperature is adjusted by an amount δT , so that $T_0^D = T_0^W \pm \delta T$. The value of δT , which must be evaluated on a case-by-case basis, is determined by the change of the gas temperature at the test section with respect to the initial link temperature T_0 . Once the desired steady-state conditions are obtained, a plunge test is conducted similarly to the wet case. The temperatures are again recorded until the link reaches a plateau, then the link is returned to the initial conditions. Three runs are performed in the dry case, as well. However, because of the uncertainty associated with the determination of δT during the course of the experiments, the three tests are conducted with a different initial link temperature (respectively: $T_0^D + \delta T$, $T_0^D + \delta T - 2^\circ\text{C}$, $T_0^D + \delta T + 2^\circ\text{C}$). During the processing of the data, the "correct" initial link temperature is calculated with more accuracy, thus allowing to determine which of the three dry tests can be compared with the wet runs.

Test matrix

In order to validate the proposed model, a series of experiments need to be conducted over a wide range of **boundary** conditions. As mentioned earlier, the control of three parameters is permitted at the ECSAT facility: the gas velocity, the water droplet volumetric fraction and the gas temperature.

In particular, a broad range of variation of the gas velocity and temperature is allowed. Instead, the interval of variation of the water volumetric fraction is quite narrow. In fact, on one hand, it is necessary for the water droplets to be present in appreciable quantity at the test section in order to obtain a significant cooling effect and to perform the optical measurement with the necessary accuracy and repeatability. On the other hand, too much water would overflow the test section, causing water build-up on the sprinkler link, which may lead to significant run-off or re-entrainment of water in the gas stream. This constrains the water volumetric fraction within a rather narrow range (about 1 to 8 ppm) and also imposes a correlation between the gas velocity and temperature during each test. For example, if the gas temperature is increased, the droplets evaporate more rapidly. Therefore a higher gas velocity is necessary in order to prevent the water droplets to evaporate before they reach the test section. Conversely, if the gas temperature is decreased, it is necessary to lower the gas velocity.

The gas velocity is determined by the blower characteristics and the configuration of the secondary air inlets and is therefore bounded between approximately 3 and 9 m/s. The gas temperature can only be varied between about 100 and 250 °C, since higher temperature would damage the air blower at the end of the duct.

Table 5 lists the experiments conducted. Two different spray nozzles are utilized (PJ8 and PJ10). The water volumetric fraction in the two cases is comparable, but the water droplet size distribution is quite different.

test ID	T _G (°C)	U (m/s)	β (ppm)	nozzle type
02-16-1	212	7.7	4.9	PJ8
02-16-2	114	5.3	5.4	"
02-17-1	213	7.4	6.2	"
02-17-2	105	4.5	9.4	"
02-18	163	6.1	3.8	"
02-19	167	5.8	4.6	"
02-22	221	7.4	5.2	"
02-23	167	5.8	7.6	"
02-24	207	6.1	2.6	"
02-25-1	104	3.2	8.1	"
02-25-2	89	4.5	5.9	"
02-26	87	3.5	8.2	"
03-01-1	131	3.9	6.1	"
03-01-2	151	3.9	5.6	"
03-02	169	4.8	5.4	"
03-03	140	4.0	7.9	"
03-04	169	7.1	3.8	"
04-01	195	7.9	8.2	PJ10
04-02	170	5.8	7.1	"
04-05	124	6.4	8.1	"

04-12	133	3.2	7.8	PJ10
04-12	169	3.6	7.2	"
04-14	112	3.6	5.7	"
04-15	113	4.6	3.9	"
04-16	157	5.8	3.7	"
04-19-1	108	4.1	4.4	"
04-19-2	164	5.3	5.6	"

Table 5. Test conditions

The test identifier (ID) follows the notation **mm-dd(-nt)**, where

- **mm-dd** is the date (month and day) in which the test is executed
- **nt** is the sequential order of the tests, in case more than one set is executed on the same day

As discussed in the previous chapter, each test generates a substantial amount of data.

Specifically:

- Gas velocity measurements, as well as water droplet counts, are obtained from CCD camera pictures
- Temperature measurements are obtained from thermocouples placed in the sprinkler link and other locations along the duct

The images taken during the wet tests to measure U and β are named as **mm-dd(-nt)-ni-""p**, where:

- **mm-dd(-nt)** identify the test
- **ni** is the sequential image number for each run (typically, at least thirty images are taken for each plunge test)
- **p** is the plunge test number (each test is repeated three times)

The temperature measurements are stored in MS Excel files, named according to **mm-dd(-nt)-elab**.

DATA ANALYSIS

Equation (5.1) illustrates how the rate of change of the link temperature is affected by the balance of two counteracting effects: the convective heat gained from the hot gas and the cooling effect due to the evaporation of the water droplets from the link surface. The gas and link temperatures, as well as the gas velocity and the water volumetric fraction can be measured as discussed previously. This leaves two quantities (RTI and C) to be determined. The value of these two parameters cannot be calculated from a single test, but must be obtained from a set of experiments conducted over a wide range of conditions. For this purpose, a number of experiments are performed at the ECSAT facility by plunging the simulated sprinkler link into the test section. Initially, one aluminum cylinder with a diameter of 6.4 mm is used. The

link thermal response, for gas velocities between 3 and 9 m/s and gas temperatures between 100 and 250 °C, is investigated.

Determination of the RTI and the parameter C

The RTI remains defined as in the original sprinkler response model. Therefore, the RTI value can be obtained by fitting Equation (5.6) to the experimental data from a dry test. Figure 53 shows the fitted versus experimental curves for one such case.

The RTI is found to be equal to 97 ± 22 for a 6.4 mm-diameter cylinder. Do note that, from Equation (3.8), the RTI of a simulated sprinkler link depends on the cylinder diameter (See "Section dependency of RTI and C on the link size"). Figure 54 summarizes the values of RTI calculated for the simulated sprinkler link during the experimental campaign. A calculation of the RTI by using Equation (3.8) provides a value of RTI equal to 100, which compares favorably with the experimental value.

The scatter of the calculated values about the average value is somehow significant. But the overall results for the RTI , over such a wide range of variation of U and T_G , justifies the conclusion that the RTI may be considered constant with respect to the gas velocity and the gas temperature.

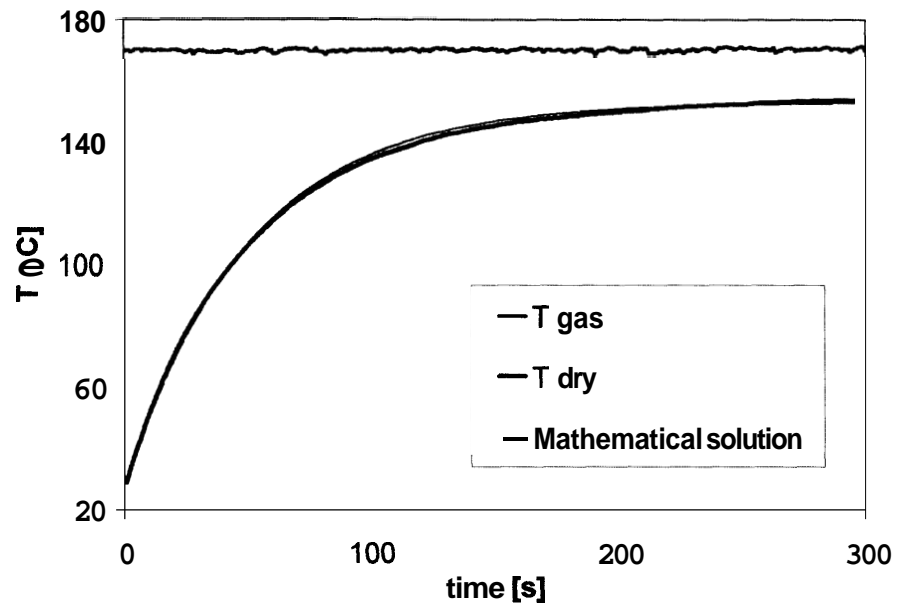


Figure 53. Measure of RTI from dry condition tests

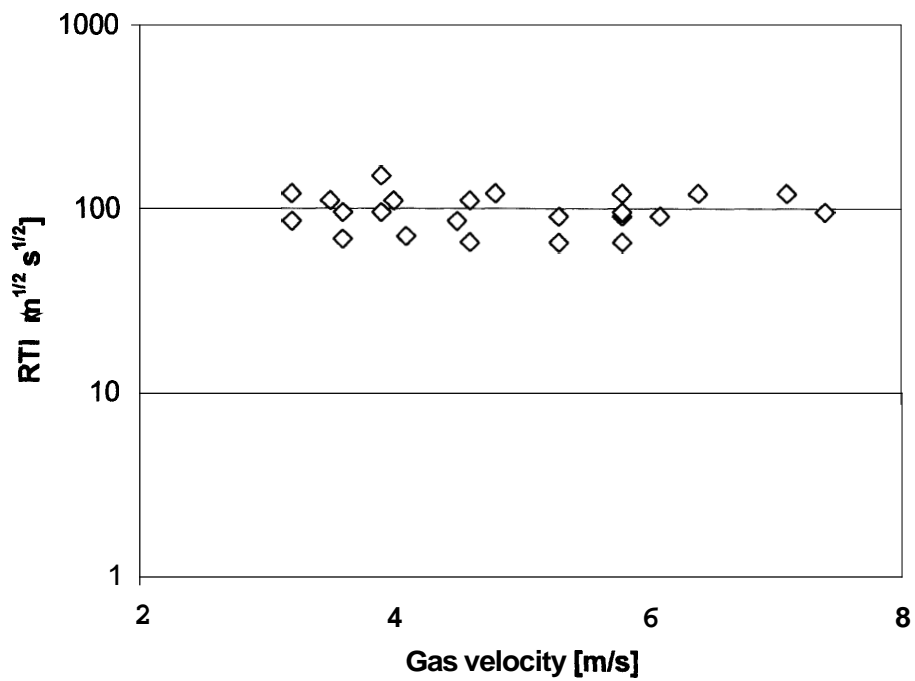


Figure 54. RTI values for different tests ($d = 6.4 \text{ mm}$)

If β , U and T_G are known experimentally, the evaporative cooling parameter C can be calculated from:

$$C = \frac{\Theta^D - \Theta^W}{O^D - 1} \frac{T_G - T_0}{\sqrt{U} \beta} \quad (6.8)$$

The first fraction on the right hand side of (6.8) is obtained by comparing the transient link temperature traces during wet and dry tests run under the same boundary conditions. An example of these traces is shown in Figure 55, where the remarkable evaporative cooling effect, observed during the wet test, results in a large temperature difference with respect to the dry case. The figure also shows that the presence of water does not influence the time response of the simulated sprinkler link significantly, as assumed in the implementation of the model. The time constant is simply the RTI divided by the square root of the gas velocity, as one may briefly find from the definition of RTI and Equation (5.4).

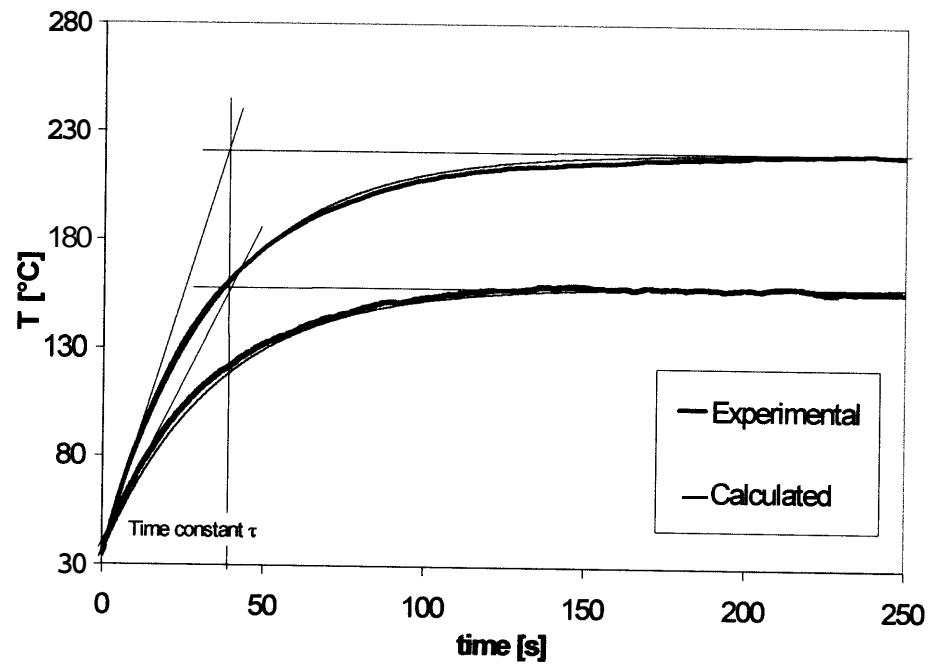


Figure 55. Determination of the evaporative cooling parameter

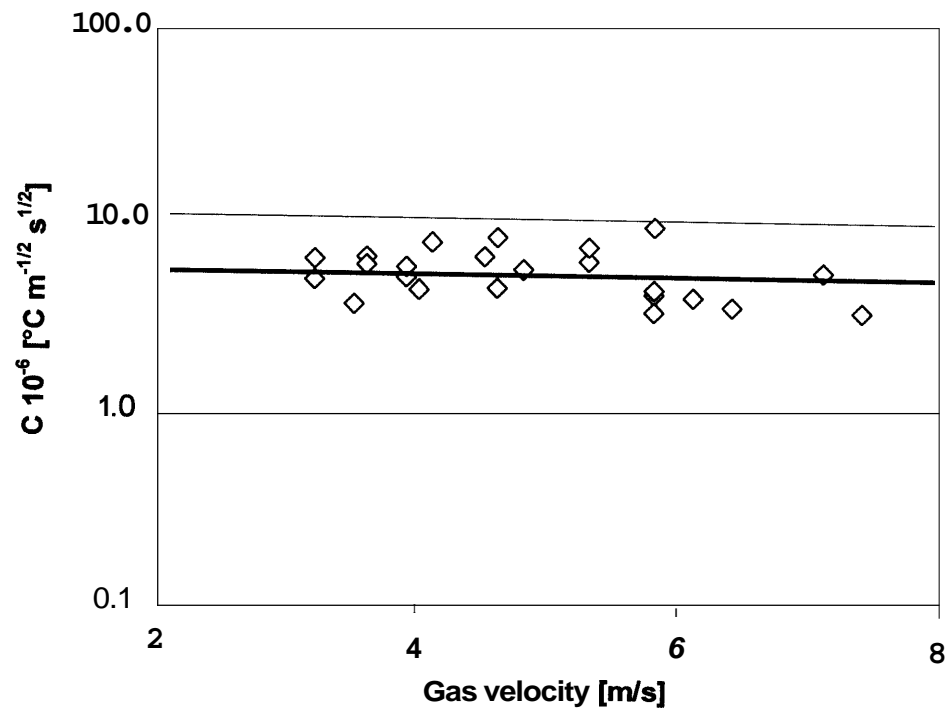


Figure 56. Values of parameter C for various gas conditions

Figure 56 summarizes the values of C , calculated from the tests conducted during the experimental campaign. The figure is relative to the **6.4** mm aluminum cylinder. It can be noticed that the values are contained in a narrow band, which indicates that, for any given cylinder size, C can indeed be considered a constant **as** assumed in the derivation of the evaporative cooling model. The solid line indicates the average value of the parameter $C = 6 \cdot 10^6 \text{ } ^\circ\text{C s}^{1/2} / \text{m}^{1/2}$, which is valid for **an** aluminum cylinder with a 6.4 mm diameter. The dependency of the parameter C on the diameter of the simulated sprinkler link will be given in the following section. The uncertainty on the measurement of the water volumetric fraction is approximately 60 percent and this affects the uncertainty associated with the determination of the parameter C . This result also validates the assumption made on the collection efficiency κ being constant.

Dependency of RTI and parameter C on the link size

In Chapter 3 the following formulas have been introduced:

$$\text{RTI} = \frac{\rho_S c_S V_S \sqrt{U}}{h \cdot S} \quad (6.9)$$

$$C = \frac{\kappa \rho_L A_S \Lambda \sqrt{U}}{h \cdot S} \quad (6.10)$$

The cylinder cross-sectional area A_S , the surface area S , the volume V_S and the convective heat transfer coefficient h depend on the link dimensions. In the previous section, we arrived at the conclusion that the two parameters, RTI and C , do not depend on the **gas** velocity and the gas temperature. As one may notice, **only** the relationship of RTI and the evaporative cooling parameter C with the simulated sprinkler link size must be determined. From the two above relations, it is clear that the size affects the parameters in the following fashion:

$$RTI \propto \frac{V_S}{hS} = \frac{\frac{\pi}{4} d^2 L}{K_1 \cdot d^{\eta-1} \pi d \cdot L} = K_2 \cdot d^{2-\eta} \quad (6.11)$$

$$C \propto \frac{A_S}{hS} = \frac{d \cdot L}{K_1 \cdot d^{\eta-1} \pi d \cdot L} = K_3 \cdot d^{1-\eta} \quad (6.12)$$

In particular, the parameter C is proportional to the square root of the simulated link diameter under the range of Reynolds numbers considered ($40 < Re < 1000 \Rightarrow \eta=0.5$).

K_1 , K_2 , K_3 are constant for a specified type of liquid (water, in this case). Using an array of seven brass cylinders with different diameters (ranging from 2 mm to 7 mm) and testing all the probes under the same operational condition ($T_G=150$ °C, $U=4$ m/s and $\beta=4$ ppm), we have calculated RTI and C using expressions (5.6) and (5.9). The cylinder diameters are contained in a range of values (2-7 mm) which may seem not too wide to the reader. However, both the necessity to remain in the low range of

Reynolds number and the practical objectives of our research project (to simulate commercial fire sprinklers) limit this range of variation. The analysis of the data confirms the dependency of RTI and C on the diameter of the simulated sprinkler link indicated by Equations (6.11) and (6.12). The value of the parameter η (and therefore the exponents of the diameter in both expressions) confirms the theoretical value of 0.5 since experimentally it is found to be equal to 0.47. Figure 57 reports the RTI results, while Figure 58 shows the parameter C . On this basis, another quantity is introduced hereafter: it is defined as the ratio between the evaporative cooling parameter C and the square root of the diameter:

$$\hat{C} = \frac{C}{\sqrt{d}} \quad (6.13)$$

Note that \hat{C} is a constant for any given fluid.

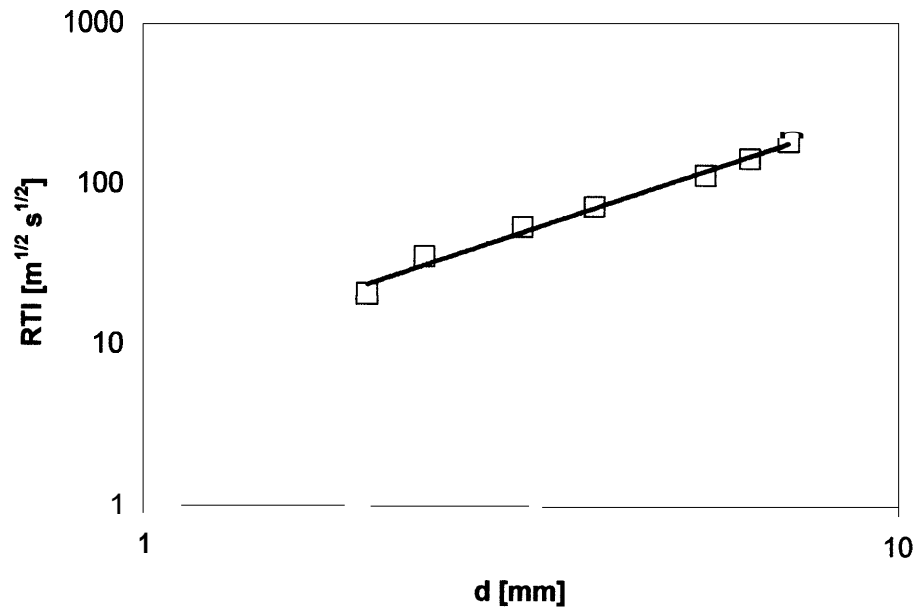


Figure 57. *RTI* for different brass cylinders, same operative condition

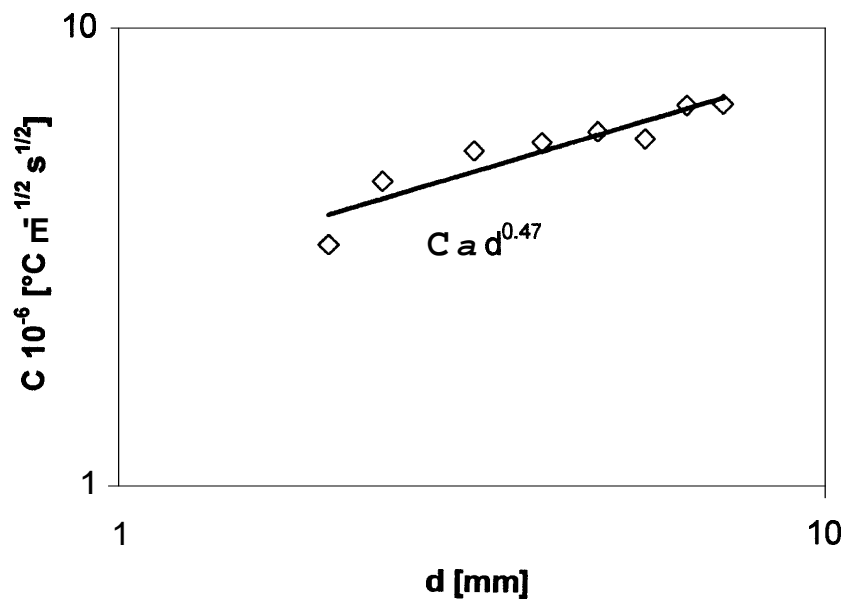


Figure 58. Parameter *C* for different brass cylinders, same operative condition

Additional considerations

From Chapter 3, we can express the water volumetric fraction in the following form:

$$\beta = \frac{T_G - T^W}{\hat{C} \cdot \sqrt{U \cdot d}} \quad (6.14)$$

Also the quantity χ was introduced such that:

$$T_G - T^W = \chi \beta_0 f(x) \quad (6.15)$$

By comparing Equation (6.14) with Equation (6.15), one may easily find that the following relation can be written as well:

$$\chi = \hat{C} \cdot \sqrt{U \cdot d} \quad (6.16)$$

The previous relationship gives us the possibility to double-check the calculation made by the EC model in a totally independent way. Several temperature distributions are analyzed to generate an indirect estimate of the evaporative cooling constant \hat{C} . The procedure is similar to that used to determine the gas temperature of a wet gas flow. The only difference is the determination of both the coefficient λ and χ from the fitting of the experimental data in both dry and wet conditions through Equations (5.17) and (5.18). The analysis of the data suggests a value for \hat{C} equal to $(83 \pm 9) 10^6$.

A more comprehensive analysis of the experimental data is also performed, by plotting the cooling effect ($T_G - T^w$) produced by the water droplets on a simulated sprinkler link (see Figure 59 and Equation (6.14)). The experiments in this case are those executed with the 6.4 mm cylinder plus the experiments involving the array of seven cylinders with a diameter ranging from 2 to 7 mm. The analysis provides a value of \hat{C} equal to $(82 \pm 13)10^6$, which is substantially close to the one found in the other way.

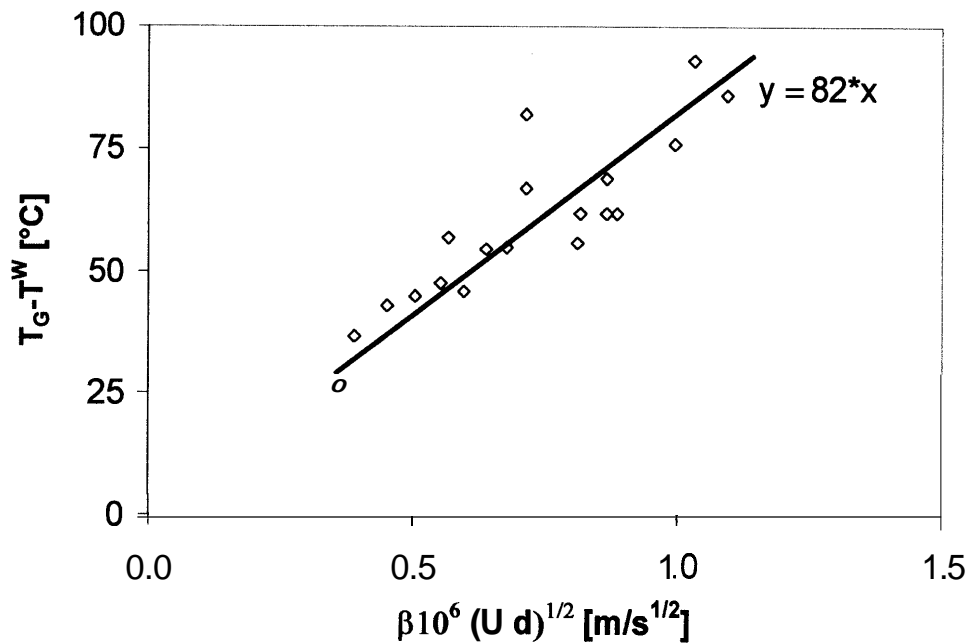


Figure 59. Fit to determine the evaporative cooling constant \hat{C}

An additional consideration can be made on the water volumetric fraction measurement. Using Equation (6.14), we have the chance to verify indirectly the measurements that have been performed with the laser technique. In fact, we can write the following relationship between the volumetric fraction and the quantity χ :

$$\beta = \frac{T_G - T^W}{\chi} \quad (6.17)$$

With a gas velocity of **4 m/s**, a temperature difference of **50 °C** and considering a wet temperature sensor diameter of 6.4 mm, χ assumes a value of almost $13 \cdot 10^6$ °C, yielding a volumetric fraction of **4 ppm**, which is definitively consistent with the experimental results of 4.7 ppm.

TESTS ON COMMERCIAL SPRINKLERS

Several basic assumptions of the model have been validated throughout the first series of experiments. The two parameters at the base of the entire theory have been quantified for various simulated sprinkler links. Consequently, the next step is to assess the capability of the model to predict the activation time of commercial sprinklers, especially when water droplets are carried by the gas flow. Four types of commercial sprinklers are tested under three different combinations of **gas** velocity,

gas temperature and water volumetric fraction. Two orientations of the sprinkler head with respect to the **gas** flow direction are considered.

Determination of the sprinkler time of activation

Commercially available sprinklers are tested in the **ECSAT** facility in order to **assess** the new model predictions in simulated fire-scenario situations. By solving Equation (3.25) with respect to the time, one obtains the activation time of a sprinkler immersed in a hot gas laden with water droplets as:

$$t_A^W = \frac{RTI}{\sqrt{U}} \text{Ln} \left(\frac{T_G - C \sqrt{U} \beta - T_0}{T_G - C \sqrt{U} \beta - T_A} \right) \quad (6.18)$$

The *RTI* of a sprinkler type is calculated through an initial series of experiments in dry conditions. From Equation (5.4), one may find that the *RTI* can be expressed as follows:

$$RTI = \frac{t_A^D \sqrt{U}}{\text{Ln} \left(\frac{T_G - T_0}{T_G - T_A} \right)} \quad (6.19)$$

Once the time of activation in dry conditions, t_A^D , has been measured for any sprinkler type, Equation (6.19) provides an estimate for the *RTI* of that particular sprinkler set.

The temperature of activation of the sprinkler T_A is provided by the manufacturer, while the remaining quantities are obtained as described in the previous chapter.

Concept of equivalent diameter

For any given sprinkler type, we need to determine the correct value of C to introduce in Equation (6.18). Since each sprinkler is different from another, the parameter C is not identical for any device. Remember that the parameter C depends on the size of the sprinkler link, as shown in Equation (6.12). Given that the link size is different for each type of sprinkler, it is convenient to introduce a correction for the parameter C in Equation (6.18). Consider the concept of *equivalent diameter* as the diameter of the aluminum cylinder that would have the same RTI of the sprinkler itself.

In the following, we assume that the heat transfer coefficient is given by Equation (3.4) and that the volumetric heat capacity of the sprinkler material does not vary significantly from a sprinkler type to another. Table 6 presents the value of the volumetric heat capacity for various materials used in the sprinkler manufacturing industry. For the link materials commonly used, this assumption introduces an error of less than 20 percent on the determination of the parameter C . The error is considerably small when compared to the other uncertainties included in the measurement process.

Material	density ρ [kg/m³]	specific heat c [kJ/(kg °C)]	volumetric heat capacity $\rho \cdot c$ [kJ/(m³ °C)]
Aluminum	2702	0.902	2437
Cadmium	8650	0.231	2000
Copper	8933	0.385	3439
Brass	8800	0.420	3696
Steel	7801	0.473	3690
Zinc	7140	0.388	2770
Methanol	3034	1.185	3595
n-Butane	2104	1.908	4014
Glass	3000	0.9	2700

Table 6. Physical properties of several sprinkler link materials

Therefore, from Equation (3.8), the aluminum cylinder with a RTI equal to that of a given sprinkler type has a diameter equal to:

$$d_{eq} = \left| \frac{0.52 \cdot k_G \cdot Pr^{0.37}}{\pi \cdot \rho_S \cdot c_S \cdot v_G^{0.5}} RTI \right|^{\frac{2}{3}} \quad (6.20)$$

We have already established that the parameter C is proportional to the square root of the diameter. Under the aforementioned assumptions, a relationship between C and RTI can be obtained as follows:

$$C = C_{Ref} \cdot \left(\frac{RTI}{RTI_{Ref}} \right)^{113} \quad (6.21)$$

In this equation, the reference values C_{Ref} and RTI_{Ref} are those for an aluminum cylinder with a diameter of 6.4 mm, which have been determined experimentally.

With these values Equation (6.21) becomes:

$$C = 1.3 \cdot 10^6 RTI^{1/3} \quad (6.22)$$

Using Equation (6.22), we can estimate the value of parameter C for **any** type of sprinkler once its RTI is known.

Sprinklers types and experimental conditions

In order to assess the capability of the new model to predict the activation time of a sprinkler in the presence of water droplets, an extensive experimental campaign is conducted in the ECSAT facility using four different types of sprinklers. They are identified **as**:

- a) Standard response solder Element sprinkler (SE);
- b) 5 mm bulb Standard Response sprinkler (SR);
- c) 3 mm bulb Quick Response sprinkler (QR);
- d) Quick response solder Element sprinkler (QE).

The four types of sprinklers are reported in Figure 60. Table 7 summarizes the values of the RTI values obtained for each sprinkler type from testing the devices in dry conditions. The orientation with the sprinkler frame orthogonal to the flow (the flow hits the link and the two frame arms simultaneously) is used in conditions A, B, D and E. The orientation with the frame parallel to the flow (the flow hits one frame arm, then the link then the other frame arm) is used in conditions C and F. As one may notice, two orientations are considered for the first three types of sprinklers, while the orientations considered for the QE type are three. This is necessary since the sprinkler type QE is nonsymmetrical with respect to the longitudinal axis of the device. The three orientations used for the QE sprinkler are depicted in Figure 61.

	Condition A	Condition B	Condition C
SE sprinkler	109 ± 13	108 ± 8	114 ± 9
SR sprinkler	98 ± 13	90 ± 10	133 ± 8
QR sprinkler	41 ± 4	39 ± 3	46 ± 5

	Condition D	Condition E	Condition F
QE sprinkler QE sprinkler	27 ± 2	27 ± 2	27 ± 1

Table 7. $RTI [m^{1/2} s^{1/2}]$ of the sprinklers used in the study

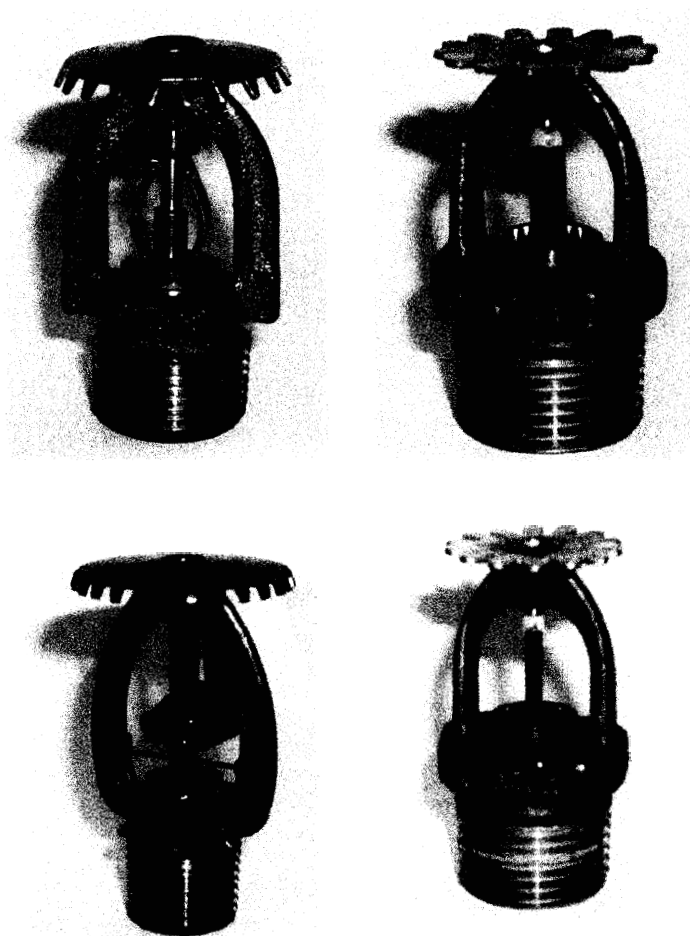


Figure 60. Commercial sprinklers (clockwise from top-left SE, SR, QR, QE)

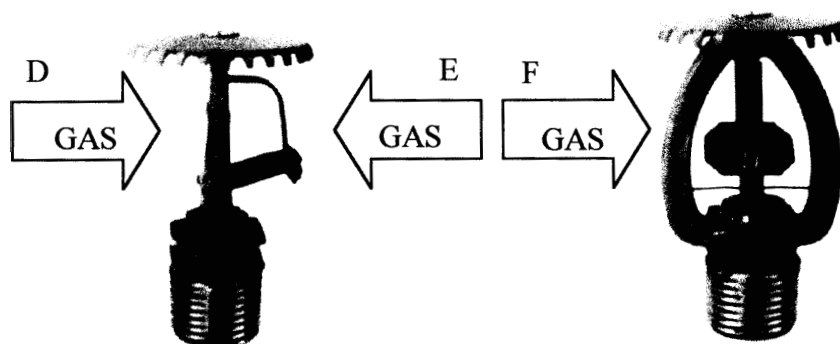


Figure 61. Sprinkler QE: different orientations

In all cases, the conduction losses from the sprinkler to its support are minimized by mounting the sprinkler on a plastic support (PTFE Teflon) that exhibits very low thermal conductivity. A sketch of the sprinkler support frame is reported in Figure 62.

	Condition A	Condition B	Condition C
Gas temperature in <i>dry</i> conditions [°C]	178	140	156
Gas temperature in wet conditions [°C]	164	127	134
Continuous sensor temperature measured in wet conditions [°C]	96	97	79
Initial & ambient temperature [°C]	32	29	22
Gas velocity [m/s]	3.8	3.5	3.7
Water volumetric fraction [ppm]	7	4	5

	Condition D	Condition E	Condition F
Gas temperature in <i>dry</i> conditions [°C]	156	163	168
Gas temperature in wet conditions [°C]	133	150	151
Continuous sensor temperature measured in wet conditions [°C]	84	99	95
Initial & ambient temperature [°C]	28	31	33
Gas velocity [m/s]	3.9	3.9	3.7
Water volumetric fi-action [ppm]	5	4	5

Table 8. Test matrix

The sprinklers are tested under a set of **six** different conditions as listed in Table 8. Conditions B, D, E and F are close to those prescribed for the standard plunge test (UL, 1992). However, the wafer volumetric fraction must be low enough to avoid sprinkler failure to activate. In conditions A and C, a larger amount of water is used. In order to ~~obtain~~ the sprinkler activation, the gas temperature is also raised. Condition B is achieved with one PJ10 nozzle, while conditions A, C, D, E and F are achieved with three PJ8 nozzles on a triangular pitch. A minimum of ten sprinklers is used for each experimental data point.

Commercial sprinklers - Experimental procedure

The procedure followed during each test can be subdivided into three parts:

SYSTEM SET-UP. The apparatus is started and adjustments are made to the **gas** burner power and to the air intake louvers, until the specified gas temperature and velocity are obtained. The test conditions are reported in Table 8. The system is then allowed to reach steady state.

DRY CONDITION TEST. While the **gas** flow reaches steady state, the sprinkler is maintained at ambient temperature. The recording of the thermocouple measurements along the duct is initiated. Subsequently, the sprinkler head is mounted on the plunge-

test support, **as** shown in Figure 62, a back pressure is generated by means of an adequate air supply and the sprinkler is plunged into the test section. The time of activation in dry conditions is measured from the very moment that the sprinkler head enters the test section to the moment it activates. That is, from the operator's standpoint, when the air pressure inside the plunge-test support drops. At this point, the support is extracted and returned to its initial temperature, T_0 . The plunge-test procedure is repeated ten times, with the same boundary conditions, in order to obtain a statistically meaningful value of the time of activation in *dry* conditions.

WET CONDITION TEST. The water sprays are activated in order to create a two-phase flow of hot gas and water droplets in the duct. The water flow rate and droplet size distribution can be adjusted by varying the type of spray and the number of active sprays. Once the system conditions are stabilized, the gas velocity and the water volumetric fraction are measured with the optical techniques described in the previous chapter. As soon **as** the desired steady state conditions are obtained, a plunge test is conducted similarly to the dry case. A series of ten sprinklers is tested in this new situation **as** well.

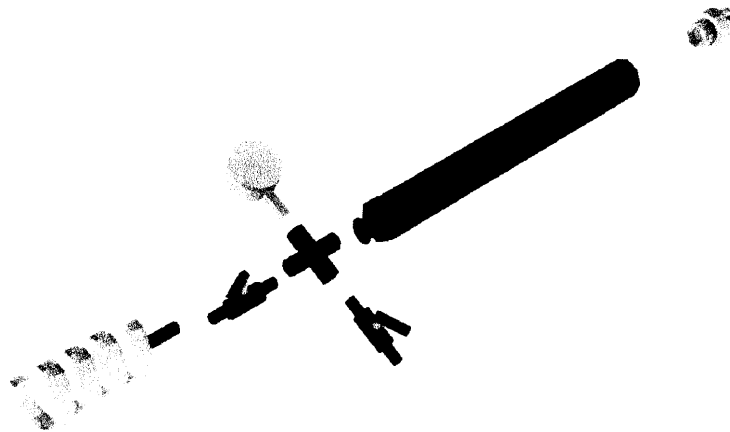


Figure 62. Sprinkler frame

Results

Typical results are presented in Figure 63, where the x-axis represents the sequence of experiments. It is evident that the time of activation under wet conditions is three to four times longer than in the dry conditions. Also, the experimental scatter in wet conditions is quite remarkable.

Table 9 and Figure 64 report all the findings. Consider the first three types of sprinkler (SE, SR, QR). For conditions A and B, the model predictions are in reasonable agreement with the experiments, with discrepancies within one standard deviation of the experimental data. In condition C, one of the two flame arms is upstream of the sprinkler link, shielding it from the incoming water droplets. Therefore, a significant fraction of the water droplet impacts the frame arm rather than the link, reducing the

evaporative cooling effect on the link. This is particularly true for the SR and QR sprinklers, whereas the SE sprinkler does not show any major effect of orientation on the activation time. The reason for this behavior can be found by looking at the geometrical configuration of the SE sprinkler, which has a solder element at the base of the sprinkler. Therefore, conductive heat transfer between the upstream frame arm and the base compensates for the reduced evaporative cooling. For the bulb type sprinklers (SR and QR), thermal conduction plays a negligible role because the glass bulb is not a good thermal conductor. Therefore, a shorter activation time is observed experimentally due to the reduced amount of evaporative cooling. In Table 9, these two instances are highlighted with bold characters for ease of identification.

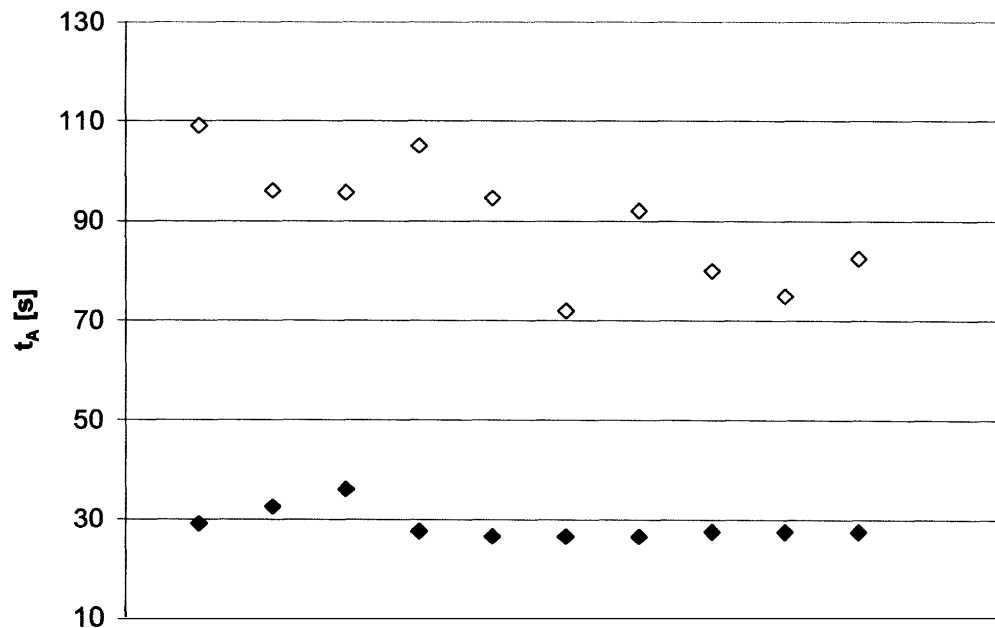


Figure 63. Measured times of activation (SE sprinkler, Condition B, +dry, 0 wet)

For the QE type sprinkler, the analysis of the data presented in Table 7 and Table 9 shows that the RTI of the sprinkler does not vary significantly with the orientation of the sprinkler frame. Further, for all the test conditions, the experimental values are reasonably well predicted by the model.

Figure 64 reports the sprinkler activation times predicted by the model versus the measured values. We can conclude that the proposed model predicts reasonably well the activation time of various sprinkler types over a broad range of conditions.

	Condition A	Condition B	Condition C
t^D measured	19 ± 2	29 ± 3	29 ± 3
t^W measured	91 ± 20	90 f 13	135 k 48
t^W calculated	89 ± 21	95 ± 14	122 ± 9
SR sprinkler			
t^D measured	13 ± 1	19 ± 3	29 ± 2
t^W measured	54 ± 21	47 ± 14	73 \pm 8
t^W calculated	53 ± 10	53 ± 8	115 \pm 7
QR sprinkler			
t^D measured	6 ± 1	8 f 1	10 ± 1
t^W measured	17 \pm 4	18 ± 3	24 \pm 3
t^W calculated	15 ± 2	19 f 4	26 \pm 2

	Condition D	Condition E	Condition F
QE sprinkler			
t^D measured	5 \pm 1	4 f 1	4 \pm 1
t^W measured	20 ± 3	10 ± 1	9 \pm 1
t^W calculated	18 ± 2	9 + 2	10 f 2

Table 9. Sprinkler time of activation [s]: model predictions and experiments

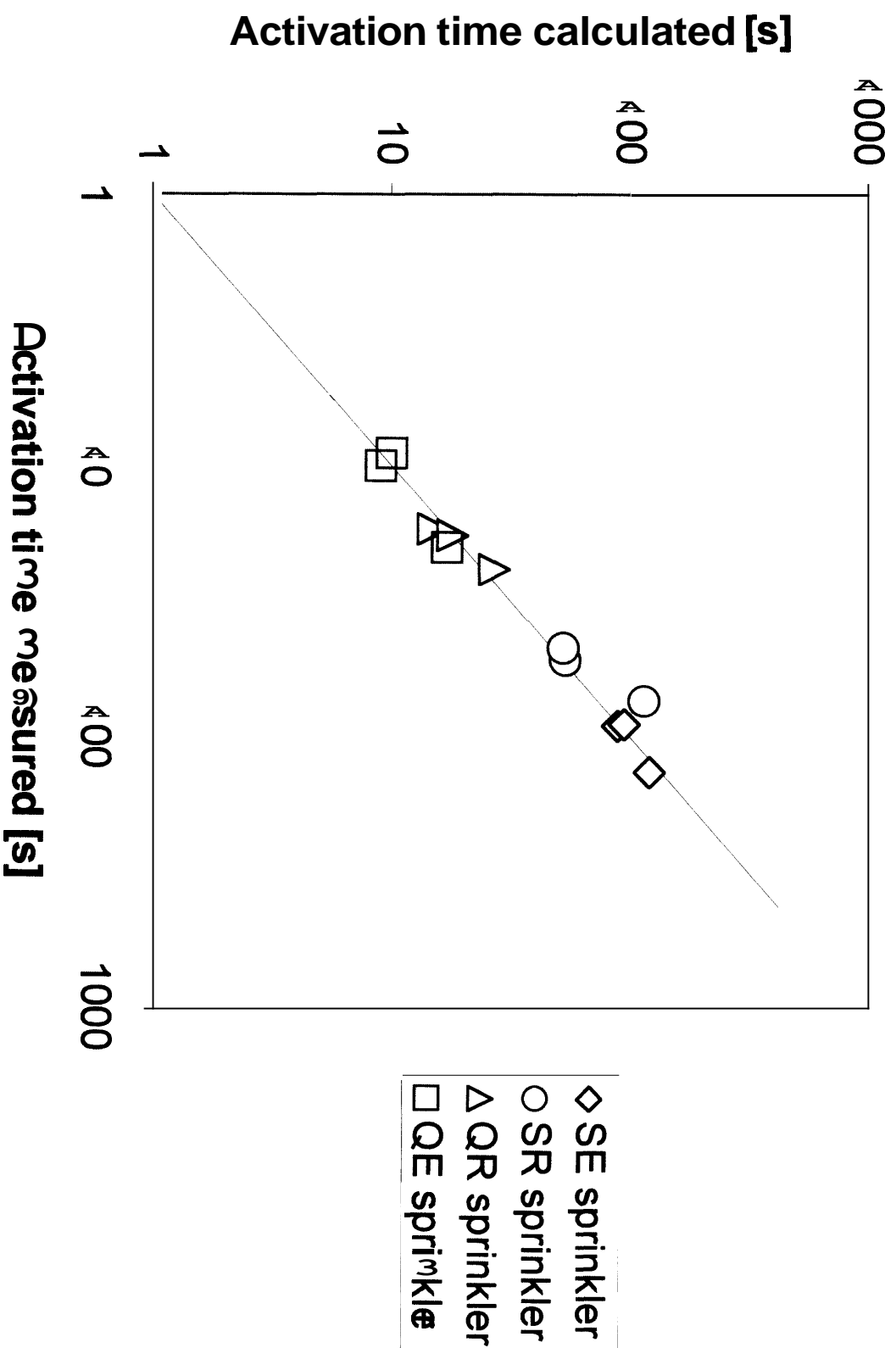


Figure 64. Sprinkler time of activation: comparison between the predictions of model and the experimental data

SIMULATION OF COMMERCIAL SPRINKLERS

The ~~first~~ part of the thesis ~~has~~ been dedicated to the formulation of the EC model and its validation on commercial sprinklers based on optical methods. We believe that the EC model should be able to actually determine the size and the material of an *equivalent cylinder* that, over a broad range of gas velocity, gas temperature and water volumetric fraction, behaves similarly to the sprinkler itself.

The experimental procedures used in plunge-testing both the equivalent cylinders and the sprinklers have already been described in this chapter. The interested reader is invited to review sections "EXPERIMENTALPROCEDURE" and "Commercial sprinklers - Experimental procedure", respectively. A simulated sprinkler link is inserted into the test section to simulate the sprinkler head. A series of ten sprinklers is also tested under the same conditions by plunging the sprinkler into the test section.

The size and material of the simulated sprinkler link are chosen accordingly to the following formulas derived from the EC model:

$$RTI = \frac{t_A^D \sqrt{U}}{\ln \frac{T^D - T_0}{T^D - T_A}} \quad (6.23)$$

$$C = \frac{1}{\beta\sqrt{U}} \frac{T_G \cdot (1 - e^{-\frac{t_A^W \sqrt{U}}{RTI}}) + T_A \cdot e^{-\frac{t_A^W \sqrt{U}}{RTI}} - T_0}{1 - e^{-\frac{t_A^W \sqrt{U}}{RTI}}} \quad (6.24)$$

Equation (6.23) derives from the solution of the thermal transient of a simulated sprinkler link exposed to a dry flow (Equation 3.10). Equation (6.24) is obtained by solving Equation (3.25) with respect to the parameter C. In this way, the experiments on commercial sprinklers provide the RTI and the parameter C representative of any given sprinkler type. The size of the simulated sprinkler link and its material can therefore be evaluated through the following equations, where the 6.4 mm-diameter aluminum cylinder is considered as the reference case:

$$d = \left(\frac{C}{\bar{C}} \right)^2 \quad (6.25)$$

$$\rho_S \cdot c_S = \left(\frac{d_{Ref}}{d} \right)^{1.5} \cdot \frac{RTI}{RTI_{Ref}} \cdot (\rho_S \cdot c_S)_{Ref} \quad (6.26)$$

The sprinklers tested in this situation are the Solder Element sprinkler type (SE), the Standard Response glass bulb sprinkler type (SR) and the Quick Response glass bulb sprinkler type (QR). The sensors, determined by the experimental data and the previous equations, are a 7 mm diameter zinc cylinder and a 3.7 mm aluminum cylinder. In fact, Equation (6.26) suggests a value of the volumetric thermal capacity equal to 2700 kJ/(m³ °C) for the SE and SR sprinklers and 2240 kJ/(m³ °C)

for the QR sprinkler. From Table 6, the materials that are closest to these values are respectively the zinc and the aluminum. Therefore, the 7 mm diameter cylinder simulates the SE and SR sprinklers while the 3.7 mm diameter cylinder is equivalent to the QR sprinkler. The very same Sensor is used in both the conditions (G and H) employed in the study.

Table 10 reports the test conditions and the results for every sprinkler. Condition G is a combination of low temperature, high velocity and low water volumetric fraction, while in condition H the gas temperature is increased significantly and the gas velocity decreased. In both situations, PJIJ nozzles are employed, one in condition G and two in condition H, respectively, to create the necessary evaporative cooling effect on the tested element. The water volumetric fraction is calculated using Equation (3.29) and a **6.4** mm diameter Sensor plunged into the test section, in the same position of the sprinkler heads. As one may notice in Table 10, some properties are given **as** an interval of values, since the experiments, nominally at the same condition, have been performed in different days. The activation time of the sprinkler is given **as** the average value and one standard deviation, calculated from the ten plunge tests.

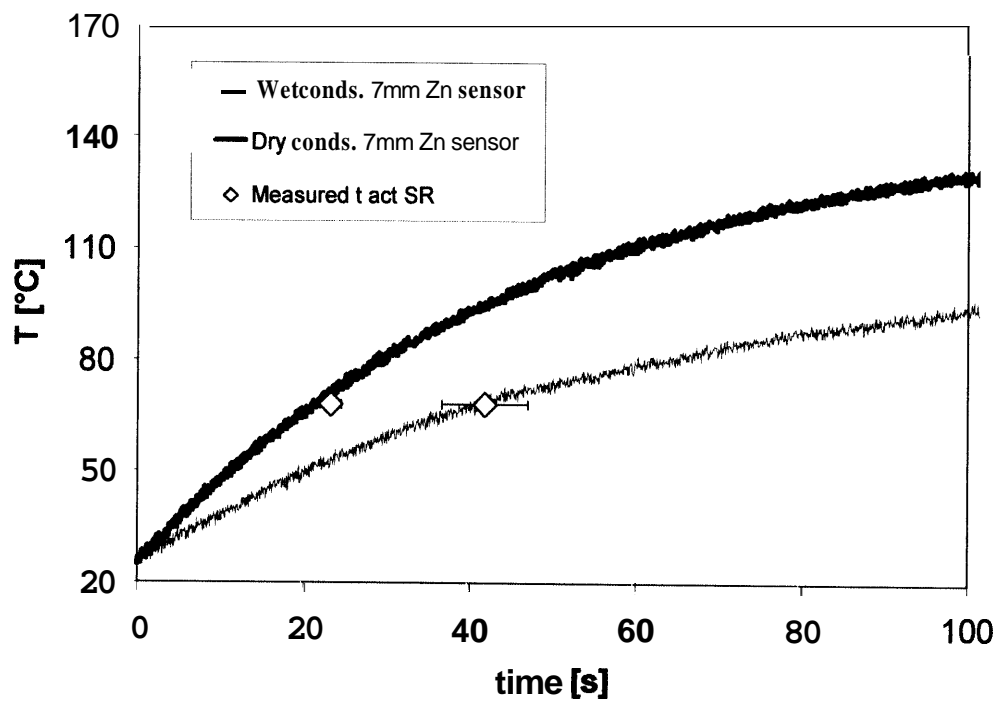
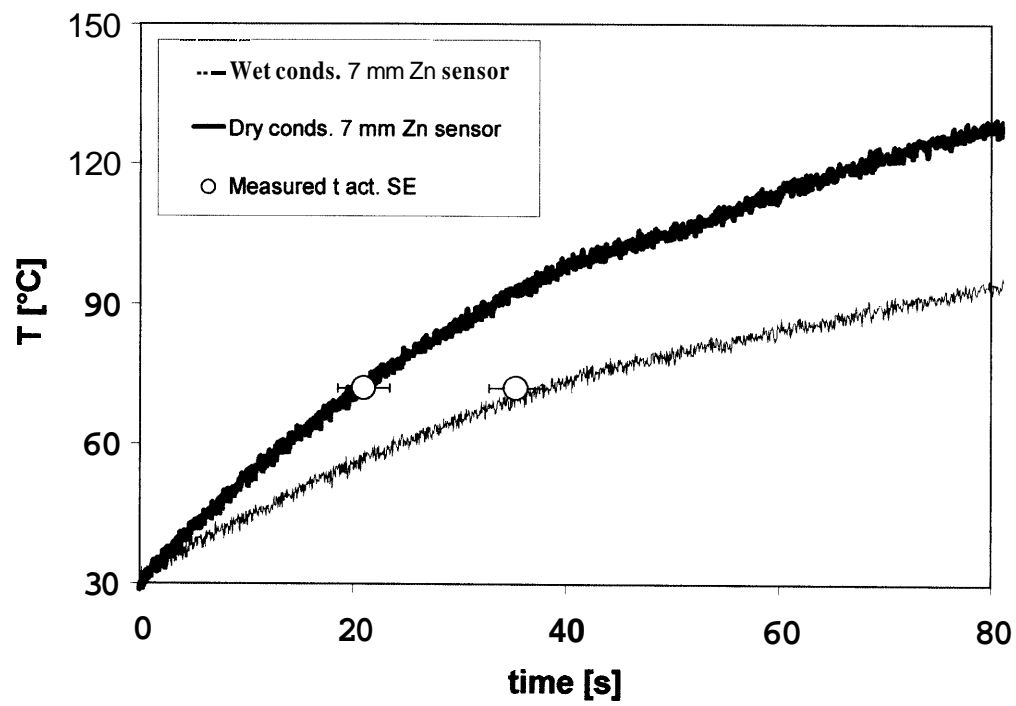
	Condition G	Condition H
Gas temperature in dry conditions [°C]	146-149	208-210
Gas temperature in wet conditions [°C]	132-137	182-186
Continuous sensor temperature measured in wet conditions [°C]	100-105	138-142
Initial & ambient temperature [°C]	25-30	32-33
Gas velocity [m/s]	4.4-4.6	3.7
Water volumetric fraction [ppm]	2	3.7-4
Sprinkler SE - RTI $m^{1/2} s^{1/2}$	100	98
Sprinkler SE - $C \cdot 10^{-6}$ $^{\circ}C m^{-1/2} s^{1/2}$	6.6	7.1
SE sprinkler activation time - dry conditions measured [s]	21.4 ± 1.4	13.7 ± 1.4
SE sprinkler activation time - wet conditions measured [s]	35.0 ± 2.6	27.1 ± 1.8
Temperature of activation SE [°C]	72	
Sprinkler SR - RTI $m^{1/2} s^{1/2}$	110	109
Sprinkler SR - $C \cdot 10^{-6}$ $^{\circ}C m^{-1/2} s^{1/2}$	6.9	6.5
SR sprinkler activation time - dry conditions measured [s]	23.2 ± 2.3	13.1 ± 1.7
SR sprinkler activation time - wet conditions measured [s]	41.8 ± 6.2	24.0 ± 2.6
Temperature of activation SR [°C]	68	
Sprinkler QR - RTI $m^{1/2} s^{1/2}$	42	44
Sprinkler QR - $C \cdot 10^{-6}$ $^{\circ}C m^{-1/2} s^{1/2}$	4.5	4.3
QR sprinkler activation time - dry conditions measured [s]	8.0 ± 1.5	4.5 ± 1.2
QR sprinkler activation time - wet conditions measured [s]	12.4 ± 3.1	8.1 ± 1.5
Temperature of activation QR [°C]	68	

Table 10. Test conditions and results

Figure 65 and Figure 66 report the measured temperature evolution of the simulated sprinkler links, **as** described in the legend. Also, the measured values of the activation time are plotted together with their standard deviation. The error bar represents **two** standard deviations. The **standard** deviations include the systematic errors (such as the error involved in the insertion of the sprinkler frame into the test section and the time delay between activation of the sprinkler link and the operator's response associated with the chronometer stop). From the plots, it can be observed that, in each situation, the simulated sprinkler link behaves like the real sprinkler head, at least within one standard deviation from the average time of activation. In condition G, the better agreement is reached for the QR sprinkler, in which the temperature trend of the simulated link intersects almost exactly the activation time, in both *dry* and wet conditions. In the SE sprinkler situation, the simulated **link** thermal response appears somewhat slower than necessary, while in the SR situation it is slightly faster.

In condition H, the better agreement is obtained for the SE sprinkler. For the SR sprinkler **type**, the simulated **link** appears somewhat faster in *dry* conditions, while in the QR situation it is slightly slower in wet conditions.

In conclusion, this proves that the EC model is capable to define completely (size and material) the cylinder that actually simulates the behavior of a given commercial fire sprinkler under **any** operative condition.



-CONTINUE-

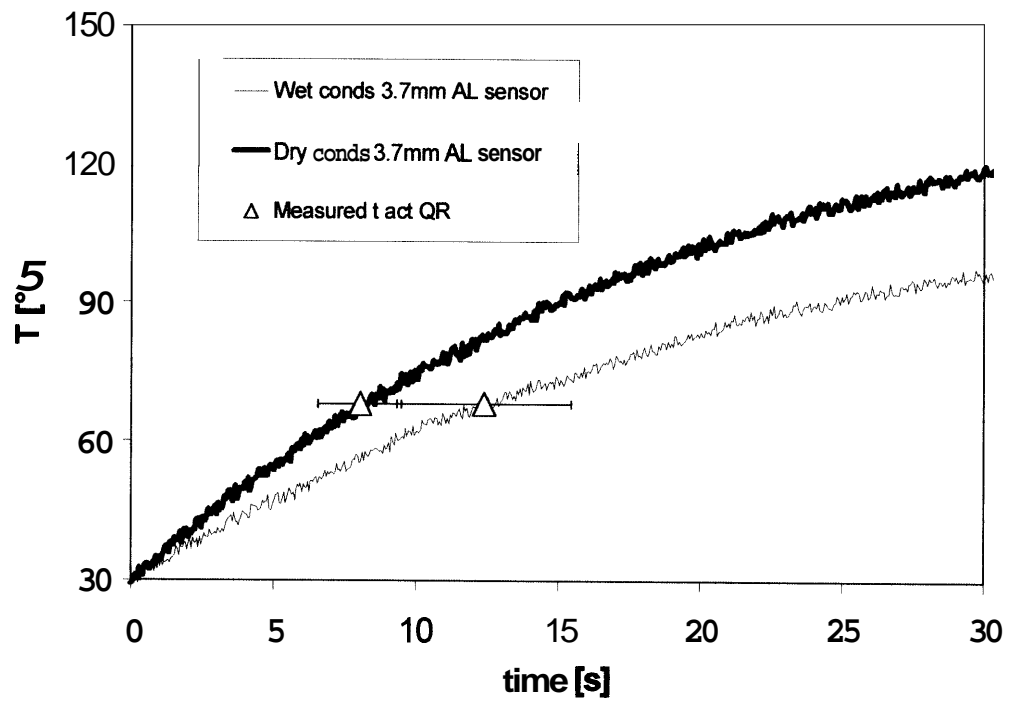
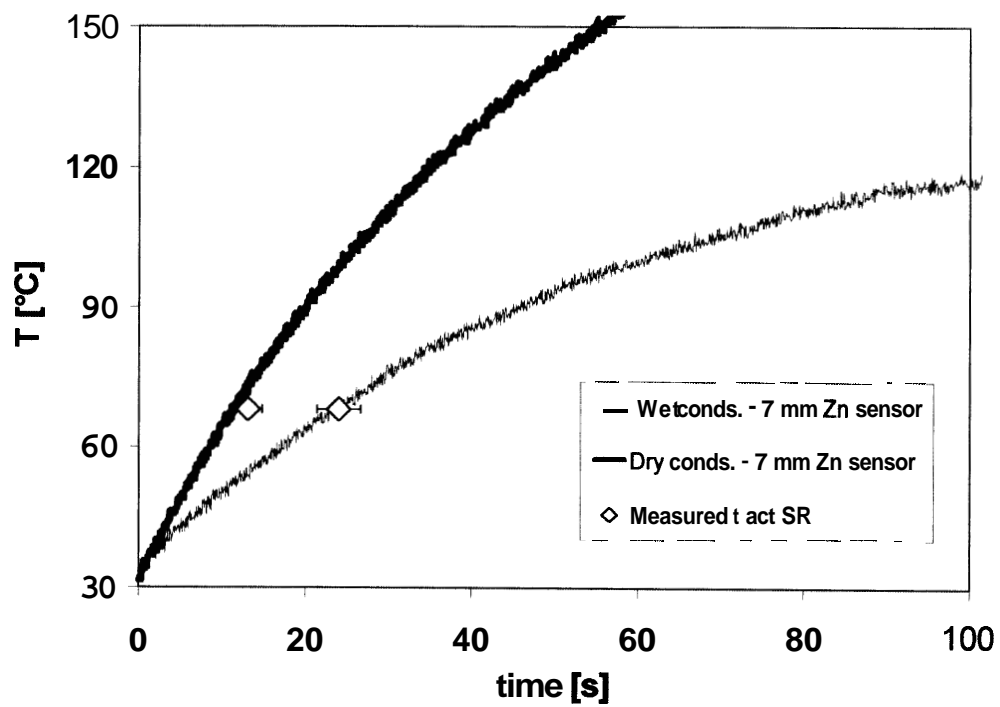
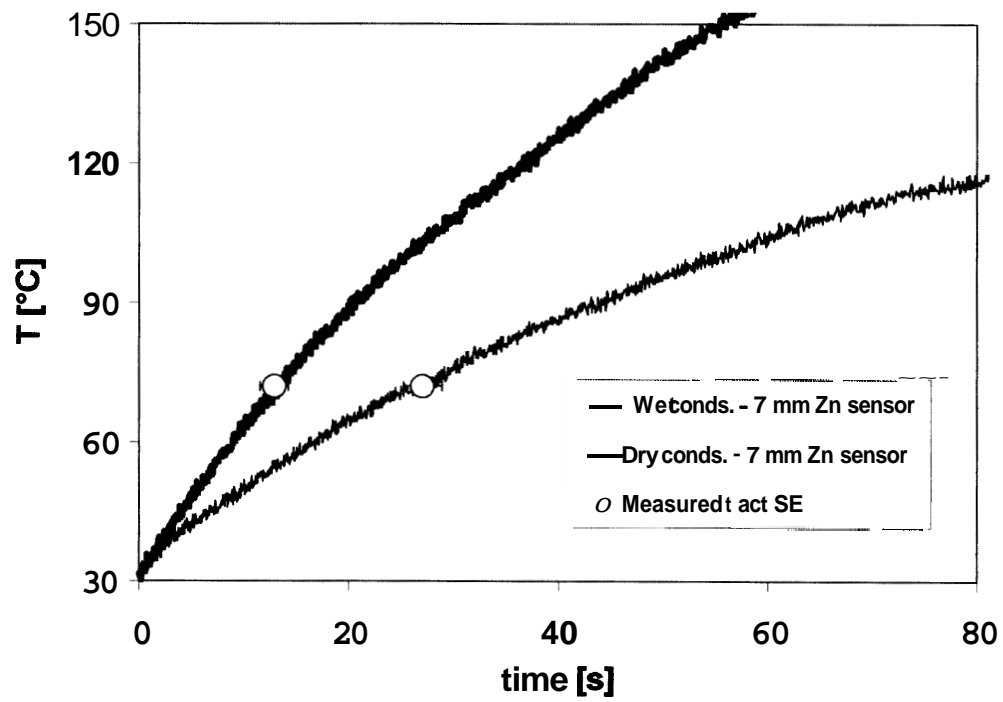


Figure 65. Results for Condition G: SE sprinkler (top), SR sprinkler (middle), QR sprinkler (bottom)



-CONTINUE-

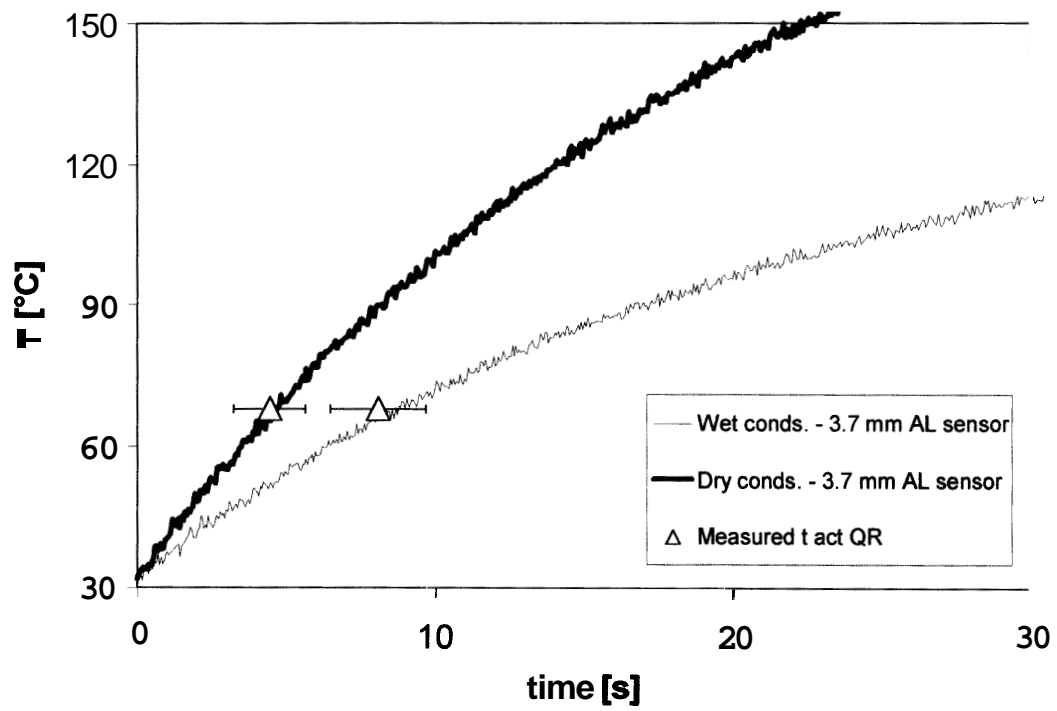


Figure 66. Results for Condition H: SE sprinkler (top), SR sprinkler (middle), QR sprinkler (bottom)

CHAPTER 7

A NOVEL APPROACH TO TEMPERATURE AND VOLUMETRIC FRACTION MEASUREMENTS

In the previous chapters, the experimental procedure to measure the temperature and the water volumetric fraction of a hot gas laden with water droplets has been described. The technique is viable in a research laboratory, where expensive laser devices are available and the difficulty of calculations is affordable. The time to elaborate all the data is not problematic, **as** well.

Imagine instead a large-scale test in an industrial environment, where fast, reliable and inexpensive measurements are necessary to determine the gas temperature or the volumetric fraction of a liquid in a gas flow. Current technology makes it difficult to accurately detect the wet gas temperature when the hot **gas** is laden with water droplets. This problem is particularly evident in fire sprinkler arrays installed in warehouses to protect against the damages of a fire. In these applications, for instance, the temperature and velocity of the hot gases associated with the spread of a fire have to be easily read. Optical methodologies **based** on the use of laser light

are not very convenient both because they are very expensive and because the presence of soot and particulate generated by the fire can affect significantly the readings. Further, they do not provide direct measurements, increasing the time consumed and the possibility of inaccuracy.

Conventional temperature sensors (thermocouples, for example) do not measure the temperature of the gas as well. The droplets tend to deposit on the detecting surfaces, resulting in evaporative cooling that causes inaccurate measurement of the gas temperature. In the following, we will introduce a novel methodology to obtain valuable information on a two-phase flow.

OBJECTIVES AND PROOF-OF-CONCEPT

Two temperatures can be detected in a hot gas laden with water droplets. One is the temperature read by a thermocouple exposed to the flow. This measurement is affected by a significant evaporative cooling effect, which results in readings much below the real gas temperature. We referred to this temperature as the wet temperature T^w . The second is the real gas temperature, T_G .

The concept behind this new methodology is to obtain measurements of the gas temperature from two heating elements kept at temperature T_H and T_C , respectively. These two temperatures are above the Leidenfrost transition and hence they are

unaffected by the water droplets. Simple calculations show that the temperature of the **gas** is a function of the two heater temperatures and the ratio of the powers supplied to the two heating elements.

To demonstrate this conceptual approach, consider a heating element immersed in a gas kept at constant temperature and flowing at constant velocity over the heater.

Consider also the measurement of the heat power **as** a function of the temperature of the heater. In *dry* conditions, the power is linearly proportional to the temperature.

This is under the assumption that the heat transfer coefficient does not change significantly with the heater temperature and that the temperature of the element is not too high such that the radiative contribution can be neglected. When water droplets are present, this linear dependence is true if the heater temperature is above the Leidenfrost transition. For liquid water, this transition happens at about 250 - 300 °C. The power dissipated by the heater under wet conditions deviates from the linear behavior below that temperature because the heater must also supply the energy to vaporize the water droplets deposited on its surface.

THE INFLUENCE OF DROPLETS ON SENSORS

A calculation is performed in order to estimate the relative influence of the heat transfer between the water droplet and the cylinder with respect to the heat transfer between the gas and the cylinder. Our assumption that the droplets do not affect the heat transfer mechanism at the interface between **gas** and cylinder, kept at a

temperature above the Leidenfrost transition, holds true if the ratio between the two heat exchanges is relatively small.

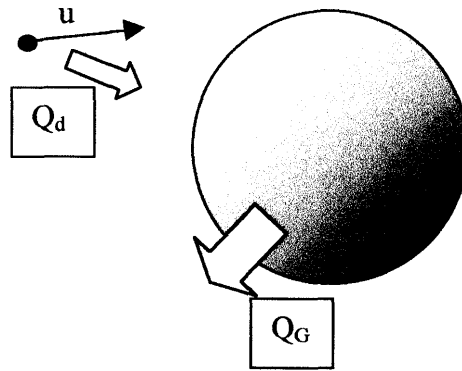


Figure 67. Heat exchanges between a droplet, the gas flow and a wire

Let us consider the time interval Δt . If we consider the length of the cylinder unitary ($L_S = 1$), the cylinder cross sectional area can be written as:

$$A = d \cdot L_S = d \quad (7.1)$$

The volumetric flow rate of the hot gas is represented as well by the following expression:

$$\dot{V}_G = U \cdot A \quad (7.2)$$

Considering the definition of volumetric fraction in Equation (5.30), the water flow rate is obtained as:

$$\dot{V}_L = \beta \cdot \dot{V}_G = \beta \cdot U \cdot A \quad (7.3)$$

The total water droplet surface associated with the heat transfer can be obtained as:

$$S_L = \xi \cdot (\dot{V}_L \cdot \Delta t) \cdot S_d \quad (7.4)$$

S_d is the unitary droplet surface for unit of volume and it is equal to $6/D$. ξ is a factor that takes into consideration how much of the total surface actually exchanges heat with the cylinder. In our calculation, this quantity is set equal to 1/2, but, as one may notice at the end of the section, an even bigger value (at most ξ equal to 1) will not affect our conclusions as well.

The time of residence of the droplet δt (i.e. the time that each droplet employs to move along half the cylinder circumference) is given by:

$$\delta t = \frac{\pi d / 2}{U} = \frac{\pi d}{2 \cdot U} \quad (7.5)$$

Therefore, after defining Q_d and Q_G as the heat transfer exchanged between the droplet and the cylinder and between the gas and the cylinder, respectively, we can express the ratio between the two quantities in the following form:

$$\frac{Q_d}{Q_G} = \frac{h_{fb} \cdot (T - T_d) \cdot S_L \cdot \delta t}{h_{conv} \cdot (T - T_G) \cdot S \cdot \Delta t} \quad (7.6)$$

For Reynolds number between 10^3 and $2 \cdot 10^5$, the convective heat transfer coefficient between cylinder and gas is found by applying the following correlation (Zukauskas, 1985):

$$Nu = 0.26 \cdot Re_d^{0.6} Pr^{0.37} \quad (7.7a)$$

The film boiling heat transfer coefficient can be expressed accordingly to Ito et al. (1981) by the following correlation:

$$Nu = 0.025 \cdot Re_{d,L}^{0.5} \frac{\mu_L}{\mu_V}$$

$$Re_{d,L} = \frac{U \cdot d}{\nu_L} \quad (7.7b)$$

$$Nu = \frac{h_{fb} \cdot d}{k_V}$$

Substituting the expressions for the different terms in Equation (7.6), one may express the ratio between the two heat transfers as:

$$\frac{Q_d}{Q_G} = 0.144 \cdot \beta \cdot \frac{d^{0.9} U^{-0.1}}{D} \cdot \frac{\frac{k_V}{k_G} \frac{v_G^{0.6}}{v_L^{0.5}} \frac{\mu_L}{\mu_V}}{\text{Pr}_G^{0.37}} \cdot \frac{T - T_d}{T - T_G} \quad (7.8)$$

T is the temperature of the cylinder. The following set of values is typical in our applications:

- water volumetric fraction $\beta = 5$ ppm,
- T_d , T_G and T equal to **100 °C**, 200 °C and 500 °C, respectively,
- gas velocity $U = 4$ m/s
- diameter of the heating element $d = \mathbf{9.3 \text{ mm}}$,
- average droplet diameter $D = 65 \text{ }\mu\mathbf{m}$.

With these values, Equation (7.8) suggests that the ratio between the two heat transfers is smaller than 2 percent.

Note that correlation (7.7b) is for a flow film-boiling situation, whereas, in our applications, the water content is extremely small. This conservative approach has increased significantly the estimation of the heat transfer coefficient h_{fb} and consequently the heat transfer ratio. In fact, other authors (Inada and Yang, **1994**; Bromley *et al.*, **1953**) provide film boiling coefficients substantially lower than the one used in this situation. Therefore, the ratio calculated by Equation (7.8) is probably much lower than 2 percent, reducing even further the influence of the water droplets over the behavior of the sensor. Experimental results obtained with

the prototype (heaters' diameter equal to 9.3 mm) confirm that the presence of water droplets affects the heat transfer by almost the same percentage, over a broad range of gas temperature and gas velocity conditions. It is indeed possible that the dynamics of the drops in between the **two** heating elements could enhance the energy transfer, thus increasing the influence of the water over the measurement process.

However, a better arrangement of the heating elements as implemented in the intermediate and final versions of the sensor will considerably reduce the influence of the water droplets over the readings. Further, as one may notice from Equation (7.8), the ratio depends almost linearly on the diameter of the heaters. If the heater diameter decreases, so does the relative influence of the water droplets over the heat transfer between the hot gas and the cylinder. The heaters of the intermediate and final version of the sensor will have a diameter equal to 0.2 mm.

LEIDENFROST TRANSITION VERSUS GAS VELOCITY

Another issue to clarify is whether the Leidenfrost transition for water droplets carried by a hot **gas** flow depends on the gas velocity. Several authors have addressed this point in the recent past, as they studied the influence of the velocity of water droplets impacting over **a** hot surface kept above the Leidenfrost transition. The Leidenfrost temperature is usually represented against the Weber number, for several values of the droplet impinging frequency (**i.e.** how many droplets per

minute are deposited on the hot surface). Their studies (in particular, Bernardin *et al.*, 1997b) suggest that neither the velocity of the water droplets, incorporated into the Weber number, nor the impact frequency influence significantly the Leidenfrost transition. Figure 68 reports the findings. Typical Weber numbers for our applications are in the range between 10 and 40.

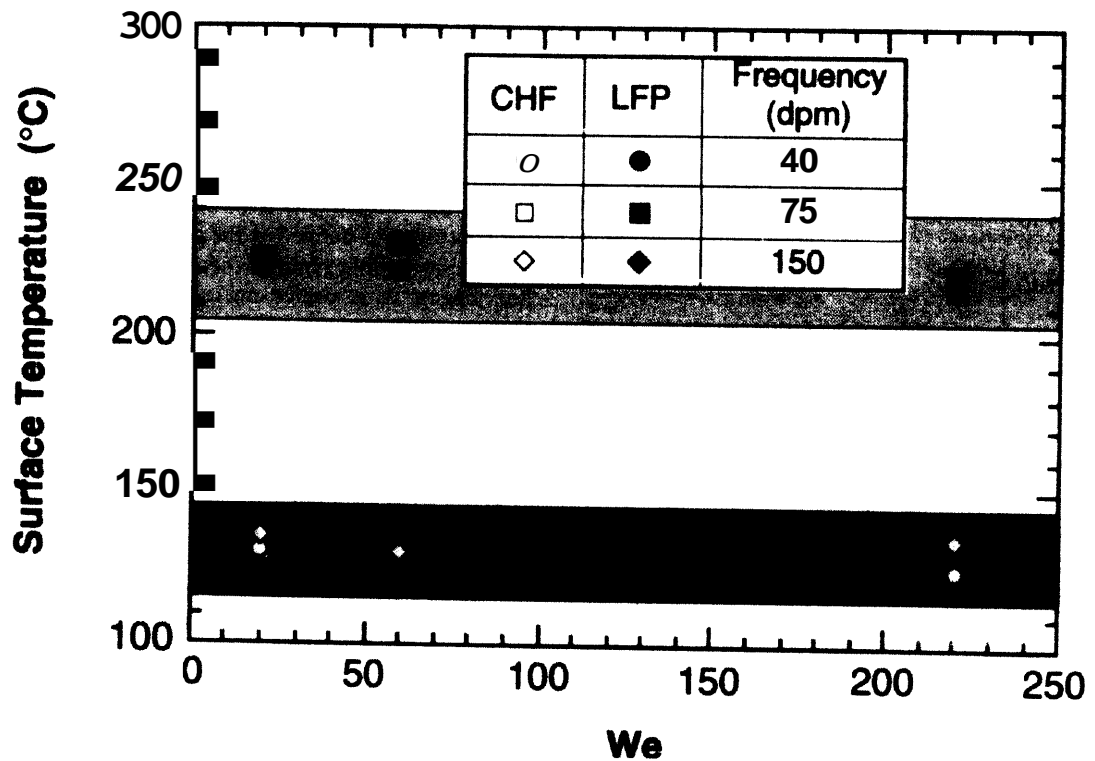


Figure 68. Leidenfrost transition versus Weber number and the droplet frequency (in droplets per minute) according to Bernardin *et al.* (1997)

DEVELOPMENT OF THE SENSOR

The design and the construction of the ALTEC sensor are performed in three subsequent steps. A prototype of the sensor is initially constructed to validate our assumptions and to gather some data to verify the feasibility of the device as a whole. A redesign of the control circuit board and an in-line arrangement of the heating sensors have led to a second intermediate version of the sensor, which is tested more carefully in the ECSAT facility. A calibration curve over a broad range of gas temperatures and gas velocities is carried out, as well as a comparison of the results with the data analyzed accordingly to what described in Chapter 5. Finally, a commercial version is designed with a new control board and with several additional features, such as a LCD read-out and a moving average algorithm to eliminate signal noise present in the previous acquisition system.

PROTOTYPE

The simplest configuration of the dual heater Sensor is considered using off-the-shelf items readily available in the conceptual phase of this invention. Figure 69 shows the preliminary version of the sensor. The sensor is designed to measure the temperature of a one-dimensional gas stream with velocity orthogonal to the sensor plane. The sensor plane is the plane containing the longitudinal axes of the two heating elements. The heaters are controlled electronically in ac mode.

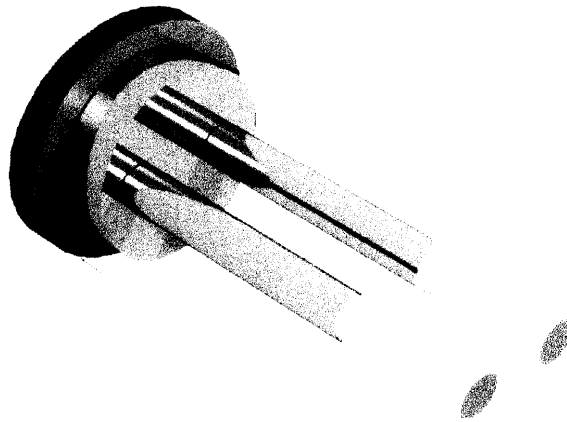


Figure 69. Preliminary sensor configuration

Each heater is supplied by a solid state power relay. A J-type thermocouple, inserted along the **axis** of the heater, **40 mm** far from the tip of the heater provides the feedback signal. The current dissipated into the heater is acquired through **an** electric transducer, whose output is read by an external acquisition board. Figure 70 illustrates the control system.

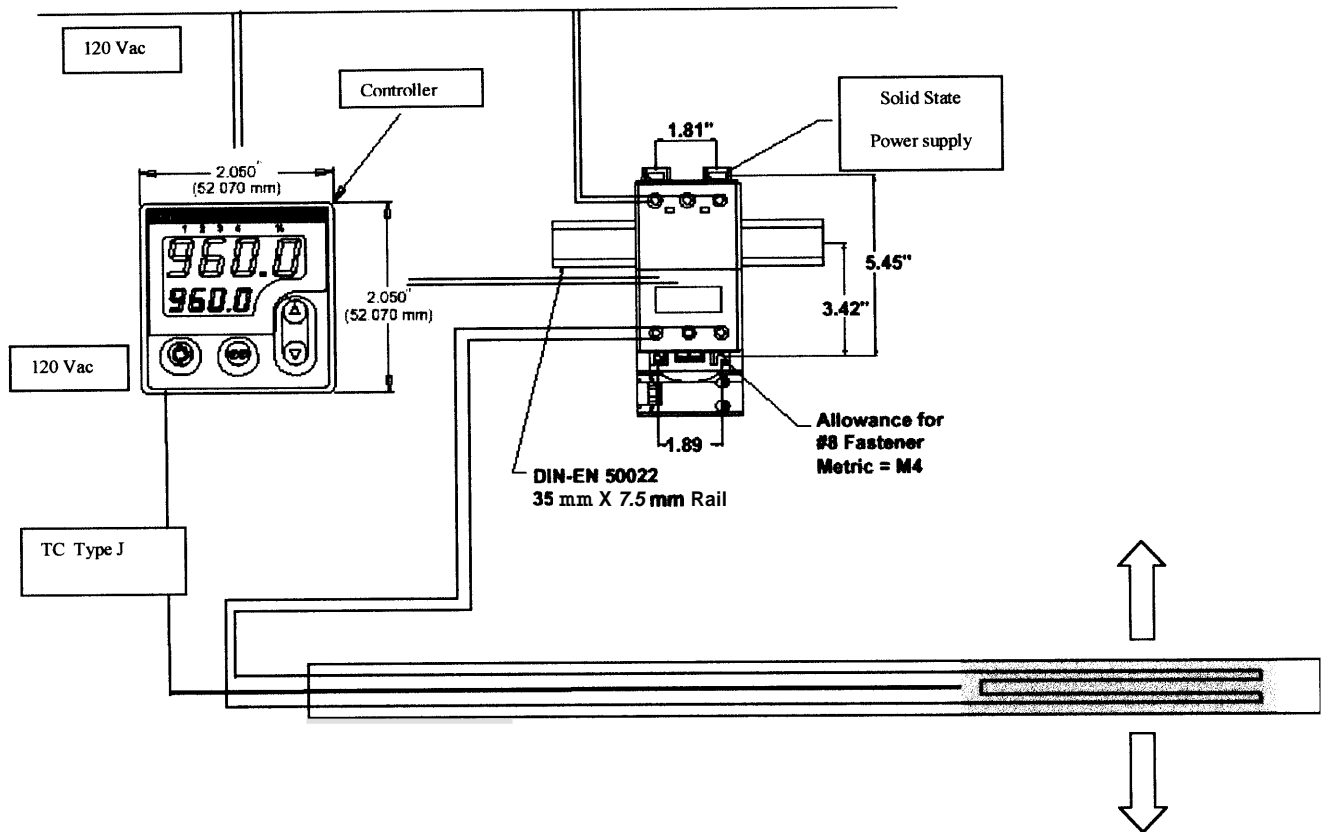


Figure 70. Control system of each heater in the preliminary sensor

Gas temperature measurement

From Newton's law of convection, we can write for the cold and the hot heater respectively:

$$Q_H = h_H \cdot S \cdot (T_H - T_G) \quad (7.9a)$$

$$Q_C = h_C \cdot S \cdot (T_C - T_G) \quad (7.9b)$$

Dividing Equation (7.9a) by Equation (7.9b) (which is always different from zero since the cold heater temperature is greater than **any** possible gas temperature in our applications), we derive the following expression:

$$\frac{Q_H}{Q_C} = \frac{h_H}{h_C} \cdot \frac{T_H - T_G}{T_C - T_G} \quad (7.10)$$

Although Equation (7.10) is theoretically correct, it does not match very well with preliminary test results gathered from actual experiments, probably because convection is not the only heat transfer mechanism involved in the measurement, though absolutely the most significant.

In a slightly different fashion, the gas temperature is obtained considering three points in a plane Temperature T versus Power Q :

1. The hot heater temperature T_H and its power Q_H
2. The cold heater temperature T_C **and** its power Q_C
3. The actual gas temperature T_G which corresponds to zero heater power

From these three conditions and again from the expressions of heat transfer, the following relationship can be obtained for air laden with water droplets:

$$\frac{T_H - T_G}{T_C - T_G} = F \cdot \left(\frac{Q_H}{Q_C} \right)^b \quad (7.11)$$

F is a coefficient depending on the ratio of the heat transfer coefficients. However, experimental tests performed at gas temperatures ranging between 100 and 250°C have shown that its value is very close to 0.9. The exponent b should be almost equal to the unity if the heat transfer mechanism was only convective. In this case Equation (7.11) reduces to Equation (7.10). But, since we believe that radiation could play a small, but not negligible, role in this configuration (see section "Influence of the radiation on the measurement" for more detail on this issue), the exponent b is introduced as a parameter in Equation (7.11). It will also be clarified that the exponent b is indeed smaller than one due to the relation between the heat flux dissipated by the heater and the temperature of the heater itself

However, the effect of radiation will be eliminated by a different orientation of the heating elements in the successive versions of the sensor.

In Equation (7.11), the temperatures, T_H and T_C , are known because they are set by the operator and they are electronically controlled. The powers Q_H and Q_C are easily obtained from the formula $Q = i^2 R$, where i is the quadratic mean value of the current flowing into the heater and R is the resistance of the heater. The resistance of the heater is measured by changing the temperature in the range 100 - 900°C, performing a measurement every 100 °C. The analysis of the experimental data

shows that the resistance has an average value of 112Ω and it ranges from 100Ω at 100°C to 124Ω at 900°C .

Therefore, Equation (7.1 1) can be rearranged in the following way:

$$\frac{T_H - T_G}{T_C - T_G} = F \left(\frac{i_H^2 \cdot R_H}{i_C^2 \cdot R_C} \right)^b = F \cdot \left(\frac{R_H}{R_C} \right)^b \left(\frac{i_H}{i_C} \right)^{2b} \quad (7.12)$$

Let us define the quantities F' and b' as:

$$F' = F \cdot \left(\frac{R_H}{R_C} \right)^b \quad (7.13, 7.14)$$

$$b' = 2b$$

Thus, it is possible to rewrite Equation (7.1 1) in a substantially similar way:

$$\frac{T_H - T_G}{T_C - T_G} = F' \left(\frac{i_H}{i_C} \right)^{b'} \quad (7.15)$$

Since the resistance of the heating elements increases with the temperature, it is clear that the ratio R_H/R_C is somewhat larger than the unity. This implies that **F' is** even closer to the unity than F , thus simplifying considerably the analysis of the data.

Several experiments are performed at the ECSAT facility using the prototype and Equation (7.15). An initial dry series of tests is used to evaluate the coefficient F' and b' : $F' = e^{-0.12} \approx 0.9$ and $b' \approx 1.7$, as the plot reported in Figure 71 clearly shows.

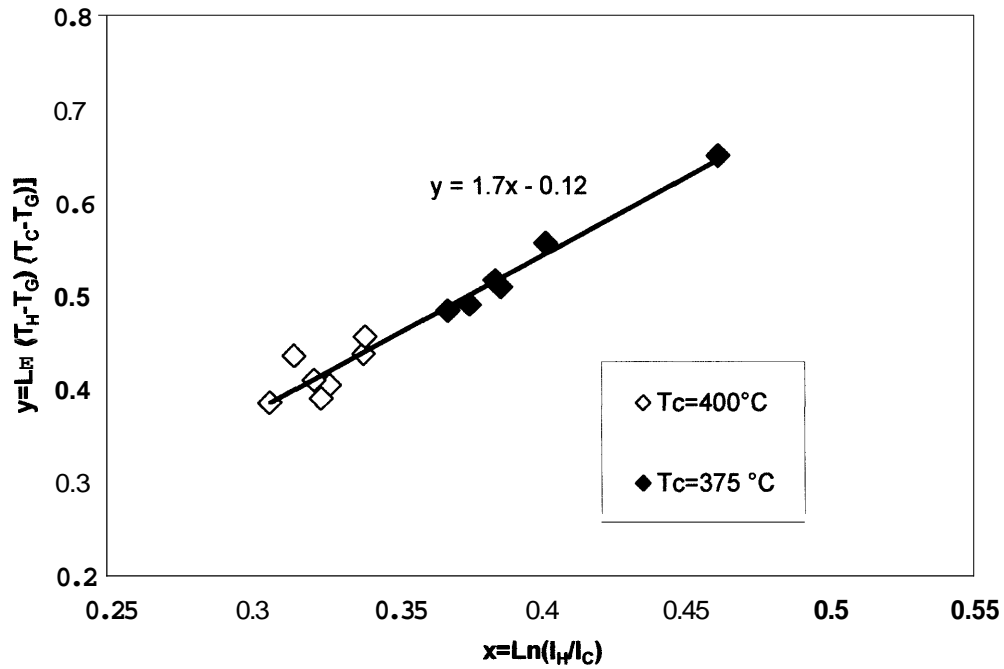


Figure 71. Dry condition results: evaluation of the constants in Equation (7.15)

The calibration curve obtained from the dry tests is utilized to test the sensor in presence of water droplets into the hot gas flow. As a result, Figure 72 provides a validation of this measurement technique by comparing the sensor measurements with the gas temperature estimates obtained from a series of detailed measurements

at the ECSAT facility, for three different gas velocities. The procedure to obtain the calculated gas temperature ~~has~~ been given in Chapter 5. The error associated with the ALTEC measurements can be as large as 15 percent. However, the figure demonstrates the feasibility of the concept.

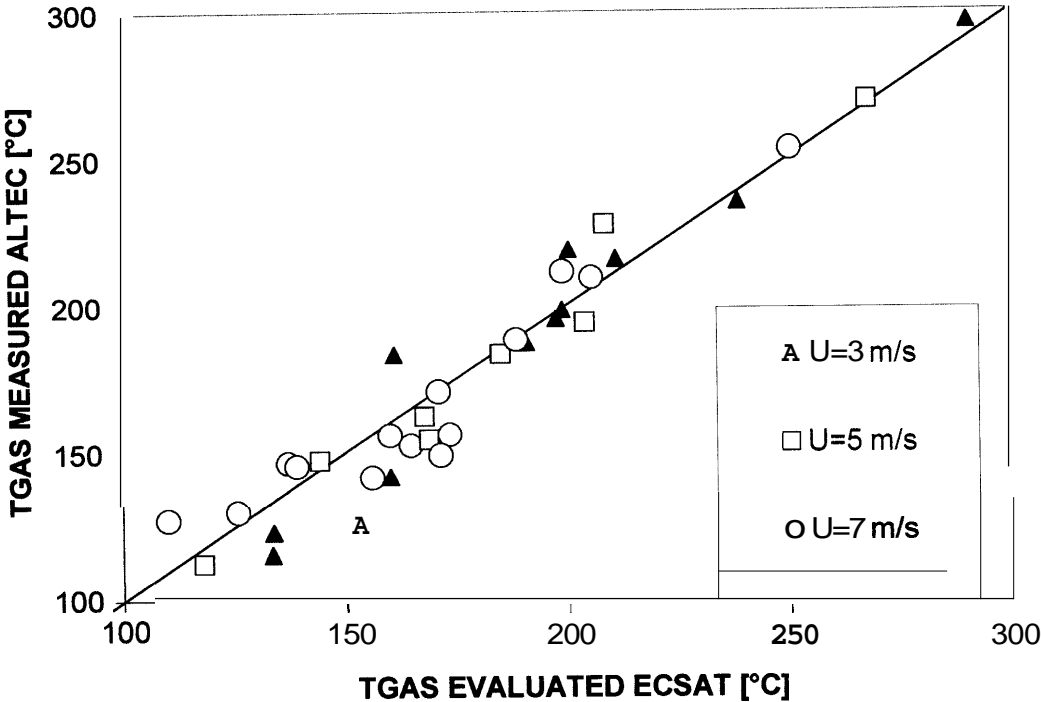


Figure 72. Comparison between two different methodologies

Gas velocity determination

The configuration of the cylindrical heater used in the prototype of the ALTEC sensor provides a solution to double-check the gas velocity measurements performed by the PTV laser technique described in Chapter 5. Being essentially a cylinder in cross-flow, maintained at constant temperature regardless of the external flow conditions, the heating element outputs a heat power Q , which obeys the Newton's law of convection (7.9). It is therefore possible to obtain the convective heat transfer by dividing the heat power Q by the surface of the heater and the temperature difference between cylinder and gas. The velocity can finally be obtained through correlations for the Nusselt number versus Reynolds number available in the literature. For a 9.3 mm diameter cylinder in cross-flow, in our range of applications, the Reynolds number ranges from 600 to 2000. The heater is maintained at a relatively low temperature (400 °C) in order to avoid significant heat transfer by radiation.

A comparison of the values obtained by this technique and the data estimated by the PTV methodology is presented in Figure 73. Tests in both dry and wet conditions are performed. The agreement is very satisfactory and the average error is smaller than 5%. The points farthest away from the solid line in the plot are the runs conducted in wet conditions where some heat transfer enhancement effect by the water droplets on the heating element is likely to occur (~ 4%). This technique (basically Constant Temperature Anemometry, CTA) may be used as a simpler way to measure the **gas** velocity at the test section of the ECSAT facility.

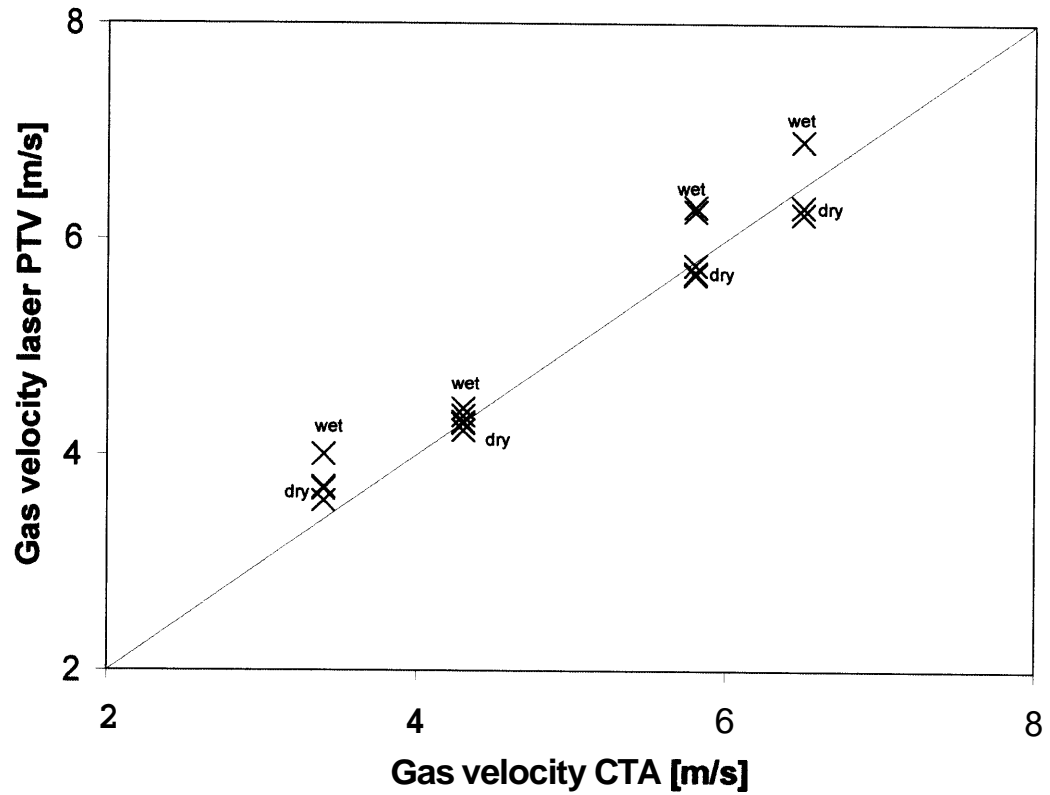


Figure 73. Comparison between the results obtained with the CTA and the PTV technique

INFLUENCE OF RADIATION ON THE MEASUREMENT

At this point, we need to quantify the influence of the radiative heat transfer with respect to the convective heat transfer dissipated by each heater.

By considering the expression for the radiation between two bodies at temperature T_H and T_C (K) ($T_H > T_C$) and the expression for a small cylinder in a large cavity, the ratio between the radiative and the convective heat transfers can be evaluated as:

hot heater)

$$\frac{Q_{\text{rad}}}{Q_{\text{conv}}} = \frac{\frac{\sigma \cdot S \cdot (T_H^4 - T_C^4)}{\frac{1}{F_{H,C}} + 2 \frac{(1 - \epsilon_{\text{rad}})}{\epsilon_{\text{rad}}}} + \sigma \cdot S \cdot \epsilon_{\text{rad}} \cdot (T_H^4 - T_G^4)}{h \cdot S \cdot (T_H - T_G)} \quad (7.16h)$$

cold heater)

$$\frac{Q_{\text{rad}}}{Q_{\text{conv}}} = \frac{-\frac{\sigma \cdot S \cdot (T_H^4 - T_C^4)}{\frac{1}{F_{H,C}} + 2 \frac{(1 - \epsilon_{\text{rad}})}{\epsilon_{\text{rad}}}} + \sigma \cdot S \cdot \epsilon_{\text{rad}} \cdot (T_C^4 - T_G^4)}{h \cdot S \cdot (T_C - T_G)} \quad (7.16c)$$

o is the Stefan-Boltzman constant ($5.67 \cdot 10^{-8} \text{ W m}^{-2} \text{ K}^{-4}$), $F_{H,C}$ is the sight factor between the two heaters and S is the surface area of a heater. The diameter of each heater is equal to 9.3 mm and the length of the heating surface is almost 120mm.

Consider a test with gas velocity of 7 m/s, gas temperature of 180°C and temperature of hot and cold elements equal to 525 °C (798 K) and **400 °C (673 K)**, respectively. Let us assume conservatively a sight factor of 0.2 and a value for the emissivity of the heater surface equal to 0.2 (which is above the value for a metallic surface at these temperatures, especially considering that the heaters are gold

plated). Equations (7.16) suggest that the radiative heat transfer accounts for about 20 % and 6 % of the convective heat transfer, for the hot and cold heater respectively. In particular, for the hot heater, the radiative heat exchange between the two heaters accounts for only 4% of the convective heat transfer, while the radiative heat exchange to the surroundings accounts for 16%. The smaller influence of radiation on the cold heater derives from the balance between the radiative heat transfer to the surroundings (11 %) and the radiative heat transfer from the hot heater (5%).

Experimental results obtained exposing the heaters in two different arrangements are reported in Table 11. The first column refers to experiments performed by exposing one heater in the hot air-flow. This is likely to provide the value of one of the two heat transfers by radiation (precisely, the second term in the nominator of (7.16)) and an indirect measure of the mutual influence of the heaters when they are exposed together. This is the case reported in the second column, which confirms the suggestion that the radiation plays a not negligible role in the overall heat transfer. Consider the last row of the table: as expected, the radiative energy transfer with respect to the convective increases for the hot heater if the heating elements are exposed to the hot gas flow simultaneously. In fact, the hot heater has to provide additional power to maintain its temperature constant, since, according to Equation (7.16h), it loses radiative heat flux to the cold heater. Conversely, the cold heater is less affected by radiation in a double-heater arrangement since the net contribution of the two radiative heat fluxes in Equation (7.16c) is almost zero.

However, a better configuration and a smaller size of the two heating elements will improve significantly the operation of the ALTEC sensor and reduce the error committed in the measurement. Rearranging the two heating elements in-line will eliminate the radiative heat transfer between the heaters. **Also**, reducing the diameter of the elements will lower the heat transfer to the surroundings, since:

- the radiative heat power Q_{rad} depends linearly on the diameter of the heaters,
- the convective heat power Q_{conv} depends on the square root of the diameter.

Hence, the convective heat transfer will decrease less than the radiative heat transfer if a smaller diameter of the heating elements is used.

	One heater (180 °C, 7 m/s)	Two heaters (180 °C, 7 m/s)
Heat flux measured (W)		
hot heater (525 °C)	108	116
cold heater (400 °C)	62	60
Heat flux by convection' (W)		
hot heater (525 °C)	90	94
cold heater (400 °C)	60	60
Relative importance rad./conv.		
hot heater (525 °C)	20%	23%
cold heater (400 °C)	~ 2%	~ 0%

INTERMEDIATE DESIGN OF THE SENSOR

The intermediate design of the sensor features ~~an~~ in-line assembly of the two heating elements on the same longitudinal axis. This results in a more flexible and effective geometry, which enables the measurements of the gas temperature for flows orthogonal to the sensor axis. It means that the gas flow can approach the Sensor from almost 360° in the orthogonal plane (the support structure does not shadow the heater elements). Also, the diameter of the heating elements is reduced to 0.2 mm. Advantages of this improved configuration are:

1. The elimination of heater-to-heater radiative exchanges that were present in the preliminary arrangement
2. The reduction of the influence of the water droplets over the heat transfer between cylinder and gas
3. The reduction of the radiative heat transfer to the surroundings
4. The reduction of the sensor response time from several minutes to few Seconds

The two principal components of the sensor are the electronic circuit and the measurement ~~sensor~~. A wet temperature sensor is also needed to implement the reading of the water volumetric fraction and it will be described in the last sections

of the chapter. The ALTEC sensor consists of a support **frame** for the two platinum wires **as** illustrated in Figure **74**. Three 6.4 mm diameter copper rods are curved and joined together so that their extremities are equally distant from each other. The spacing is equal to the platinum wires length (30 mm). The wires are attached to the tips of the three rods. Temperature-shrinking Teflon tubing insulates the copper rods from each other. Similarly, another temperature-shrinking Teflon tubing keeps the overall sensor assembly together. The heating elements are two identical platinum wires of 0.2 mm in diameter.

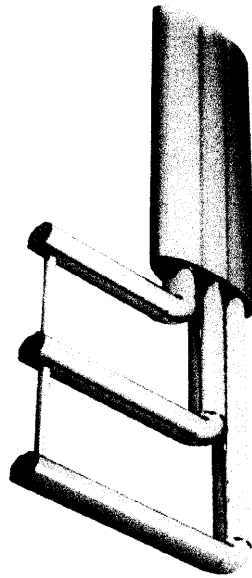


Figure 74. Intermediate design of the sensor - supporting frame

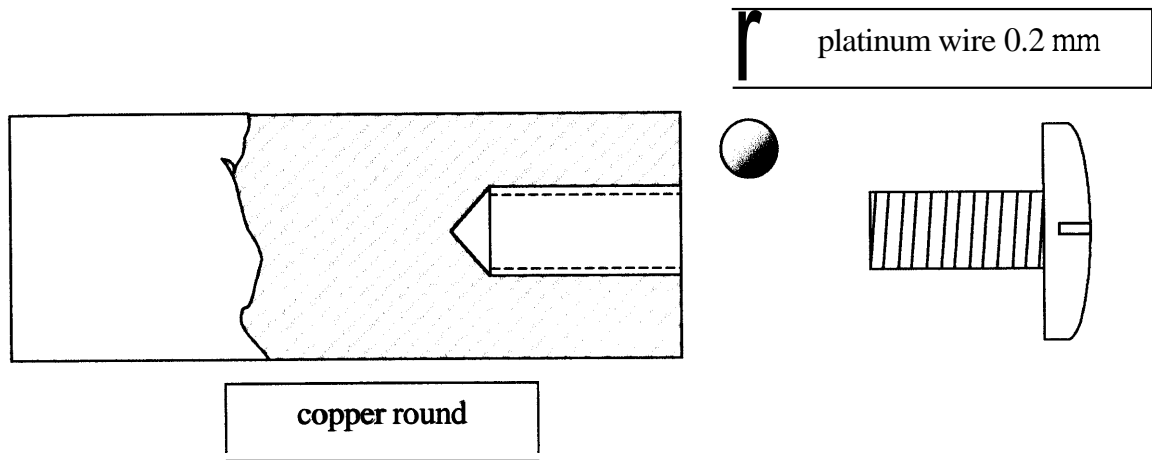


Figure 75. Detail of the connection between the wire and the copper round

Control system

A typical arrangement to control a single heater temperature ~~has~~ been designed by Rule (1997). We elaborated this scheme and adapted to the dual heater configuration. Figure 76 illustrates the resulting wiring scheme. Resistor BS is introduced in the circuit since we need the wires to be at different temperatures T_H and T_C , $T_H > T_C$. All the components in the circuit have constant resistance, except the platinum wires.

The control system maintains the resistance of the overall element B constant by varying the current flowing into the bridge and the voltage at the top of the bridge. Theory suggests that the resistance of element B is constant when the difference of voltage between point E and F is zero, since the resistance of the components on the other legs of the bridge is constant.

Suppose that the bridge is balanced. In this situation, points E and F are at the same voltage and the power transistor supplies only the current necessary to the heaters to maintain their temperature. The operational amplifier monitors the voltage difference between point F and point E, ΔV_{EF} . If a change in the gas temperature or gas velocity occurs, the operational amplifier outputs a signal V_O proportional to the difference of voltage ΔV_{EF} . The power transistor reacts to the signal V_O by generating enough current to reach a new equilibrium point.

In this way, the control circuit maintains the resistance of element B constant, whatever the boundary conditions are, at least within the power capabilities of the power transistor and the power rating of the resistors in the circuit.

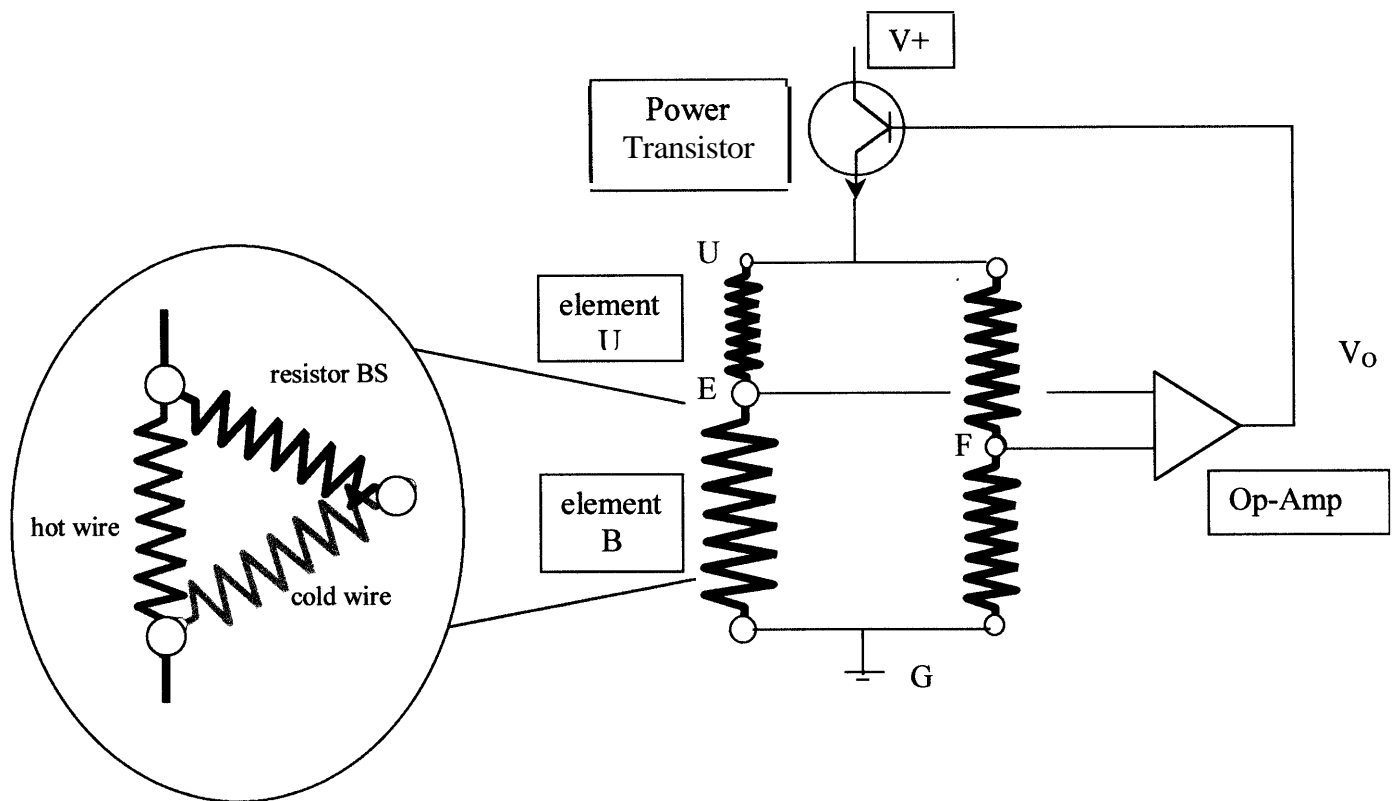


Figure 76. Control wiring scheme

Figure 77 shows a distinct benefit obtained with this control strategy. The figure represents the behavior of the heater temperatures as the gas temperature changes. In the figure, the trends are calculated as shown in the following section. Note that the resulting cold heater temperature is in between the hot heater temperature and the gas temperature. This means that the power ratio for the two heaters remains nearly constant. This is a very important point since the ratio of the heat transfer

coefficients for the two heaters becomes nearly constant over a wide range of gas temperatures.

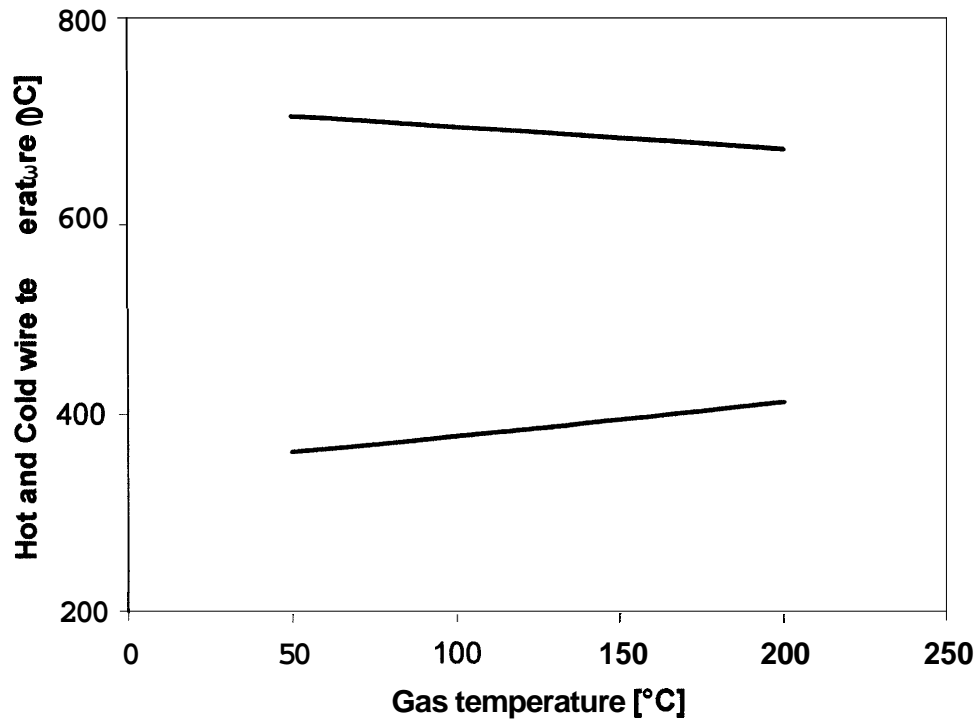


Figure 77. Heaters' temperature versus the hot gas temperature (calculated values)

Further, by keeping the cold heater temperature equally distant from the hot heater temperature and from the gas temperature, the optimal accuracy in the sensor measurements is achieved.

Measurement theory

Consider a cylindrical heater positioned in cross flow. For temperatures above 300 °C, the power required to maintain the heater at a given temperature above the gas temperature, in dry and wet conditions, shows similar trends indicating that the evaporative cooling effect is not a factor. For temperatures below 300 °C, the heater in wet conditions must supply additional power to evaporate the water depositing on its surface. The reason for this behavior is that the Leidenfrost transition occurs at about 280 - 300 °C and the water droplets do not wet the surface for temperatures above the transition.

Two identical heaters consisting of platinum wire are kept above the Leidenfrost transition, at different temperatures from each other. The energy balance for each platinum wire can be written as:

$$\frac{\Delta V^2}{R} = h \cdot S \cdot (T - T_G) \quad (7.17)$$

The typical arrangement for controlling a double wire component (element B) is essentially a Wheatstone bridge, with an operational amplifier whose output is proportional to the voltage difference between points E and F shown Figure 76. The operational amplifier controls a bipolar gate power transistor so that the ratio of the resistances on the left side of the bridge is constantly equal to the ratio of the

resistances on the right side of the bridge. By insuring that there is no voltage difference between points E and F, the controller maintains the overall resistance of the leg EG to a set value chosen identical to the resistance R_U . Also, the resistance of the element BS is chosen equal to R_U . Introducing the variable w as the ratio of the voltages across the cold heater and the resistor BS, one obtains:

$$\frac{\Delta V_C}{\Delta V_{BS}} = \frac{R_C}{R_U} = w \quad (7.18)$$

The electrical resistance of a platinum wire is a linear function of its temperature, $R = \alpha \cdot T + \gamma$. If T is measured in Celsius degrees, the coefficients α and γ are given respectively by:

$$\alpha = 0.003927 \cdot R_{20} \cdot l \quad (\text{Ohm}/^\circ\text{C}) \quad (7.19)$$

$$\gamma = R_{20} \cdot l - 20 \cdot \alpha \quad (\text{Ohm}) \quad (7.20)$$

where l is the length of the wire expressed in cm and R_{20} is the resistance of platinum per unit length of wire, expressed in Ohm/cm, at 20°C . R_{20} depends only on the diameter of the wire. Hence, Equation (7.18) becomes:

$$\frac{\alpha T_C + \gamma}{R_U} = w \quad (7.21)$$

Solving Equation (7.21) with respect to the temperature of the cold wire, we obtain the following relationship:

$$T_C = \frac{R_U \cdot w - \gamma}{\alpha} = \frac{R_U}{\alpha} \cdot w - \frac{\gamma}{\alpha} \quad (7.22)$$

Do note that, from Equations (7.19) **and** (7.20), the ratio $\frac{\gamma}{\alpha}$ is a constant equal to 234.6 °C for the platinum.

Similarly, by recalling that the overall resistance of the leg EG is equal to R_U , one can relate the temperature of the hot wire to w as follows:

$$T_H = \frac{R_U}{\alpha} \frac{w+1}{w} - \frac{\gamma}{\alpha} \quad (7.23)$$

By assuming that the heat transfer coefficient is similar for both heaters (i.e. h does not change with temperature, **as** shown previously in the thesis), Equation (7.17), written for both heaters, yields the following ratio:

$$\frac{w^2}{w+1} \frac{\Delta V_H^2}{\Delta V_C^2} = w+1 = \frac{T_H - T_G}{T_C - T_G} \quad (7.24, 7.25)$$

By combining Equations (7.22), (7.23) and (7.25), one may obtain the temperature of the gas as:

$$T_G = \frac{R_U}{a} \left(w + 1 - 1/w - 1/w^2 \right) - \frac{\gamma}{a} \quad (7.26)$$

Equivalently, in the range of voltage ratio w between 1 and 1.4 (suggested by the experiments and calculations), the following relation approximates the expression in parenthesis with the necessary accuracy (see Figure 78):

$$g(w) = w + 1 - 1/w - 1/w^2 \approx 2.7685w - 2.6569 \quad (7.27)$$

Consequently, Equation (7.26) assumes the following form:

$$T_G = 2.7685 \frac{R_U}{a} w - \frac{\gamma + 2.6569 R_U}{a} \quad (7.28)$$

A number of important observations can be made by the analysis of Equations (7.22) and (7.28):

- From Equation (7.22), it is evident that, if we change the platinum wire diameter from d_1 to d_2 , keeping constant the length of the wire, the relationship between the temperature of the cold wire and the voltage ratio does not change if the ratio R_U/α remains the same. This simplifies significantly the design process of the

electric circuit. It is possible to maintain the ratio R_U/α constant (and the temperature of the heaters above the Leidenfrost transition) while changing the wire diameter if we change the resistance R_U (and therefore R_{BS}) proportionally to the temperature coefficient α .

- From Equation (7.28), one may notice that if the ratio R_U/α does not change while varying the wire diameter, the sensibility of the ALTEC sensor does not change. Remember that the sensibility of a measurement device is proportional to the derivative of the calculated quantity (T_G) with respect to the measured one (w).

Therefore, we can conclude that it is possible to decrease the current flowing into the circuit by simply using a thinner wire, without losing accuracy in the measurement process and remaining above the Leidenfrost transition with both the heating elements. However, other practical restrictions limit the choice to wire diameters that are not too small.

As one can see from Equation (7.28), the relationship between the gas temperature and the voltage ratio does not depend either on the gas velocity or the presence of the water droplets in the hot air flow (as long as both heaters are above the Leidenfrost transition). An increase of the gas velocity translates into an increase of the voltage applied to the bridge in such a way that all the voltages in the bridge rise proportionally to each other. This explains why the ratio w is not affected by changes in the velocity as well as its relationship with the gas temperature. The

presence of water droplets causes a similar effect on the voltages of the bridge. This is a tremendous simplification since ~~just~~ one calibration curve is needed.

Figure 78 confirms that the functional shown in parenthesis on the right hand side of Equation (7.28) is almost linear in the range of interest, $1.1 < w < 1.4$. Therefore, the gas temperature can be obtained as:

$$T_G = \tau_1 \cdot w + \tau_2 \quad (7.29)$$

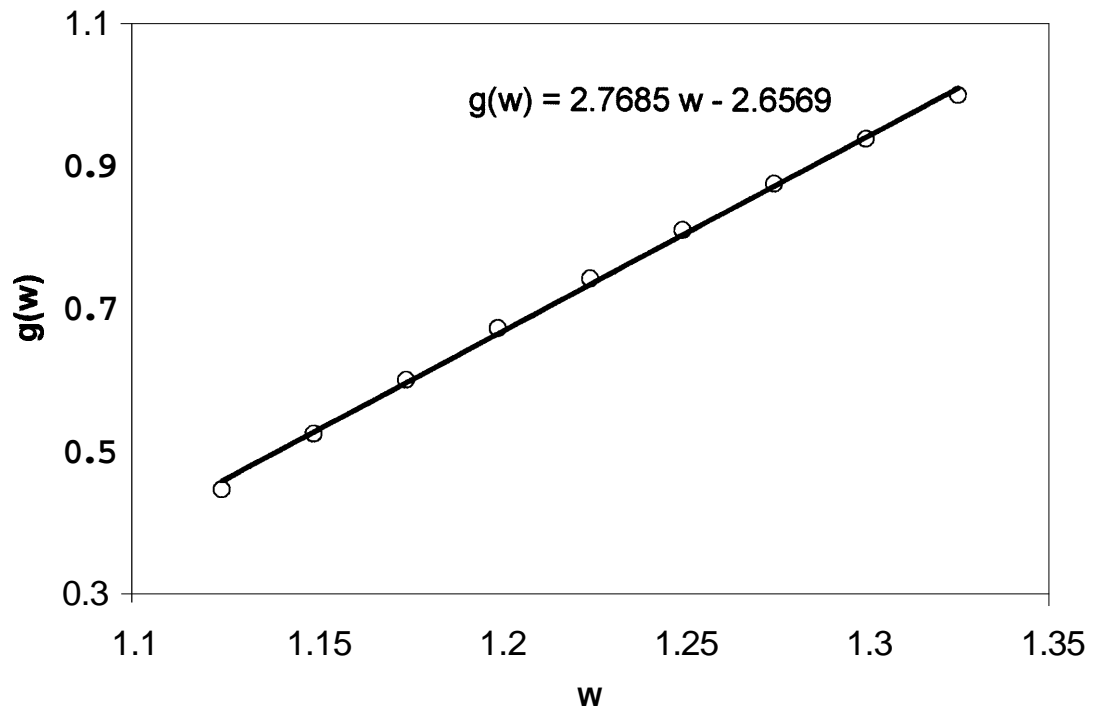


Figure 78. Linearity of $g(w)$

The value of the slope τ_1 in Equation (7.29) can be determined experimentally for a variety of conditions. For this reason, a large number of tests are performed both with and without water droplets. The results are plotted in Figure 79. The gas temperature is read directly with a thermocouple for the *dry* tests and it is estimated from the ECSAT facility measurements for the wet tests as previously described. The slope τ_1 is consistent for all tests and its numerical value is $990 \pm 110^\circ\text{C}$.

A single point calibration is used to determine the parameter τ_2 in Equation (7.29). The test is performed in *dry* conditions by exposing the ALTEC sensor to hot gases. With the previous information, the calibration is completed to yield:

$$T_G = 990 w - 1060 \quad (7.30)$$

Figure 79 shows that the data fall in a band $\pm 10^\circ\text{C}$ about the calibration curve represented by the solid line.

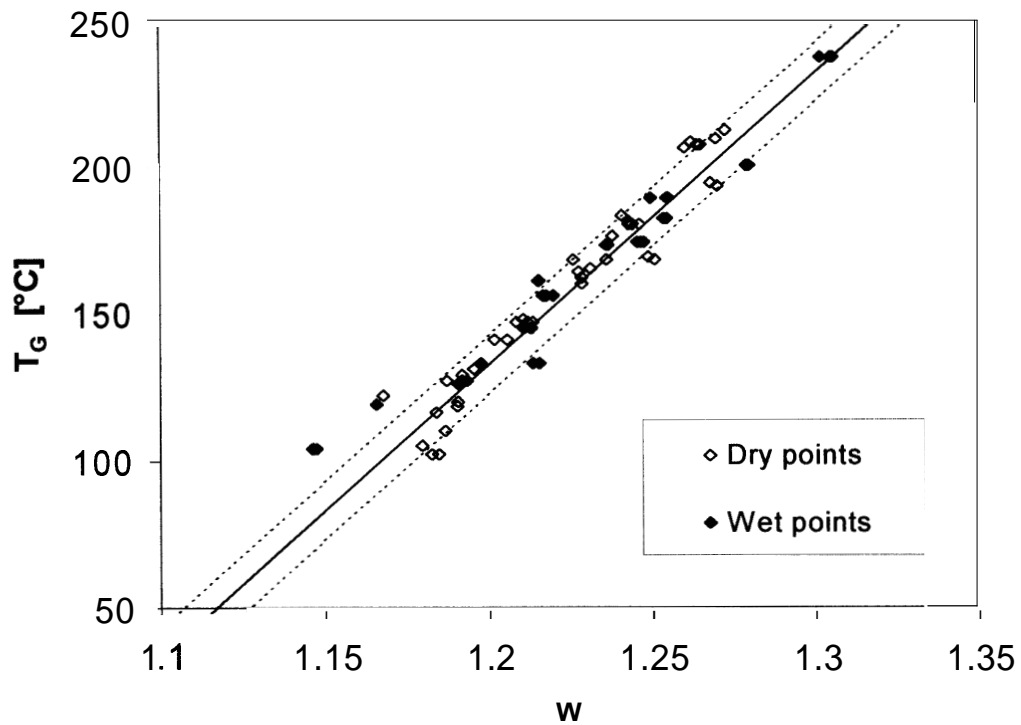


Figure 79. Calibration curve: dry and wet results

At low temperatures, the flow velocity measured at the test section of the ECSAT facility is quite high compared to the typical ceiling jet velocity expected in a fire situation. The reason is the necessity of maintaining an adequate one-dimensionality of the flow downstream the ECSAT orifice. The minimum velocity is about 3 m/s. Alpert (1972) provides a functional relationship between the ceiling jet velocity and temperature in a fire situation, given the ceiling height and the radial distance from the impingement point of the fire plume on the ceiling. Figure 80 depicts the velocity-temperature relationship for various values of the dimensionless ceiling height H^* , defined as the ratio of the ceiling height by the spacing between

the sprinklers. Considering that the sprinklers are placed 3 m from each other, these ratios correspond to ceiling heights ranging from 6 m to 9 m. The ALTEC experimental conditions are also shown in the figure. The error bar around each experimental point represents two standard deviations.

It is important to consider that in a real fire scenario it is unlikely to observe velocities of 3 m/s in absence of a hot plume. Therefore, in the ECSAT facility, the ALTEC sensor occasionally performs at unusually high-flow-low-temperature combinations that are not observed in real fire situations. These conditions are off-design and result in inaccuracies for the low values w (shown in Figure 79) corresponding to these situations since the sensor requires an unusual high power output.

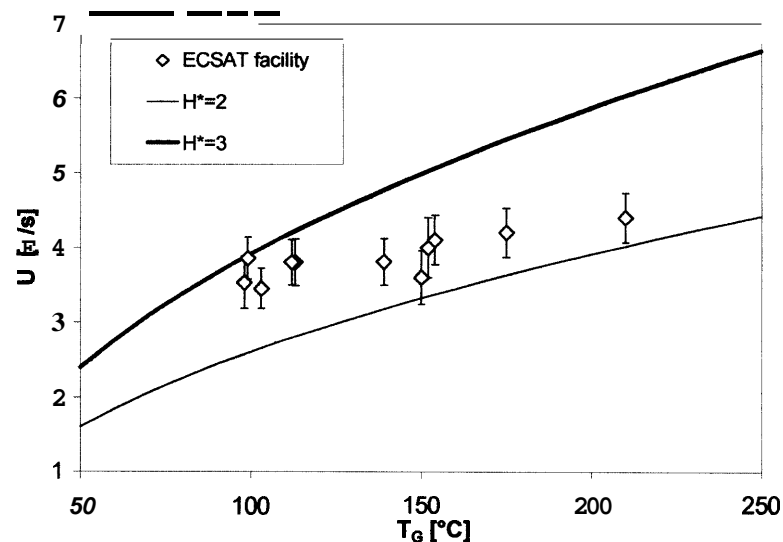


Figure 80. Velocity-temperature correlation for a natural convection plume versus the ECSAT facility operating conditions

Design feasibility

The behavior of the control board and the sensor is simulated through a software algorithm implemented in Engineering Equation Solver (EES). The lines of the code are reported in Appendix 3 for the sake of completeness. Basically the program couples the heat transfer exchanges between the wires and the gas flow with the electrical equations written for every component of the bridge. This **has** been a major tool in the initial development of the sensor design because it is possible to perform a sensitivity analysis of the sensor behavior to changes of several parameters influencing the accuracy of the sensor. The principal quantities that play a major role on the circuit characteristics are:

- The length and the diameter of the platinum wires.
- The value of the resistor U (and therefore the value of R_{BS}).
- The ratio between the top and bottom resistances of the right side of the bridge.

The set of optimal values for these quantities is chosen trying to achieve the best sensibility and accuracy of the instrument, compatibly with the constraint imposed by the availability of the commercial components.

ALTEC sensor experiments

Two series of experiments are performed at the ECSAT facility. The range of gas temperatures investigated is between 100 and 250 °C, while the gas velocity is approximately within the 3 to 5 m/s interval in this case.

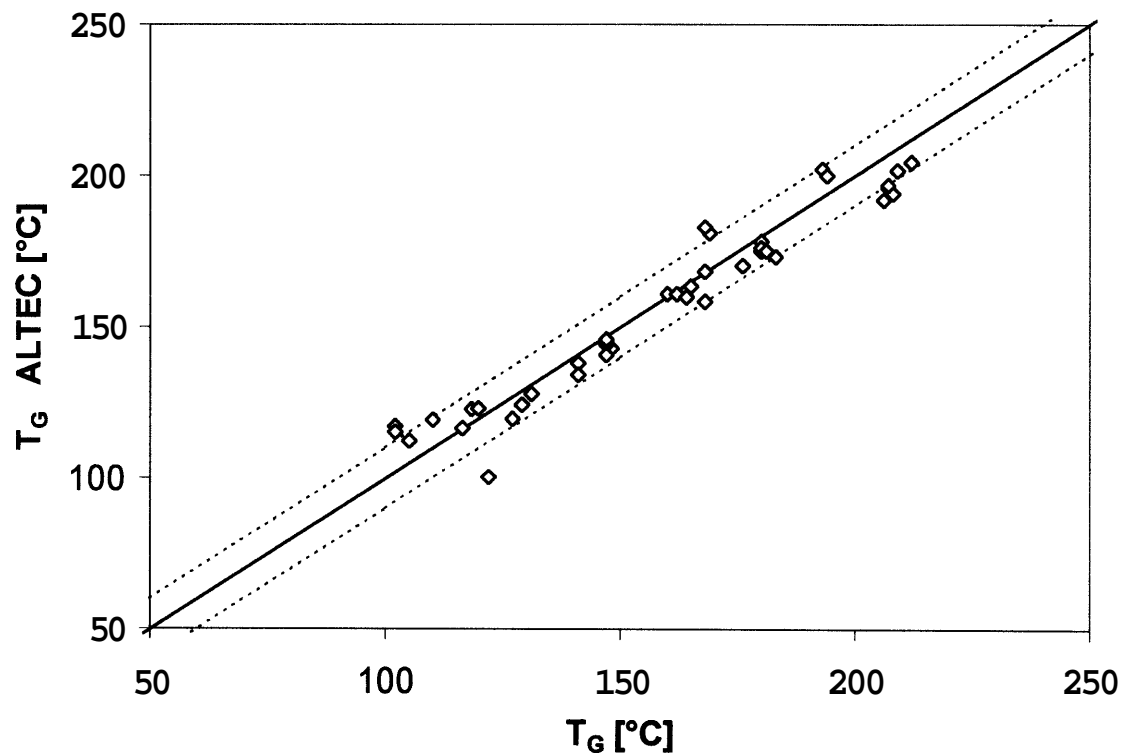


Figure 81. Comparison between the temperature measured by the ALTEC sensor and the values read by a thermocouple in dry conditions

The first set of tests is performed in dry conditions and the ALTEC readings are compared with the ones obtained from a K-type thermocouple. Figure 81 illustrates the results. Most of the data fall within a band ± 10 °C about the exact value. There are some slight discrepancies at temperature less than 130 °C. This is expected due to the high power output required by the sensor as previously explained. Figure 81 provides a validation of this measurement technique by comparing the sensor measurements with the gas temperature obtained experimentally. The figure demonstrates the effectiveness of the sensor. The average error in the range of gas temperature between 100 °C and 200 °C is 7 percent.

A second series of tests is performed in wet conditions. The procedure to evaluate the temperature of the gas in presence of water droplets has been explained in Chapter 5. The gas temperature determined with this approach is identified as the ECSAT temperature. Figure 82 compares the ECSAT temperature with the ALTEC temperature obtained from the sensor. Also in this case, slight discrepancies are observed for temperatures below 130 °C. The average error in the range of gas temperature between 100 °C and 200 °C is 5 percent. The results shown in the figure clearly demonstrate the insensitivity of the ALTEC sensor to the water droplets and the accuracy of the gas temperature readings.

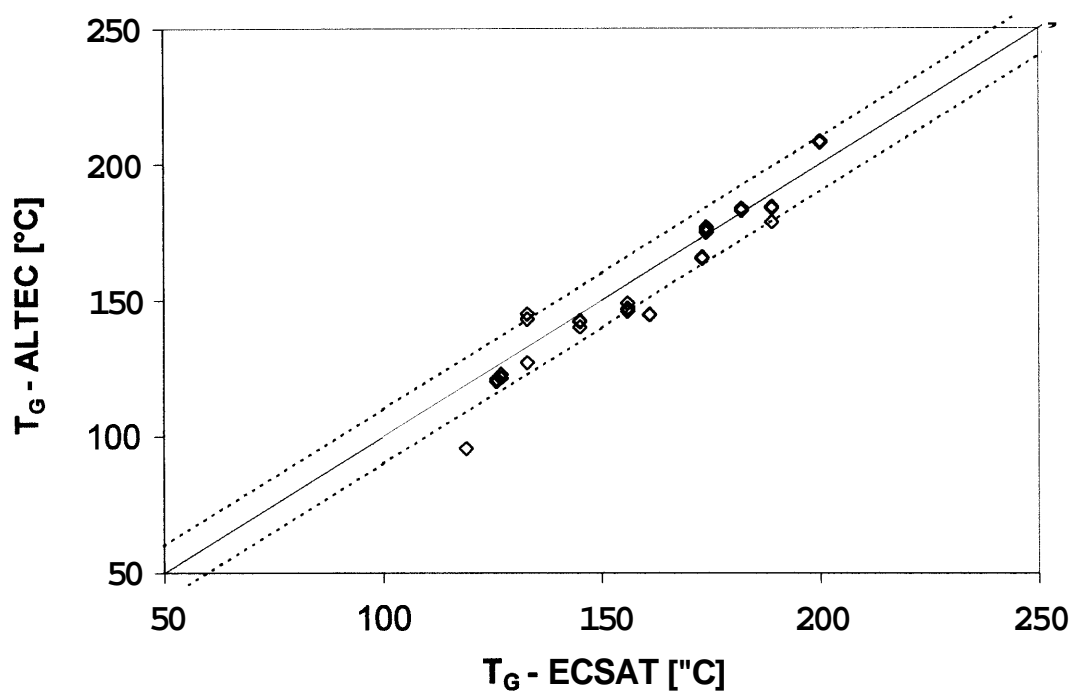


Figure 82. Temperature comparison in wet conditions

Figure 83 shows the temperature of the hot heater and the cold heater versus the **gas** temperature. The heater temperature traces are linear functions of the heater resistance. Therefore, the linearity of the temperature trace of the cold heater confirms the validity of the assumptions made in the measurement theory section.

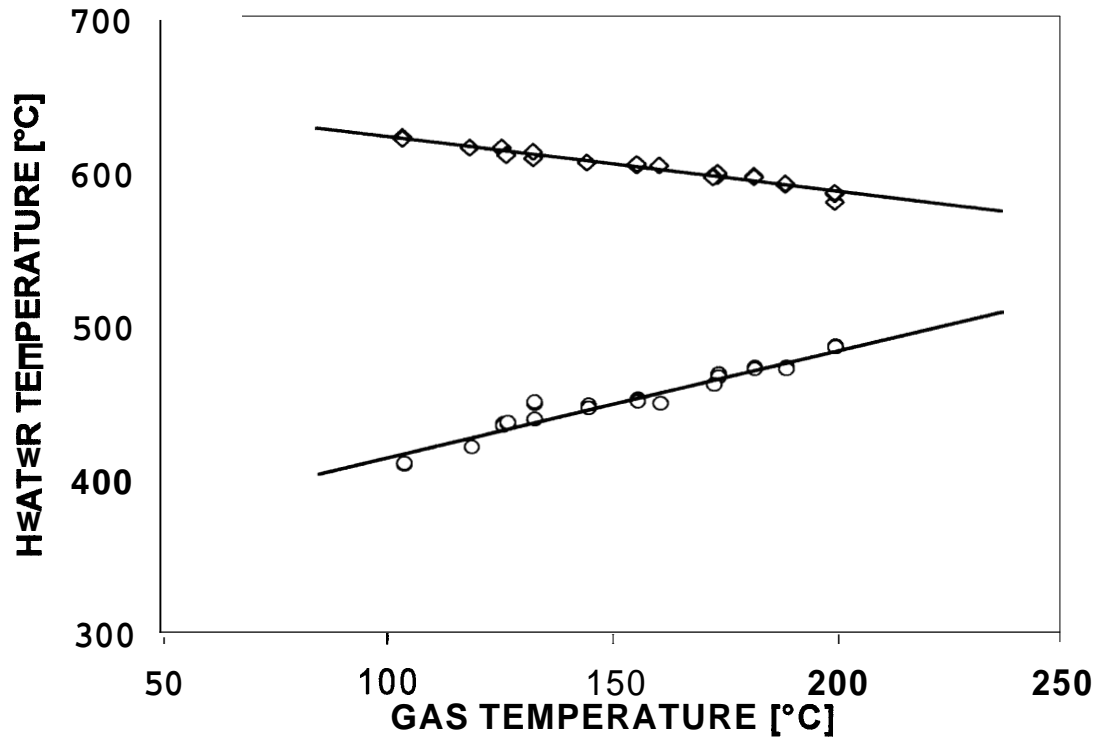


Figure 83. Wires temperature versus the gas temperature (experimental results)

WATER VOLUMETRIC FRACTION MEASUREMENT

As previously shown, we can relate the water droplet volumetric fraction β to the temperature difference between the hot gas and the temperature detected by a wetted sensor T^W . The sensor, in this last case, is a thermocouple inserted in a cylinder. The cylinder is a common pipe of brass or copper with a high aspect ratio. The thermocouple is inserted along the axis and the space between the thermocouple and

the internal wall of the pipe is filled with conductive mixture. The diameter of the cylinder influences both the measurement resolution and the collection efficiency κ in opposite ways (see Chapter 3). Therefore, the choice of the diameter of the cylinder must be carefully optimized in order to minimize the error related to the temperature measurement. The gas velocity U is also necessary to obtain the volumetric fraction as shown in the following relationship:

$$\beta = \frac{T_G - T^W}{\hat{C}\sqrt{U \cdot d}} \quad (7.31)$$

Note that similar measurements with the available technology would require complex and expensive laser-based optical methods and significant sample statistics to obtain the same measure. From (7.31), it is clear that the error associated with the measurement of the water volumetric fraction depends mostly on the inaccuracy on the determination of the constant \hat{C} (13 %) and the error associated with the determination of the gas temperature (8%). The error associated with the measurement of the gas velocity accounts only for 5 percent, since the velocity appears under the square root operator.

Equation (7.31) shows that for identical flow conditions (U and β constant), the difference of temperature is proportional to the square root of the sensor diameter. The experimental results, gathered from several tests with cylinders of different outside diameter and reported in Figure 84, show a slope of 0.47 that confirms the

theoretical observations. Therefore, it seems reasonable to have a diameter of the sensor as large as possible in order to achieve a good separation between the two temperatures and consequently an increased accuracy in the determination of the water volumetric fraction. However, the diameter of the sensor affects the collection efficiency and the time response constant of the sensor, as well.

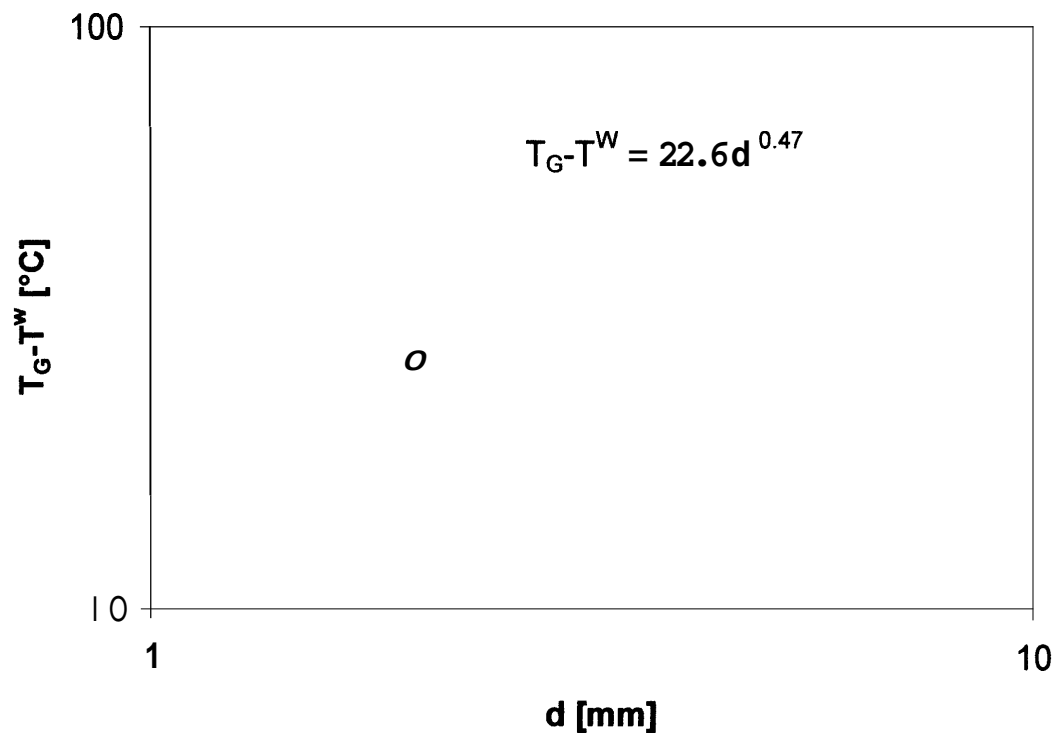


Figure 84. Dependency of the evaporative cooling on the diameter

Collection Efficiency

As the reader may remember from Chapter 3, the collection efficiency provides a measure of the fraction of droplets that cannot avoid the cylindrical obstacle and deposit on its surface.

The collection efficiency has been calculated for a wide range of the inertia parameter Z and the results have been fitted analytically by the following correlation (see Chapter 3):

$$\kappa = \frac{Z^{1.08}}{Z^{1.08} + 8.80} - 0.04 \quad (7.32)$$

Figure 85 shows the fitted curve for the collection efficiency versus the diameter of the cylindrical Sensor under conditions typical of a fire scenario. Two observations can be drawn:

- The collection efficiency approaches an asymptotic value of 0.97 for small sensor diameters.
- The collection efficiency decreases if the diameter of the cylinder increases.

Therefore, this constraint is conflicting with the results illustrated in Figure 84.

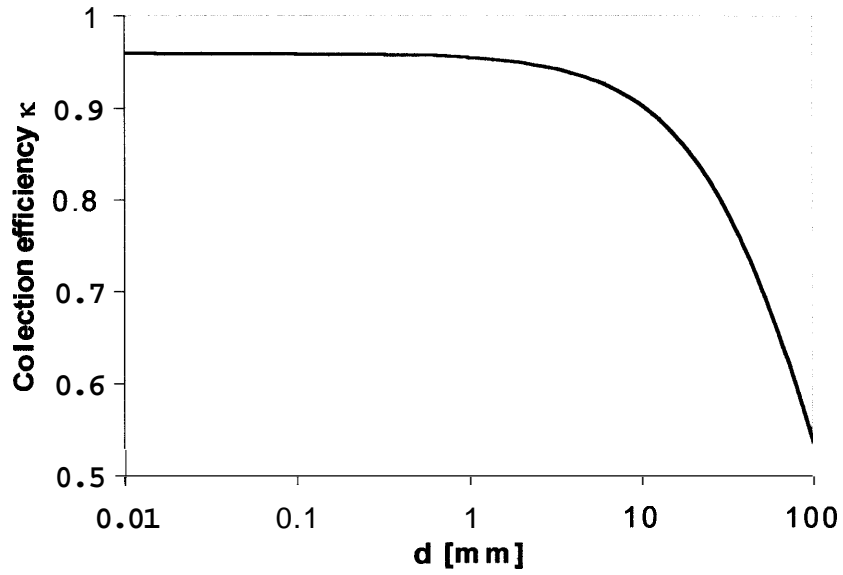


Figure 85. Collection efficiency as a function of the diameter

Sensor Time Constant

The time constant of the wet sensor can be obtained from a transient lump-capacity energy equation written as:

$$\rho_s c_s V_s \frac{dT_s}{dt} = h \cdot S (T_G - T_s) \quad (7.33)$$

By introducing the heat transfer correlation represented by Equation (3.4), the solution of Equation (7.33) yields a time constant given by:

$$\tau = \frac{\rho_S c_S v_G^{0.5}}{2.08 k_G U^{0.5} Pr^{0.37}} d^{1.5} \quad (7.34)$$

Several brass Sensors of different diameter are suddenly exposed to a *dry* gas at a fixed temperature and velocity. The time constant for each sensor is evaluated from the experiments. Figure 86 illustrates the results. The regression of the data suggests an exponent of 1.58. This finding is in reasonable agreement with the value of **1.5** suggested by the theory. The time constant constraint favors small sensor diameters if a fast response time is desirable.

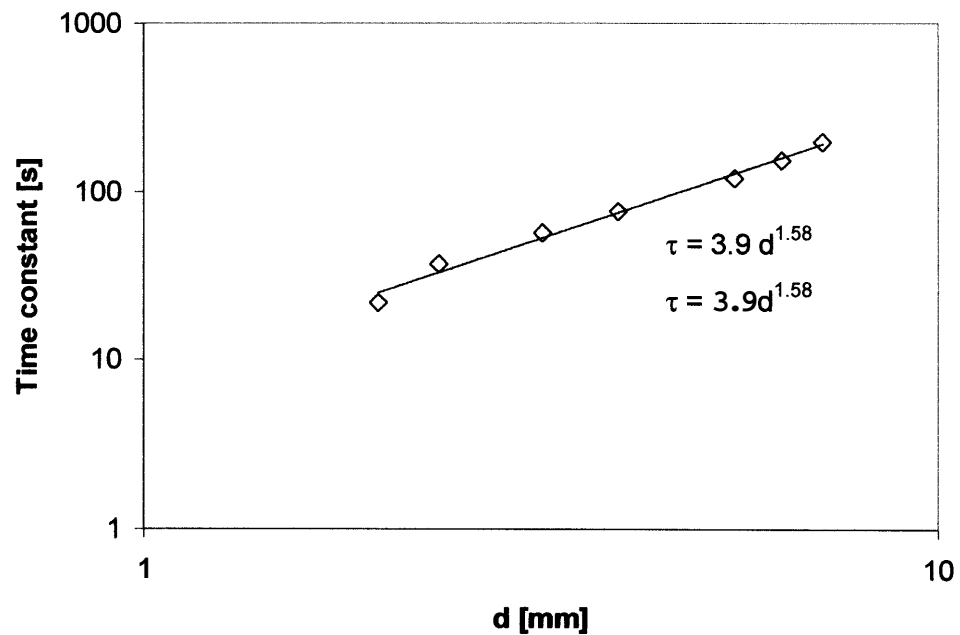


Figure 86. Time response of a cylinder versus its diameter ($T_G=150\text{ }^{\circ}\text{C}$, $U=4\text{ m/s}$)

Determination of the optimal wet sensor size

On the basis of the results previously obtained, the optimal diameter of the wet sensor can be chosen so that the time response is compatible with the time response of the ALTEC sensor. Also, the restriction to remain in the asymptotic region of the droplet collection efficiency curve is desirable, together with the best measurement accuracy possible. Note that dealing with constant collection efficiency greatly simplifies the implementation of the technique.

The ALTEC sensor time response is estimated experimentally to be 50 seconds. Consider using aluminum instead of brass for the wet sensor to achieve a faster response, while maximizing the cylinder diameter, due to the aluminum lower heat capacity. A 4.8 mm aluminum cylinder yields a time constant of about 30 seconds and collection efficiency in the asymptotic range. From Equation (7.31), the water volumetric fraction is therefore simplified as:

$$\beta \approx 0.17 \cdot \frac{T_G - T^W}{\sqrt{U}} \quad (7.35)$$

Experiments and results

Several experiments are performed at the ECSAT facility by changing gas temperature, gas velocity and spray nozzle arrangement. The procedure followed during the experiments is very straightforward:

- 1) First, a dry test is performed in order to acquire the temperature profile along the duct.
- 2) Once the data have been saved on disk for further analysis, the sprays are turned on and the new steady-state conditions are awaited.
- 3) At this point, measurements of gas velocity and water volumetric fraction are performed using the optical techniques that have been described in Chapter 5. Thirty images of the test section are taken within every measurement in order to obtain a statistical value of each quantity. These measurements are repeated three times.
- 4) The ALTEC sensor, permanently inserted in the test section, is turned on. When it reaches steady-state with the gas flow, the acquisition system is started and the data are recorded on disk. The recorded quantities are the voltage ΔV_{BS} , the voltage ΔV_C and the voltage ΔV_U .

Figure 87 compares the measurements of the water volumetric fraction obtained with the optical method (see Chapter 5 for full details) and from Equation (7.31) measuring T_G with the ALTEC sensor and T^w with the wet temperature sensor. The appropriate error bars for each technique are shown in the figure. The proposed

technique, based on the ALTEC sensor and on the wet temperature sensor measurements, provides a more precise value of the water volumetric fraction than that obtained with the optical method. Note that while the optical method requires steady state conditions and it is based on the examination of a statistically relevant number of picture frames, the new method proposed here is only limited by the response time of the ALTEC sensor.

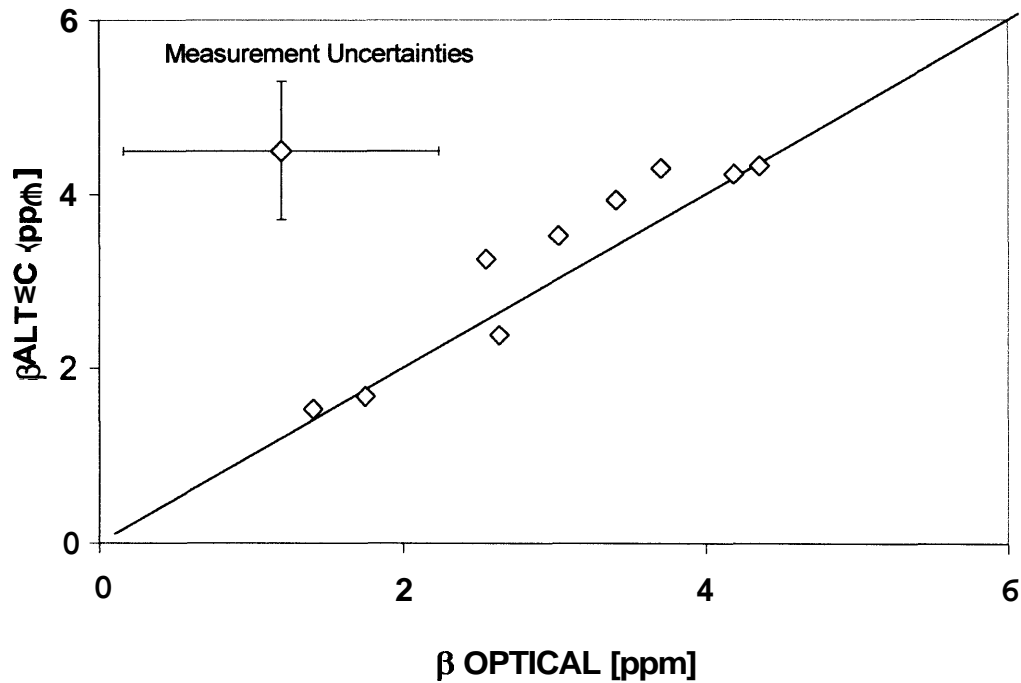


Figure 87. Experimental results for the water volumetric fraction readings

FINAL DESIGN OF THE ALTEC SENSOR

A new innovative type of controlling circuit is designed for the final version of the ALTEC sensor. A change in the design of the electronic circuit is motivated by the necessity to save more space and to compact all the functionality of the previous board and acquisition system in a single chip. The ultimate electronic board is shown in Figure 88. The micro-controller is a PIC18C452 CPU **from** Microchip Inc., selected because it has a C-compiler which runs under MATLAB IDE (Integrated Development Environment). **Also**, the CPU is compatible with other series of CPUs in case of necessity. The electronic board has a voltage regulator for the digital logic, a separate regulator for the analog circuits and a switching power supply to produce -5 V for the analog circuits. A power connector (Power in Figure 88) and a switch connection (marked **sw**) are supplied'.

The analog inputs for the micro-controller are diode clamped between 0 and 5 V. A rail to rail op-amp (National Semiconductors LMC6484) shifts and amplifies input and output signals for the analog inputs and outputs. Outputs are handled by a 12 bit DAC (Linear Technology LTC1448). The voltage is supposed to range between **-5** and +5 Volts for analog inputs and outputs.

¹ **From Private Communications with Dr. Walsh.**

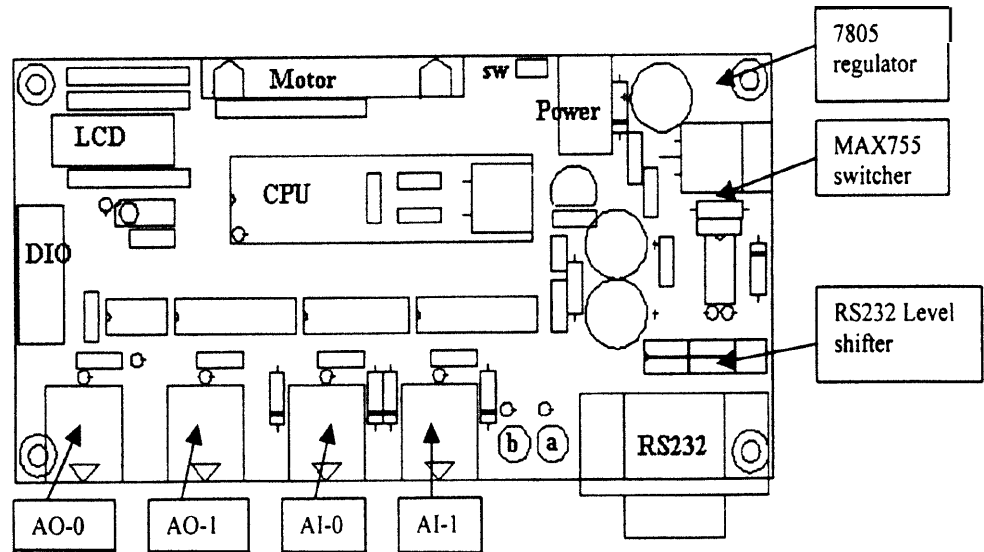


Figure 88. Final version of the control board

On the front of the board, there are four connectors. These are the analog outputs (AO) and inputs (AI) respectively. To the right there are two LEDs, **a** and **b**, a test signal and a power indicator respectively. To the right of the LED there is a mount connector which can be plugged directly into a serial port using a standard serial-port extender cable. The **LCD** (14 pin connector) connector is directly connected to the read-out, which displays two voltage differences (ΔV_H and ΔV_C), the ratio w and the estimated gas temperature T_G . Both instantaneous and running-averaged values are displayed.

Design of the board

The ~~main~~ feature of the board is to ~~maintain~~ in ~~any~~ condition the resistance of element B constant and equal to the resistance of element U. Aside from this, the additional features of the electronic board should allow for a fast and reliable acquisition of the sensor outputs. The following points have been considered in the design of the board:

1. Develop a feedback to control the temperature of the wires and to maintain it above specified minimum values.
2. Develop a system that performs a 128 point moving average filter for incoming data sampled at 10 **Hz**. The need of a moving average is required by the background noise present in the measurements and the oscillations present in the gas flow.
3. Develop a system that provides fixed-point arithmetic to convert incoming voltages to temperature.
4. Develop a system that displays incoming data on LCD. The quantities to be displayed on the LCD screen are the sensor outputs (two voltages and their ratio) and the gas temperature calculated from the calibration curve of the device.
5. Develop a system that outputs data in serial and analogic format. A direct reading of the sensor output should be available as well ~~as~~ an output for an external data acquisition system.

6. Develop a system that provides a potentiometer input and 8 position dip switch input **as** scaling factors for the temperature conversion. This feature is required since the board needs to be calibrated and the coefficients of the linear calibration curve have to be easily modified to display the correct gas temperature on the LCD screen.

No major changes are done to the supporting structure of the platinum wires. Minor, but significant (from a practical point of view) improvements involve the copper round extremity exposed to the gas flow, **as** shown Figure 89. In this new arrangement, the wire is placed below a metal clamp, so that the mounting of the wire on the support frame is much easier than with the previous solution. A better match between the copper surface and the platinum wire is achieved, as well, resulting in a lower resistance of contact. The final assembly of the ALTEC sensor is shown in Figure 90.

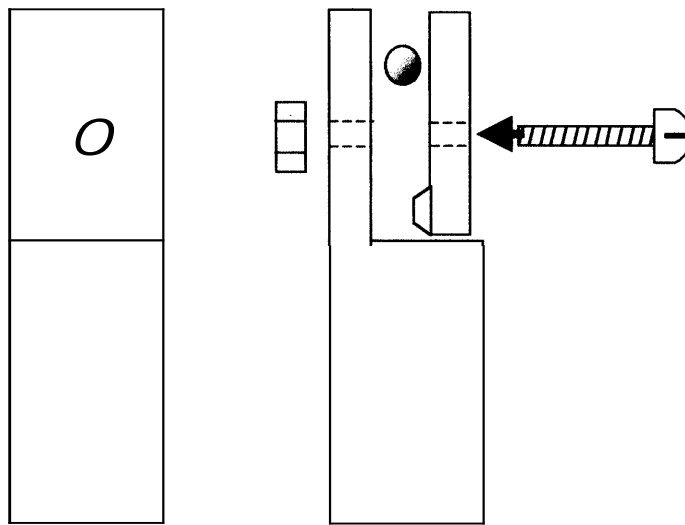


Figure 89. Modification of the wire support terminals

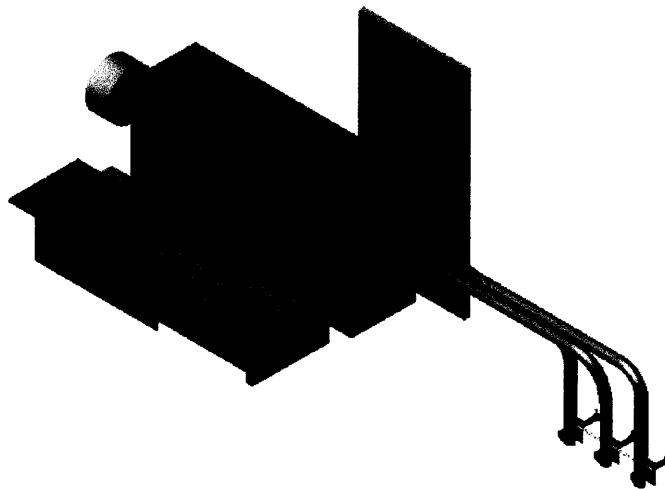


Figure 90. Final assembly of the ALTEC sensor

CONCLUDING REMARKS

The primary motivation at the base of this project **has** been to develop a device, which can easily measure the temperature and the liquid volumetric fraction of a hot gas laden with liquid droplets. The sensor may find applications in any of the following fields:

- Fire protection: several tests are performed in order to verify and certify the functioning of fire sprinklers. Although activation failures due to the presence of water droplets in the fire plume have occurred in both full-scale tests and real life situations, little progress has been done to investigate further this kind of problem. Under these circumstances, the ALTEC sensor can effectively contribute to study the sprinkler failure to activate phenomena, giving the operators a real-time monitoring of the flow characteristics. Combustion Science & Engineering, Inc., a Maryland based engineering company, has already expressed its interest to act **as** an independent consulting corporation by leasing the technology and performing on-situ measurements during certification tests. Also, Factory Mutual Research Corporation and TYCO Inc. are interested in testing the new sensor in full-scale fire experiments and possibly acquiring the technology.
- Aerospace Engineering: the ALTEC sensor can easily find applications in the cooling process of turbo-machinery blades and in the study of fuel evaporation within the combustion chamber.

- Automotive Engineering: an interesting application of the device can be the investigation of the fuel evaporation process between the point of injection and the engine cylinder inlet.
- Chemical/ Process Industry and Laboratories: further applications can be found in any process where a liquid is entrained and carried by a gas flow, such as cooling towers and multiple phases mixing.

CONCLUSIONS

The model for the prediction of the transient thermal response of a fire detection sprinkler has been extended to include the presence of water droplets in the hot gas plume. These droplets are introduced when the first sprinkler activates. The plume transports away part of the droplets, which deposit on the surrounding sprinklers. The evaporation of the droplets on the surface of the sprinkler ~~link~~ results in a cooling effect. This causes a delay in the activation of the sprinklers, that cannot be predicted by the previous model.

An experimental facility has been built at the University of Maryland to conduct small-scale experiments. The facility allows for measurements of temperature, velocity and volumetric fraction of a hot gas laden with water droplets. A first experimental campaign ~~has~~ been performed at the ECSAT facility to obtain the two quantities needed to assess the model, RTI and C . Also, the dependency of the evaporative cooling parameter C on the simulated sprinkler ~~link~~ ~~has~~ been validated. The procedure used to determine the temperature of a hot gas containing water droplets allows for an implicit validation of the optical techniques and the model parameters.

The model predictions have been compared with the experimental data gathered from tests on commercially available sprinklers. Four **types** of sprinklers have been tested under six different boundary conditions. The six conditions include various combinations of gas temperature and velocity, water volumetric fraction and sprinkler orientation. The model predictions are generally in good agreement with the experimental data, within the scatter associated with the experimental results.

Further, the evaporative cooling model has been used to design an equivalent cylindrical sensor that would simulate the behavior of a commercial sprinkler under any condition. Three sprinkler types have been tested in both *dry* and wet conditions, for two completely different situations. The corresponding simulated sprinkler links have been built and tested in the same conditions used for the sprinklers. The results compare favorably. This proves once and again the capability of the model to predict the behavior of fire sprinklers under any circumstance and may indicate its efficacy to design sprinkler arrays more accurately.

Additionally, the evolution of water droplets in a hot gas flow **has** been investigated over a wide range of temperatures and velocities. The experimental results have been used to validate the droplet evaporation model of the NIST Fire Dynamics Simulator (FDS). Numerical simulations have been performed at three different gas velocities and initial gas temperatures. A comparison with the experimental data

has shown that the temperature profiles are qualitatively well predicted by the code and that the temperature differences between the wet and the *dry* conditions are similar to those obtained at the ECSAT facility. Additional improvements to the code, such a more comprehensive water droplet-hot gas heat transfer model and a better implementation of the boundary conditions, should result in a much closer agreement between the two sets of data.

We have implemented a new methodology to measure the temperature and volumetric fraction of a hot gas laden with water droplets. The preliminary sensor has been constructed at the ECSAT facility using components commercially available. The design and the realization of a new controlling circuit have led to a faster and more compact configuration of the sensor as well as a more accurate measurement over the range of interest. The final commercial version of the ALTEC sensor features a software-imbedded microchip, which controls the electric circuit and ~~has~~ data acquisition capabilities to time-average and filter the temperature readings.

Experimental tests have been performed to study the behavior of the ALTEC sensor under a wide range of boundary conditions. The versions of the sensor have been tested to gather the calibration curve and to control the precision of the measurements ~~as~~ opposed to traditional optical methodologies.

The commercial device will be demonstrated to companies such as Tyco and Factory Mutual Research Corporation for further testing and utilization in large-scale facilities. Additional applications of the sensor can be foreseen in the automotive and gas turbine industries as well as in the aerospace and industrial process business. A patent is pending on this technology.

APPENDIX 1 - DROPLET EVAPORATION THEORY²

Special Topics in Fire

Lecture #9 (11-11-96)

Material provided by dr. Jose' Torero

DEFINITION

The burning of single droplets or droplet arrays is a subject of great interest due to its multiple applications. Droplets can burn in a number of different ways, as a single droplet, as part of a number of droplets but with no droplet-to-droplet interaction or as a part of a droplet array where all the droplets interact with each other. The many applications of these three cases include propulsion, industrial burners, cable burning, melting and dripping surfaces. Other practical applications not related to combustion are water sprinklers and water mists.

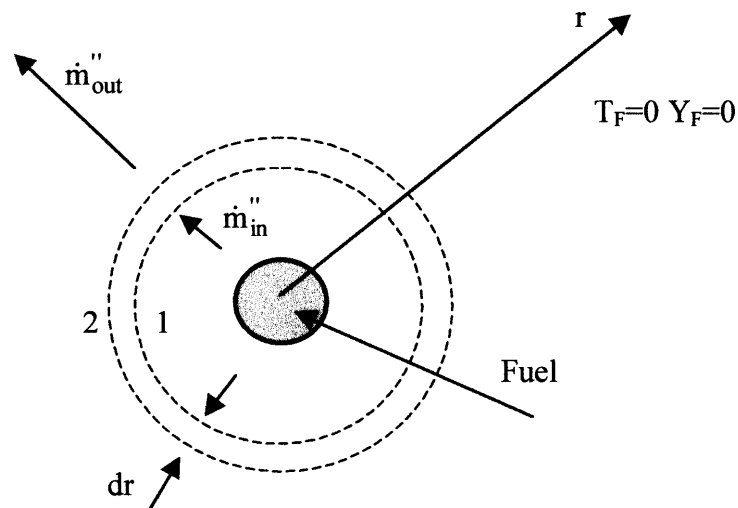
APPROACH AND ASSUMPTIONS

The main hypothesis behind the analysis that follows is that of infinitely fast chemistry. The flame is very thin (flame sheet approximation) and the burning rate is controlled by evaporation (slowest mechanism). The flame is established inside the boundary layer and therefore diffusion and fuel convection control transport. All external forced flow effects are considered negligible. Only one droplet is considered and droplet-to-droplet interactions are incorporated through empirical approximations. Radiative heat transfer is neglected due to the typical small sizes of

² The nomenclature used in this Appendix may be different from that used in the thesis

the droplets. The droplet diameter is generally very small when compared to the stand-off distance. Therefore the flame can be considered infinitely far from the droplet surface.

PROBLEM DEFINITION



- The control volume is used to derive the conservation equations.
- The flame is considered far away from the surface; therefore the boundary conditions will be established at $r \rightarrow \infty$.
- The droplet is considered spherical; therefore the equations are derived in spherical coordinates.
- Since the problem is axisymmetric on both angular variables, the only coordinate to be considered is r
- The droplet initial diameter is $2 \cdot R_0$ and it decreases as a function of time.

- Mass and energy transport are quasi-steady, meaning that for each droplet radius $R(t)$, transport reaches steady conditions before the radius changes again. Therefore, the problem can be treated as a steady state problem for each droplet radius.

Mass Flux

\dot{m}'' = radial mass flux per unit area = $\text{kg m}^{-2} \text{s}^{-1}$

\dot{m}_S'' = radial mass flux per unit area at the droplet surface

Regression rate

$\dot{R} = \frac{dR}{dt} = -\frac{\dot{m}_S''}{\rho} = \text{rate at which the droplet diameter decreases with time}$

Mass conservation

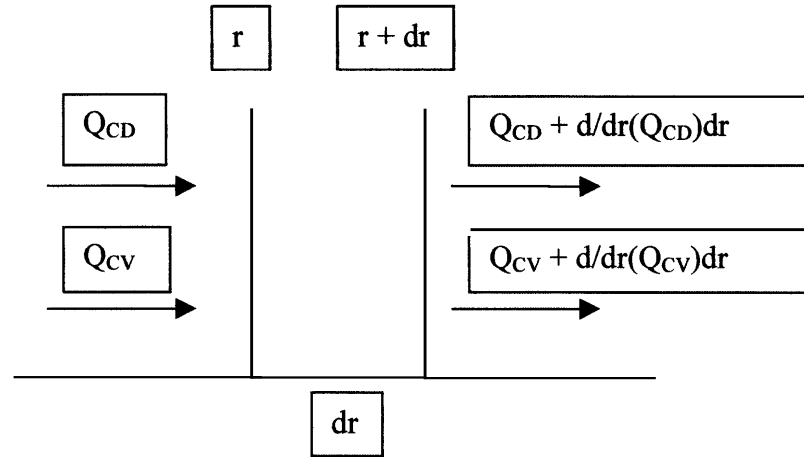
The basic hypothesis that is used to derive an expression for mass conservation is that mass going through each concentric spherical surface should remain constant. This is necessary since mass transport is axisymmetric on both angular variables and the analysis assumes steady state conditions (thus, no mass is accumulated in a control volume). Therefore, the total mass flowing through surface (1),

$\dot{M}_r = 4\pi r^2 \dot{m}_r''$, and through surface (2), $\dot{M}_r = 4\pi(r + dr)^2 \dot{m}_{r+dr}''$. Since the total

mass flow has to be conserved, then the following expression can be written:

$$4\pi r^2 \dot{m}_r'' = 4\pi(r + dr)^2 \dot{m}_{r+dr}'' = 4\pi R^2 \dot{m}_S'' = \text{constant} \quad (\text{A.1})$$

This expression is valid for both the condensed and the gas phases, but it breaks



down for $r \rightarrow 0$ since $\dot{m}_0'' = \frac{R}{r} \cdot \dot{m}_S'' \rightarrow \infty$.

Energy conservation

Assumptions:

- Steady state
- Taylor Series Expansion (first order approximation)
- Gas phase ($r > R(t)$)

$$Q_{\text{in}} - Q_{\text{out}} = 0 \quad (\text{A.2})$$

$$Q_{\text{in}} = Q_{\text{CD}} + Q_{\text{CV}}$$

$$Q_{\text{out}} = Q_{\text{CD}} + \frac{d}{dr}(Q_{\text{CD}}) dr + Q_{\text{CV}} + \frac{d}{dr}(Q_{\text{CV}}) dr$$

$$\frac{d}{dr}(Q_{cd}) + \frac{d}{dr}(Q_{cv}) = 0$$

where:

$$Q_{cd} = -4\pi r^2 k \frac{dT}{dr}$$

$$Q_{cv} = 4\pi r^2 \dot{m}'' C_p T = 4\pi R^2 \dot{m}_s'' C_p T$$

Substituting:

$$\frac{d}{dr} \left[4\pi r^2 \rho \alpha \frac{d(C_p T)}{dr} \right] - (4\pi R^2 \dot{m}_s'') \frac{d(C_p T)}{dr} = 0 \quad (A.3)$$

where α is the thermal diffusivity and if no subscripts are indicated properties are those of the gas phase.

Note. *Expression (A.3) is also valid for the condensed phase if all properties are substituted for those of the condensed phase, but, for this analysis, only the gas phase is of interest. So no subscripts are used restricting equations (A.1) and (A.3) to the gas phase.*

Species conservation (Fuel)

Following a similar analysis for species conservation equations can be derived for fuel and oxidizer. For the sake of simplification only the fuel equation is treated here.

$$\frac{d}{dr} \left[4\pi r^2 \rho \delta \frac{d(Y_F)}{dr} \right] - (4\pi R^2 \dot{m}_S) \frac{d(Y_F)}{dr} = 0 \quad (\text{A.4})$$

where δ is the molecular diffusivity.

BOUNDARY CONDITIONS

Equation (A.3) and (A.4) are second order differential equations. Therefore they require two boundary conditions for the temperature (T) and two for the fuel concentration (Y_F).

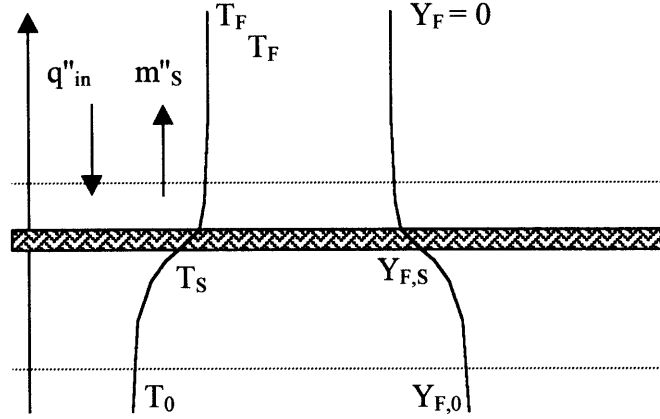
at $r \rightarrow \infty \Rightarrow T = T_F, Y_F = 0$

at $r \rightarrow R \Rightarrow T = T_S, Y_F = Y_{F,S}$

where T_S is the boiling or pyrolysis temperature and $Y_{F,S}$ is yet to be determined.

The value of T_S can be easily determined based on the ambient conditions. Instead $Y_{F,S}$ represents a much bigger challenge. A first order approximation could be used to assume $Y_{F,S}$ the saturation concentration at $T=T_S$. In this case $Y_{F,S}$ is obtained by means of mass conservation at the fuel surface. A third unknown in equations (A.3) and (A.4) is \dot{m}_S'' . Again, this value can be obtained from the energy conservation at the fuel surface.

FUEL SURFACE



Heat balance

Heat is transferred towards the surface (\dot{q}''_{in}). This heat **has** to bring the **fuel** from its ambient temperature T_0 to the vaporization temperature T_S and provide the vaporization of the fuel.

$$\dot{q}''_{in} = \dot{m}''_S \cdot [C_L(T_S - T_0) + \Lambda] = \dot{m}''_S \cdot Q \quad (A.5)$$

where C_L is the heat capacity of the liquid and A is the latent heat of vaporization. The quantity in square brackets **has** been called Q for convenience.

Also

$$\dot{q}''_{in} = k \frac{dT}{dr} \Big|_S = \rho \alpha \frac{d(C_p T)}{dr} \Big|_S = \dot{m}''_S \cdot Q$$

which leads to

$$\rho \alpha \left. \frac{d(C_p T / Q)}{dr} \right|_S = \dot{m}_S''$$

and the definition of an appropriate dimensionless variable f_1

$$f_1 = \frac{C_p(T - T_F)}{Q} \quad (\text{A.6})$$

The absolute value of f_1 at the surface is known as the mass transfer number or the Spalding B number:

$$B = \frac{C_p(T_S - T_F)}{Q} \quad (\text{A.7})$$

Mass balance

Fuel is conserved into the control volume with a concentration $Y_{F,-}$ and convected and diffused out to the gas phase with a concentration $Y_{F,S}$.

Therefore, the mass balance at the control volume (steady state) is given by:

$$\dot{m}_S'' Y_{F,0} = \dot{m}_S'' Y_{F,S} - \rho \delta \left. \frac{dY_F}{dr} \right|_S$$

which leads to:

$$\rho \delta \left. \frac{d(Y_F / Y_{F,S} - Y_{F,0})}{dr} \right|_S = \dot{m}_S''$$

and the formation of a second dimensionless group:

$$f_2 = \frac{Y_F}{Y_{F,S} - Y_{F,0}} \quad (\text{A.8})$$

Assumptions

For the purpose of obtaining one single differential equation to solve, the Lewis number is assumed to be unitary, leading to the following assumption

$$B = \frac{C_p(T_S - T_F)}{Q} = \frac{Y_{F,S}}{Y_{F,S} - Y_{F,0}}$$

NORMALIZED ENERGY AND SPECIES CONSERVATION

Substituting (A.6) and (A.8) on Equations (A.3) and (A.4) as well as on the respective **boundary** conditions, the following set of normalized equations is obtained:

$$\frac{d}{dr} (4\pi r^2 \rho a \frac{df_1}{dr}) - (4\pi R^2 \dot{m}_S'') \frac{df_1}{dr} = 0 \quad (\text{A.9})$$

Boundary conditions

- at $r \rightarrow \infty \Rightarrow f_1 = 0$
- at $r \rightarrow R \Rightarrow f_1 = -B, \left. \frac{df_1}{dr} \right|_S = \frac{\dot{m}_S''}{\rho \alpha}$

$$\frac{d}{dr} (4\pi r^2 \rho \delta \frac{df_2}{dr}) - (4\pi R^2 \dot{m}_S'') \frac{df_2}{dr} = 0 \quad (\text{A.10})$$

Boundary conditions

- at $r \rightarrow \infty \Rightarrow f_2 = 0$
- at $r \rightarrow R \Rightarrow f_2 = -B, \left. \frac{df_2}{dr} \right|_S = \frac{\dot{m}_S''}{\rho \delta}$

For Lewis number equal to one, $a = \delta$ and both equations can be reduced to one where f could be f_1 or f_2 .

$$\frac{d}{dr} (4\pi r^2 \rho \delta \frac{df}{dr}) - (4\pi R^2 \dot{m}_S'') \frac{df}{dr} = 0 \quad (\text{A.11})$$

Boundary conditions

- at $r \rightarrow \infty \Rightarrow f = 0$
- at $r \rightarrow R \Rightarrow f = -B, \left. \frac{df}{dr} \right|_S = \frac{\dot{m}_S''}{\rho \delta}$

Integrating (A.11) we obtain the following equation, which provides an expression for f :

$$\text{Ln} \left(\frac{B+1}{f+B+1} \right) = \frac{R^2 \dot{m}_S''}{\rho a r} \quad (\text{A.12})$$

THE D^2 LAW

At the surface, $r=R$ and $f=-B$ from the **boundary** conditions. Therefore:

$$\dot{m}_S'' = \frac{\rho \alpha}{R} \ln(B+1) \quad (\text{A.13})$$

In many situations it is of interest to know the diameter of the water droplet and the time it takes to completely evaporate. By substituting

$$\dot{m}_S'' = -\rho \frac{dR}{dt}$$

and integrating as a function of time, the following expression is found for the radius of the particle:

$$R^2 = R_0^2 - \alpha \cdot \ln(B+1) \cdot t$$

or equivalently:

$$D^2 = D_0^2 - 4\alpha \ln(B+1) \cdot t$$

The D^2 Law is commonly expressed as:

$$D^2 = D_0^2 + \lambda \cdot t \quad (\text{A.14})$$

where λ is a constant.

APPENDIX 2 - CONFIRMATION OF THE OPTICAL MEASUREMENTS

T_G	T^D	T^W	U	n	beta PTV	I pr. Beta
(°C)	(°C)	(°C)	(m/s)		(ppm)	(ppm)
137	156	80	3.9	13.2	2.5	1.6
147	162	115	3.9	18.2	3.5	3.7
137	143	92	3.6	8	3.5	5.4
134	157.5	101	3.7	15.2	3.1	2.9
133	147	77.9	4	17.2	3.2	3.4
114	121	38	5.3	27.2	5.4	7.6
105	115	36	4.5	35.2	5.1	5.9
163	168	100	6.1	33.6	6.3	7.4
167	176	121	5.8	22.4	4.6	4.7
221	227	172	7.4	35.2	5.2	5.6
167	178	105	5.8	38.4	7.6	5.5
104	116	35	3.1	43.2	8.1	9.2
89	97	33	4.6	44.8	5.9	6.5
87	91	32	3.5	51.2	8.2	11.7
131	142	71	3.9	40	6.1	7.5
151	160	89	3.9	36.8	5.6	8.1
169	179	104	4.8	43.2	5.4	5.9
144	150	76	4	52.8	7.9	9
169	178	113	7.1	44.8	3.8	3.2

APPENDIX 3 - EES CODE

{The independent variable is the temperature of the gas}

{input data}

$Re_q=0.2$

$S=0.2$

$T_{inf}=30$

$d=0.20/1000$

$L=0.03$

$a=0.09$

$b=0.0004$

{non-constant velocity situation}

$u=1.2549*(T_g-T_{inf})^{0.2398}$

{computation of the heat transfer coefficients}

$T_{fc}=(T_c+T_g)/2$

$\mu_{fc}=\text{viscosity}(\text{AIR}, T=T_{fc})/\text{density}(\text{AIR}, T=T_{fc}, P=1.013)$

$Re_c=u*d/\mu_{fc}$

$Nu_c=0.785*Re_c^{0.39}$

$h_c=Nu_c*\text{conductivity}(\text{AIR}, T=T_{fc})/d$

$T_{fh}=(T_h+T_g)/2$

$$\text{nih}=\text{viscosity}(\text{AIR},\text{T}=\text{Tfh})/\text{density}(\text{AIR},\text{T}=\text{Tfh},\text{P}=1.013)$$

$$\text{Reh}=\text{u}*\text{d}/\text{nih}$$

$$\text{Nuh}=0.785*\text{Reh}^{0.39}$$

$$\text{hh}=\text{Nuh}*\text{conductivity}(\text{AIR},\text{T}=\text{Tfh})/\text{d}$$

{equations of the electric circuit}

$$\text{hh}*3.14*\text{d}*L*(\text{Th}-\text{Tg})=\text{Vh}^2/(\text{a}+\text{b}*\text{Th})$$

$$\text{hc}*3.14*\text{d}*L*(\text{Tc}-\text{Tg})=(\text{Vh}/(\text{S}+\text{a}+\text{b}*\text{Tc}))^2*(\text{a}+\text{b}*\text{Tc})$$

$$\text{Req}=(\text{a}+\text{b}*\text{Th})*(\text{S}+\text{a}+\text{b}*\text{Tc})/(\text{a}+\text{b}*\text{Th}+\text{S}+\text{a}+\text{b}*\text{Tc})$$

$$\text{dVc}=\text{Vh}/(\text{S}+\text{a}+\text{b}*\text{Tc})*(\text{a}+\text{b}*\text{Tc})$$

$$\text{ratio_w}=(\text{a}+\text{b}*\text{Tc})/\text{S}$$

$$\text{I}=\text{Vh}/\text{Req}$$

$$\text{Vtop}=\text{Req}*\text{I}+\text{Vh}$$

$$\text{ratio_h}=\text{hh}/\text{hc}$$

$$\text{Ph}=\text{hh}*3.14*\text{d}*L*(\text{Th}-\text{Tg})$$

$$\text{Pc}=\text{hc}*3.14*\text{d}*L*(\text{Tc}-\text{Tg})$$

BIBLIOGRAPHY

Adrian R.J. "Particle-imaging techniques for experimental fluid mechanics", *Annual Review of Fluid Mechanics*, Vol. 23, pp.261-304, 1991.

Alpert R. L. "Calculation of Response Time of ceiling-mounted fire detectors", *Fire Technology*, Vol. 8, pp. 181-195, 1972.

Alpert R. L., "Calculated interaction of sprays with large scale buoyant flows", *Transactions of the ASME, Journal of Heat Transfer*, Vol. 106, pp. 310-317, 1984.

Avedisian C.T., Fatehi M. "An experimental study of the Leidenfrost evaporation characteristics of emulsified liquid droplets", *International Journal of Heat and Mass Transfer*, Vol. 31, no. 8, p. 1587-1603, 1988.

Avedisian C.T, Witte L.C. "Fundamental of phase change: Boiling and Condensation", *American Society of Mechanical Engineers*, New York, 1990.

Baumeister K.J., Schoessow G.J. "Diffusive and radiative effects on vaporization times of drops in film boiling", *AIChE symp. Ser.*, Vol. 69, no. 131, pp. 10-17, 1973.

Bergles A.E. "Engineering Foundation Conference on Pool and External Flow Boiling", *Published on behalf of the Engineering Foundation by the American Society of Mechanical Engineers*, New York, 1992.

Bernardin J. D., Stebbins C. J., Mudawar I. "Effects of surface roughness on water droplet impact history and heat transfer regimes", *Int. J. Heat Mass Transfer*, Vol. 40, no. 1, pp. 73-88, 1997.

Bernardin J. D., Stebbins C. J., Mudawar I. "Mapping of impact and heat transfer regimes of water drops impinging on a polished surface", *Int. J. Heat Mass Transfer*, Vol. 40, no.2, pp. 247-267, 1997.

Bete Nozzles Inc., Private Communications.

Betta V., Mazzei P., Naso V., Vanoli R. "Further contributions to the study of the Leidenfrost phenomenon", *Journal of Heat Transfer*, Vol. 101, pp. 612-616, 1979.

Brodkey R.S. "The phenomena of fluid motions", *Dover Publications, Inc.*, New York, 1995.

Bromley L.A., Leroy N.R., Robbers J.A. "Heat transfer in forced convection film boiling", *Industrial Chemical Engineering*, Vol. 45, pp. 2639-2646, 1953.

- Buglayev V.T., Vasil'yev F.V., Strebkov A.S. "Experimental investigation of heat transfer in evaporative cooling of air flows with fine droplets", *Heat Transfer - Soviet Research*, Vol. 17, no.5, pp. 97-103, 1986.
- Buttsworth D.R., Jones T.V. "A fast-response high spatial resolution total temperature probe using a pulsed heating technique", *Transactions of the ASME, Journal of Heat Transfer*, Vol. 120, pp. 601-607, 1998.
- Buttsworth D.R., Jones T.V., Chana K.S. "Unsteady total temperature measurements downstream of a high-pressure turbine", *Transactions of the ASME, Journal of Heat Transfer*, Vol. 120, pp. 760-766, 1998.
- Chow W.K. "On the effect of a sprinkler water spray", *Fire Technology*, pp. 364-373, 1989.
- Chow W.K., Cheung Y.L. "Selection of differencing schemes on simulating the sprinkler hot-air layer problem", *Numerical Heat Transfer, Part A (Applications)*, Vol.35, no.3, pp. 311-30, 1999.
- Chow W.K., Tao B. "Numerical modeling for interaction of a water spray with smoke layer", *Numerical heat transfer, Part A (applications)*, Vol. 39, no.3, pp. 267-283, 2001.
- Cooper L. Y. "The interaction of an isolated sprinkler spray and a two-layer compartment fire environment", *Int. J. Heat Mass Transfer*, Vol. 38, no. 4, pp. 679-690, 1995.
- Crowe C., Sommerfeld M., Tsuji Y. "Multiphase flow with droplets and particles", *CRC Press*, 1998.
- Cui Q., Chandra S., McCahan S. "The effect of dissolving gases or solids in water droplets boiling on a hot surface" *Private Communications*, 2000.
- di Marzo M., Evans D.D. "Dropwise evaporative cooling of high thermal conductivity materials", *Heat and Technology*, Vol.5, no. 1-2, pp. 126-36, 1987.
- di Marzo M., Tartarini P., Liao Y., Evans D., Baum H. "Evaporative cooling due to a gently deposited droplet", *International Journal of Heat and Mass Transfer*, Vol.36, no.17, pp. 4133-9, 1993.
- di Marzo M., Tinker S. "Evaporative Cooling due to a sparse spray", *Fire Safety Journal*, Vol. 27, pp. 289-303, 1996.
- Edson J.B., Anquetin S., Mestayer P.G., Sini J.F. "Spray droplet modeling. 11. An interactive Eulerian-Lagrangian model of evaporating spray droplets", *Journal of Geophysical Research*, Vol. 101, no.C1, pp. 1279-93, 1996.

Emerson G. S. "The effect of pressure and surface material on the Leidenfrost point of discrete drops of water", *International Journal of Heat Mass Transfer*, **18**, 381-386, 1975.

Fire protection handbook, *National Fire Protection Association*, 1997.

Fossa M. "A simple model to evaluate direct contact heat transfer and flow characteristics in annular two-phase flow", *International Journal of Heat and Fluid Flow*, Vol. **16**, pp. 272-279, 1995.

Fossa M., Pisoni C., Tagliafico L.A. "Experimental and theoretical results on upward annular flows in thermal non-equilibrium", *Experimental Thermal and Fluid Science*, Vol. **16**, pp. 220-229, 1998.

Fox R.W., McDonald A.T. "Introduction to fluid mechanics", *John Wiley & Sons*, New York, 1985.

Fuchs N.A. "The mechanics of Aerosols", *Dover Publications Inc.*, New York, 1964.

Fukai J., Shiiba Y., Miyatake O. "Theoretical study of droplet impingement on a solid surface below the Leidenfrost temperature", *Int. J. Heat Mass Transfer*, Vol. **40**, no. 10, pp. 2490-2492, 1997.

Gavelli F., Ruffino P., Anderson G., diMarzo M. "Evaporative Cooling and Thermal Fire Detector Response", *17th National Conference on Heat Transfer*, Italy, 1999.

Gottfried B.S., Lee C.J., Bell K.J. "The Leidenfrost Phenomenon: Film boiling of liquid droplets on a flat plate", *Int. J. Heat Mass Transfer*, Vol. **9**, no. 14, pp. 1167-1186, 1976.

Grissom W. M. and Wierum F.A. "Liquid spray cooling of a heated surface", *Int. J. Heat Mass Transfer*, Vol. **24**, pp. 261-271, 1981.

Harpole G.M. "Droplet evaporation in high temperature environments", *Transactions of the ASME. Journal of Heat Transfer*, Vol. **103**, no. 1, pp. 86-91, 1981.

Hatta N., Fujimoto H., Takuda H., Kimoshita K., Takahashi O. "Collision dynamics of water droplet impinging on a rigid surface above the Leidenfrost temperature", *ISIJ International*, Vol. **35**, pp. 50-55, 1995.

Healy W. M., Hartley J. G., Abdel-Khalik S.I. "Comparison between heretical models and experimental data for the spreading of liquid droplets impacting a solid surface", *Int. J. Heat Mass Transfer*, Vol. **39**, no. 14, pp. 3079-3082, 1996.

- Heskestad G. and Bill R.G., Jr. "Quantification of thermal responsiveness of automatic sprinkler including conduction effects", *Fire Safety Journal*, Vol. 14, pp. 113-125, 1988.
- Heskestad G., Smith H.F. "Investigation of a new sprinkler sensitivity approval test: the plunge test", *FRMC* 22485, Factory Mutual research corporation, Norwood, MA, 1976.
- Hiromitsu N., Kawaguchi O. "Influence of flow turbulence on the evaporation rate of a suspended droplet in a hot air flow", *Heat Transfer - Japanese Research*, Vol.24, no.8, pp. 689-700, 1995.
- Hishida K., Maeda M., Ikai S. "Heat transfer from a flat plate in two- component mist flow", *Transactions of the ASME. Journal of Heat Transfer*, Vol. 102, no.3, pp. 513-18, 1980.
- Hwang T.H., Moallemi M.K. "Heat transfer of evaporating droplets in low pressure systems", *International Communications in Heat and Mass Transfer*, Vol. 15, no.5, pp. 635-44, 1988.
- Inada S. and Yang W.J. "Film boiling heat transfer for saturated drops impinging on a heating surface", *International Journal of Heat and Mass Transfer*, Vol. 37, no. 16, pp. 2588-2591, 1994.
- Ito T., Nishikawa K., Shigechi T. "Forced convection film boiling heat transfer from a horizontal cylinder to liquid cross-flowing upward", *Bulletin of Japanese Society of Mech. Eng.*, Vol. 24, pp. 2107-2114, 1981.
- Kitagawa T., Torii K., Nishino, K. "Heat transfer of air-water dispersed flow in a vertical pipe", *Heat Transfer - Japanese Research*, Vol.27, no.4, p. 255-70, 1998.
- Kulmala M., Vesala T., Schwarz J., Smolik J. "Mass transfer from a drop. 11. Theoretical analysis of temperature dependent mass flux correlation", *International Journal of Heat and Mass Transfer*, Vol.38, no.9, pp. 1705-8, 1995.
- Kurosaki Y., Satoh I., Ishize T. "Mechanisms of heat Transfer Enhancement of gas-solid fluidized bed: estimation of direct contact heat exchange from heat transfer surface to fluidized particles using an optical visualization technique", *Transaction of the ASME, Journal of Heat Transfer*, Vol. 117, pp. 105-112, 1995.
- Lee S.L., Yang Z.H., Hsyua Y. "Cooling of a heated surface by mist flow", *Transaction of the ASME, Journal of Heat Transfer*, Vol. 116, pp. 167-173, 1994.
- Makino K., Michiyoshi I. "The behavior of a water droplet on heated surfaces", *Int. J. Heat Mass Transfer*, Vol. 27, no. 5, pp. 781-791, 1984.

- Mastanaiah K., Ganic E.N. "Surface effect on droplet deposition in two-phase flow", *International Journal of Heat and Mass Transfer*, Vol.25, no.3, pp. 422-4, 1982.
- McCaffrey B.J., Heskestad G. "A robust bi-directional low-velocity probe for flame and fire protection", *Combustion and Flame*, Vol. 26, pp. 125-127, 1976.
- McGrattan K.B., Baum H.R., Rehm R.G., Hamins A. and Forney G.P. "Fire Dynamics Simulator, Technical reference guide", *Technical Report NISTIR 6467*, NIST, Gaithersburg, MD, 2000.
- Montlucon J. "Heat and mass transfer in the vicinity of an evaporating droplet", *International Journal of Multiphase Flow*, Vol.2, no.2, pp. 171-82, 1975.
- Mosdorf R., Poniewski M. "Statistic analysis of the boiling curve for a droplet", *International Journal of Heat and Mass Transfer*, Vol.30, no.7, pp. 1479-85, 1987.
- Panton, R. L., "Incompressible flow", *John Wiley & Sons*, 1984.
- Renksizbulut M., Yuen M.C. "Experimental study of droplet evaporation in a high-temperature air stream", *Transactions of the ASME. Journal of Heat Transfer*, Vol.105, no.2, pp. 384-8, 1983.
- Renksizbulut M., Yuen M.C. "Numerical study of droplet evaporation in a high-temperature stream", *Transactions of the ASME. Journal of Heat Transfer*, Vol. 105, no.2, pp. 389-97, 1983.
- Ross R.H., Davis J.R. "Experimental results of water film formation on various fuel forms from a fire suppression system", *Transactions of the American Nuclear Society*, Vol.70, pp. 204-5, 1994.
- Ruffino P., diMarzo M. "Experimental study on the effect of evaporative cooling on the thermal response of commercial fire sprinklers", *ASME National Heat Transfer Conference 2000*, Pittsburgh PA, 2000.
- Senda J., Yamada K., Fujimoto H., Miki H. "The heat-transfer characteristics of a small droplet impinging upon a hot surface", *JSME International Journal, Series II (Fluids Engineering, Heat Transfer, Power, Combustion, Thermophysical Properties)*, Vol.31, no.1, pp. 105-11, 1988.
- Society of Fire Protection Engineers, "Fire Protection Handbook", Second edition, 1995.
- van Paassen C.A.A. "Thermal droplet size measurements using a thermocouple", *International Journal of Heat and Mass Transfer*, Vol. 17, no. 12, pp. 1527-48, 1974.

Wu-Shung Fu, Gih-Cheng Yang "Influence of droplets' trajectories and size distribution on heat transfer from a wedge in an air-water mist flow", *Numerical Heat Transfer, Part A (Applications)*, Vol. 16, n0.2, pp. 155-74, 1989.

Yao C. "Overview of sprinkler technology research", *Fire Safety Science - Proc. 5th Int. Symposium*, ed. Curtat, M.R. & Bodart, XI, IAFSS, Bethesda, MD, 1999.

Yao S.C., Hochreiter L.E., Cai K.Y. "Dynamics of droplets impacting on thin heated strips", *Journal of Heat Transfer*, Vol. 110, pp. 214-220, 1988.

Yuen M.C., Chen, L.W. "Heat-transfer measurements of evaporating liquid droplets", *International Journal of Heat and Mass Transfer*, Vol.21, no.5, pp. 537-42, 1978.

Zakauskas A., Ziugzda J. "Heat transfer of a cylinder in cross-flow", *Hemisphere Publishing Corporation*, 1985.

"Standard for Automatic Sprinklers for Fire-Protection Service", *UL199 8th edition*, Underwriter Laboratories Inc., Sect. 19, 1992.

NIST-114 U.S. DEPARTMENT OF COMMERCE (REV. 6-93) NATIONAL INSTITUTE OF STANDARDS AND TECHNOLOGY ADMAN 4.09 <h2 style="text-align: center;">MANUSCRIPT REVIEW AND APPROVAL</h2>		(ERB USE ONLY)	
INSTRUCTIONS: ATTACH ORIGINAL OF THIS FORM TO ONE (1) COPY OF MANUSCRIPT AND SEND TO: WEBB SECRETARY, BUILDING 820, ROOM 125 TITLE AND SUBTITLE (CITE IN FULL) <h3>Measurements of Temperature in a Hot Gas Laden with Water Droplets</h3>		ERB CONTROL NUMBER PUBLICATIONS REPORT NUMBER No. NIST GCR 01-827	
		DIVISION CATEGORY CODE	
		PUBLICATION DATE September 2001	
CONTRACT OR GRANT NUMBER 60NANB8D0012		TYPE OF REPORT AND/OR PERIOD COVERED May 2, 1999 to August 31, 2001	
AUTHOR(S) (LAST NAME, FIRST INITIAL, SECOND INITIAL) Rufino, P. and di Marzo, M. University of Maryland College Park, MD 20742		PERFORMING ORGANIZATION (CHECK (X) ONE BOX) <div style="display: flex; align-items: center;"> <input type="checkbox"/> NIST/GAITHERSBURG <input type="checkbox"/> NIST/BOULDER <input type="checkbox"/> NIST/JILA </div>	
SPONSORING ORGANIZATION NAME AND COMPLETE ADDRESS (STREET, CITY, STATE, ZIP) U.S. Department of Commerce, Natl. Inst. of Stds & Tech., Gaithersburg, MD 20899			
<input type="checkbox"/> JOURNAL OF RESEARCH (NIST JRES) <input type="checkbox"/> J. PHYS. & CHEM. REF. DATA (JPCRD) <input type="checkbox"/> HANDBOOK (NIST HB) <input type="checkbox"/> SPECIAL PUBLICATION (NIST SP) <input type="checkbox"/> TECHNICAL NOTE (TN)		<input type="checkbox"/> MONOGRAPH (NIST MN) <input type="checkbox"/> NATL. STD. REF. DATA SERIES (NIST NSRDS) <input type="checkbox"/> FEDERAL INFO. PROCESS. STDS. (NIST FIPS) <input type="checkbox"/> LIST OF PUBLICATIONS (NIST LP) <input type="checkbox"/> INTERAGENCY/INTERNAL REPORT (NISTIR)	
PROPOSED FOR NON-NIST PUBLICATION (CITE FULLY):		<input type="checkbox"/> - U.S. <input type="checkbox"/> FOREIGN -	
PUBLISHING MEDIUM: <input checked="" type="checkbox"/> PAPER		<input type="checkbox"/> DISKETTE <input type="checkbox"/> CD-ROM <input type="checkbox"/> WWW <input type="checkbox"/> OTHER	
ABSTRACT (A 2000-CHARACTER OR LESS FACTUAL SUMMARY OF MOST SIGNIFICANT INFORMATION. IF DOCUMENT INCLUDES A SIGNIFICANT BIBLIOGRAPHY OR LITERATURE SURVEY, CITE IT HERE. SPELL OUT ACRONYMS ON FIRST REFERENCE.) (CONTINUE ON SEPARATE PAGE, IF NECESSARY.) <p>Arrays of fire sprinklers are installed in buildings to protect property and occupants against the damages of fire. When a fire occurs, the sprinkler closest to the fire location typically activates first and releases water droplets into the rising plume of hot gases. Part of these droplets is entrained by the plume and may impact on adjacent sprinklers providing evaporative cooling and thus delaying their activation. The current model that simulates the thermal response of fire sprinklers does not include this evaporative cooling effect. Therefore, a new model is proposed to extend the applicability of the previous formulation. The new model includes one parameter, determined experimentally, that is associated to the evaporative cooling effect. Commercially available sprinklers are tested to assess the accuracy of the proposed model for a range of boundary conditions. The sprinkler activation times predicted by the model are found to be in good agreement with the measurements, within the experimental uncertainties. A new methodology to measure the gas temperature and the water volumetric fraction of a gas-water flow is also implemented and the results are compared with those gathered by optical techniques.</p>			
KEY WORDS (MAXIMUM OF 9; 28 CHARACTERS AND SPACES EACH; SEPARATE WITH SEMICOLONS; ALPHABETIC ORDER; CAPITALIZE ONLY PROPER NAMES) droplets; fire detection systems; high temperature gases; mathematical models; sprinklers; temperature			
AVAILABILITY: 3 UNLIMITED <input type="checkbox"/> FOR OFFICIAL DISTRIBUTION - DO NOT RELEASE TO NTIS ORDER FROM SUPERINTENDENT OF DOCUMENTS, U.S. GPO, WASHINGTON, DC 20402		NOTE TO AUTHOR(S): IF YOU DO NOT WISH THIS MANUSCRIPT ANNOUNCED BEFORE PUBLICATION, PLEASE CHECK HERE.	